



Proceedings of 1st International Conference on Advances in Mechanical, Materials, Mechatronics and Energy Engineering (ICAME-24)

BOOK OF PROCEEDINGS

Organized By

**Faculty of Mechanical and Aeronautical Engineering
University of Engineering & Technology, Taxila**

ISBN : 978 - 627 - 94520 - 0 - 9



Patron-in-Chief

Prof. Dr. Muhammad Inayatullah Khan
Vice Chancellor,
UET Taxila.



Patron

Prof. Dr. Qaiser-uz-Zaman Khan
Pro Vice Chancellor,
UET Taxila.



Conference Chair

Prof. Dr. Riffat Asim Pasha
Chairman Department of Mechanical Engineering,
UET Taxila.



Conference Chief Organizer

Prof. Dr. Muhammad Ali Nasir
Director Postgraduate Studies,
UET Taxila.



Conference Secretary

Dr. Aneela Wakeel
Assistant Professor,
Department of Metallurgy & Materials Engineering,
UET Taxila.



Editor-in-Chief

Prof. Dr. Riffat Asim Pasha

Editors

Dr. Aneela Wakeel

Dr. Ammar Ul Hassan Khawaja

Technical Advisors

Prof. Dr. Muzaffar Ali

Dr. Shahid Mehmood

Dr. Azhar Hussain

Prof. Dr. Muhammad Ali Nasir

Dr. Mubashir Gulzar

Dr. Muhammad Khurram Saleem

Technical Review Committee

Prof. Ir. Dr. Mohd Sapuan Salit

Prof. Dr. Müslüm Arıcı

Dr. Hafiz Muhammad Ali

Prof. Dr. Yasir Nawab

Prof. Dr. Adeel Waqas

Prof. Dr. Emad Ud Din

Prof. Dr. Umar Shahbaz Khan

Prof. Dr. Mohsin Ali Raza

Dr. Taqi Ahmed Cheema

Dr. Zabdur Rehman

Dr. Abdul Wadood

Dr. Ramzan Karim

Dr. Rizwan Ahmed Malik

Dr. Mohsin Abbas

Dr. Adnan Dawood

Dr. Saeed Badshah

Dr. Sahar Noor

Dr. Waheed ur Rehman

Dr. Luqman Ahmad Nizam

Dr. Hafiz Farhan Maqbool

Dr. Waqar Shahid Qureshi

Prof. Dr Lida Shen

Prof. Dr. Mehmet Karahan

Prof. Dr. Muhammad Tufail

Prof. Dr. Muhammad Abid

Prof. Dr. Nadeem Ahmed Sheikh

Prof. Dr. Rizwan Mehmood Gul

Prof. Dr. Fahd Nawaz Khan

Prof. Dr. Adnan Tariq

Dr. Khurram Pervaiz

Dr. Wajid Ali Khan

Dr. Sheraz Yaqub

Dr. Muhammad Abdul Ahad

Dr. Fahad Butt

Dr. Saad Nouman

Dr. Abdul Qadir

Dr. Naeem Abbas

Dr. Hassan Elahi

Dr. Roman Kalvin

Dr. Rizwan Gull

Dr. Muhammad Awais Hafeez

Dr. Hashim Iqbal

TABLE OF CONTENTS

Sr. No.	Keynote Talks/ Paper ID	Paper Title	Page No.
1	Keynote Talk	Advantages and Challenges of 3D Printed Components for Aerospace Applications	5
2	Keynote Talk	Role of phase change materials in sustainable development goals: Performance evaluation indexes and performance comparison with conventional methods	5
3	Keynote Talk	Effect of ZnO Filler Modification on Aging and Mechanical Properties of Carbon-Epoxy Composites	6
4	Keynote Talk	Progress in condensation heat transfer on external horizontal tubes for surface condensers	6
5	Keynote Talk	Advancement in sustainable composites embedded with smart electronics	7
6	Keynote Talk	Composite Materials Research and Applications: A Focus on Global Trends and the Landscape in Pakistan	7
7	Keynote Talk	Graphene Oxide: From Coatings to Composites and Beyond	8
8	Keynote Talk	Applications of advanced composite materials towards aerospace design and manufacturing	8
9	Keynote Talk	Efficient techniques to recover power from waste using CO ₂ as working fluid	9
10	Keynote Talk	Navigating Tomorrow: Pakistan's Robotic Odyssey	9
11	Keynote Talk	Advance In Use of UHMWPE in Total Joint Replacements	10
12	Keynote Talk	Progress in condensation heat transfer on external horizontal tubes for surface condensers	10
13	Keynote Talk	Interactions Between Fluids and Flexible Bodies: Engineering Insights from Nature	11
14	Keynote Talk	Sedimentation: A Threat to Water-Energy-Food Nexus	11
15	Keynote Talk	Evaluation of Lower Limb Amputees using Inertial Measurement Units	12
16	Keynote Talk	Energy Consumption in Pakistani Residential Buildings: Insights from Degree Days Analysis and Appliance Consumption Patterns	12
17	Keynote Talk	Thermal Management of the Batteries for Electric Vehicles	13
18	Keynote Talk	Empowering Energy Storage: Unveiling the Potential of Transition Metal Based electrode materials for Supercapacitors	13
19	ME-101	Incorporating Power Law for The Estimation of Maximum Strain Under Pressure Loading for Solid Propellant Grain in Conjunction With FEM	14
20	ME-102	Supply Chain Management in Oil & Gas Field in Pakistan - Challenges and Solutions	18
21	MCT-104	Temporal Assessment Box: Neurological Disease Diagnosis through Manual Dexterity Analysis	22
22	ME-106	Quantitative Assessment of Ground Penetrating Radar for Concrete Structure Integrity	27
23	ME-107	Electromagnetic Testing: Prospects and Advancements for Industrial Inspections	32
24	MAT-108	Parametric optimization and comparison of Digital Radiography with Conventional Radiographic Testing	38
25	ME-109	Finite Element Analysis of Portable Grain Segregation System	45
26	ENE-113	Investigation of heat exchange performance with stainless steel double-walled pipe of power plant	50
27	ME-114	Structural and Thermal Numerical Investigation of Multiple Configurations of Super Insulated Cryogenic pipe for Liquid Nitrogen	55
28	ME-115	Design and Development of Solar Assisted Hybrid Bicycle	61
29	MCT-119	Wearable Data Acquisition System for Biomechanical Analysis	67
30	ME-121	FEM Based Complex Multivariate Random Vibration Fatigue Life Prediction of a Tracked Vehicle Balance Arm Using Various Road Surface Profiles	72
31	MCT-123	Simulation of Collaborative Controlled Collision Avoiding Robot	78
32	ME-124	Performance Analysis of V-Trough Concentrators	84
33	ENE-125	Experimental Comparative Investigation of EGR and Water Injection for Lean and Rich Combustion in Turbocharged Diesel Engine	90
34	MAT-126	Experimental Investigation of Mechanical Properties of Biodegradable Polymer Composite for Artificial Orthopedic Implants	95
35	MAT-131	Evaluating the Influence of SiC coating on Surface Characteristics of UHMWPE	100
36	MAT-134	Estimation of Creep Behaviour of CFRP Composite under Hoop Stress through ASTM D2290 and Accelerated Testing Methodology	104
37	ME-144	Enhancing Mint Yield through IoT-Integrated Vertical Hydroponic Systems: A Sustainable Solution for Future Agriculture	109
38	MAT-150	Assessment of Erosive Wear Resistance Characteristics of 3D Printed Polymers Agitator Blade	115
39	ME-151	Experimental Identification of Campbell Diagram of a Flexible Rotor Supported by Active Magnetic Bearings	119
40	MAT-158	Study on the Impact of Ozone and Humidity on the Aging of Polymeric Composite Materials	124
41	ENE-161	Evaluating Capillary Pressure and Relative Permeability Models for Enhanced Reservoir Management	128
42	ENE-162	Investigating Public Opinion to Overcome Energy Policy Hurdles in Pakistan	133
43	MCT-167	Enhancing the Accuracy of SSVEP Target Frequency Detection: A User-Friendly Approach	138
44	ENE-173	Analysis Of Vertical Axis Wind Turbine Utilizing Dissimilar Airfoil Blade Combination	144
45	ME-176	Topology Optimization of Bell Crank Lever using FEA	152
46	MCT-179	Intelligent System for Real-time Health Monitoring of Power MOSFETs	157
47	MAT-180	Superelasticity of Mesoscopically Porous Ni-Fe-Ga Shape Memory Alloy Foam with 69% Porosity	164
48	ME-181	Optimization Analysis of Innovative Counter Flow Spiral Absorber Tubes for Thermal Management of Photovoltaic Modules	169
49	MAT-182	Corrosion Inhibition through Biofilms: A Comprehensive Review	175
50	MAT-183	Recent Advances in Energy Materials for Sustainable Energy Materials	180
51	ME-185	Eco-Transit Revolution: Design and fabrication of Three Wheeled reverse trike Vehicles	187
52	ENE-186	Numerical Analysis and Performance Optimization of Multi-Stage Regenerative Heat and Mass Exchanger	192
53	ME-187	Unmanned Under Water Vehicle (UUV) Pressure Hull Design using Composite Materials	197
54	ME-188	Effect of Pressure on Rough Piston Skirt in Iso-Thermal Hydrodynamic Lubrication Case for High Torque Low Speed Diesel Engine	206
ME: MECHANICAL ENGINEERING, MAT: MATERIALS ENGINEERING, ENE: ENERGY ENGINEERING, MCT: MECHATRONICS ENGINEERING			

KEYNOTE SPEAKERS

INTERNATIONAL SPEAKERS



**Prof. Ir. Dr. Mohd
Sapuan Salit**
Head of (LBT), (INTROP),
(UPM) Malaysia



Prof. Dr. Lida Shen
Nanjing University of
Aeronautics &
Astronautics China



Prof. Dr. Müslüm Arıcı
Kocaeli University,
Turkey



Prof. Dr. Mehmet Karahan
Uludag University,
Turkey

NATIONAL SPEAKERS



**Prof. Dr. Muhammad
Tufail**
NED University, Karachi



Prof. Dr. Yasir Nawab
Kamalia University,
Faisalabad



Prof. Dr. Adeel Waqas
NUST



**Prof. Dr. Nadeem
Ahmed Sheikh**
IIUI



**Prof. Dr. Mohsin
Ali Raza**
UOP



**Prof. Dr. Rizwan
Mehmood Gul**
UETP



**Prof. Dr. Emad
Ud Din**
NUST



**Prof. Dr. Umar
Shahbaz Khan**
NUST



**Engr. Dr. Khuram
Pervez Amber**
MUST



Dr. Hafiz Muhammad Ali
KFUPM, SA



Dr. Taqi Ahmad Cheema
GIKI Swabi



**Dr. Muhammad
Ramzan Abdul Karim**
GIKI Swabi



Dr. Mohsan Haider
CEO
Turkish Aerospace



**Dr. Hafiz Farhan
Maqbool**
UET Lahore



Dr. Noman Naseer
Air University
Islamabad



Advantages and Challenges of 3D Printed Components for Aerospace Applications

Prof. Dr. Lida Shen

Institute of Additive Manufacturing (3D Printing), NUAA
College of Mechanical and Electrical Engineering
Nanjing University of Aeronautics & Astronautics, 29 Yudao Street, Nanjing 210016, China
ldshen@nuaa.edu.cn

ABSTRACT

3D printing has become one of the major focuses in the aerospace domain, and a considerable amount of integrated components have been manufactured with innovation in design and functionalization. The main focus of the presentation will be on the Voronoi and triply periodic minimal surface TPMS-based 3D-printed components for aerospace applications. Furthermore, the advantages and the potential methods to solve challenges in this research direction will be highlighted and discussed. The Voronoi and TPMS-based lightweight porous structures can be fabricated via 3D printing with various porosity distributions and similar structural strength as solid structures. Particularly, integrated performance such as vibration isolation, and heat management can also be realized based on innovative structures. Based on these two aspects, functional components such as heat exchangers with low volume, and enhanced heat transfer performance can be obtained, while L-PBF could ensure the interior design of the component. However, challenges remain for 3D printing, especially the deformation control for thin-walled structures. The high-temperature gradient and residual stress could give rise to severe deformation. In addition, the fatigue performance of components is strongly associated with defects such as micropores introduced during the printing process. Therefore, the presentation will discuss the genetic algorithm neural network which is a potential approach to regulate deformation and defects simultaneously. The information shared in this talk is intended to stimulate more research development and provide engineering solutions to 3D-printed parts for aerospace applications.

Role of Phase Change Materials in Sustainable Development Goals: Performance Evaluation Indexes and Performance Comparison with Conventional Methods

Prof. Dr. Müslüm Arıcı

Head of International Joint Laboratory on Low-Carbon and New-Energy Nexus Research and Development,
Department of Mechanical Engineering, Faculty of Engineering
Kocaeli University, 41001, Kocaeli, Turkey
muslumarici@kocaeli.edu.tr

ABSTRACT

Considering the ongoing energy crisis throughout the world and expected shortages in energy production as well as supply in the upcoming years, it is obvious that the development of methodologies regarding the energy saving/reduction in buildings has great importance. To combat such highly potential risks associated with energy and reach sustainable development goals, different materials and methods are proposed by researchers in literature. One of the novel methods is the utilization of phase change materials (PCM) to store energy and shift peak loading period. PCMs have high latent heat capacity which can be benefited during solid-liquid (or vice versa) phase change process. Besides, they are available in a wide range of phase change temperatures making them proper candidates in different fields from cryogenic applications to concentrated solar power plants. In this talk, we will focus on PCM applications in buildings. Since the performance of PCM is affected by several parameters, i.e., phase change temperature, latent heat content, besides to other thermophysical properties, existing methods used for thermal performance evaluation are inadequate and a novel index or evaluation method is necessary to quantify the effectiveness of PCM. Besides, in this talk, a comparison based on a case study will be presented to reveal the advantages or disadvantages of each method/parameter so that they can be interpreted more insightfully. Moreover, the performance of PCM will be compared with the conventional materials, and the synergetic effect will be addressed.



Recent Advances in Biocomposites in Engineering Applications: Piezoelectric Sensor and Electric Vehicles Battery Casing

Prof. Dr. Mohd Sapuan Salit

Advanced Engineering Materials and Composites Research Centre (AEMC)
Department of Mechanical and Manufacturing Engineering
Universiti Putra Malaysia, 43400 UPM Serdang, Selangor, Malaysia
sapuan@upm.edu.my

ABSTRACT

Biocomposites, materials derived from a combination of natural fibers and biodegradable polymers, have emerged as a sustainable and promising alternative in engineering applications. This presentation will highlight the recent advances in the utilization of biocomposite, focusing on two critical applications: Piezoelectric Sensor and Electric Vehicles (EVs) Battery Casing. In the realm of sensing technology, biocomposite materials exhibit exceptional properties conducive to the development of efficient and environmentally friendly Piezoelectric Sensors. The integration of these sensors into structural components allows for the conversion of mechanical energy into electrical signals, presenting novel opportunities for smart structures, health monitoring, and energy harvesting. Furthermore, in this presentation, we will explore into the application of biocomposite in the fabrication of Electric Vehicles Battery Casings. As the demand for sustainable transportation grows, the development of lightweight, durable, and eco-friendly materials becomes imperative. Biocomposites offer a compelling solution by providing a balance between structural integrity, thermal management, and environmental impact, contributing to the evolution of electric vehicle technologies. This comprehensive exploration of Recent Advances in Biocomposites showcases their potential in enhancing the performance, sustainability, and versatility of engineering applications. The findings presented in this presentation aim to contribute to the ongoing discourse on biocomposite materials and inspire further research in the quest for innovative and eco-conscious engineering solutions.

Effect of ZnO Filler Modification on Aging and Mechanical Properties of Carbon-Epoxy Composites

Prof. Dr. Mehmet Karahan^{1*}, Fatmagül Dede^{2,3} and Muhammad Ali Nasir⁴

¹ Bursa Uludag University, Vocational School of technical Sciences, 16059, Nilufer, Bursa, Turkey

² Bursa Uludag University, Faculty of Engineering, Mechanical Engineering Department, Gorukle Campus, 16059, Nilufer, Bursa, Turkey

³ Bursa Technology Coordination and R&D Center, Demirtas Dumlupinar OSB District, 2nd Cigdem Street No:1/4, 16245, Osmangazi, Bursa, Turkey

⁴ University of Engineering & Technology, Department of Mechanical Engineering, Taxila, Pakistan

* mkarahan@uludag.edu.tr

ABSTRACT

Polymer composites tend to age over time, which leads to a decrease in their mechanical properties. Both internal and external factors can cause this, such as high temperature, humidity, ultraviolet rays, ozone, chain structure, combination, and aggregation. To prevent the aging of polymer matrix composite materials due to moisture and ozone, chemical fillers have been used. The purpose of this study is to demonstrate through experimental studies, tests, and analyses that the use of aging retarding or preventive agents in composite production can extend the life and improve the safety of composite materials. The study investigates the aging effect of carbon/epoxy composites at different humidity and ozone concentrations and determines the effect of ZnO added to the epoxy resin on the aging life. The results showed that ZnO used as a filler reacted with ozone and improved the mechanical properties of the composite material. The tensile strengths of samples exposed to ozone and to which ZnO powder was added at the rates of 1%, 2%, and 4% increased by 2.26%, 10.62% and 20.08%, respectively, compared to pure samples. This experiment was repeated at different ozone and humidity concentrations and the results were recorded. Tensile strengths increased and mechanical properties improved as a result of ozone exposure in all ZnO-doped samples.



Progress in Condensation Heat Transfer on External Horizontal Tubes for Surface Condensers

Dr. Hafiz Muhammad Ali

Mechanical Engineering Department, King Fahd University of Petroleum and Minerals, Dhahran, 31261, Saudi Arabia
hafiz.ali@kfupm.edu.sa

ABSTRACT

Condensation heat transfer plays a vital role in various applications, one of the major applications of condensation heat transfer is on horizontal tubes used in surface condensers of nuclear thermal power cycle to produce electricity. Surface condenser is responsible to create low pressure that provides the thrust force to steam moving to turbine for efficient power generation. Therefore, the role of condensation heat transfer on horizontal tubes has significant importance in thermal power plants. This talk will review the progress on fundamentals of condensation heat transfer by considering the various parameters that impact on condensation heat transfer such as condensate retention, tube geometries, role of fluids hydrodynamic and thermofluidic properties, type of pure or mixture of steam, limitations and advances of surface structures, free and forced convection condensation heat transfer experimental results and model developments. This talk will identify the gaps to be further explored to enhance the heat transfer performance of surface condensers horizontal tubes.

Advancement in Sustainable Composites Embedded with Smart Electronics

Engr. Shehroze Ali Baig, Prof. Dr. Bilal Zahid and Prof. Dr. Muhammad Tufail

NED University of Engineering & Technology, Karachi
mtufail@neduet.edu.pk

ABSTRACT

The development of natural fiber composites (NFCs) has poised to redefine industries with having a sustainable material possessing favorable specific properties i.e., high strength to weight ratio which is due to their being lightweight, high-strength, and sustainable properties. Although, composite materials have already revolutionized major sectors like aerospace, construction, sports, and automotive industry where the weight of the component/part is considered to be very crucial. To further expand the benefits of the composite materials, the integration of embedded electronics into these composites had opened groundbreaking avenues wherein proper feedback mechanisms are incorporated in these materials. However, an optimized mechanism or process for incorporating these feedback systems into composite materials is still considered as a significant concern. Although there are several techniques to produce textile fabric, weaving is mainly considered due to the reason that they offer better control over fabric resulting in better stability and strength which is essential as reinforcement. These smart composites hold immense potential to transform diverse fields, from structural engineering to wearable technology, offering a sustainable and technologically advanced alternative in industries such as automotive, construction, and packaging. The integration of electronics into woven composites offers not only enhanced functionality but also opens avenues for environmentally friendly manufacturing processes. Not only limited to research basis, but smart composite is also one of the trendy topics in current era for Industries focused upon IR 4.0 and IR 5.0, which further validates the significance of the topic.

Recent advancements in textile technology, driven by the demand for high-quality products, have led to the use of fibers with special characteristics such as energy collection, color tuning, health monitoring, shape memory, and heat storage. This new generation of textiles includes passive smart textiles (sensing external conditions), active smart textiles (responding to external conditions), and ultra-smart textiles (sensing, reacting, and adapting to conditions). Applications range from basic reinforcement in composites to sophisticated functionalities such as conductive or antibacterial properties, energy harvesting, energy storage, and thermo-regulated fabrics. Smart textiles represent a significant leap in the versatility and adaptability of textile materials in response to modern societal needs.

Despite recent advancements in composite materials, there remains a gap in bringing a seamless integration of embedded electronics with functional fibers through a sustainable and intelligent manner. This research aims to address this gap by exploring novel weaving techniques for creating smart and sustainable composites.



Composite Materials Research and Applications: A Focus on Global Trends and the Landscape in Pakistan

Prof. Dr. Yasir Nawab

National Center for Composite Materials, School of Engineering & Technology, National Textile University, Faisalabad
ynawab@ntu.edu.pk

ABSTRACT

Fiber reinforced polymeric composites are one of the highly value-added applications of textiles and considered as the major type of Technical Textiles. These are one of the emerging materials replacing metals rapidly in engineering applications especially in sports equipment, marine, wind turbine, aerospace, defense and automotive applications. The global market for composite materials is projected to reach \$130.8 billion by 2024, with a compound annual growth rate of 7.8%. This growth is fueled by ongoing research and development efforts aimed at meeting specific industry requirements. In the aerospace sector, there is a continuous quest for innovative solutions to enhance the structural integrity and protective capabilities of composite materials. Recent advancements include the development of Fiber Metal Laminates (FML), Composite Metal joining techniques, and the incorporation of nano reinforcements for structural health monitoring, to achieve electromagnetic interference (EMI) shielding, structural stability, etc. In Pakistan, 120 to 150 small and medium sized organizations related to composites are operating but their share to global market is minute due to unavailability of well-trained human resource, research & development facilities, testing facilities and lack of new entrants/startups in the domains. These are mainly operating in sports, automotive, aerospace, and civil structural applications.

This paper provides an overview of global trends in composite materials research and applications, with a focus on the status and prospects in Pakistan.

Graphene Oxide: From Coatings to Composites and Beyond

Prof. Dr. Mohsin Ali Raza

Institute of Metallurgy and Materials Engineering, Faculty of Chemical and Materials Engineering,
University of the Punjab, Lahore, Pakistan

mohsin.imme@pu.edu.pk

ABSTRACT

Graphene, with remarkable properties such as high surface area, mechanical strength, electrical and thermal conductivity, has gained enormous attraction for electronics, energy, coatings, biomedical and aerospace applications. Graphene oxide (GO), derived from natural graphite through chemical exfoliation, represents a promising low-cost alternative to graphene with significant potential across diverse applications. This talk will give an overview of research activities carried out in our laboratory. The first segment of the talk will present anti-corrosive behavior of GO coatings deposited on copper, steel, magnesium and neodymium iron boron substrates, achieved through techniques like electrophoretic deposition or chemical vapour deposition. The subsequent part of the talk will focus on utilization of GO as filler in epoxy, polyester and acrylonitrile butadiene styrene composites. The factors such as dispersion, functionalization, processing parameters as well as potential applications of GO/polymer composites will also be highlighted. The final part of the talk will explain the application of GO, doped GO or reduced GO in supercapacitors and biomedical applications.



Applications of Advanced Composite Materials Towards Aerostructure Design and Manufacturing

Dr. Mohsin Haider

Turkish Aerospace Industries. Islamabad, Pakistan

pakoffice5@gmail.com

ABSTRACT

The aerospace industry, over a span of more than 100 years of its history, has been a pioneer in pushing the boundaries of technological innovations. Many technologies that got developed for the primary use in aerospace applications later on found their applications in many other industries. Same is the case with advanced structural materials including composites. Aerospace structures have very stringent performance requirements that require superior material properties. Furthermore, strength-to-weight and stiffness-to-weight ratios are important design criteria for aerospace designs where lower structural weights are considered ideal for minimizing platform operational costs and to achieve mission goals. Advanced composite materials are materials of choice for aerospace structures due to their superior specific stiffness, strength and fatigue properties compared with conventional materials. Use of these materials also give designers the choice to design monolithic structures which are structurally superior with reduced part and fastener count. This all seems like a perfect match between composites and aerostructures, however it is not as straightforward as it appears. The choice of the best material and best manufacturing process is critical for the success of a platform. This talk is aimed at covering the state of the technology in terms of advanced composite materials and associated manufacturing processes in use today in the aerospace industry. This will also cover some of the challenges and issues with in-use materials and processes, and further where innovations in materials and processes need to go to address current and future challenges. We will also establish the strong link between engineering design, materials, manufacturing processes and quality assurance in light of design-for-manufacturing, design-for-cost and design-for-repairability aspects of advanced composite materials.

Efficient Techniques to Recover Power from Waste Using CO₂ as Working Fluid

Prof. Dr. Nadeem Ahmed Sheikh

Professor of sustainable and digital thermal systems engineering
Department of Mechanical Engineering, Faculty of Engineering & Technology
International Islamic University Islamabad, Pakistan

nadeemahmed@iiu.edu.pk

ABSTRACT

As the world progresses towards sustainable production and usage, the amount of waste generated, and the end use of waste is becoming one core challenge. Several wastes to fuel/energy conversion technologies are available depending on the type of waste and content of energy available. One key challenge to convert waste low-to-medium energy density waste into electricity is the unavailability of technology, which is compact, economical and can be scaled according to size and availability. In this regard, a compact and efficient waste to electricity generation can be achieved using super critical sCO₂ based working fluid in a Bryton cycle configuration. The sCO₂ based cycle is not only compact, but it can also be scaled according to size of the plant from micro to mini size power generation set with possibility of off-grid as well as on-grid integration. Here we present the thermodynamic assessment of sCO₂ based cycles using CO₂ as working fluid. The recovered power can be used for diverse applications including electricity generation for green Hydrogen production.



Navigating Tomorrow: Pakistan's Robotic Odyssey

Prof. Dr. Umar Shahbaz Khan

National Centre of Robotics and Automation (NCRA)
Department of Mechatronics Engineering College of E&ME, NUST
u.shahbaz@ceme.nust.edu.pk

ABSTRACT

Robotics stands at the forefront of technological evolution, promising to revolutionize industries, redefine human interaction, and reshape our world. This presentation delves into the significance of robotics as an emerging field, tracing its historical roots to its current expansive applications. From manufacturing to healthcare, from exploration to entertainment, robots are increasingly becoming indispensable partners in our daily lives. Through collaborative efforts across academia, industry, and government sectors, Pakistan is harnessing the power of robotics to address societal challenges, enhance productivity, and foster economic growth. From agricultural automation to disaster response, Pakistani innovators are crafting tailored solutions that resonate with local needs and aspirations. Join us on a journey of exploration and inspiration as we uncover the untold stories of Pakistani robotics pioneers. Discover how they are leveraging their talents, resources, and cultural heritage to shape a brighter future for Pakistan and the world at large. Together, let us celebrate the spirit of innovation and collaboration that propels us towards a future where robots and humans coexist harmoniously, enriching each other's lives in ways yet to be imagined.

Advance in Use of UHMWPE in Total Joint Replacements

Prof. Dr. Rizwan M. Gul

Department of Mechanical Engineering, University of Engineering and Technology, Peshawar, Pakistan
rgul@uetpeshawar.edu.pk

ABSTRACT

Ultra-high molecular weight polyethylene (UHMWPE) has been widely used as acetabular cup in total hip replacement (THR) and tibial component in total knee replacement (TKR). Crosslinking of UHMWPE has been successfully used to improve its wear performance leading to longer life of orthopedic implants. Crosslinking can be performed by radiation or organic peroxides. To address the issue of the long-term stability of these materials; vitamin E has been successfully used in this application. A review of the use of UHMWPE in total joint replacements and recent development in this field will be covered in this presentation.

Progress in condensation heat transfer on external horizontal tubes for surface condensers

Dr. Hafiz Muhammad Ali

Mechanical Engineering Department, King Fahd University of Petroleum and Minerals,
Dhahran, 31261, Saudi Arabia
hafiz.ali@kfupm.edu.sa

ABSTRACT

Condensation heat transfer plays a vital role in various applications, one of the major applications of condensation heat transfer is on horizontal tubes used in surface condensers of nuclear thermal power cycle to produce electricity. Surface condenser is responsible to create low pressure that provides the thrust force to steam moving to turbine for efficient power generation. Therefore, the role of condensation heat transfer on horizontal tubes has significant importance in thermal power plants. This talk will review the progress on fundamentals of condensation heat transfer by considering the various parameters that impact on condensation heat transfer such as condensate retention, tube geometries, role of fluids hydrodynamic and thermofluidic properties, type of pure or mixture of steam, limitations and advances of surface structures, free and forced convection condensation heat transfer experimental results and model developments. This talk will identify the gaps to be further explored to enhance the heat transfer performance of surface condensers horizontal tubes.



Interactions Between Fluids and Flexible Bodies: Engineering Insights from Nature

Prof. Dr. Emad ud Din

Department of Mechanical Engineering,
School of Mechanical & Manufacturing Engineering (SMME),
National University of Sciences and Technology (NUST),
H12, Islamabad, Pakistan.

emaduddin@smme.nust.edu.pk

ABSTRACT

The interplay between fluid dynamics and flexible structures, as observed in nature's flapping wings and flags, provides a fascinating lens to understand fluid-structure interactions. This study delves into the hydrodynamics of fish schooling, a behavior enhancing movement efficiency in fluid environments. By modeling a group of flexible bodies in tandem and side-by-side formations, we uncover how vortices shed from an upstream body significantly affect downstream counterparts through complex vortex interactions. Employing an advanced immersed boundary method, our investigation focuses on flexible flags in viscous flows across triangular, diamond, and conical formations—mimicking the fundamental patterns of fish schooling. Our findings reveal that strategic adjustments in gap distances and flag flexibility can significantly reduce the drag on downstream flags, influenced by the interplay between upstream shed vortices and those encircling downstream flags. This work extends to examining the drag reduction mechanisms and the optimal positioning of trailing flags under various conditions. Notably, we observe single- and multi-frequency modes corresponding to constructive and destructive vortex interactions, which elucidate the drag variations on downstream flags. Further exploration into the active flapping behaviors of fish and cetaceans reveals the propulsive and maneuvering forces generated, drawing parallels to a combined pitch-and-heave motion of the tail fin. The study investigates the intricate interactions when an actively flapping flexible flag is introduced downstream of a passively flapping one, focusing on the effects of phase differences, amplitudes, and frequency on drag coefficient. The findings highlight the nuanced interplay between constructive and destructive vortex interactions, alongside slaloming and vortex interception modes, offering novel insights into drag variation mechanisms. This research not only enhances our understanding of fluid flexible body interactions but also informs the design and optimization of bio-inspired engineering applications.

Sedimentation: A Threat to Water-Energy-Food Nexus

Prof. Muhammad Abid

Director Interdisciplinary Research Center,
COMSATS University Islamabad, Wah Campus, GT Road, Wah Cantt, Pakistan
drabid@ciitwah.edu.pk

ABSTRACT

Tarbela dam is one of the largest earths filled dams in the world used for power generation and irrigation purposes. Indus basin is also regarded as backbone of Pakistan as it is the biggest source of electricity generation and is called as a food factory for Pakistan. Like all reservoirs the sediments inflow in the Tarbela reservoir has also resulted in reduction in water storage capacity and is also causing damage to the tunnels, the power generating units and ultimately to the plant equipment. The main source of the River Indus is the glacial melt water from the Himalayas with an annual flow rate of 94 MAF which carries along huge number of sediments, and the gross capacity of the reservoir has reduced. The annual suspended sediment load is about 430 million tons meaning that, over time, the reservoir will fill. The life of the dam and reservoir was estimated to be somewhere around fifty years in 1976 when the dam was constructed, meaning that the reservoir will be full of sediments by 2030 and will not be functional anymore unless maintained. This study presents life prediction of Tarbela reservoir in terms of its storage capacity, erosion rate and strength of the tunnels for different times of the year i.e. during flooding (summer) and drought (winter) situations. In addition to the reservoirs of Tarbela and Mangla Dams, almost all barrages and most canals are reasonably full of sediments. An important issue with reservoirs to dredge out sediments is the closing of the dams as they are a major source of electric power as per most recommendations of experts. In addition, sediments are increased observed going into the tunnels hence damaging inner liners and turbine machinery and choking filters etc. This means without closing the power supply, there is a great need to study the sediments flow patterns, dredging patterns, land slide patterns and many others. As such kind of work has not been done so far in any of the hydel power plants in Pakistan; the numerical methods developed provide a base for the study of the behavior of water and sediment flows in Tarbela Dam reservoir, spillways and tunnels and



strength analysis of the tunnels using FSI. The developed methodology can also be implemented to study the water and sediment flow behavior of water in other reservoirs, dams, rivers, barrages and canals present throughout in Pakistan in specific; provided the required data for those are available. As Erosion is observed in the tunnels and of turbine blades and other components; so erosion rate density measurement studies due to sediments and cavitation are carried out with different compositions of sediments (Sand, silt, clay); different flow rates i.e. quantity of flow of sediments through tunnels; different sizes and shapes of particles (circular, triangular, square, etc) for line and area cutting; different injection techniques and others parameters. The Sedimentation Issue needs Serious Consideration as projects on other tunnels, and that can result in delta initiation for movement and suction of sediment. Inlets on Tunnels need to be raised to control sediments. Dredging of sediments needs to be considered through simulations. A comprehensive integrated plan for power generation and water management considering sediments needs attention. Academia / research organizations can help in indigenous studies and can help saving huge amount of foreign exchange.

Evaluation of Lower Limb Amputees using Inertial Measurement Units

Dr. Hafiz Farhan Maqbool

Department of Mechanical, Mechatronics & Manufacturing Engg.
UET Faisalabad Campus.
farhan.maqbool@uet.edu.pk

ABSTRACT

Numbers of individuals undergo the amputation of their lower limbs every year as a result of vascular disease and complications associated with conditions such as diabetes, cancer and trauma have increased worldwide. Limb loss has a significant impact on individual's physical, mental and vocational abilities, generally resulting in the degradation of amputees' quality of life (QOL). Following an amputation, prosthetic devices can improve the amputees' QOL. Rapid technological advancement in the prosthetic field over the last few decades has caused prosthetic devices to evolve from purely passive (mechanical) devices to more advanced devices incorporating microprocessor controlled and powered components. Wearable sensors are frequently used to assess spatio-temporal, kinematic and kinetic parameters providing the means to establish an interactive control of the amputee-prosthesis-environment system. Human gait can be divided into a sequence of repeated phases and events associated with its cyclic nature with the stance and swing phases being the two main phases of the gait cycle. In terms of events, initial contact (IC) and toe off (TO) mark the beginning of a stance and swing phase respectively and provide information about stance time, swing time, cycle duration and gait asymmetry. They are thus important assessment parameters and are frequently used in clinical studies as objective measures for evaluating the efficiency of the rehabilitative processes. The timing of these events supports the analysis of temporal parameters such as stride time and periods of single and double support. The talk will revolve around the utility of IMU based data acquisition platform that could potentially be used for objective evaluation of lower limb amputees when performing activities of daily livings.

Energy Consumption in Pakistani Residential Buildings: Insights from Degree Days Analysis and Appliance Consumption Patterns

Engr. Dr. Khuram Pervez Amber

Department of Mechanical Engineering
MUST, Mirpur, AJ&K
khuram.pervez@must.edu.pk

ABSTRACT

The presentation will offer a comprehensive exploration of energy consumption dynamics in Pakistani residential buildings, integrating innovative approaches such as Degree Days analysis and appliance consumption patterns to inform policy and practice towards greater energy efficiency. The session will commence with an examination of Degree Days maps of Pakistan, highlighting regional variations in heating and cooling requirements based on climatic conditions. By leveraging Degree Days data, attendees will gain insights into the predictive capabilities for energy consumption across diverse regions, facilitating informed decision-making for energy planning and resource allocation. Subsequently, an overview of Pakistan's energy mix and consumption patterns will be provided, contextualizing the challenges and opportunities inherent in the country's energy landscape. Special emphasis will be placed on residential electricity consumption patterns, with a detailed analysis of the impact of various appliances on energy demand. Through comparative studies between AC and non-AC homes, attendees will elucidate the differential energy consumption patterns driven by climatic factors and appliance usage. Furthermore, the presentation will delve into the electricity usage intensity of domestic buildings, exploring factors influencing energy intensity and identifying opportunities for efficiency improvements. By examining key determinants such as building size, occupancy patterns, and appliance usage, participants will uncover actionable insights for optimizing energy performance in residential



settings. A pivotal aspect of the discussion will revolve around the imperative for effective building energy codes and policies in Pakistan. By highlighting the benefits of robust regulatory frameworks, including enhanced energy efficiency, reduced carbon emissions, and improved comfort levels for occupants, attendees will be encouraged to advocate for the implementation of stringent building standards. In conclusion, the presentation will empower stakeholders with practical strategies and evidence-based insights to promote energy efficiency in Pakistani residential buildings. By harnessing the predictive capabilities of Degree Days analysis, understanding appliance consumption patterns, and advocating for effective policy interventions, participants will contribute to the realization of a sustainable and resilient built environment in Pakistan.

Thermal Management of the Batteries for Electric Vehicles

Dr. Adeel Waqas

US Pakistan Center for Advanced studies in Energy (USPCAS E)
National University of Science and Technology (NUST) H-12 campus- Islamabad-Pakistan adeel@uspcase.nust.edu.pk;
adeelwaqas@gmail.com

ABSTRACT

Efficient thermal management of batteries is paramount for maximizing the performance, longevity, and safety of Electric Vehicles (EVs). In this context, a comprehensive approach integrating passive and active cooling techniques alongside advanced materials and intelligent control systems emerges as essential. Passive methods, such as effective insulation and material selection, offer initial cost-effectiveness by reducing heat transfer, yet may falter under extreme conditions or high-power demands. Conversely, active cooling systems like liquid cooling, which circulates coolants within the battery pack, and air cooling, utilizing fans or heat exchangers, provide more robust solutions, with liquid cooling excelling in high-demand scenarios while air cooling offers simplicity and reduced weight. Additionally, advanced strategies incorporating phase change materials (PCMs) and thermoelectric cooling exhibit promise; PCMs stabilize temperatures via latent heat absorption/release, particularly beneficial during charging and discharging cycles, while thermoelectric cooling enables precise temperature control albeit with energy efficiency considerations. Furthermore, the integration of predictive modeling and control algorithms enables dynamic optimization of thermal management systems, leveraging real-time data on ambient conditions, battery usage patterns, and internal temperatures to adapt cooling strategies proactively, thereby enhancing overall battery performance and extending lifespan. Ultimately, a comprehensive approach to thermal management, combining diverse cooling techniques with advanced materials and intelligent control, is essential for ensuring the reliability and efficiency of EV batteries across varied operating conditions, advancing the widespread adoption and sustainability of electric mobility. In current research we have investigated a novel battery management system which is based on the evaporative cooling technique. The system provides maximum cooling with minimum energy utilization.

Empowering Energy Storage: Unveiling the Potential of Transition Metal Based electrode materials for Supercapacitors

Prof. Dr. Muhammad Ramzan Abdul Karim

Ghulam Ishaq Khan Institute of Engineering Sciences and Technology,
ramzan.karim@giki.edu.pk

ABSTRACT

Supercapacitors are proven as energy storage devices with more energy density than capacitors, and better power density than batteries (lithium-ion batteries (LIBs), sodium-ion batteries (SIBs) with highrate performance. Transition metal compounds (TMCs) and Transition metal based organic frameworks (TMOFs) are being researched as promising electrode materials for supercapacitors. Among different TMCs, transition metal sulfides (TMSs), transition metal oxides (TMOs), transition metal hydroxides (TMHs), transition metal nitrides (TMNs), transition metal phosphates (TMPs) and their nanocomposites with carbonaceous materials like carbon nanotubes (CNTs), graphene nanoplatelets (GNPs), reduced graphene oxides (rGO), and graphitic carbon (GC) are generally being employed. Similarly, among different TMOFs, Ni, Co, Zn, Mn etc. based unary, binary, and ternary frameworks and their composites with CNTs, GOs, GNPs etc. are being researched for their electrochemical energy potentials. The proposed topic would include covering these various types of transition metal compounds and TMOFs based electrode materials in general while Cu, Ni, Co, Mn, Zn based TMOFs and transition metal phosphates (TMPs) in particular, prepared through various synthesis routes. TMPs and TMOFs based electrode materials have feasible structures, good surface area due to engrossed porosity, rich active redox reaction sites and variable valance metallic ions that make them ideal to be used for supercapacitor electrode materials. Moreover, their composites with CNTs, rGO, GC and other carbon-based materials further enhance surface area, and the excellent electrical conductivity of carbon materials combined with the variable valency of metallic ions in transition metal-based structures enhance their electrochemical performance.

Incorporating Power Law for The Estimation of Maximum Strain Under Pressure Loading for Solid Propellant Grain in Conjunction With FEM

Syed Faiq Musharraf^{1*}, Faizan Ali¹, Obaid Ur Rehman¹, Ahmed Abdul Moeed¹,
Muhammad Adnan², Riffat Asim Pasha¹

¹University of Engineering and Technology Taxila,

²Centres of Excellence in Science & Applied Technologies Islamabad

[*syedfaiqshah4649@gmail.com](mailto:syedfaiqshah4649@gmail.com)

ABSTRACT

The primary objective of this study is to critically examine the propellant grain's structural integrity in solid propellant star grain under pressure loading. Structural integrity is crucial for applications like space launch vehicles and military missile systems. As FEA needs a lot of time at the design stage, the research method gives almost equal results without the use of FEA but with only 3 to 4% deviation. The research encompasses structural analysis, stress mitigation, finite element analysis, parametric analysis, and the derivation of a power law equation to model propellant strain. Several simulations have been performed on star grain shape by doing parametric analysis on FEA tool to drive the equation for power law which will predict the maximum principal strain of star grain shape within a minute, instead of an hour using FEA. This study facilitates efficient exploration of grain geometry, benefiting design consideration in rocket motor development.

KEYWORDS: Finite Element Analysis, Grain geometries, Parametric analysis, Power law equation, Pressure loading

1. INTRODUCTION

Trade-offs between the conflicting requirements of geometric constraints, mission reliability, structural integrity, and ballistic performance are typically necessary for a solid propellant grain design [1]. Solid propulsion technology finds extensive application in both military and commercial domains. Large solid booster motors are intended for use in spaceship launches, although smaller models are more commonly utilized in military applications [2].

Star grain shape has been widely used configuration in solid propulsion system, because of its reliability, simplicity, and neutral burning [3]. Solid rocket motors are utilized in many applications because they are dependable and require minimal maintenance. From the time it is cast until it has burned away during its mission, a solid propellant rocket grain is subjected to a number of stressful situations. These include the constant pull of gravity, loads resulting from temperature excursions and propellant curing [7], pressures and accelerations associated with ignition, launch, and flight; finally, shocks and vibrations from handling and captive flight. These loads typically cause the grain to undergo displacements, strains, and stresses as well as the potential for internal heat generation [4,9]. For this purpose, maximum principal strain during its whole life cycle is being analysed.

Himanshu Shekhar [1] calculated the maximum principal strain of case bonded finocyl shape solid propellant using FEM. The study focuses on conducting parametric analysis on finocyl shape in order to obtain maximum strain that resulted in derivation of universal power law. This Power law is utilized for finding the maximum strain and minimizing the use of FEA. The study concluded that

the finite element analysis results and the theoretical results are almost similar. Aqeel and et' al [10] also performed the investigation of the grain geometry of a convex port star and presents a parametric evaluation to evaluate the impact of seven distinct and defining geometric variables of the star as well as other ballistic factors, such as propellant density and characteristic exhaust velocity, on the burn pattern and performance profile for the qualitative analysis of sliver fraction and neutrality.

This paper focuses on implementing strategies to mitigate the structural stress induced in the propellant during the internal pressure loading that occurs during the rocket operation. The primary objective is related to structural analysis of solid rocket propellant for pressure loading using finite element methods for the star grain shape. FEA assesses the stress induced on rocket propellant under various parameters due to pressure loading. Parametric Analysis of maximum principal strain versus different design parameters of propellant, casing and insulation have been performed on ANSYS Workbench. The ranges of the parameters will be set. By assuming some parameters constant, a few parameters are varied to find the effect on the strain produced. The same procedure is adapted for every parameter and because of this parametric analysis, graphical relationships between all parameters versus maximum principal strain are obtained which derive the Power Law for the star grain geometry. This will result in a power law equation to predict maximum principal strain without the need for repetitive finite element analysis.

Assumptions For FEA

The analysis is based on the following assumptions:

- In most of the time, the propellant and insulation both exhibit same mechanical properties.
- The insulation and propellant have Poisson's ratios of 0.4990, which suggests almost incompressible behaviour.
- The metallic casing has a Poisson's ratio of 0.3.
- The process of elastic analysis is underway. The study assumes that the ends are free and does not take longitudinal loading circumstances into account.
- All strain values produced fall in between the elastic limit.
- Before or after the analysis, there are no gaps, fractures, or discontinuities in any of the contacts, which are all thought to be continuous.

2. Methodology

Loading Conditions

The propellant grains experience different types of loading conditions throughout their life cycle [7]. However, this study focuses solely on pressurization. During ignition, the propellant grains face pressurization through the ports, making it crucial to ensure the design can withstand the resulting strain adequately.

Material Properties

While solid propellant typically exhibits viscoelastic behaviour, elastic analysis is commonly favoured to provide initial estimates of strain values [8]. Propellers are handled like linear elastic materials in this method. Additionally, this work makes it easier to use superposition to simulate modifications to geometry, material characteristics, and loading conditions.

Grain Geometry

The geometry was made parametrically so that the finite element solver can change the parameters as required. The first step is to input the data of design variables which fully describes the star grain geometry, and their values is described in Table 1. Figure 1 describes the half star grain geometry in detail.

Table 1: Input Data and Design Variables for star grain geometry.

Variable	Variable Name	Variable Value
N	Number of Star Points	5
R _g	Grain Outer Radius	1500 mm
WT	Web Thickness	675 mm
SR	Maximum Star Radius	1580 mm
FR	Fillet Radius	45 mm
CR	Cusp Radius	45 mm
ϵ	Angular Fraction	0.75
ξ	Star Angle	9°
θ	Star Point Semi-Angle	31.13°

Parametric Analysis

To study the effect of the strain that will be produced, these variables of star grain geometry were considered as critical parameters. Table 2 provides the ranges of these parameters that have been set. To see the effect of strain produced, some parameters have been varied and remaining parameters have been kept constant. The same procedure is adapted for every parameter.

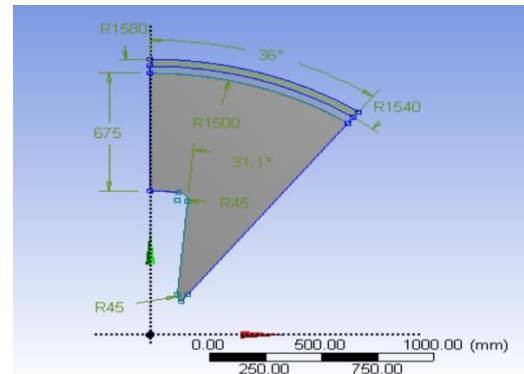


Figure 1: Half Star Grain Geometry

Table 2: Range of Star Grain Parameters for Parametric Analysis

Parameters	Range	Units
Web Thickness	600 - 800	mm
Star point semi angle	28 - 34	deg
Grain Outer Radius	1350 - 1650	mm
Propellant Modulus	2.0 - 6.0	MPa
Casing Thickness	6.0 - 16.0	mm
Fillet Radius	10.0 - 60	mm
Pressure	3 - 7	MPa
Poisson's Ratio	0.4987 - 0.4993	-
No. of star points	4.0 - 9.0	-

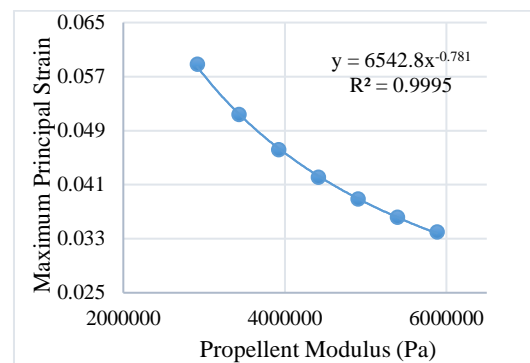


Figure 2: Variation of Maximum Principal Strain with Propellant Modulus

Modelling

The form of grain, loading conditions, and the material characteristics all affect the maximum principal strain. Additionally, pressure has a significant impact; the maximum principal strain will increase with increasing pressure. The maximum principal strain reduces as we decrease the propellant modulus as shown in figure 2.

Finite element analysis can be used to get effect quantification. The power law relation that follows expresses how each of these parameters affects the star grain geometry:

$$\varepsilon = K. (WT)^a. (\theta)^b. (Rg)^c. (E_{prop})^d. (CT)^e. (FR)^f. (P)^g. (PR)^h. (NOS)^i \quad (1)$$

Where:

- ε = Maximum Principal strain
- K = Constant to determine by computation
- WT = Web Thickness
- θ = Star Point Semi-Angle
- R_g = Grain Radius
- E_{prop} = Propellant Modulus
- CT = Casing Thickness
- FR = Fillet Radius
- P = Pressure
- PR = Poisson's Ratio
- NOS = Number of Star Points

In this case, the constants denoted by the exponents a, b, c, d, e, f, g, h, and i are to be derived by studying the data using FEM and changing one parameter at a time.

3. Results and Discussions

Initially, just two parameters, the star point semi-angle, and the number of star points formulation are changed from 27 to 37 degrees and 4 to 8 stars, respectively. Finite element analysis is then used to determine the maximum strain for a half-star grain structure in each case. The point of maximal strain is present in every case. However, the value of maximum strain increases as star point semi angle increases and reduces when number of star points are increased. Plotting maximum strain values against various parameters allows for the fitting of a power law to the data. For parametric studies, the power law exponent is found to be -0.452 for the number of star points and 0.626 for the star point semi angle. The values of the exponents obtained from parametric analysis discusses previously are as follows:

$$a = 1.169, b = 0.626, c = 2.2819, d = -0.781, e = -0.264, f = -0.336, g = 1, h = -358.3, i = -0.452$$

By taking the ratio of changing parameters and their related exponents, one may use the resultant power law to calculate the maximum principal strain in the propellant configuration. If the reference configuration serves as the base configuration, the maximum principal strain in a trial configuration is represented by the correlation that follows:

$$\varepsilon_r = \left(\frac{WT_r}{WT_t}\right)^a \cdot \left(\frac{\theta_r}{\theta_t}\right)^b \cdot \left(\frac{R_{g_r}}{R_{g_t}}\right)^c \cdot \left(\frac{E_{prop_r}}{E_{prop_t}}\right)^d \cdot \left(\frac{CT_r}{CT_t}\right)^e \cdot \left(\frac{FR_r}{FR_t}\right)^f \cdot \left(\frac{P_r}{P_t}\right)^g \cdot \left(\frac{PR_r}{PR_t}\right)^h \cdot \left(\frac{NOS_r}{NOS_t}\right)^i \cdot (\varepsilon_t) \quad (2)$$

Where the r and t subscripts stand for reference and trial case respectively.

Power law validation through case studies

Two trial cases were chosen and executed as a case study. Table 3 lists all other parameters as well as the input criteria. Maximum principal strain for trial configurations was obtained using power law, and the findings were validated by finite element analysis. For Trial Case 1, the power law gave the value of 4.64687% and the finite element analysis gave the value of 4.8377% as shown in Figure 4. For Trial Case 2, the power law gave the value of 4.01609% and the finite element analysis gave the value of 4.1458% as shown in Figure 5. As all the power law results are closely matching to their respective finite element analysis results, so we can say that these exponents are universal and can be utilized for the star grain shape under the provided range of parameters.

Table 3: Comparison of FEM Results and Power Law Results

Parameters	Reference Case	Trial Case 1	Trial Case 2
Web Thickness (mm)	675	650	685
Star Point Semi-Angle (deg.)	31	25	27
Grain Radius (mm)	1500	1560	1530
Propellant Modulus (Pa)	4903000	4612700	4412700
Casing Thickness (mm)	40	30	45
Fillet Radius (mm)	45	40	47
Pressure (MPa)	5	7	6
Poisson's Ratio	0.499	0.4991	0.4991
Number of Star Points	5	7	6
Maximum Strain by Power Law (%)	3.8563	4.64687	4.01609
Maximum Strain by FEM (%)	3.8563	4.8377	4.1458

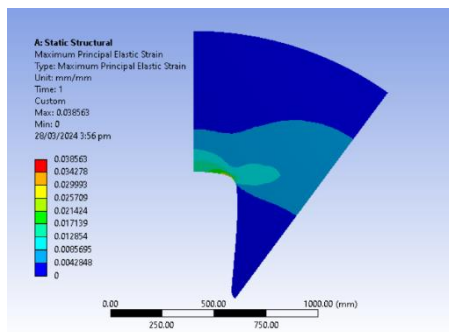


Figure 3: Reference Case results through FEM

By performing Finite Element Analysis on Star Shape Solid Rocket Propellant, while following the design set of values and loading conditions, Maximum Principal Plane Strain is found to be 3.8563% as shown in figure 3. To find the effect of a few critical parameters of Star grain geometry on maximum strain, variation in that parameter using parametric analysis is performed with a limited range of values.

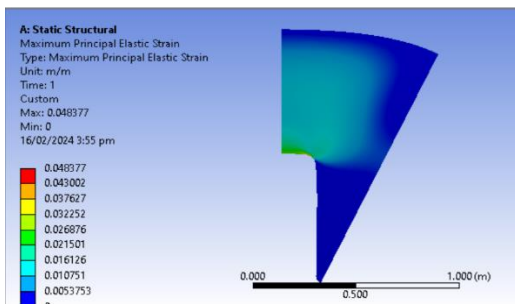


Figure 4: Trial Case 1 results through FEM

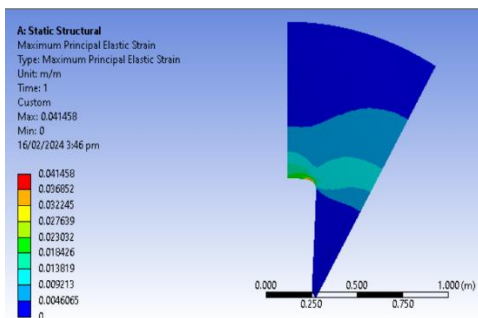


Figure 5: Trial Case 2 results through FEM

Finite element analysis through ANSYS needs skilled manpower to run the preprocessing and requires a lot of time for the analysis to be performed [1]. So, it is better to use the power law to predict the maximum principal strain for the star grain shape and it is very quick and to save time rather than use of computer for doing analysis again and again.

4. CONCLUSION

This work examines the parametric studies of star grain shape for the prediction of maximum principal strain under pressure loading for the change in each parameter or configurations. A simple correlation in the form of power law is also derived to predict the maximum principal strain for star grain shape under pressure loading that is not previously derived in the literature. Software for repeating finite element analysis can be avoided by using the power law to anticipate the maximum principal strain. In order to validate the power law correlation, the two trial cases had also been resolved. This allowed the power law and finite element analysis results to closely match each other.

REFERENCES

1. Himanshu Shekhar, Prediction of Maximum Strain in Finocyl Port Case-bonded Solid Propellants under Pressure Loading, Defence Science Journal, 56 (3) (2006) 417-422.
2. Ceyhun TOLA and Hatice Begüm EYLENOĞLU, Structural Behavior Examination of Frequently Used Solid Propellant Sections Under Centrifugal Loading Using Response Surface Method, Journal of Aeronautics and Space Technologies, 14 (2) (2021) 231-242.
3. Muhammad Adnan, SUN Bing, ZHANG Jian-wei and Ali Sarosh, Structural optimization of elliptical-tip star propellant grain using sub-problem approximation, Journal of Aerospace Power, 27 (2) (2012) 457-464.
4. Noel and James S., Solid propellant grain structural integrity analysis, NASA-SP-8073 (1973)
5. Mateen Uddin Qazi, Khayyam Masood, Khurram Mahmood, Rapid Prediction of Star Propellant Grain Regression using CAD Software, 6th International Bhurban Conference on Applied Sciences and Technology, Islamabad, Pakistan (2009)
6. M. Anderson, J. Burkhalter and R. Jenkins, Design of a Guided Missile Interceptor Using a Genetic Algorithm, AIAA Journal of Spacecraft and Rockets, 38 (1) (2001) 28-35.
7. Shiang-Woei Chyuan, Studies of poisson's ratio variation for solid propellant grains under ignition pressure loading, International Journal of Pressure Vessels and Piping, 80 (2003) 871-877.
8. AGARD, Structural Assessment of Solid Propellant Grains, AGARD-AR-350
9. Davenas, Alain, ed. Solid rocket propulsion technology, Newnes, (2012)
10. Aqeel Nawaz, Muhammad Ali Kamran, Parametric sensitivity analysis of convex star port propellant grain for solid rocket motor, Journal of Engineering and Applied Sciences, 35 (2) (2016)

Supply Chain Management in Oil & Gas Field in Pakistan - Challenges and Solutions

Faizan Ali, Obaid Ur Rehman, Ahmed Abdul Moeed, Syed Faiq Musharraf*, Amar Ul Hassan Khawaja

University of Engineering and Technology Taxila

*syedfaiqshah4649@gmail.com

ABSTRACT

The research explores the significance of supply chain management (SCM) in the oil & gas industry. It outlines various stages involved in oil & gas supply chain, encompassing exploration, production, transportation, refining, storage, and distribution design networks. The case study of Sui Northern Gas Pipelines Limited (SNGPL) in Pakistan exemplifies the intricacies of natural gas supply chain management. Furthermore, the research emphasizes the importance of SCM in ensuring operational efficiency, cost reduction, and environmental sustainability within the oil & gas field. It also highlights challenges faced by the industry, such as inadequate infrastructure, fluctuating regulations, and skilled manpower shortage, alongside potential solutions like infrastructure development, technology adoption, and robust risk mitigation strategies.

KEYWORDS: Supply Chain Management, Oil and Gas Supply Chain, Natural Gas, Importance of SCM, Challenges and Solutions

1. INTRODUCTION

The oil & gas field serves as the primary source for the extraction, production, and refinement of crude oil and natural gas, which are pivotal energy resources globally [1]. According to the United States Energy Information Administration (EIA), Pakistan is estimated to have more than 9 billion barrels (1.4×10^9 cubic meters) of petroleum oil and approximately 105 trillion cubic feet (3.0 trillion cubic meters) of natural gas reserves, including shale gas. The country's first gas field was discovered in Balochistan, near the massive Sui gas field, in the late 1950s. The most abundant resource is found in the Khaur Company area of Attock, spanning 122.67 square kilometers [9]. The largest natural gas field in Pakistan is the Sui gas field, located in the vicinity of Sui in Balochistan. Oil and gas fields are critical to the global economy as they provide a major portion of the world's energy supply [2]. These resources play a fundamental role in various sectors, including transportation, manufacturing, electricity generation, and heating. The development and utilization of oil and gas fields significantly impact geopolitical relations, economies, and environmental concerns due to their extraction and consumption. Supply Chain Management (SCM) in the oil & gas field is pivotal for maintaining operational efficiency and continuity throughout the complex processes from exploration to distribution [3,4]. SCM professionals in this sector manage diverse supply chains, overseeing procurement, logistics, inventory, and risk mitigation. Effective SCM strategies optimize inventory levels, facilitate complex logistics operations, and leverage technology to enhance visibility and efficiency while complying with safety regulations and environmental standards [1-3]. However, the industry also faces challenges related to environmental impact,

sustainability, and the transition toward renewable energy sources as the world aims to reduce carbon emissions and combat climate change [4].

The oil industry, a dominant force since the mid-20th century, faces a complex landscape with upstream exploration and production, midstream transportation and storage, and downstream refining and marketing [8]. This intricate supply chain necessitates meticulous control and planning, including real-time information sharing, vendor integration, multi-modal transportation management, and demand forecasting. Effective Supply Chain Management practices are paramount for optimizing product delivery from refineries to end-users [1,3]. These practices encompass creating efficient communication networks, studying market demands, planning deliveries to avoid stockouts or oversupply, and fostering long-term relationships with distributors [2].

The main aim of this article is to comprehensively examine and understand the introduction, strategies, implementation methods, significance, and digital transformation approaches utilized by organizations within the oil and gas industry to manage their supply chains effectively.

2. METHODOLOGY/ FLOW PROCESS OF OIL SUPPLY



Figure 1: Supply Chain of Oil in oil field

Design network identification for oil and Gas supply

Sui Northern Gas Pipelines Limited (SNGPL) is taken as the case study as it is the largest natural gas distribution company in Pakistan, serving over 7.2 million consumers across Punjab, Khyber Pakhtunkhwa, and Azad Jammu & Kashmir [7]. The company's supply chain involves a complex network of procurement, transportation, storage, distribution, and sales.

The oil and gas development process, from exploration to distribution, involves several stages in the supply chain. Here is an overview of the complete process:

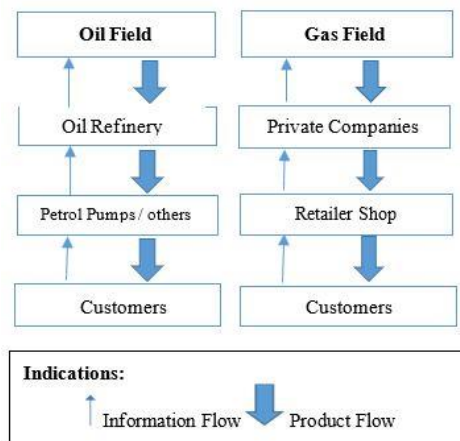


Figure 2: Design Network Distribution for Oil and Gas Supply

Procurement

Rigs:

Rigs are essential for drilling wells to extract crude oil or natural gas from underground reservoirs. Rigs are used for exploration and production activities. They drill wells, install casing, and facilitate the extraction of hydrocarbons [2]. Rigs are strategically positioned in areas where geological surveys and seismic studies have identified potential oil and gas reservoirs.

Drilling and Well Construction:

Drilling operations will commence if a promising site is identified. This involves creating a wellbore through the Earth's surface to reach the oil reservoir. Wells can be vertical or horizontal, depending on the geological characteristics of the site. Once the well is drilled, a casing is installed to secure the hole, and cement is used to reinforce the casing and prevent leaks [2].

Field:

An oil field refers to a geographical area containing one or more oil reservoirs under the same geological structure [3]. Oil fields are where extraction and separation operations take place. Multiple wells may be drilled within a field to maximize production. Fields are managed

by oil companies, and production facilities are set up to process and extract oil and gas.

Extraction and Production:

After drilling, the oil can start flowing to the surface due to natural pressure or by using artificial lift methods such as pumps [3]. Production facilities separate oil, natural gas, and water. The extracted oil undergoes initial processing at the production site.

Logistics

Transport:

The transportation phase involves moving crude oil to refineries or distribution centers from the production site. Pipelines are a very common mode of transportation for long distance transportation [5]. Tanker Ships are used for transporting oil across oceans. Trucks and Rails are utilized for shorter distances or areas without pipeline infrastructure.

Transportation to Refineries:

The crude oil is transported from the production site to refineries using various means such as pipelines, tanker ships, trucks, or rail [5]. Pipelines are a common and cost-effective method for transporting large quantities of oil over long distances.

Refining:

At the refinery, crude oil undergoes a refining process to separate it into different components such as diesel, gasoline and various petrochemicals. Cracking, distillation, and other refining processes are employed to achieve this separation.

Distribution of refined oil:

The refined products are then transported to distribution centers and storage facilities via pipelines, ships, trucks, or rail. Distribution centers store the products until they are needed by retailers, industries, or end consumers.

Inventory

Storage:

Oil storage facilities play a crucial role in the supply chain for providing a link between production and consumption, allowing for smooth operation, and addressing fluctuations in demand.

Types of Storage:

Large tanks are used for storing crude oil and refined products. Some countries maintain strategic reserves for energy security. Oil can be stored on tanker ships during periods of oversupply or low demand.

Distributor

Distributors are entities responsible for managing the storage and movement of refined oil products to various end-users. Distributors receive refined products from refineries and supply them to retail outlets, industries, and other consumers [2,3]. Distribution centers and storage facilities play a crucial role in managing inventory and ensuring a steady supply of products.

Retail and End-User Distribution:

Retailers, such as gas stations, receive the refined products from distribution centers. Consumers purchase these products for various uses, including transportation, heating, and industrial processes.

Consumer:

Consumers are the end-users who utilize oil and its products for various purposes, such as transportation, heating, and industrial processes like:

- Individuals purchasing gasoline for vehicles.
- Industries use oil-based products for manufacturing processes.
- Residential users rely on oil for heating.

3. FLOW PROCESS OF GAS PRODUCTION

For gas production, crude oil is extracted from oil wells that passes through Nodal Compressors to increase their pressure. The raw material is transported to Early Production Facility using pipelines. Furthermore, it passes through different stages to separate oil and gas. Gas Dehydration Units via inlet filter separators separate the gas from oil and allow it to be transferred to storage facility and Sui Gas Pipelines.

Procurement

Natural Gas Production:

Sui Northern Gas Pipelines Limited primarily sources natural gas from the Sui Gas Fields in Baluchistan, Pakistan. The gas is extracted from wells and processed at the Sui Gas Field Production Plants to remove impurities and make it suitable for transportation.

LNG Import:

To supplement domestic production, Sui Gas Fields also imports Liquefied Natural Gas from various international suppliers. The Liquefied Natural Gas is transported by specialized Liquefied Natural Gas tankers and offloaded at Liquefied Natural Gas terminals in Pakistan.

Logistics

Transmission System:

The processed natural gas and imported Liquefied Natural Gas are transported through Sui Gas Field's extensive transmission network. The transmission system consists

of large-diameter pipelines that carry high-pressure gas to distribution centers [5].

Distribution System:

From distribution centers, the natural gas is further distributed through a network of smaller-diameter pipelines to residential, commercial, and industrial consumers. Sui Gas Field's distribution network covers over 142,998 kilometers, reaching over 7.22 million consumers [7].

Inventory

Storage Facilities:

Sui Northern Gas Pipelines Limited maintains underground storage facilities to store natural gas during periods of low demand and ensure a consistent supply during peak seasons. These storage facilities are strategically located across the distribution network to optimize gas distribution.

Metering and Billing:

Sui Gas Field installs and maintains gas meters at customer premises to measure and record natural gas consumption. Based on meter readings, Sui Gas Field generates and sends out bills to customers for their gas consumption.

Customer Service:

Sui Gas Field provides customer service support to address customer queries, resolve issues, and handle complaints. Customers can contact Sui Gas Field through various channels, including phone, email, and online platforms.

4. CHALLENGES IN OIL AND GAS FIELD AND THEIR SOLUTIONS

The oil and gas industry in Pakistan faces various challenges in supply chain management, which can significantly impact operations and efficiency. A few of the key challenges along with potential solutions are being mentioned:

Challenges

- Inadequate infrastructure, including transportation networks and storage facilities, can lead to delays and inefficiencies in the supply chain [5].
- Frequent changes in regulations, government policies, and political instability can disrupt the supply chain and create uncertainty for investors.
- Ensuring adherence to quality standards and safety regulations throughout the supply chain can be challenging, leading to potential risks and accidents [6].



- Natural disasters, geopolitical tensions, and global market fluctuations pose significant risks of disruption to the supply chain.
- Fluctuating oil prices and rising operational costs can impact the profitability of the supply chain [7].
- Lack of skilled manpower and specialized talent can hinder effective supply chain management.

Potential Solutions

- Investment in infrastructure development, including pipelines, ports, and storage facilities, to improve logistics and enhance the movement of oil and gas products.
- Encourage stable regulatory frameworks and government policies that promote investment and provide a predictable environment for businesses. Engaging in dialogue with policymakers to address industry concerns can also help.
- Implement robust quality control measures, regular inspections, and safety protocols at every stage of the supply chain. Providing continuous training and education to employees regarding safety measures is crucial.
- Enhance adaptability by maintaining surplus supplies and exploring alternative sourcing options.
- Focus on cost-saving measures through process optimization, adopting lean principles, negotiating better contracts with suppliers, and investing in energy-efficient technologies to reduce operational expenses.
- Investing in training programs, partnering with educational institutions, and offering attractive career opportunities to attract and retain skilled professionals within the industry.

5. CONCLUSION

Effective supply chain management is essential for the oil & gas industry, which stretches across vast geographical distances and involves complex logistics. From exploration and production to refining, storage, and distribution, a well-managed supply chain optimizes costs, ensures operational efficiency, and minimizes environmental impact. However, the industry faces challenges like inadequate infrastructure, fluctuating regulations, and skilled labor shortages. These hurdles can be addressed through infrastructure development, embracing new technologies, and implementing robust risk mitigation strategies.

REFERENCES

1. A. Muhindo, Impact of Logistics Outsourcing Strategy in Oil and Gas Industry in Uganda, *International Journal of Business and Management*, **9**(6) pp. 922-23 (2014)
2. Gray, B., Jones, E. C., Weatherton, Y., Bussey, R. S., & Armstrong, H., Utilizing pipeline quality and facility sustainability to optimize crude oil supply chains, *International Journal of Supply Chain Management*, **2**(4), pp. 9-16 (2013).
3. Al-Husain, Raed & Assavapokee, Tiravat & Khumawala, Basheer, Supply Chain Management in the Petroleum Industry: Challenges and Opportunities, *International Journal of Global Logistics & Supply Chain Management*, **1**, pp. 90-97 (2006)
4. Weidenbaum, M., Outsourcing: Pros and cons., *Business Horizons*, **48**(4), pp. 311–315 (2005).
5. <https://ru.scribd.com/document/258403805/Supply-chain-management-in-Petroleum-Industry-General-View>
6. W, F. Gross, About the impact of rising oil price on logistics networks and transportation greenhouse gas emission **4**(3–4), 147–148 (2012)
7. Muhammad Shafiq, Waqas Bin Nisar, Matteo Mario Savino, Zahid Rashid, Zaheer Ahmad, Monitoring and controlling of unaccounted for gas (UFG) in distribution networks: A case study of Sui Northern Gas Pipelines Limited Pakistan, *IFAC-Papers Online*, **51**(11), pp. 253-258, 2018.
8. Svetlana Lisitsa, Anastasia Levina, and Aleksander Lepekhin, Supply-chain management in the oil industry, *E3S Web of Conferences SPbWOSCE-2018*, **110**, 2019.
9. https://en.wikipedia.org/wiki/Petroleum_industry_in_Pakistan

Temporal Assessment Box: Neurological Disease Diagnosis through Manual Dexterity Analysis

Khadija Shakeel, Raheel Naveed*, Hussain Abdullah, Awais Hafeez, Asim Ghaffar

University of Engineering and Technology, Lahore
*raheelnaveed01@yahoo.com

ABSTRACT

Healthcare technology is advancing rapidly to improve the clinical measures that are currently in use, which are mainly based on subjective assessments by neurologists. Clinical measures, like UPDRS, MBRS, and NHPT, AHTD, are critical indicators and activities for assessing neurological disorders and motor impairments but, they frequently lack consistency and accuracy. In response to this, we proposed and employed a kinematic assessment procedure to describe the severity and evolution of upper limb dysfunctions in people with neurological disorders. We as a team of mechatronics engineers designed a mechanical structure that incorporated a microcontroller. We presented the Temporal Assessment Box (TAB), a quantitative tool, designed to provide us with temporal parameters of the upper limb movements in patients with neurological disorders with a special focus on manual dexterity. Therefore, as a part of our methodology, we first gathered data on reach-to-grasp-to-lift-to-transport movement from the healthy participants. This assessment uses four distinct objects of varying grasp sizes and base holes at particular distances. Through the data analysis of participants, we aim to find consistent kinematic pattern differences between patients with mild and severe conditions, especially related to the object grasp dimensions. In conclusion, TAB will utilize kinematic analysis and quantitative measures to determine whether a person has a neurological disorder. The expected outcomes include enhancing the accuracy of the detection of manual dexterity.

KEYWORDS: Kinematic assessments, neurological disease, temporal analysis, Manual dexterity, upper limb dysfunctions

1. INTRODUCTION

The neurological disorders including Alzheimer's disease (AD) and Parkinson's disease (PD), Multiple Sclerosis are severe issues affecting the social and economic status of the population significantly and affecting the quality of life. This, due to a rapidly increasing aging population, is expected to quadruple in the coming decades [1].

One of the major features of these diseases is motor dysfunction. Neurological diseases are traditionally characterized as motor system disorders with common symptoms involves, slowness of movement, shaking of hands and arms respectively, rigidity in limbs and trunks and instability in posture [2]. One of the primary motor symptoms of neurological diseases is Bradykinesia. This delayed motion is observed during the performance of isolated activities and is even more apparent during the performance of sequential movements, thus causing a decrease in manual dexterity.

Manual dexterity is explained as goal-directed activities with hands and fingers involves reaching, grasping, coordinated, and controlled movements and they are important factors in Activities of Daily Living (ADLs) [3]. Manual Dexterity has a major influence on how well someone performs in tasks involves taking care of themselves like using a computer keyboard, buttoning shirts, finishing tasks related to their work, and having leisure time activities [4]. Individuals with neurological

disorders are still able to plan and anticipate motions, but they have more trouble coordinating reach and grasp movements during active mobility, especially when the grip requires using all fingers. Also, studies have revealed upper-limb deficiencies associated with bilateral asymmetric motor impairments. These deficits involve difficulties dissociating the left and right arms, lack of coordination, delayed hand opening, and delayed forearm movement initiation [4].

Various techniques of evaluation are employed to assess the manual dexterity of individuals suffering from neurological disorders. Basic evaluations of motor function are provided by conventional clinical measures such as Box and Block Test (BBT) and Nine Hole Peg Test. The Nine Hole Peg Test (NHPT) is one of the most popular tests used to measure the manual dexterity [6]. However, they have limitations in obtaining effective data on specific kinematic factors or finding minor abnormalities. Conversely, laboratory tools such as objective kinematic analysis like motion analysis systems. They provide a thorough measurement of upper limb motions in both spatial and temporal analysis. But, to accurately evaluate the data, these systems may be expensive and need specialized tools and training [3].

To counter this issue, we aim to develop a Temporal Assessment Box (TAB) that records temporal data during reach-to-grasp-to-lift-to-transport assessment. Our tool can be helpful for neurologists in early and accurate diagnosis, by precise measure of manual dexterity.

2. METHODOLOGY

Design

To improve the reach-to-grasp and pick-and-place actions, we have developed the Temporal Assessment Box (TAB) hardware which is designed with an average arm length for any participant. The ergonomic design improves the accuracy of temporal assessments for patients with neurological conditions. During the kinematic assessments, the TAB has incorporated the pegs that are made through 3D printing. These pegs are located in three different points; 15 cm, 30 cm, and 45 cm from a reference point.

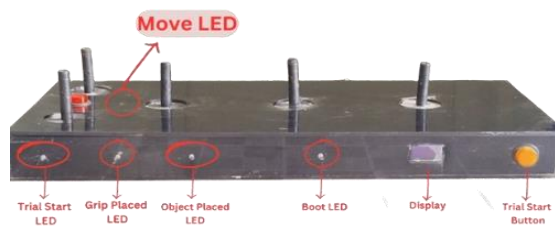


Figure 1: Temporal Assessment Box (TAB) with pegs at varying distances

The objects to be placed on pegs differ in the grasp and the base hole diameter in order to assess the level of dexterity. Objects with large diameters are easy to manipulate in terms of placement while the small ones need precision in grasping them and placing them in a certain position which is a problem. Such progression in object design helps in evaluating various facets of manual dexterity to the extent possible.



Figure 2: Four wooden objects used for the assessments, each with different base hole and grasp size.

Software Design

The design of TAB is made using the Computer-Aided Design Software, SolidWorks by Dassault Systems, with careful consideration of precise alignment of pegs, electronic devices, and their proper installation with a laser cutting board of sheets. The visual appearance helps

the subjects to understand and interact with it quickly, as a game-like resemblance. This approach will facilitate ease for experimenters and patients to collect data during trials.

Hardware Design

Several important considerations were taken into account during the hardware selection process, such as adaptability, user-friendliness, affordability, and reliability. We ensured the selected components were compatible to interface with Raspberry Pi which we considered as the main processing unit. The design of the TAB ensured the selected components were compatible with connecting and interfacing with Raspberry Pi which is the main processing unit and emphasized the simple process for experimenters to use buttons, sensors, and indicator LEDs. TAB has a rechargeable battery that has the capability of lasting for two days before needing to be charged again this enhances long-term usability. Lastly, the final prototype of the TAB was improved by the body of laser-cut acrylic sheets.

Table 4: List of Components and their prices

Components	Price in PKR	Price in Dollars
Indicator LEDs	20	0.07
Push Button and Switches	400	1.40
USB	500	1.75
Raspberry Pi 4B	30,000	104.9
OLED Display	850	2.97
HDMI and USB Mount Cable	600	2.10
Lithium ion Battery	1000	3.50

Data Acquisition

The data acquisition was done by collecting data from 15 control individuals, focusing on diverse demographics across different age groups, genders and both left handed and right handed. Each participant was instructed to sit in a sagittal plane and to press and release a grip button in response to an LED signal. Following the release, they were to pick up an object and place it in the respective sagittal plane. The 40 trials of each participant from the left hand and similarly 40 from the right hand were recorded. The counterbalancing of the object was done, to prevent participants from memorizing the sequence of objects. This helped avoid the participants getting acquainted with the sequence of the objects thereby eliminating order effects that could otherwise affect integrity of the data collected.

Data Analysis

Following the data collection, we obtained reaction time, reaching time ((Movement- to-object), placing time (Movement- to-object-to-target), and total movement time from the Temporal Assessment Box (TAB), which will serve as the foundation for our analysis. Initially, pre-processing is applied which includes processes such as; filtering anomalies, and scaling of data. Afterward, the R analysis is performed which begins with the use of

descriptive statistics to present the mean and variations of the outcomes.

Analysis of Variance (ANOVA) test is employed to determine which time variable has a significant impact. The ANOVA test assists in comparing the means of different groups and detecting if these means differ significantly. This test provides F-values, which indicate the ratio of variance between the groups to the variance within the groups, and P-values, which provide the probability that the observed differences occurred by chance. The study identifies the most influential time metrics, providing the aspects of participant's movement that are significantly affected. The findings provide insights into the temporal dynamics of the factors influencing movement and aid in the development of diagnostic tools for neurological issues.

3. RESULTS

We collected a total of 1200 trials from 14 subjects. The analysis of the collected data involved the use of an ANOVA test to determine the impact of the various factors on the time data. Specifically, we analyzed the impact of hand use i.e. dominant or non-dominant, grasp size, and base hole on the reaction times, reaching time, placing time, and total time of placing objects recorded using the Temporal Analysis Board (TAB). The results were considered statistically significant if the p-values were less than 0.05. On the other hand, the results of the hypothesis testing attested p-values greater than 0.05 stated that none of these factors influenced the time data.

The ANOVA test assisted us in defining the variability of the reaction time in the current research. The interaction between grasp size and base hole was significant ($p = 0.0330$). The three-way interaction between grasp size, base hole, and hand was also significant ($p = 0.0224$). For reaching time, the hand factor had a significant effect ($p = 2.25 \times 10^{-6}$), and the interaction between grasp size and base hole was significant ($p = 0.0348$). For placing time, the base hole showed a significant effect ($p = 0.00141$), and the hand factor ($p = 1.394 \times 10^{-4}$). For total time, the base hole factor had a significant effect ($p = 0.004728$), and the hand factor ($p = 6.045 \times 10^{-5}$). This shows that these certain factors and the interaction between the factors have an impact on reaction time, reaching time, placing time, and total movement time in this study.

DISCUSSION

Dexterous difficulties may cause significant limitations to the manual ADL function at early stages. Most of the kinematic parameters differed significantly with the respective impairment severity and between patients and healthy controls [5]. Therefore, to enhance the diagnosis of manual dexterity in neurological disorders, we developed the Temporal Assessment Box. In our study, the participants were able to engage with TAB where parameters involved placing the hand on a button; upon a light signal, the participants had to release the button (reaction time), grab the object (reaching time), and put it

on a peg (placing time). ANOVA analysis identified three key factors influencing dexterity, Hand used (right or left), Size of the grasp, and Aperture of the base hole. All these variables influenced movement times to some extent, and they also showed how difficult it was to move around these areas. Our results shed light on these factors to alterations in manual dexterity and can inform specific interventions for those with concerned abnormalities. The following figures show how such factors affect the participant's performance in reaction, reaching, and placing tasks.

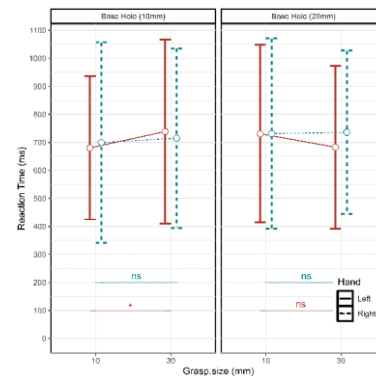


Figure 3: The time taken to release the grip button after the indicator light triggers. The right hand takes longer than the left hand.

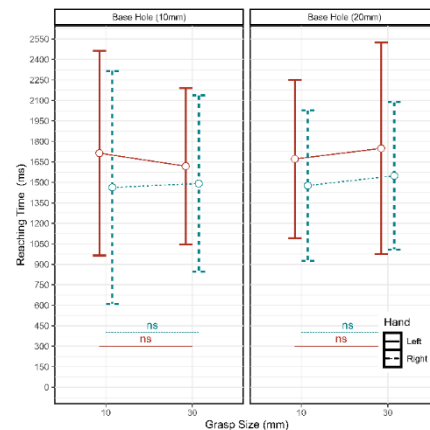


Figure 4: The time taken to pick up the object. The left hand takes longer than the right hand.

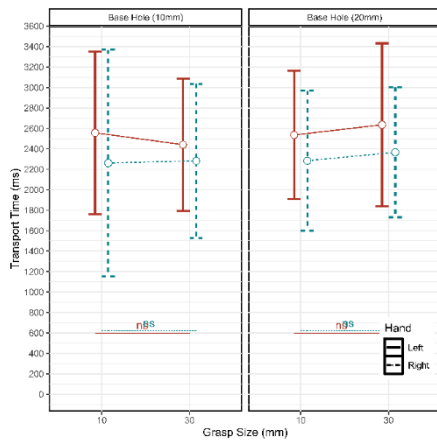


Figure 5: The time taken to place the object. The left hand takes longer than the right hand.

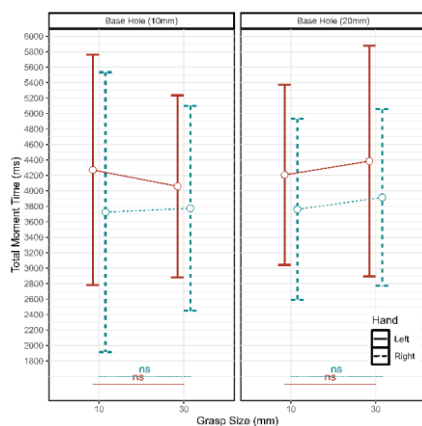


Figure 6: The total time from reaching to grasping, picking, and placing the object. There is a significant difference in time between both hands.

Hand Used

The study showed that the hand (right handed and left handed) used to perform a task determines the effectiveness of the task in reaching, placing, and picking tasks, making the hand a significant determinant of manual dexterity. The study revealed that participants showed significant differences in the motor control and the performance of movements depending on the hand used. This can be because neurological disorders like PD bilaterally affect the body, meaning that one side of the body will be more impaired than the other. The results imply that specific therapeutic interventions might be required to address the needs of each hand, which may result in better treatment of the affected.

Base Hole Dimensions

The base hole size is another significant factor as it finds the level of accuracy needed to position the objects. Participants with neurological disease often experience tremors and shaking, which can severely affect their ability to position objects within the designated holes. The findings suggests that objects with bigger base holes are easy to place while small holes are difficult to place, which

worsens the effects of tremors. This stresses the need to develop assistive devices and rehabilitation tasks that take into account these limitations to improve the outcomes of the therapeutic processes.

Grasp Size

The grasp size emerged as a non-significant factor affecting manual dexterity. Most of the tasks that involved precision and delicate hand movements were difficult for the participants with neurological disorders because of the tremors and weak grip strength as the objects with bigger grasp sizes are easy to pick while small grasp sizes are difficult to pic. However, the results indicate that different grasp sizes did not affect performance as objects were placed on the nearest peg which is only 10 meters apart. Although grasp size is not a prominent aspect, the findings could still be helpful in designing targeted exercises for rehabilitation that would strengthen the grip and stability.

4. CONCLUSION

Based on the results of this study, it is recommended that more objective measures, such as those offered by the TAB, be utilized in order to determine important variables influencing manual dexterity in patients with neurological disease. This analysis can help to design therapeutic interventions with impaired hand function based on such factors as hand used, base hole dimensions, and grasp size. The tool can help to improve the precision of diagnosis to offer more objective data regarding the efficiency of the treatments and surpass the drawbacks of the clinical based measures. Therefore, these findings can help in the development of more accurate rehabilitation interventions, which in turn can enhance the wellbeing of people with neurological disorders.

ACKNOWLEDGEMENTS

We are very grateful to the University of Engineering and Technology (UET), Lahore for highly contributing in this research. We would like to thank Dr. Awais Hafeez and Dr. Asim Ghaffar for their great supervision and help in solving the problems that we faced. We also would like to thank all the participants who underwent trials and believed in us. It is our pleasure to acknowledge the support of all the people who have helped in the success of this research work.

REFERENCES

1. Darweesh, S. K. L., Wolters, F. J., Hofman, A., Stricker, B. H., Koudstaal, P. J., & Ikram, M. A. (2017). Simple Test of Manual Dexterity Can Help to Identify Persons at High Risk for Neurodegenerative Diseases in the Community. *The Journals of Gerontology Series A: Biological Sciences and Medical Sciences*, 72(1), 75–81. <https://doi.org/10.1093/gerona/glw12>
2. Church, F. C. (2021). Treatment Options for Motor and Non-Motor Symptoms of Parkinson’s Disease.



- Biomolecules*, 11(4), 612.
<https://doi.org/10.3390/biom11040612>
3. Department of Occupational Therapy, School of Rehabilitation Sciences, Iran University of Medical Sciences, Tehran, Iran., Nodehi, Z., Behzadipour, S., Department of Mechanical Engineering, Sharif University of Technology, Tehran, Iran, Azad, A., Rehabilitation Research Center, Department of Occupational Therapy, School of Rehabilitation Sciences, Iran University of Medical Sciences, Tehran, Iran, Soltanzadeh, A., Rehabilitation Research Center, Department of Occupational Therapy, School of Rehabilitation Sciences, Iran University of Medical Sciences, Tehran, Iran, Taghizadeh, G., & Department of Occupational Therapy, School of Rehabilitation Sciences, Iran University of Medical Sciences, Tehran, Iran. (2020). The Correlation Between Reach and Grasp Kinematic Measures and Clinical Measures of Manual Dexterity in Patients With Parkinson Disease. *Function and Disability Journal*, 3(1), 27–34. <https://doi.org/10.32598/fdj.3.35.3>
 4. Mateos-Toset, S., Cabrera-Martos, I., Torres-Sánchez, I., Ortiz-Rubio, A., González-Jiménez, E., & Valenza, M. C. (2016). Effects of a Single Hand-Exercise Session on Manual Dexterity and Strength in Persons with Parkinson Disease: A Randomized Controlled Trial. *PM&R*, 8(2), 115–122. <https://doi.org/10.1016/j.pmrj.2015.06.004>
 5. Choi, H., Park, D., Rha, D.-W., Nam, H. S., Jo, Y. J., & Kim, D. Y. (2023). Kinematic analysis of movement patterns during a reach-and-grasp task in stroke patients. In *Frontiers in Neurology* (Vol. 14). Frontiers Media SA. <https://doi.org/10.3389/fneur.2023.1225425>
 6. Temporiti, F., Mandaresu, S., Calcagno, A., Coelli, S., Bianchi, A. M., Gatti, R., & Galli, M. (2023). Kinematic evaluation and reliability assessment of the Nine Hole Peg Test for manual dexterity. In *Journal of Hand Therapy* (Vol. 36, Issue 3, pp. 560–567). Elsevier BV. <https://doi.org/10.1016/j.jht.2022.01.007>

Quantitative Assessment of Ground Penetrating Radar for Concrete Structure Integrity

Mahmood Khan^{1&3*}, Ahsan Ali³, Muhammad Athar Khan Chandia², Safiullah Noor², Abdul Moez², Muhammad Shahid Aslam², Muhammad Nouman³, Khurram Shahzad³, Zahid Suleman Butt², Ragnhild Elizabeth Aune¹

¹Norwegian University of Science and Technology (NTNU), Trondheim, Norway,

²Department of Mechanical Engineering, University of Engineering and Technology, Taxila, Pakistan,

³National Centre for Non-Destructive Testing (NCNDT), Islamabad, Pakistan

*postmottak@ntnu.no

ABSTRACT

Ground Penetrating Radar (GPR) is emerging as a promising tool for assessing the condition of reinforced concrete structures. This study focuses on evaluating the effectiveness of GPR mapping techniques in detecting and characterizing reinforcement bars, voids, and other anomalies within concrete structures. Utilizing a high-frequency GPR system, data was collected from various reinforced concrete specimens, including beams, columns, and slabs. The research methodology involved systematic scanning of the specimens to capture GPR signals reflected from the internal features of the concrete. Signal processing techniques were employed to enhance data clarity and extract meaningful information regarding the depth, size, and orientation of reinforcement bars, as well as the presence of voids or defects. The results of the study demonstrate the capability of GPR mapping in providing accurate imaging and assessment of reinforced concrete structures. Insights gained from the data analysis contribute to a better understanding of the structural integrity, corrosion potential, and overall health of the concrete elements. This research has implications for maintenance strategies, structural health monitoring, and non-destructive evaluation practices in the construction industry. By showcasing the efficacy and reliability of GPR in mapping reinforced concrete, this study contributes to the advancement of non-invasive inspection techniques and supports informed decision-making in structural maintenance and rehabilitation projects.

KEYWORDS: Ground Penetrating Radar (GPR), Civil Structures, Defects, Damage Mechanism, Non-Destructive Testing (NDT), Structural Integrity, Reinforced Concrete Structures

INTRODUCTION

Concrete structures, though durable, degrade over time due to defects like cracking, voids, and rebar corrosion, threatening structural integrity. Traditional Non-Destructive Testing (NDT) methods, such as Rebar Locators and Ultrasonic Pulse Velocity (UPV), have limitations in depth penetration and defect detection, while advanced techniques like Phased Array Ultrasonics and Ground Penetrating Radar (GPR) face challenges with material inconsistencies and data interpretation. This thesis seeks to enhance NDT techniques by integrating multiple methods and developing advanced data processing algorithms to improve accuracy and comprehensiveness in defect detection. Machine learning and real-time monitoring systems will also be explored to offer continuous, reliable assessments of concrete integrity. The research aims to provide better tools for structural health monitoring and maintenance of concrete structures.

This research evaluates the accuracy of various GPR data capture techniques for subsurface utility mapping (SUM), revealing that along-pipe scanning is the optimal approach. Contrary to the widely used perpendicular scanning, along-pipe scanning offers superior penetrative power, target detectability, and accuracy, aligning with Quality Level A utility data. The study sets a new standard for mapping businesses, recommending along-pipe scanning as the preferred method for GPR data collection in SUM.[\[1\]](#)

The experiments confirm that radar technology is effective for civil construction applications, particularly in assessing internal morphology, defects, and locating steel reinforcements. While efficient, this approach can be superficial and prone to distortion if misused. It requires careful modulation, especially when material behaviors differ from expected dielectric properties. The study highlights the technology's ability to provide detailed structural information, including steel bar placement, aiding in seismic vulnerability assessments. Additionally, raw-data filtering methods significantly enhance location accuracy and resolution.[\[2\]](#)

This research explores the use of ground penetrating radar (GPR) for subsurface utility detection, focusing on location and material composition. The study clarifies industry uncertainties by accurately identifying utilities and extracting backscatter amplitudes based on material type. It introduces an optimal image thresholding method to improve existing GPR tools for detecting material features. The findings suggest GPR is effective for identifying utility form and dimensions, while backscatter amplitudes can indicate operational conditions, including flaws from aging or environmental factors.[\[3\]](#)

The frequency spectrum of pavement is influenced by the type of material used. Tests on bituminous mixes, granular solids, and cement-treated materials showed amplitude changes in relevant frequency ranges. Statistical analysis of transmitted waves detected amplitude fluctuations at layer interfaces, enabling the assessment of mean thicknesses for each pavement layer.[\[4\]](#)

This study demonstrates the effective evaluation of rebar corrosion in concrete slabs using 2 GHz ground-penetrating radar (GPR). Through A-scan and B-scan methods, GPR detected early-stage corrosion before visible damage occurred. A-scan results showed reduced wave amplitudes and longer travel times due to elevated chloride levels and corrosion byproducts. B-scan images revealed blurred and dimmed rebar features, indicating corrosion. The findings highlight GPR's ability to identify localized corrosion in concrete related to chloride content and corrosion products, providing valuable insights into rebar deterioration.[5]

This assessment of GPR applied to bridge components demonstrates significant technical and operational advancements, especially in non-destructive evaluation. GPR's ability to rapidly survey large areas while providing depth and reinforcement data makes it invaluable for analyzing bridges and viaducts without compromising stability. The research compares methodologies for assessing bridge degradation, highlighting GPR's versatility in slabs, beams, and pillars. While numerous studies focus on slabs and beams, fewer address columns, suggesting the need for further exploration in this area. GPR's potential for time and cost savings in bridge evaluation is also emphasized.[6]

2. MATHEMATICAL MODEL

A mathematical model for the GPR 8000 describes the interaction between electromagnetic waves and subsurface materials.

- Wave Propagation and Maxwell's Equations
For radar systems, including the GPR 8000, Maxwell's equations in a medium describe how electric and magnetic fields E and B interact with the subsurface environment. Maxwell's equations in free space are given as Eqs. (1) - (2).

Gauss's Law for Electricity:

$$\nabla \cdot E = \frac{\rho}{\epsilon} \quad (1)$$

Where ϵ is permittivity of the medium and ρ is electric charge density.

Faraday's Law of Induction:

$$\nabla \times E = -\frac{\partial B}{\partial t} \quad (2)$$

where $\frac{\partial B}{\partial t}$ is the time rate of change of the magnetic field.

These equations model the wave propagation through concrete, which can be influenced by water content, rebar, and other anomalies.[7]

- The depth of embedded objects (e.g., rebar) or defects in concrete can be calculated based on the time it takes for the radar signal to travel to the object and return as shown in Eqs. (3).

$$d = \frac{v \cdot t}{2} \quad (3)$$

where v is the velocity of the radar wave in concrete, and t is the time it takes for the radar pulse to return.[8]

- Stepped-Frequency Continuous Wave (SFCW) Radar for Concrete Structures

The GPR 8000 uses Stepped Frequency Continuous Wave (SFCW) technology, which sweeps through a range of frequencies to produce high-resolution subsurface images which is shown in Eqs. (4).

$$\Delta R = \frac{c}{2\Delta f} \quad (4)$$

Where Δf is the bandwidth of the signal and c represents the speed of light in a vacuum.

Frequencies between 40 MHz and 3.4 GHz, the GPR 8000 achieves high-resolution detection of rebar.[9]

3. EXPERIMENTATION

The experiment consists of several key stages, including calibration, data collection, signal processing, and analysis. A block diagram is presented in Fig.1 to provide an overview of the methodology.

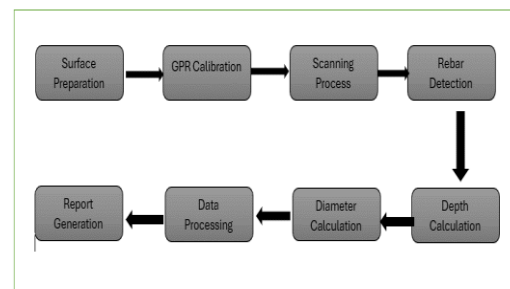


Figure 1: Migrated View of Dry Concrete

The experimentation initiated by preparing the testing area, ensuring that the surface is clean and ready for scanning. This is followed by setting up the GP 8000 and calibrating it based on the expected conditions of the concrete, including its thickness and rebar depth.

A scanning grid was then created on the concrete surface using chalk or tape. The grid spacing typically ranged between 10 cm and 50 cm, depending on the specific area being scanned and the level of detail required. Horizontal and vertical lines marked the area to be scanned, ensuring systematic coverage while minimizing overlap and the likelihood of missed areas. For basic experiments, grid paper was utilized to facilitate this marking process as shown in Fig. 2.



Figure 2: Calibration of GPR

Once the device was calibrated and the testing area prepared. The GPR probe was placed at one end of the testing area and moved systematically along the marked grid lines as shown in Fig. 3.



Figure 3: Scanning of Concrete block using GPR

Maintaining a steady speed during scanning was crucial to ensure consistent data collection across the entire grid; sudden stops or changes in direction were avoided to prevent distortion of the radar signal. The Proceq GP 8000 provided real-time 2D and 3D imaging, enabling the use of live feedback to ensure full coverage of the testing area, thereby enhancing the overall effectiveness of the experiment.

The diameter of the rebar was then estimated by analyzing the width of the hyperbolic reflection using Eqs. (5).

$$D = \frac{\sqrt{t} \cdot v}{2} \quad (5)$$

where \sqrt{t} is the time difference between the radar signal and reflection points, and v is the velocity of the signal.

This processed data is then used to create a report, which summarizes all the key findings, including the rebar layout and dimensions.

4. RESULTS AND ANALYSIS

The quantitative assessment of Ground Penetrating Radar (GPR) for concrete structure integrity was conducted through multiple experiments using the Proceq GP 8000. The results from these experiments highlight GPR's ability to detect rebar, pipes, and internal features under various conditions, both dry and wet.

In experiments involving dry concrete blocks, the depth slice view revealed clear and distinct hyperbolic reflections representing rebars as shown in Fig. 4. These reflections were symmetrical and consistently spaced, confirming the presence of uniformly placed rebar.

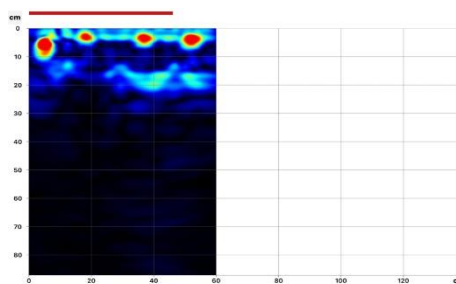


Figure 4: Depth Slice View of Dry Concrete

The migrated view further refined these reflections, collapsing them into sharp points, providing greater clarity in the positioning and depth of the rebar. The overall integrity of the concrete was verified, with no significant internal defects detected in these dry conditions as shown in Fig. 5.

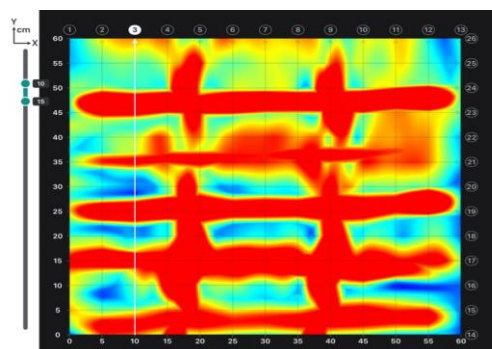


Figure 5: Migrated View of Dry Concrete

When a pipe was introduced in one of the concrete blocks, the depth slice view displayed a horizontal line below the rebars, indicating the presence of a subsurface object i.e. pipe. The radargram clarified the pipe's location, distinguishing it from the rebars as shown in Fig. 6.

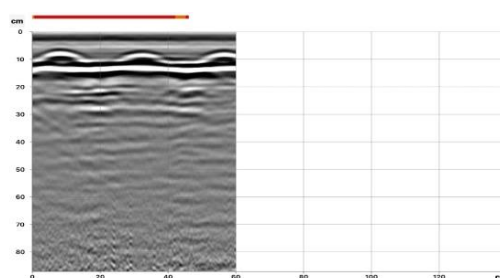


Figure 6: Depth Slice View of Embedded Pipes in Concrete Block

This experiment demonstrated GPR's versatility in detecting not only rebar but also utilities within the concrete.

However, when the concrete was wet, as tested in one of the experiments, the signal was attenuated due to the presence of moisture, leading to weaker reflections on the radargram as shown in Fig 7.

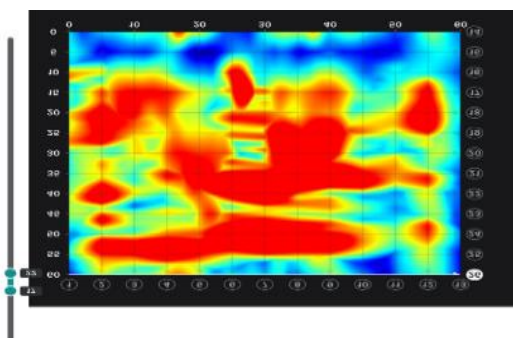


Figure 7: Migrated View of Wet Concrete Block

Although the rebar was still detectable, the reflections were less distinct compared to the dry conditions. This indicates that while GPR can function in wet conditions, the clarity of subsurface features is reduced, and smaller defects or finer details might be obscured. These experiments underline GPR’s effectiveness in mapping internal structures of concrete, ensuring that the integrity of rebar and other subsurface elements can be accurately assess.

In addition to traditional GPR data analysis, Augmented Reality (AR) was employed to provide an enhanced visualization of the internal structure of the concrete specimens as shown in Fig. 8.

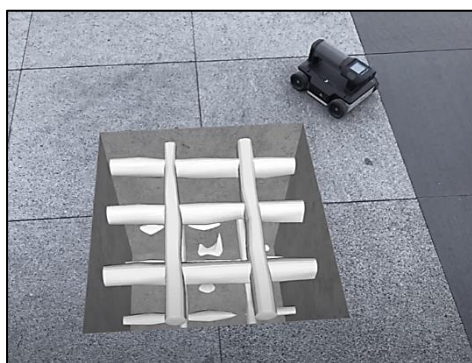


Figure 8: Augmented Reality feature of GPR

Moreover, the thickness of the concrete cover over the reinforcement bars plays a crucial role in preventing corrosion. GPR accurately measured the depth of the concrete cover, with deeper cover layers indicating better protection of the rebars from moisture ingress and aggressive environmental conditions. In our experiments, the GPR scans revealed that the concrete cover was uniformly distributed across all specimens and exceeded the minimum required thickness, which significantly reduces the chances of corrosion.

Also, we conducted a sensitivity analysis of various GPR frequencies to evaluate their effectiveness in detecting defects and assessing structural integrity across different depths. Antennas with frequencies ranging from 300 MHz to 900 MHz GHz were employed to analyze penetration depth and resolution trade-offs. Lower frequency antennas were tested to assess their penetration capabilities in thick concrete samples, while higher frequency antennas were utilized to observe their performance in detecting near-surface defects with high-resolution detail. During testing, the lower frequency antennas demonstrated greater penetration, successfully reaching depths up to several meters in the concrete, albeit with a reduced resolution that limited their ability to accurately detect smaller or closely spaced defects. Conversely, higher frequency antennas showed high-resolution imaging for defects close to the surface but were quickly attenuated, with reduced effectiveness beyond shallow depths. This experimental approach allowed us to characterize the relationship between frequency and penetration depth, highlighting the inherent trade-offs between depth and resolution.

In heavily reinforced concrete, we examined the effects of rebar density on GPR signal clarity and depth penetration by testing concrete samples with varying levels of reinforcement. To simulate realistic scenarios, both single and double reinforced concrete samples were created, with different rebar spacings. During testing, heavily reinforced samples exhibited significant reflection and scattering, resulting in cluttered radargrams that obscured subsurface features and made accurate interpretation of rebar depth and layout challenging. For double-reinforced samples, the GPR signals faced substantial interference from the first layer of rebar, with strong reflections that masked any data from the second layer. This resulted in minimal signal penetration beyond the first rebar layer, particularly in closely spaced configurations, which increased signal attenuation and limited the GPR’s ability to detect deeper subsurface features.

By integrating the GPR data with AR technology, we were able to overlay the detected reinforcement bars, voids, and anomalies directly onto the real-world view of the concrete samples. This approach allowed for a more intuitive understanding of the internal conditions, facilitating more effective decision-making for structural evaluation.

5. CONCLUSIONS

The use of Ground Penetrating Radar (GPR) in this study provided valuable insights into the detection of subsurface features within concrete structures. Across multiple experiments, the Proceq GP 8000 demonstrated high accuracy in identifying rebar and other internal elements, such as pipes, under varying conditions. The primary objective was to evaluate GPR’s effectiveness in both dry and wet concrete environments, as well as its ability to detect different types of objects and potential defects.

The dielectric properties of concrete, including moisture content, aggregate type, and salinity, have a

substantial effect on GPR signal performance. High moisture and salinity levels increase conductivity, causing faster signal attenuation and reducing clarity, especially with high-frequency GPR. Sensitivity analysis of material composition highlights the importance of accounting for these variations to adjust GPR protocols and enhance result accuracy, particularly in aging or underground structures. GPR proved highly effective in dry conditions, providing clear, accurate radargrams for rebar detection, with migrated views enhancing depth and location precision. This accuracy confirms GPR's value for structural inspections in dry environments. However, in wet concrete, moisture caused signal attenuation, weakening reflections and reducing clarity. While migration partially mitigated these effects, accuracy was still lower than in dry conditions, underscoring the need for careful data interpretation in wet environments. The experiment demonstrated GPR's versatility in detecting embedded objects within concrete. The clear differentiation between the pipe and rebar reflections in the radargram confirms GPR's effectiveness in identifying both metallic and non-metallic objects. This capability broadens GPR's application from rebar detection to utility mapping, making it a valuable tool for comprehensive structural and subsurface assessments.

It is also concluded that lower frequency antennas, while offering greater penetration depths are suitable for thicker structures, sacrifice resolution and may miss smaller defects. Higher frequencies provide detailed imaging for near-surface analysis but are limited in depth due to rapid attenuation in dense materials like concrete. Balancing these trade-offs allows us to tailor GPR frequency selection to the specific requirements of each application, ensuring accurate and robust structural evaluation across varying concrete thicknesses and reinforcement densities. Our analysis also reveals that high rebar density in concrete significantly interferes with GPR signals, creating cluttered radargrams that obscure subsurface features and reduce the accuracy of rebar layout detection. In double-reinforced structures, strong reflections from the first rebar layer prevent effective assessment of deeper layers, limiting GPR's penetration depth. This underscores the challenges of using GPR in heavily reinforced concrete and emphasizes the importance of considering rebar density when interpreting GPR data.

Despite the limitations observed under complex conditions, the overall performance of GPR in detecting rebar and subsurface features was strong. The linear features captured in the radargrams across various experiments suggest that GPR is effective for identifying the internal layout of rebar and ensuring that structural elements are well-aligned. One of the key conclusions drawn from this research is GPR's superiority over other Non-Destructive Testing (NDT) methods, such as Ultrasonic Pulse Velocity (UPV) and Profometer, in terms of both speed and depth penetration. GPR offers real-time imaging capabilities, which, combined with its non-invasive nature, make it ideal for civil engineering applications such as infrastructure maintenance and monitoring. The findings from these experiments reinforce the importance of using GPR for concrete inspection, rebar corrosion and subsurface mapping. The study also emphasizes the potential for GPR to be further enhanced through the integration of advanced signal

processing techniques and machine learning algorithms. These enhancements can improve the detection and classification of defects within concrete, allowing for more precise assessments of structural integrity. As GPR continues to evolve, its application in structural health monitoring and maintenance will become increasingly valuable, particularly in cases where accurate, deep, and non-invasive testing is required.

ACKNOWLEDGEMENT

This study was supported by the National Centre for Non-Destructive Testing (NCNDT), whose provision of concrete samples and state of the art equipment was essential to the experimental process. The technical guidance and resources offered by NCNDT were invaluable in ensuring the successful completion of this work.

REFERENCES

1. J. Siow Wei and M. Hashim, "Accuracy of Data Acquisition Approaches with Ground Penetrating Radar for Subsurface Utility Mapping."
2. V. Barrile and R. Pucinotti, "Application of radar technology to reinforced concrete structures A case study," *NDT and E International*, vol. 38, no. 7, pp. 596–604, Oct. 2005, doi 10.1016/j.ndteint.2005.02.003.
3. J. Siow Wei and M. Hashim, "DETECTION AND MAPPING OF SUBSURFACE UTILITY USING GROUND PENETRATING RADAR."
4. J. P. Rodés, A. M. Reguero, and V. Pérez-Gracia, "GPR spectra for monitoring asphalt pavements," *Remote Sens (Basel)*, vol. 12, no. 11, Jun. 2020, doi 10.3390/rs12111749.
5. A. Zaki, M. A. M. Johari, W. M. A. W. Hussin, and Y. Jusman, "Experimental Assessment of Rebar Corrosion in Concrete Slab Using Ground Penetrating Radar (GPR)," *International Journal of Corrosion*, vol. 2018, 2018, doi 10.1155/2018/5389829.
6. P. Boldrin, G. Fornasari, and E. Rizzo, "Review of Ground Penetrating Radar Applications for Bridge Infrastructures," *NDT*, vol. 2, no. 1, pp. 53–75, Mar. 2024, doi 10.3390/ndt2010004.
7. Daniels, D. J. (2004). *Ground Penetrating Radar* (2nd ed.). IET.
8. Yilmaz, Ö. (2001). *Seismic Data Analysis: Processing, Inversion, and Interpretation of Seismic Data*. SEG Books.
9. Daniels, D. J. (2004). *Ground Penetrating Radar* (2nd ed.). IET.



Electromagnetic Testing: Prospects and Advancements for Industrial Inspections

Mahmood Khan^{1&3*}, Muhammad Kashan Haider², Muhammad Tayyab², Muhammad Zahid², Jabran Ali², Khurram Lal³, Raheel Zia³, Mubashir Gulzar², Ragnhild Elizabeth Aune¹

¹Norwegian University of Science and Technology (NTNU), Trondheim, Norway,

²Department of Mechanical Engineering, University of Engineering and Technology, Taxila, Pakistan,

³National Centre for Non-Destructive Testing (NCNDT), Islamabad, Pakistan

*postmottak@ntnu.no

ABSTRACT

Electromagnetic testing methods cover a wide range of Non-Destructive Testing (NDT) of engineering components installed in petrochemicals, power plants, fertilizer and many others. Heat exchanger tubes are the center of operation, w.r.t heat transfer and chemical reactions. Generally, the degradation mechanisms prefer thinnest pressure boundaries subject to failures. The present study covers the major four NDT methods of tubes testing, namely, Eddy Current testing, Remote field testing, Alternating current field measurement and Magnetic flux leakage. These techniques offer a wide range of coverage of the suspected areas of degradation. The choice of inspection and testing parameters lead to successful detection of flaws and corrective maintenance procedures. Recent developments in engineering technology have helped in detecting very subtle damage and defects in structures and materials, Robotics system, Smart Multi-Modal approach and utilization of physical principles of magnetism. Incorporation of Data Analysis techniques via artificial intelligence and machine learning algorithms results in the ability to read information faster, identify trends and patterns, predictive maintenance practices and the swift management of the assets making them more reliable. The features of electromagnetic methods of being portable and field-deployable systems enable quick inspections at multiple locations on the site which further expedites evaluations and prevents undue downtime. The integration with Industry 4.0 technologies with IoT platforms and cloud systems connected in real time, monitoring, remote inspection, and data sharing can be done to collaboratively and ensure quality measurement by networking. In the present study we will cover the basics of electromagnetic testing, their impact and detectability of industrial defects which can hinder the safe and reliable operation of the plants and efforts concerning the continual growth of electromagnetic testing technologies.

KEYWORDS: Electromagnetic testing, Eddy Current testing, Differential bobbin probe, thickness loss, thickness variation, Non-Destructive Testing, industrial failures.

1. INTRODUCTION

Non-destructive testing (NDT) is a significant method that is applied in many fields to check state of different materials and structures without damaging them. It enables the identification of defects on the product including metals, composites and ceramics without changing their usefulness [1]. Standard techniques like ultrasonic testing, radiography, and visual assessment are widely used in the structural assessment for arial, military, power industries and storage tanks assessments. Such methods are especially preferred due to their correlation between internal and surface defects contributing to safety and performance in crucial applications [2]. The combination of various techniques in NDT improves the results of the assessments by providing a broad perspective in the inspected material. NDT not only makes substantial cut in cost but also retards the usable life of parts and machinery as they do not fail suddenly [3]. Electromagnetic testing (ET) is an important non-destructive evaluation technique employed for the inspection and assessment of the properties of the

conductive materials including metals without the phenomenon of destruction [4]. It works with the electromagnetism principle based on generation of induced current commonly referred to as eddy current into the substance being tested. These current interact with the structural make-up on the material in such a way that it is possible to identify cracks, corrosion, or changes in conductivity or permeability [5].

ET is one of the well-known principles of non-destructive testing and however it has some constraints. This work primarily identifies Surface and sub-surface irregularities and conceals more profound abnormalities without additional approaches. Though ET has demonstrated good effectiveness, this technique can only be employed on conductive materials making it difficult to make use of in modern non-conductive materials such as composites [6]. Second, data interpretation is difficult, and common techniques require technicians, and this involves human errors. At the same time, ET along with Automation and Extra Deep Detection approaches are still in their formative years demanding improvement for mainstream Industrial use [7].

Eddy current testing (ECT) is routinely applied for shell and tube heat exchangers, air cooled heat exchangers and feedwater heaters especially when tubes are of non-ferromagnetic material. These materials include stainless steel, copper, brass, aluminium and nickel based alloys [8, 9]. Electromagnetic current tomography is very effective to detect surface cracks, corrosion and small defects because non-ferromagnetic material has low magnetic permeability. The testing is very quick and does not demand that removing the heat exchanger so that it can be inspected for faults. Compared to ECT there are some limitations in defect measurement especially size and depth, which is very essential to measure the degree of damage [10].

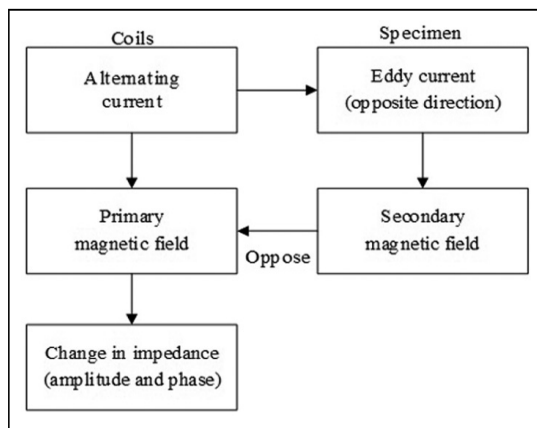


Figure 1: Principle for the Eddy Current Testing Operation

Since probe and coils are the most vital components of eddy current sensors, the configuration of the probe as well as the coil should be optimized. The primary objectives of this research are to identify and subsequently optimize coil parameters, such as geometry, sensing wire material and operational frequency to enhance the subtlety and accuracy of the developed sensors. This study will be helpful to expand the knowledge on several optimization approaches to establish better optimization of eddy current testing systems for non-destructive testing applications.

The Principle of ECT

One of the most famous laws in physics, Faraday's law of induction [11], is the basis of ECT. A main magnetic field is created when an alternating current (AC) passes through a coil in this operation. Eddy currents are generated in conductive materials when this coil is brought near to them, as they generate an alternating magnetic field. Eddy currents produce an auxiliary magnetic field that is diametrically opposed to the main field [12]. The presence of inhomogeneities in a material may affect the secondary magnetic fields by disrupting the passage of certain eddy currents. A signal describing the location and type of the defect is produced when this disturbance alters the coil's impedance. The use of several probe geometries for different intended operations and areas of concern is commonplace in electromagnetic testing, particularly in ECT [13]. Currents called e in the material under examination are generated by the coil that generates the

main magnetic field. This interaction between these currents and the material properties enables defects to be detected. Coil testing is sensitive to coil geometry, size and shape of the coil significantly affects the testing performance. Closely wound coils give higher resolution movements and are useful for finding small surface flaws. More widely spaced coils give less resolution but allow the probe to penetrate deeper into the material. Another parameter is the operating frequency of the coil with it being higher yielding better resolution on surface defects while lower frequencies allow for penetration into the sample. It is equally crucial to design the structure which contains the coil forming the probe [14]. Depending on the application and the area under test, probes like the surface probe, encircling coil or internal probes are used. While designing the probe's material and its structure, the interference must be kept at the lowest levels while the signal response must be boosted. Also, shielding used in probes avoids interferential electromagnetic signals, and focusing is used to increase the sensitivity of the probe in a particular area [15]. Several factors affect coil and probe performance in ECT. Such parameters include impedance and inductance that are significant in the generation of eddy currents and the coil's behaviour in response to the material. Coil can be operated at near resonance frequency to increase sensitivity and thus detect the defects easily.

Eddy Current Probes

Design and operating mode are the primary determinants of ECT probe classification. Thus, it may be described by the manner in which the coils are attached to the testing area; on the other hand, the system's mode of operation can be classified into several categories, such as absolute mode, differential mode, and a combination of the two. The most common types are surface probes, bolt hole probes, inner diameter or sheet probes, and outer diameter probes [16]. There are two primary varieties of bobbin probes often used in electroconvulsive therapy (ECT). Figure 2 shows two kinds of bobbin probes: the absolute and the differential. The so-called 'differential bobbin probe' consists of two coils each of which is wound 180° out of phase. This configuration enables the sensor to have high sensitivity to capture sudden changes in the material such as the formation of small cracks and defects. Meanwhile, the absolute bobbin probe comprises of one coil together with another similar coil – the reference coil. The reference coil is meant for the electromagnetic shielding and balancing of all the electronics when a test is being conducted [17].

ECT is one of the important methods for inspection of heat exchanger tube since these tubes contain some defects such as corrosion, crack and thinning of wall thickness. Heat exchangers work under extreme conditions, and hence the need to diagnose the defects as early as possible to avoid compromise of the heat exchangers entire running [10]. Differential probes in ECT employ two coils in which the basic idea is determining the steep changes in eddy currents in the region of the flaws such as crack and pit. These probes respond to tiny, acute defects and are efficient in removing noise and are useful in surface and almost surface examinations [18]. The absolute probes, on the other hand, provide an indication of the change in impedance on the whole material of the pipe, and as a result it will be appropriate for wall thinning or corrosion detections whereby the change is gradual. Absolute probes

are especially useful to monitor the global properties of the material over a large area while the Differential probes often perform exceptionally well in detecting localized sharp defects. Both probes are utilized jointly to offer a detailed evaluation of the status of heat exchanger tubes. This approach provides an opportunity for an early prognosis of both zones' damage and global heat exchangers' degradation, enhancing the maintenance schedule and the heat exchangers' service life [19]. The employment of these probes in combination aids in the safe and effective function of heat exchangers particularly in industries.

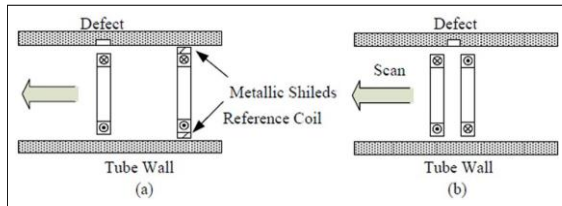


Figure 2: Tube inspection bobbin probes; (a) absolute and (b) differential

2. EXPERIMENTAL

Eddy current probe is the most important connection between the eddy current instrument and the item that must be tested. The probe has two functions – it itself produces eddy currents, and it also ‘feels’ what happens to the flow of these currents upon encountering a defect. The coil inside the probe is a copper wire with a size according to the probe body hole, wire diameter, number the turns and coil dimensions are among the parameters that need to be set to get the desired inspection results. The work of the eddy current probe design and development is crucial in this area because the probe defines the probability of detection. For the coil, the number of turns per layer to fill the cross-section space in the eddy current probe is maintained to be the same to control the inter-turn effect to the barest minimum. In general, the distance between coils should be less than the anticipated length of the defect and equal to the thickness of the component. The probe body is typically made of a non-conductive material that includes Teflon or any composite material that exists. Wear of the probe is typically minimized with the use of coating at the head or tip of the probe. In the subsequent sections of this paper, the manufacturing of eddy current probes will be described in more detail.

3. MATHEMATICAL MODEL

An essential task for the creation of an eddy current sensor is to improve the coil since it determines the sensitivity, resolution and overall performance of the sensor. Here’s a generalized approach to create a mathematical model for optimizing coils [20].

However, to achieve optimization it is necessary to determine some parameters of the coil. These include number of turns (N), Coil radius (R), Wire thickness (d_w), Resistivity (ρ), Inductance (L), Frequency (f), Impedance (Z), Quality factor (Q) and Mutual Inductance (M).

- **Impedance of the Coil:** Hence the impedance (Z) of the coil is most crucial in its influence on the result of the coil interaction with the target material and the performance of the sensor.

$$Z = R + j\omega L \quad (1)$$

Where R is the resistance and $j\omega L$ is the inductive reactance. R is the ‘real’ component of Z and is associated with the power dissipation (heating), while $j\omega$ is the ‘imaginary’ component and is associated with the energy storage in the magnetic field.

- **Resistance of the Coil:** The resistance (R) of the coil wire can be described by using equation:

$$R = \rho \frac{l}{A} \quad (2)$$

A represents the wire's cross-sectional area, ρ stands for the material's resistivity (copper), and l represents the entire length on the wire throughout the coil. A thinner skin depth makes it simpler to achieve greater optimization, which in turn reduces resistance and power losses, but larger wires are more expensive. Resistance may be decreased by increasing the radius that R or lowering the number of turns N, but there is a possibility that inductance will be decreased as well..

- **Inductance of the Coil:** The ability to store magnetic energy depends on a parameter known as inductance (L) for the coil. For a solenoidal coil, the inductance is:

$$L = \mu_0 \mu_r \frac{N^2 A}{l} \quad (3)$$

The equation may be paraphrased as follows: where l is the width of the coil, A is the longitudinal dimension of the coil, N is the number to turns coiled on the coil and is the permeability index of the core material. In this way, the optimal working point for the infrared sensor is determined by the fact that the inductance increases as the power of both N as well as R squared increases.

- **Quality Factor:** The quality factor Q is an important metric for evaluating the efficiency of the coil. It compares the stored energy to the energy dissipated in the coil:

$$Q = \frac{\omega L}{R} \quad (4)$$

Where, ω is the angular frequency, L is the inductance and R is the resistance. High Q value suggests that the coil possesses low levels of energy losses enhancing sensitivity and efficiency. However, maximizing for Q involves trade-off between inductance, in which the coil must accommodate many turns and resistance which increases with turns and wire length.

- **Mutual Inductance and Eddy Currents:** The resistance factor, namely the mutual inductance (M) between the coil and the conductive target plays a unique role in eddy current sensors. Cooperative inductance refers to the extent to which the change in coil's current causes a counter current in the target substance. These are currents induced in the target, they produce fields, which oppose coil field, thus independent coil impedance. Such impedance variations can be readily sensed to invoke characteristics of the target such as composition of

the material, distance and defects. The strength of the eddy currents is proportional to:

$$I_{eddy} \propto \frac{dB}{dt} \propto \omega B \quad (5)$$

Where, B is the magnetic flux density produced by the coil. As the frequency increases, the eddy currents are at their strongest though the skin depth and the energy loss due to the skin effect are also high.

- **Optimization Problem:** We now formulate the optimization model more precisely, with a focus on maximizing sensitivity, minimizing resistance, and achieving the desired inductance. To maximize the sensor sensitivity (S), which depends on the mutual inductance M and the change in impedance ΔZ :

$$S = f(L, R, M) \quad (6)$$

Where, L and R affect the coil's response to eddy currents and M is the mutual inductance depends on the geometry and proximity of the target.

Manufacturing of the Coil

Every single internal Eddy current probe itself is made up of two coils, which are lengths of conductive wire helically wound around a tube or rod, this is the body of the probe. These are made from copper or non-ferrous material to avoid any magnetic influence on the wire. As to the shape, the body of the probe used for the coil is tubular or ring-like and constructed with dielectric material. Knowing the geometry of the probe as seen in figure 3 is crucial in finding out the characteristic of the corresponding probe.

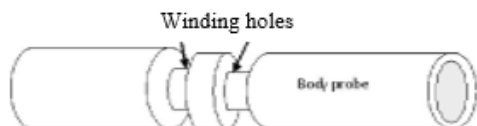


Figure 3: Differential probe body geometry parameters

Groove size to make probe with high sensitivity. Geometers, $a=b=c$, as shown in figure 4.

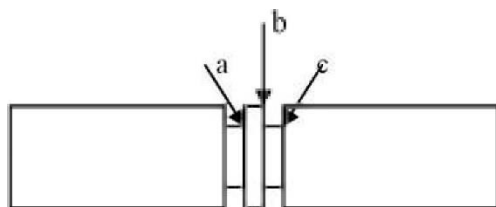


Figure 4: Front view of the probe body

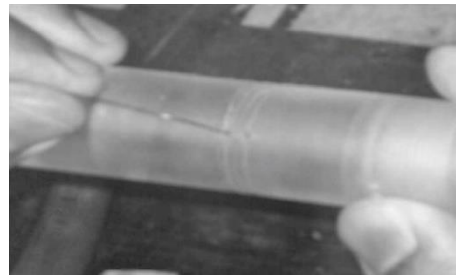


Figure 5: First hole at the center of probe body

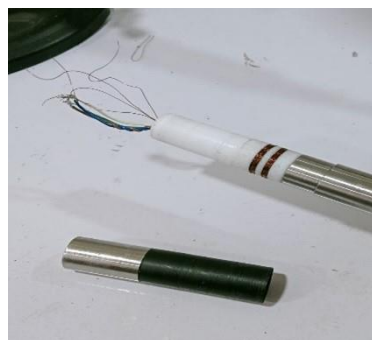


Figure 6: Probe after winding of the copper wire

The choice of probe size depends on the test object diameter for all Differential Eddy current probes. It should use a diameter that will afford at least a fill factor of 80%. It is here that the right number of coils is chosen depending on the signal produced by the probe. A good eddy current probe will give separation angle between 100% wall loss and 20% wall loss. The availability of number will be arrived in experimental manner and the material use for the coils are always copper because copper is good conductor of electric current.

Tools and Materials

1. Wire winding tool, Body probe, 0.2mm enamelled copper wire.
2. Tweezers, cutting tools, Clamping jaws.
3. Multimeter, magnifying glass.
4. Solder

Working Steps

In manufacturing of eddy current probes, there are six principal elements or components. The first step is to form the first coil turn with clockwise direction; while forming the second coil turn, it should be in anticlockwise direction. The next process is a check connection, further the identification of the terminal for cable connection and at last a check on the connection of the probe-connector.

1. The first coil of wire – the one going clockwise, place the tip of the copper wire into the first hole drilled at the centre of the probe's body as shown in figure 5. Remove the end of the copper wire in the probe body part of the device of the invention. Twirl it clockwise in a way that the coil covers the probe completely, complete one turn and start the second for winding the coil. Continue to execute all above procedure until the desired number of turns is reached. To

finish, wind the tape around the coil after the specific number of turns are made. Pass the copper wire through this hole and then remove the wire from the other end of the probe.

2. The second contour or back-and-forth line of the wire by establishing an additional coil in a counterclockwise direction. Making the second roll step-by-step is the same as making roll coil 1, the only difference is the other way around with the first coils with the anticlockwise rotation over at the top and the clockwise over at the bottom as shown in figure 6.
3. The third step is coil connection test. The intent of the test is to confirm that the copper wire is intact through the coil, that the copper cable does not have a break anywhere. The method that is taken is by measuring the coil resistance between the two ends or by the 'beep' test. It is important that the copper wire layer is stripped from the end of the wire to be tested before testing is done. The testing of equipment is done with the use of a Multimeter as shown in figure 7.
A beep sound and a resistance reading means that the two coils of wire joined along the winding at each end of the wire in the probe body hole.
4. For the terminal connector, more over there are four legs in the connector but the number of legs is two and three will be used for connection. 1st wire will be brought out to the third leg of the connector. The last of the 2nd wire will be soldered to the earth terminal of the connector. The 3rd end of the wire will be connected at the connector earth terminal. We will then press wire 4th end to the connector and connect it to the second leg of the connector.
5. However, before the actual soldering begins, the solder must be heated first. Tin the end of the wire according to the correct terminal. When soldering is done allow the connector to cool in the air for approximately five minutes.
6. The next step is probe-connector testing. As an objective of the test, the connection of the coil of wire made must be verified. Measurement on test equipment is done employing a Multimeter. If the connection is successful, there is a beep sound. Lastly, when all steps are performed, the connector will be inserted into the probe.



Figure 7: Multimeter

4. RESULTS AND DISCUSSION

To make an eddy current probe requires a lot of focus and time more so because it is a process that requires precision.

The steps explained below will describe the procedures involved. Developmental procedure in the production of differential model for pipe tube testing. There are two coils of probe wire with one of the coils of wire in clockwise spiral and the other is in the anticlockwise spiral, in order to improve on the formation of a good coil on each layer of the coil is coated using an insulating material that is cut in width and length based on the coil hole; their intention is to easily see the arrangement of the coil in the coil hole.

This is continued until the coils have been counted to its desired number. Next, testing goes on until the two coils are not broken and the resistance of the two coils is also checked.

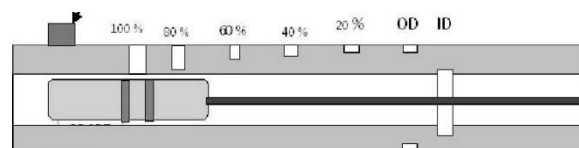


Figure 8: Standard Calibration Tube

The next process is soldering between the three ends of the wire connected with a connector as shown below; Cup-insertion testing, the probe is tested by inserted in a standard calibration tube. Attached to the standard calibration tubes are defects of 20%, 40%, 60%, 80% and 100% in thinning of the pipe wall tube.

The output signal at each defective corner will be preserved for further study, though the characteristic of this test is determined by the phase angle of signal resolution differences occurring between the 100 percent signal loss tube wall and the 20 percent signal loss tube wall of the calibration tube. The usual signal response of the differential eddy current probe when used in testing the calibration tube is depicted in Figure 8 only. From each fabricated probe the same output signal shape should be obtained and there are 8 signal shapes and can resolve the signal between 100% thinning signal of the tube wall and 20% thinning signal of the tube wall as shown in figure 9.

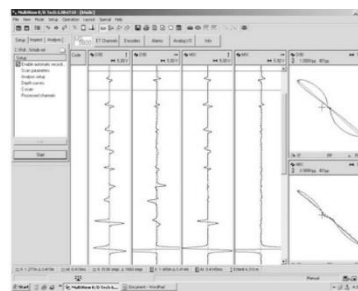


Figure 9: Calibration test signal output

If the probe does not generate the required separation output signal as read in the calibration tube, then the probe must again be re-fabricated, and the number of wire windings adjusted or reduced until the probe has met the required specifications. A turn count is chosen to be sensitive to the output signal of the probe to determine the optimum number of turns. High quality eddy current probe has a separation angle between 100% wall hole and

20% wall loss. Quantitative research methods will be applied to arrive at the best number.

The best eddy current probe is considered in relation to the signal produced by the probe in the process of operation. A suitable eddy current probe must deliver the separation angle in a specified area of 100% wall loss and 20% wall loss. Quantitative research will be employed to identify the right amount.

5. CONCLUSION

An example of an eddy current probe is one designed for use in inspection services such as inspecting heat exchanger tubes, industrial plants etc., as the probe is a distinct element in eddy current testing, with the diameter, thickness and composition of the pipe in question varying, different probes are required. From the test results, the probe with 60 turns is expected to generate a signal comparable to the standard probe signal, and then the probe is used to estimate the inspection testing services in advance, sometimes in large quantities (For instance, >2000-heat exchanger tubes) whereby the probe undergoes wear that results in deterioration of performance bearing in mind that the probe is relatively expensive. When the probe is tested using a standard calibration tube, the output result of the number of signals with reference to the number of calibration standard signals, the probe is then ready for inspection.

REFERENCES

1. Rucka, M., "Non-destructive testing of structures". 2020, MDPI. p. 4996.
2. Gupta, M., et al., Advances in applications of Non-Destructive Testing (NDT): A review. *Advances in Materials and Processing Technologies*, 2022. **8**(2): p. 2286-2307.
3. Cavalcanti, W.L., et al., Integrating Extended Non-destructive Testing in the Life Cycle Management of Bonded Products—Some Perspectives. *Adhesive Bonding of Aircraft Composite Structures*, 2021: p. 331.
4. Udpa, S.S. and P.O. Moore, *Electromagnetic testing. Nondestructive testing handbook*, 2004. **5**: p. 230.
5. Fitzpatrick, R., *Maxwell's Equations and the Principles of Electromagnetism*. 2008: Jones & Bartlett Publishers.
6. Nsengiyumva, W., et al., Advances, limitations and prospects of nondestructive testing and evaluation of thick composites and sandwich structures: A state-of-the-art review. *Composite Structures*, 2021. **256**: p. 112951.
7. Van Drunen, G. and V. Cecco, Recognizing limitations in eddy-current testing. *NDT international*, 1984. **17**(1): p. 9-17.
8. Sadek, H., NDE technologies for the examination of heat exchangers and boiler tubes-principles, advantages and limitations. *INSIGHT-WIGSTON THEN NORTHAMPTON-*, 2006. **48**(3): p. 181.
9. Reber, K., *Eddy current testing in pipeline inspection. Oil and Gas Pipelines*, 2015: p. 537-544.
10. Saffiudeen, M.F., A. Syed, and F.T. Mohammed, Failure Analysis of Heat Exchanger Using Eddy Current Testing (ECT). *Journal of Failure Analysis and Prevention*, 2023. **23**(5): p. 1898-1906.
11. Mochrie, S. and C. De Grandi, *Faraday's Law and Electromagnetic Induction, in Introductory Physics for the Life Sciences*. 2022, Springer. p. 793-829.
12. Cuevas, E., et al., *Fundamentals of Electromagnetism, in DC Motors: Modeling, Designing and Building with 3D Printers*. 2024, Springer. p. 1-15.
13. García-Martín, J., J. Gómez-Gil, and E. Vázquez-Sánchez, Non-destructive techniques based on eddy current testing. *Sensors*, 2011. **11**(3): p. 2525-2565.
14. Terry, D., The development of eddy-current testing techniques for tube inspection. *Radio and Electronic Engineer*, 1963. **26**(5): p. 373-382.
15. Machado, M.A., Eddy Currents Probe Design for NDT Applications: A Review. *Sensors*, 2024. **24**(17): p. 5819.
16. Tondo, F.A., et al., Eddy current probe identification and analysis. *IEEE Transactions on Instrumentation and Measurement*, 2017. **66**(8): p. 2166-2173.
17. Nam, M.-W., et al., Eddy Current Bobbin Probe Design for Steam Generator Tubes in NPPs. *Journal of the Korean Society for Nondestructive Testing*, 2007. **27**(2): p. 89-96.
18. Shu, L., H. Songling, and Z. Wei, Development of differential probes in pulsed eddy current testing for noise suppression. *Sensors and Actuators A: Physical*, 2007. **135**(2): p. 675-679.
19. Alencar, D.A., et al., Inspecting tubes installed in heat exchangers with a special eddy current probe and single frequency.
20. Xiaoqiu, H., D. Tianhuai, and F. Zhibin, Optimization Design of Eddy Current Sensor Coil's Parameters by Simplifying the Destination Function. *Instrument Technique and Sensor*, 2000. **11**: p. 3-5.



Parametric optimization and comparison of Digital Radiography with Conventional Radiographic Testing

Mahmood Khan^{1&3*}, Maryam Abdul Rehman², Sadia Riaz², Sajjal Nawaz²,
Muhammad Nouman³, Saad Jamal³, Riffat Asim Pasha², Ragnhild Elizabeth Aune¹

¹Norwegian University of Science and Technology (NTNU), Trondheim, Norway.

²Department of Mechanical Engineering, University of engineering and technology, Taxila, Pakistan.

³National Centre for Non-Destructive Testing (NCNDT), Islamabad, Pakistan.

mahmoodkhan77@gmail.com

ABSTRACT

Radiographic testing specializes in internal flaws and structure revelation. It has proven peerless w.r.t details and inspection capabilities. However, the hazards associated with the ionizing radiation have limited the scope of radiographic testing. Efforts are underway to oust undue exposures by advancements in technology. Nevertheless, majority of classical terminology and the basis of conceptual advancements originate from conventional film radiographic methods. Digital Radiography (DR) advanced directly to computers via software, enabling control on many operations parameters. The National Centre for Non-Destructive Testing is equipped with all the conventional NDT methods as well as state-of-the-art DR setup. A merger of both technologies for the better resolution and comparative approach is aimed hereby in this study. Optimizing DR for weld detection in pipes involve careful selection of exposure parameters, such as voltage, current, and exposure time, to ensure adequate penetration and contrast. Positioning the detector and X-ray source at optimal angles relative to the weld and using appropriate image processing techniques can enhance defect visibility. Contrast of the film, Graininess, sensitivity, IQI are specific to conventional radiographic testing. These terms have lost their core meaning in DR due to special phosphor screens or flat panels containing micro-electronic sensors or phase array diodes. However, the impact of radiographic image and their interpretation still requires the concepts and evaluation of these implicit parameters of radiation exposure. The study aims to demonstrate improvements in defect detection sensitivity and accuracy compared to conventional radiographic methods. Optimizing digital radiography involves calibrating, selecting appropriate exposure techniques and beam energy, utilizing image processing, multiple focus, dimensional scaling, and integrating with conventional RT for comprehensive results.

KEYWORDS: Radiographic testing, Digital Radiography, Non-Destructive Testing, parameters, comparison, quality, radiation.

1. INTRODUCTION

Radiography or radiographic testing (RT) comes in the family of non-destructive testing (NDT) which uses x-rays, gamma rays and neutron radiation to view internal structures and detect internal flaws such as porosity, notches, thickness variation etc. present inside a specimen.

Radiography emerged when x-rays were developed in 1895 by Wilhelm Rontgen and the announcement which was done by Marie Curie in 1898, that demonstrated existence of a new radioactive material called "Radium".

Conventional radiography involves the use of x-ray beams which is generated through a source. X-rays pass through the specimen and then image is formed on the film. Film can be seen in film viewer after it is developed.

X-rays are electromagnetic radiation just like light. The only difference between X-rays and ordinary light is that X-rays have several thousand times smaller wavelengths. X-rays usually used for radiography have wavelengths in the range 0.0001 \AA to 10 \AA where $1 \text{ \AA} = 10^{-8} \text{ cm}$ [1].

The portion from where more x-rays are passed will be shown darker whereas lighter portion depicts that less x-rays are passed. This shows thickness variation in a specimen and can also be used to check various defects. Conventional radiography has certain limitations too. The film can only be used once. If a radiograph gets rejected, whole procedure of exposure, development and inspection needs to be performed again which requires a lot of time.

In mid 1980s, computed radiography came into account. It is a digital replacement of conventional radiography. Instead of films it uses special x-ray sensitive, photo-stimulable phosphor plate known as imaging plate.

When X-rays are irradiated onto the imaging plate, electrons are released within the storage phosphor material and stored in higher energy states. A laser beam then scans the plate creating an image from the blue, fluorescent light emitted by the plate in proportion to the input amount of X-ray exposure. A high sensitivity, wide dynamic range photomultiplier tube (PMT) is then used to convert the emitted weak visible light into electronic

signals. These signals are then digitally processed to reconstruct a high contrast image of the original object that was exposed to X-rays [2].

Imaging plates used in computed radiography are sensitive to heat, light and physical damage. They require careful handling. Also, it takes much time to scan the images and resolution is also limited.

In early 2000s, digital radiography (DR) evolved and started replacing other radiographic techniques. It doesn't involve the use of films or cassettes and produces image instantly on the computer.

Digital radiography usually refers to Direct Digital Radiography (DR/DDR) which involves Digital Detector Arrays (DDAs) also known as direct Flat Panel Detectors (FPDS).

Indirect conversion FPDS have a scintillator layer which converts x-ray photons to photons of visible light and utilize a photo diode matrix of amorphous silicon to

subsequently convert the light photons into an electrical charge. This charge is proportional to the number and energy of x-ray photons interacting with the detector pixel and therefore the amount and density of material that has absorbed the x-rays.

Direct conversion FPDS use a photo conductor like amorphous selenium (a-Se) or Cadmium telluride (Cd-Te) on a multi-micro electrode plate, providing the greatest sharpness and resolution. The information on both types of detectors is read by thin film transistors. In the direct conversion process, when x-ray photons impact over the photo conductor, like amorphous Selenium, they are directly converted to electronic signals which are amplified and digitized. As there is no absent here, ensuring a sharper image. This differentiates it from indirect construction [3].

Focus on advancements in DR is continuing. It involves enhancement in resolution, sensitivity and dynamic range to provide higher quality images with lower radiation doses. AI is being integrated in DR and its algorithms can help streamline workflows and improve efficiency. Manufacturers are working on minimizing radiation dose and saving workforce from hazards of radiation. Advancements in technology have led to the development of lightweight, compact and portable DR systems.

IQIs are crucial in conventional RT and DR for assessing the quality and sensitivity of image. These are used to indicate the smallest indicatable defect present in a specimen. Exposure parameters such as voltage, current and exposure time are also important and effect the radiograph image. Understanding the optimal exposure parameters is essential for maximizing image quality and defect visibility. Contrast refers to the difference in densities between adjacent areas on a radiograph. Graininess describes the noise or texture of the image.

These parameters are also linked with image quality. Physical graininess however is eliminated in digital radiography but digital noise and artifacts can still affect image quality.

In DR, there are certain considerations and challenges that are different from conventional RT and computed radiography. It involves detector positioning and beam angle. Proper alignment is necessary so that X-rays penetrate through material uniformly and detector captures image with minimal distortion. Techniques such as contrast enhancement, noise reduction, edge detection, and multiple focus imaging allow for a higher degree of defect visibility and interpretation accuracy. However, reliance on software and digital manipulation introduces new variables which must be considered carefully to avoid artifacts and misinterpretation of data.

Digital radiography is preferred over any other radiographic techniques due to its tremendous advantages. DR setup is easy to use and requires least processing time. Conventional RT method involves processing and then developing the film which requires a lot of time and computed radiography also involves cassettes which needs to be removed from bucky tray, take it to reader, read it and then clear it. DR provides highest quality images due to latest technologies. These are typically more informative. Images can be stored for a longer time and permanent storage is available. It can easily be transferred to others. DR is considered more environment friendly because there is no chemical waste that occurs in this case.

2. OBJECTIVES

We decided to undertake industrial project to gain practical, professional experience and explore innovative solutions. This opportunity allows us to enhance our skills and contribute to new advancements in our field of study.

Schedule 40 pipes are widely used in residential, commercial, and industrial areas for different purposes including plumbing, heating, ventilation, and air conditioning systems. These pipes are essential in water treatment plants and distribution systems for conveying clean water and wastewater. They are commonly used for transporting crude oil, natural gas, and other petroleum products in the oil and gas industry. These pipes are utilized in chemical processing plants to convey acids, alkalis, and other corrosive chemicals. They are employed in power plants to convey steam and other fluids in high-temperature and high-pressure applications. These pipes are employed in structural applications, such as building supports, scaffolding, and fences. They are also used in irrigation systems for conveying water to crops

In oil and gas operations, transferring and providing access points for fossil fuels relies on the durability of schedule 40 piping. Specifically, schedule 40 is effective

for both liquid and gas conveyance due to its robust construction.

In chemical processing plants, schedule

40 piping is essential for preventing dangerous chemical leaks, as it can withstand hazardous fluids. Its custom diameters also facilitate retrofitting existing layouts.

For energy and power generation, schedule 40 is used to deliver pressurized steam across thermal power plants, thanks to its reliable pressure ratings in both small and large-bore configurations.

In water treatment infrastructure, schedule 40 piping ensures clean drinking water by being resistant to corrosion and impact, thus providing long-lasting performance.

Food and beverage facilities benefit from schedule 40's smooth, nonporous wall, which helps maintain rigorous sanitation and cleanliness standards by preventing contamination.

In mining operations, schedule 40 is crucial for withstanding severe underground conditions. It is used for ventilation, material transport, and equipment integration purposes.

The study aims to optimize digital radiography for specific industrial applications such as weld detection in pipes and compare its performance with conventional radiography.

Also, to refine the process by identifying and categorizing influential parameters. By conducting controlled experiments, we can differentiate between essential and non-essential factors that affect the accuracy and reliability of radiographic results. This approach aligns with guidelines mentioned in ASME standards, which emphasize the significance of critical parameters in ensuring precise measurements. By distinguishing these parameters, our project seeks to enhance the efficiency and precision of digital radiography, particularly in

applications where thickness variation plays a crucial role in material evaluation.

The expected outcomes of the study include improvements in the sensitivity and accuracy of defect detection using DR compared to conventional RT. The research aims to demonstrate that with proper optimization, DR can provide superior results in certain applications, while also identifying scenarios where conventional RT may still be preferable. Additionally, the study intends to highlight the potential for integrating conventional RT and DR techniques to achieve more comprehensive inspection results.

3. METHODOLOGY

Experimentation was carried out by two methods, conventional and digital radiography. For conventional radiography we used . Radiography was done on a step wedge whose length was 39.7cm. There were 6 steps on step wedge. Minimum thickness was 0.1cm and maximum thickness was 1.2cm.

3.1 Conventional Radiography

3.2 Selection of parameters

In first attempt we considered maximum thickness and set parameters for radiography. Selection of IQI was done through the reference tables. Radiation falls directly on IQI so source side is considered while checking reference tables. 1B 11 IQI was finalized. Place the IQI across the weld and thinnest wire should be away from the beam. Through exposure chart Kilovolts and amperes were also finalized. Single wall single image technique is used. Lead numbers were placed on every step.



Figure 6: Model 225 ANDREX SMART (machine used for conventional radiography)

3.2.1 Warming up procedure

Firstly, we have to warm up the machine. Insert control panel key into lock. Switch the machine to standby mode

through key. Select the 145 kV according to the (12 mm thickness) of test specimen. Add 10 kV increment to (145) required kV. Enter the input 155 kV. Machine will automatically calculate warming up time which in this case is 8 minutes. Press the green Push button. Warming up begins.

3.2.2 Setting procedure

Select image quality indicator (IQI) according to thickness which in this case is 1B 11. Place it on the specimen. Use masking tape to keep it in place. In exposure room, place D7 Pb film on the centre line marked on tube head. Place the specimen on the film. Calculate SFD (source to film distance) which is 700mm. Calculate OFD (object to film distance) which was 12mm. Turn on the gamma alarm and close the door of exposure room. Give command to control panel. Set 145 kilo volts, 4 milli amperes, and time is 1 min 45 sec. Gamma alarm will start beeping when machine is working.

3.2.3 Developing procedure

In dark room, measure developer temperature which was 30 degree centigrade. Check the graph which indicates time according to developer temperature which was 2 minutes. Turn off all lights except the safe light. Now open the film and remove screens. Put film in holder. Agitate film in developer for 15 sec and after that place film in developer for 2 minutes. Wash the film in water for 30 seconds. Agitate film in fixer for 30 seconds and then put in fixer for 6 minutes. Take out the film from fixer and again agitate in water for 30 seconds. Then put the film in dryer for 10 minutes. View the film in LED film viewer.

With maximum thickness we obtained unsatisfactory results. Some steps were not shown clearly.

3.2.4 Selection of parameters

Another radiograph was taken considering the thickness of third step. The thickness of third step was 0.72cm. IQI used was 1A 6. Place IQI across the weld and thinnest wire should be away from the beam. Single wall single image technique was used. Kilovolts and amperes were finalized using exposure charts and previous data.

3.2.4 Warming procedure

Insert the control panel key into the lock. Switch the machine to standby mode through key. Select the 140 kV according to the (72mm thickness) of test specimen. Add 10 kV increment to (150) required kV. Enter the input 150 kV. Machine will automatically calculate warming up time. Press the green Push button. Warming up begins.

3.2.5 Setting procedure

Select image quality indicator (IQI) according to thickness which in this case is 1A 6. Place it on the specimen. Use masking tape to keep it in place. In exposure room, place D7 Pb film on the centre line marked on tube head. Place the specimen on the film. Calculate SFD (source to film distance) which is 700mm. Calculate OFD (object to film distance) which was 12mm. Turn on the gamma alarm and close the door of exposure room. Give command to control panel. Set 110 kilovolts, 4 milli amperes, and time is 2 min. Gamma alarm will start beeping when machine is working.

3.2.5 Developing procedure

In dark room, measure developer temperature which was 29 degree centigrade. Check the graph which indicates time according to developer temperature which was 2 minutes and 15 seconds. Turn off all lights except the safe light. Now open the film and remove screens. Put film in holder. Agitate film in developer for 15 sec and after that place film in developer for 2 minutes 15 seconds. Wash the film in water for 30 seconds. Agitate film in fixer for 30 seconds and then put in fixer for 6 minutes. Take out the film from fixer and again agitate in water for 30 seconds. Then put the film in dryer for 10 minutes. View the film in LED film viewer.

3.3 DIGITAL RADIOGRAPHY

For digital radiography Leonardo DR system was used. Some of the components of this system include X-ray suitcase with power cord, removable shoulder strap, removable laptop with mains supply and wireless mouse, DVD-Rw external drive with storage case and USB cable, wireless flat panel detector with battery and charger as shown in figure 2.



Figure 2: Leonardo DR system with wireless flat panel detector and the generator

3.2.1 Connections

X-ray generator, flat panel detector and x-ray suitcase with laptop in it was connected. Once all the connections are complete, specimen (mild steel step wedge) was placed in front of flat panel detector. 1A 6 IQI was placed on the third step and was placed across the weld. Duplex IQI was also placed with 5 degrees tilt.

3.2.2 Procedure

Turn on the laptop. Open OR inspect. Enter the username “OR inspect” and password “x-ray”. Enter the component name, component ID, specimen thickness and some other details. On top right corner, there will be an option of Plan. Click on it, select material, grade etc. Plan a few number of exposures. Set pulses and then give exposure. Make sure that exposure room is closed. 8 shots were taken with pulses varying from 1 to 8.

4 RESULTS

After performing experimentation of conventional radiography, we used densitometer to check densities of every step. Table 1 shows densities against every step when we chose 7mm thickness and selected parameters whereas Table 2 shows densities against thickness when we chose maximum thickness and selected parameters.

Table 5: shows densities for each step with a 7 mm thickness and selected parameters.

Density	Thickness (mm)
6.8	1
5.42	2
2.36	5
1.13	7
0.67	10
0.46	12

Table 6: shows densities for varying thicknesses with maximum thickness and selected parameters.

Density	Thickness (mm)
6.8	1
6.8	2
6.8	5
5.31	7
3.68	10
2.48	12

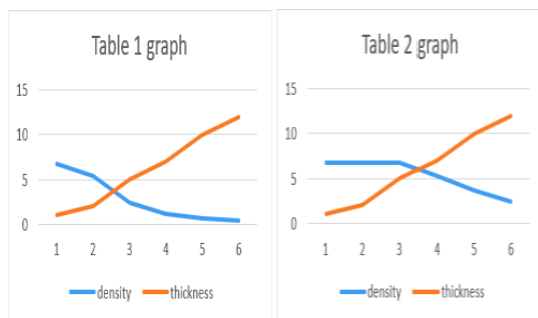


Figure 3: Graph between densities and thicknesses keeping exposure parameters constant

Graph 1 in figure 3 shows that as thickness increases density decreases. Density in radiography is just the degree of blackness and as thickness increases less radiations would pass and area would be less black. Same was the case in graph 2 but as the parameters selected for graph 2 were according to 12mm thickness that is why the 1mm, 2mm and 5mm thicknesses went totally black and density remained constant.

In digital radiography, 8 shots were taken by setting pulses from 1 to 8.

Gray values change at every single point on a single step but we worked by considering approximated values of every step. By keeping thickness constant, we plotted 6 graphs (as there were 6 different thicknesses due to 6 steps on step wedge) between pulses and gray value.

In every graph, gray value increased till 5th pulse after that it showed downfall and then again raised to higher values. This shows that 5 pulses are enough to get best results for this step wedge.

Another analysis was done by keeping pulses constant and 8 graph were plotted between thickness and gray values.



Figure 7: Digital radiography images of a step wedge, taken with pulse settings ranging from 1 to 8, demonstrating varying exposure levels

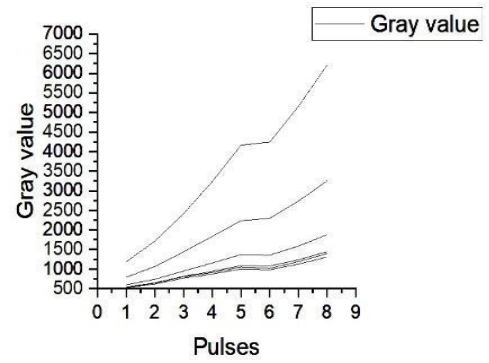


Figure 7: Merged graph between gray value and pulses

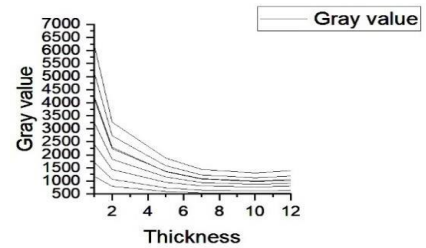


Figure 8: Merged graph between thicknesses and gray value

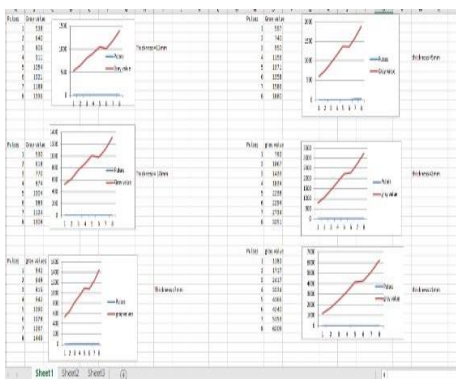


Figure 5: Individual graphs between pulses and gray value keeping thickness constant

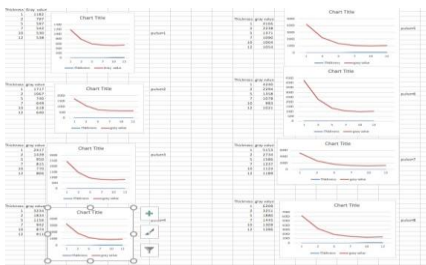


Figure 6: Individual graphs between gray value and thickness keeping pulses constant



REFERENCES

1. V. INTERNATIONAL ATOMIC ENERGY AGENCY, 1992, "Industrial Radiography, Manual for the Syllabi, Contained in IAEA-TECDOC-628," "Training Guidelines in Non-destructive Testing Techniques", November 1992. [Online]. Available: https://inis.iaea.org/collection/NCLCollectionStore/_Public/24/029/24029962.pdf. IAEA.
2. H. P. K. K. a. i. affiliates. "X-ray computed radiography (CR)." Hamamatsu Corporation. (accessed).
3. Aamir Khalid (Feb 1, Christoph Wiesner (Jul 2010–), "What is Digital Radiography and How Does it Work?," 11th September 2024 1946. [Online]. Available: <https://www.twi-global.com/technical-knowledge/faqs/digital-radiography#>.

Finite Element Analysis of Portable Grain Segregation System

Muhammad Huzaifa Ansari*, Riffat Asim Pasha, Amar Ul Hassan Khawaja, Chaudry
Muhammad Muzammil, Uzair Akram, Maryam Ismail

Department of Mechanical Engineering, University of Engineering and Technology Taxila.

*muhammadhuzaifaansari14@gmail.com

ABSTRACT

Manufacturers of high-density polyethylene (HDPE) pipes are facing the challenge of maintaining consistent quality and sizes. This is due to the presence of contaminants in the HDPE grains that are added during the recycling process. When it comes to cleaning a 130 kg grain load by hand, can be a time-consuming process. As a solution to this problem, the prototype of a portable segregation system has been proposed. The purpose of the current research is to investigate the Static Structural and Modal Analysis of portable segregation systems, to ensure that they are designed safely for industrial purposes. The main objective of this research is to analyze the strength and handling of the machine so that it can work well under different conditions and loads without failure. Structural damage due to the weight of the material or its components is analyzed by investigating the strength of the links, hopper, and frame. In addition to this, the research also emphasizes investigating the failure of the frame due to vibrations, by incorporating modal analysis. The durability of the design under stress is checked by utilizing FEA techniques to investigate the mathematical modeling, structural, and modal analysis of the design. The research evaluates the design of the machine that reduces the cost by up to 65%. Its applications can be found in the polymer, agricultural, and construction industries.

KEYWORDS: Contaminants, FEA, HDPE, Modal analysis, Recycling process, Static Structural.

1. INTRODUCTION

Machine Design is an area where Finite Element Analysis (FEA) theory is a valuable tool and it can be used to predict the performance, strength and life of components in respective real world environments condition. Furthermore, the trial production cost decreases the profit with FEA analysis in developing new machines. At best it is used across all growing industries tilting us in the direction of automation. The PVC and HDPE industry in Pakistan is significantly growing with the expansion of supply, and in infrastructure [1]. Manufacturers ensure high-quality pipes, according to international quality standards. Segregation is essential for quality control. Raw material grains quality is significantly important for a good quality product. The purpose of sieving or segregation in this context is to separate or filter out unwanted particles or impurities from the raw materials [2], used in pipe manufacturing. Before the pipe manufacturing process begins, raw materials such as HDPE grains need to be inspected and prepared. Unwanted particles can lead to defects in the final product, making it necessary to monitor and maintain the material's consistency through sieving [3]. Agricultural and Construction industries also require proper segregation. In the Agricultural industry segregation machines help to separate the crops based on their size and quality and most importantly they prevent harmful insects or animals from mixing with the final product [4]. On the other hand, in the Construction industry stones and other unwanted particles are removed from the sand and cement to achieve smooth mixtures [5].

Nanchimuthu et.al highlights durability as a factor that needs to be considered when building the sieve machine.

The sieve machine needs to be sturdy when it revolves and vibrates. The material that will be utilized ought to be readily available and appropriate for building the sieve machine. The material and manufacturing process determines this. It ought to minimize the expense [6].

Recycling of HDPE pipes contaminates the raw material due to worker oversight; manual cleaning is time-consuming with a daily load of 130 kg of material. The main objective of this research is to analyze the strength and handling of the machine so that it can work well under different conditions and loads without failure. The research uses Static Structural and Modal Analysis of the design.

2. METHODOLOGY

The methodology of the research is as follows,

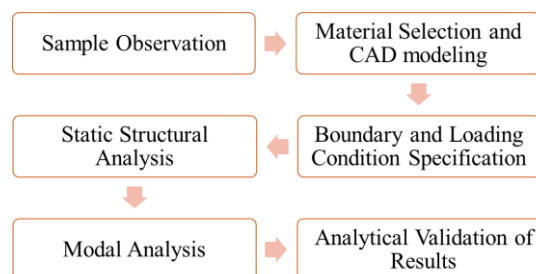


Figure 1: Research Methodology

Sample Observation

The range of sizes is used to divide the material into three groups.

Table 1: Sample Observation

No. of observation	Large Sized Grains		Medium Sized Grains		Small Sized Grains (virgin)	
	Cylindrical Dia mm	Height mm	Cylindrical Dia mm	Height mm	Cylindrical Dia mm	Height mm
1	5	6	4	6	3	4
2	4.5	5	4	5	3	4
3	5	5	4	6	3	4
4	4.5	5	4.5	5	3	4

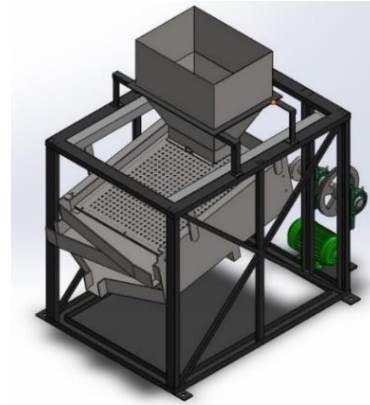


Figure 2: Grain Segregation System, Isometric View.

Design Material Selection

The components materials are listed in the table below,

Table 2: Component Material Selection

Sr.	Items	Material
1	Siever Net Support Frame	Mild steel
2	Grain Distributer Frame	Mild steel
3	Meshes	Steel with galvanized coating
4	Siever Frame	Mild steel
5	Flywheel	Cast iron
6	Driven Pully	Cast iron
7	Connecting Rod	Mild steel
8	Shaft	Steel
9	Motor	Cast iron
10	V-Belt	Rubber
11	Slider	Steel
12	Bearing	Bearings steel and Cast iron
13	Structural Frame	Hot-rolled carbon steel
14	Fasteners	Alloy steel
15	Hopper	Mild steel
16	Hopper support frame	Galvanized steel

CAD Model

The CAD model of Portable Grain Segregation System used for the FEA analysis is showed in the figure below

3. SIMULATION AND RESULTS

In software analysis, the research used “ANSYS Workbench 18.1” to find Structural stability and mode shape frequencies (check for resonance) through static structural and vibration modal analysis respectively.

Static Structural Analysis

A static structural simulation is used to study the effect of steady (or static) loading which is applied on a structure. This helps identify weak points of low strength and durability during the design process and avoid further costs. It includes the analysis of the Frame, Hopper, and hinges of the portable grain segregation system.

Loading and Boundary Conditions

The pressure of 58717.6 Nm⁻² and 6898.726 Nm⁻² are applied on one slider (due to sieve assembly) and hopper support frame (due to hopper and material of 137 kg) respectively. The frame is fixed at its bottom. A pair of 14 in. and 9 in. hinges are subjected to 1265.6 N (due to Siever assembly), which is fixed from a whole from which a roller’s pin passes. The bottom of the System’s frame is fixed to the ground.

Mesh Generation and Results

Tetrahedron is used as a method for mesh generation as it provides accurate results because of its ability of better surface contour Approximation.

The software results are shown in the figures below,

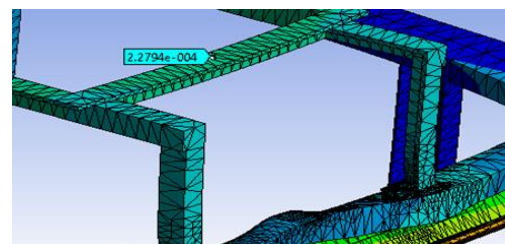


Figure 3: Deformation in Angle-iron of Frame

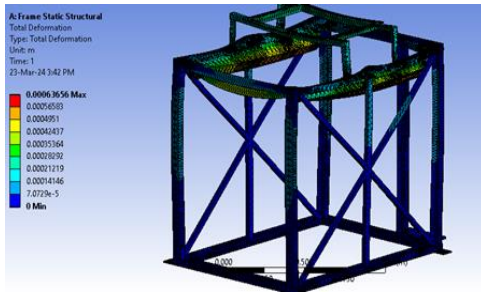


Figure 4: Deformation in Structural Frame

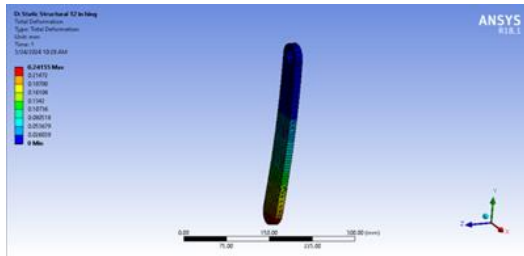


Figure 5: Deformation in 14 in. Hinge

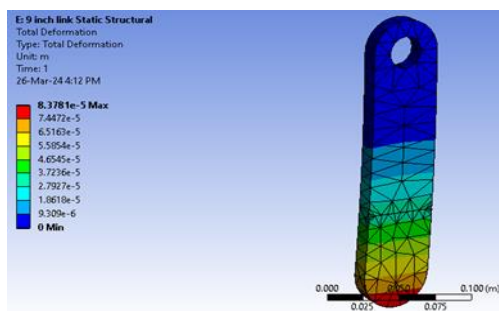


Figure 6: Deformation in 9 in. Hinge

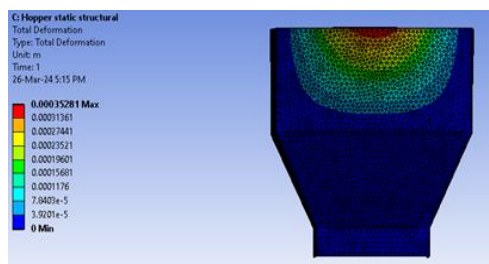


Figure 7: Deformation in Hopper of 137 kg capacity

Analytical Validation of Static Structural Analysis

Frame

C-Channel

Mass applied on one side = slider mass + hopper mass on one side

Mass = 19.054 Kg, W = 280.09 N,

Length = 1.3716 m

The total deformation in the Channel Beam considering Uniformly distributed load and simply supported beam is found by the equation below,

$$\delta = \frac{5WL^4}{384EI} \quad [7] (1)$$

$$\delta = \frac{5(280)(1.3716)^4}{384(2 \times 10^{11})387 \times 10^{-7}}$$

$$\delta = 1.19 \times 10^{-4} \text{ m} = 0.19 \text{ mm}$$

Angle Iron (L Beam)

Length= 0.536 m

Mass = Hopper + Hopper capacity

Mass= 22.14+ 137 =159.14 kg

The total weight considering the safety factor can be found by equation 2 below,

$$\text{Weight} = W = mg \times \text{factor of safety} \quad (2)$$

$$= 159.14 \times 1.5 \times 9.8 = 2339.354 \text{ N}$$

Weight on 1 L beam W= 584 N, and

$$I = 5.419 \times 10^{-8} \text{ m}^4$$

The Total deflection is found by equation 1.

$$\delta = \frac{5(589)(0.536)^4}{384 (2 \times 10^{11}) 5.419 \times 10^{-8}} = 2.018 \times 10^{-4} \text{ m}$$

Slider

Total mass of Sieve Assembly = 174.35 kg, Maximum Material on first plate = 3.8 kg, Length = 1.163 m,

Safety factor= 1.5

The total weight including the factor of safety is found by equation 2. So,

$$W = 2618.805 \text{ N.}$$

Now weight on one slider = 1309.4025 N

The total deformation in L-Beam considering Uniformly distributed load and simply supported beam is found by equation 1 below,

$$\delta = \frac{5(1309.4025)(1.163)^4}{384(2 \times 10^{11})2.529 \times 10^{-7}} = 6.27 \times 10^{-4} \text{ m}$$

Sieve Plate Holder Frame Hinges

For 14 in. Hinges

Length of beam = 14 in. = 355.6 mm,

Length on which force is applied = b = 2 in. = 50.8 mm,

Point Load to UDL = $\frac{1265.6}{50.8} = 24.91 \frac{N}{mm}$, Moment of

Inertia = $\frac{b_1 d^3}{12} = 8671.49 \text{ mm}^4$, Young's Modulus = E = $2.0 \times 10^5 \frac{N}{mm^2}$,

W = 1265.6 N

The deformation in the hinge considering a simply supported beam and a point load is found by equation 3 below,

$$\delta = \frac{Pb(3L^2 - 4b^2)}{48 EI} \quad [7] (3)$$

Putting the values we get

$$\delta = \frac{1265 \times 50.8 (3(355.6)^2 - 4(50.8)^2)}{48 \times 2.0 \times 10^5 \times 8671.49} = 0.28 \text{ mm}$$

Similarly, for 9 in. hinge the total deformation was found to be $\delta = 0.113 \text{ mm}$

Summary of Static Structural Analysis

The C-channel, hopper support frame, and slider will deflect up to 0.182 mm, 0.227 mm, and 0.637 mm, respectively, according to FEA analysis (Static) of the model. This is significantly less for a machine with a 137 kg capacity. The design is safe under loading situations because the deflection for the hopper, 14 in. and 9 in. hinges was determined to be 0.35 mm, 0.28 mm and 0.113 mm, respectively as shown in table below.

Table 3: Summary of Static Structural Analysis

Components	Deformation (Software) mm	Deformation (Analytically) mm
Hopper Support Frame	0.227	0.190
C- channel	0.182	0.201
Slider	0.636	0.627
14 in. Hinge	0.24	0.28
9 in. Hinge	0.08	0.113

Modal Analysis of Structural Frame

Modal analysis is used to investigate the mode shape frequencies of the frame to check whether there is a chance for a resonance to occur. It finds the stability of design subjected to some exciting force.



Figure 8: 10 Modes Shape Frequencies of Modal Analysis.

Force Frequency of Grain Segregation System

The forced frequency on the system is due to the Motor whose 900 RPM is reduced to 128.5 RPM using a pulley reduction mechanism providing reciprocating motion to the sieve. The operating frequency of the motor is 50 Hz, and the number of poles is six.

$$\text{rpm} = \frac{120 \times \text{frequency operating}}{\text{number of poles}} \quad [8] (5)$$

$$900 = \frac{120 \times 50 \text{ Hz}}{\text{number of poles}}$$

Number of poles = 6

Forced frequency can be found by using the equation below,

$$\text{Frequency} = \frac{\text{utilize rpm rotation speed} \times \text{number of poles}}{120} \quad [8] (6)$$

$$\text{Frequency} = \frac{128.5 \text{ rpm} \times 6}{120}$$

Frequency = 6.425 Hz

Modal Analysis Summary

The exciting frequency of the Grain segregation is 6.425 Hz which is much less than the Mode shapes Frequencies of the frame starting from 24 Hz and so on. So, there is no chance for the resonance to occur and the design is safe.

4. CONCLUSION

The FEA analysis is conducted on the portable grain segregation system design. The C-channel, hopper support frame, and slider will deflect up to 0.182 mm, 0.227 mm, and 0.637 mm, respectively, according to Static Structural Analysis. This is far less than what would be expected for a machine with a 137 kg capacity. The design is safe under loading situations because the deflection for the 14- and 9-inch hinges was determined to be 0.28 mm and 0.113 mm, respectively. Furthermore, the modal analysis revealed that the modes' form frequencies begin at 24.9 Hz, which is far higher than the system's forced frequency of 6.4 Hz, preventing resonance from happening. It shows that a portable Grain Segregation system is a cost-



effective method of separating unwanted detritus from bulk High-Density Polyethylene (HDPE) grains. Further, it is useful for various industries like construction, food, polymer, and agricultural industries.

REFERENCES

1. A. Petit-Boix *et al.*, "Integrated Structural Analysis and Life Cycle Assessment of Equivalent Trench-Pipe Systems for Sewerage," *Water Resour. Manag.*, vol. 30, no. 3, pp. 1117–1130, 2016, doi: 10.1007/s11269-015-1214-5.
2. Adedipe J.O, Aderemi A.M, Oyewole O.O, Abegunrin, O.O, Olatunji B.T, and Afolabi R.T, "Performance Evaluation of a Triple Layer Electric Sieving Machine (TLESMS)," *Int. J. Eng. Manag. Res.*, vol. 11, no. 2, pp. 178–183, 2021, doi: 10.31033/ijemr.11.2.25.
3. K. Ayodeji Afolami, S. Peter Ayodeji, and B. Oluwafemi Akinnuli, "Development and Performance Evaluation of a Yam Washing Machine for Pounded Yam Flour Processing Plant," *Int. J. Sci. Basic Appl. Res. Int. J. Sci. Basic Appl. Res.*, vol. 36, no. 1, pp. 118–129, 2017, [Online]. Available: <http://gssrr.org/index.php?journal=JournalOfBasicAndApplied>
4. A. Biju, A. Thomas, A. J. Kalarickal, J. Jose, R. A. Kurien, and U. G. Scholar, "Design and Fabrication of Domestic Sieving Machine," *Int. J. Res. Anal. Rev.*, vol. 7, no. 2, pp. 119–122, 2020, [Online]. Available: www.ijrar.org
5. Bandgar, D. Chate, V. Dongare, and D. Mirpagar, "Review of Multi-level Sand screening Machine and Analysis of Vibration mechanism," no. 3, pp. 3–8, 2018.
6. R. Sundaram, "Design and fabrication of horizontal sieving machine," no. July, 2016.
7. "Beam Deflection Calculator." <https://www.omnicalculator.com/construction/beam-deflection> (accessed Mar. 27, 2024).
8. R. Corporation, "Calculating-System-Load-and-Forcing-Frequency," p. 2015, 2015.



Investigation of heat exchange performance with stainless steel double-walled pipe of power plant

Babar Hayat^{1*}, Shijun Ji², Asif Khan³, Shah Rukh Jameel⁴, Hafiz Muhammad Muzammil^{5,6}, Mirza Abdullah Rehan¹, Muzaffar Ali^{1,2}, Muhammad Saud Khan⁷, Muhammad Waqas⁸

¹University of Science and Technology of China, Hefei 230027, China.,

²Jilin University, China,

³National of University of Sciences and Technology, Karachi Campus, Islamabad ,

⁴University of Engineering and Technology, Taxila, Pakistan.,

⁵Herbin University of Science and Technology, China,

⁶Air University, Islamabad, Pakistan,

⁷CECOS University of IT and Emerging Sciences,

⁸Institute of Space Technology, Islamabad, Pakistan.

* babarhayat91@mail.ustc.edu.cn

ABSTRACT

Heat exchangers are essential components across various industries, and many types are widely utilized. Operating these devices at high temperatures often requires a balance between maximum strength and long-term corrosion resistance. The use of traditional single-walled pipes leads to undesirable changes in pipe characteristics or operational conditions. A viable solution to overcome these challenges is the implementation of double-walled pipes, which enhance structural integrity and reduce the risk of crack propagation. In this study, the tensile method is employed to fabricate double-walled pipes, each with a wall thickness of 1 mm. Additionally, a phase-sensitive transient thermal method is applied to evaluate the heat exchange performance. The results indicate that the obtain thermal contact conductance value is 1.33×10^3 W/m²K at contact pressure of 15 MPa, while the thermal conductivity values remain approximately constant at 14.43 W/mK. Double-walled pipes are used in industries such as chemical processing, power generation, oil refining, pharmaceuticals, food production, and HVAC systems to efficiently manage and transfer heat.

KEYWORDS: Single-walled pipe, crack propagation, tensile method, heat exchange performance, Power generation

1. INTRODUCTION

When high-temperature corrosion and cracks occur in power plant facilities, particularly when metal pipes of heat exchangers fail unexpectedly due to high pressure, high temperature, and chemical environments, they often lead to costly plant shutdowns. Subsequent pipe loss prevention or control can also result in expensive repairs and maintenance during planned repairs, as well as shorter safe operating cycles between regular overhauls. Designers of new power plants have traditionally minimized the predicted thermal and mechanical stresses on pipes by enhancing performance during the design stage to limit corrosion or leakage from corrosive liquids or specific chemical processes [1].

Alternatively, upgrading the pipe material to a superior alloy, such as from ferrite to stainless steel, or increasing the wall thickness to provide a greater margin against corrosion or cracks may be sufficient. This requires designers to accurately forecast corrosion rates and have access to a material database with various corrosion and crack potentials. However, the increased efficiency,

higher temperatures and pressures, and high availability demands of modern plants, especially those utilizing advanced cycle designs, make it nearly impossible to construct durable pipes from single materials. Reducing metal temperatures and pressures through facility modifications is often not cost-effective[2].

Extending the life of power plants is an increasing trend in the industry. This approach improves the economic management of cracks and corrosion, especially when frequent repairs and maintenance are necessary to compensate for the limitations of existing pipe materials in handling high pressure and corrosive liquids while maintaining high availability. The concept of double-layer pipes, with different or the same materials on the inner and outer layers, has been around for a long time and has gained popularity as working conditions in major plants have become more severe. These bimetallic pipes can meet the dual performance requirements of high thermal and mechanical strength, and excellent corrosion and crack resistance, which a single alloy cannot achieve. However, using double-walled pipes for heat exchange increases interfacial thermal resistance, significantly impacting the heat transfer performance of the heat exchanger. Therefore, it is critical to evaluate the thermal

interface resistance of double-walled pipes for heat exchanger applications [3].

Several researchers found the thermal contact conductance by using different methods. Simon Woodland [4] proposed and demonstrated an innovative method for measuring thermal contact conductance (TCC). The setup includes an instrumented separating tube with an inner pipe washer and applies load under controlled conditions. The experimental method and data analysis were explained, and the effects of contact pressure, surface roughness, temperature, thermal conductivity, and material strength on TCC were investigated. The TCC values obtained from the experiments were normalized using relevant surface and material parameters, and the normalized results were then compared with experimental data from various models in the literature. Yu Pei [5] found that the pressure range have a strong relationship with the thermal conductance between the carbon nanotube array and the copper surface. Mihai G. Burze et al. [6] showed that thermal interface resistance decreases up to 800 KPa and after that its value became constant. Yann Chalopin [7] examined the effect of pressure and told us that with the increase of contact pressure at the Carbon Nanotube-Si interface, the interface structure changed, the apparent contact area and the number of contact atoms increased, and thus TCC increased. Y. Ohsone [8] applied a pressure of 0.8 to 10MPa between the solid contact surfaces of two wafers of aluminum and silicon using non-contact optical technique. The results show that TCC increases with increasing contact pressure. Wen-Pin Hsieh [9] checked the pressure influence and describes when pressure increases, interface bonding between Pb and diamond also increases, then as a result TCC increases. As the pressure decreases, the interfacial bond weakens and TCC decreases. It is clear that the contact pressure has a large effect on TCC, because as the contact pressure increases, the interface resistance decreases, because the actual contact area between pipes increases, and the amount of air remaining at the interface decreases [10]. After reviewing the literature, it becomes clear that pressure has a significant effect on thermal properties. Thus, it is necessary to study the influence of pressure as a result of stretching forces during the manufacturing of double-wall pipes and how it affects the thermal contact conductance (TCC) at the interface.

In this paper, samples are prepared on an MTS machine at different stretching forces, which produce different radial and tangential stress across the thickness and at the interface. Data from the MTS machine is input into ABAQUS software for material preparation. Radial stress at interface is obtained through numerical simulation which shows the contact pressure. The main focus is to check the heat transfer capability of 316 L stainless steel double-wall pipes through the transient thermal technique, which is similar to the phase-sensitive transient thermos-reflectance technique [11]. The phase-sensitive transient thermal method is a non-destructive, non-contact method used for finding TC and TCC of flat and thin materials.

The specimen is a cylindrical pipe. The phase lag between the inner and outer walls of cylindrical pipes is determined using LabVIEW software. Matlab is used for fitting to obtain TC and TCC values.

2. METHODOLOGY

Sample Preparation

A stainless steel 316 L double-walled pipe was fabricated using an MTS machine at environmental conditions for the experiment. The inner pipe has an inner diameter of 20 mm, an outer diameter of 22 mm, and a total length of 180 mm. The outer pipe has an inner diameter of 23 mm, an outer diameter of 25 mm, and a total length of 320 mm. Two solid pipes were placed at both ends of the outer pipe to support stretching during the preparation of the double-walled pipe. The Young's Modulus is 198 GPa, and the Poisson's ratio is 0.25 [12]. The MTS machine draw two pipes simultaneously and combine them effectively in a cost-efficient manner as shown in Figure 1.

The assembly of pipe was placed on the MTS machine, and stretching was initiated from the ends, as illustrated in Figure 2. As the outer pipe began to stretch, its diameter decreased, drawing closer to the inner tube. At a 23 mm displacement on the MTS machine, both pipes touched each other, but stretching continued. The external pipe further squeezed towards the internal pipe, and the inner wall of the outer pipe came into close contact with the outer wall of the inner pipe, driven by strain deformation, forming a double-wall tube. After preparation on the MTS machine, sample was cut to a final length of 150 mm using a wire-cutting machine for testing.

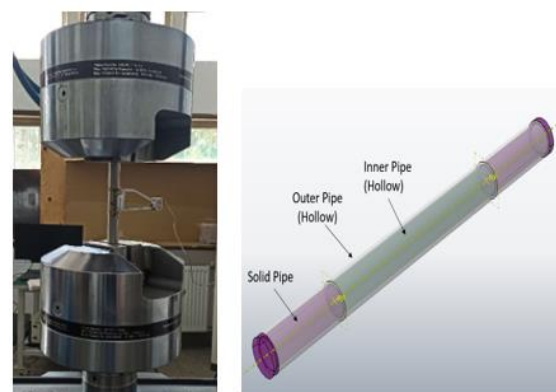


Figure 1: MTS machine and Double-walled pipe assembly used to prepare double-walled pipes on MTS machine

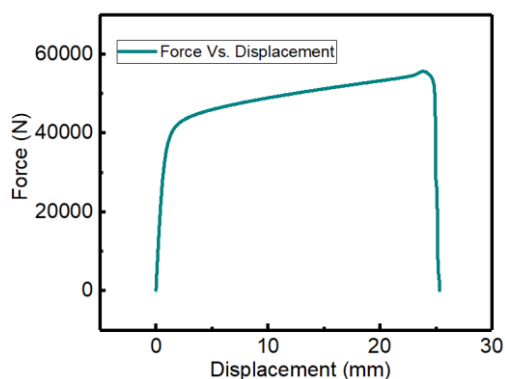


Figure 2: Force-displacement diagram of double-walled pipe prepared on MTS machine

Numerical Simulation

A 3D model is developed to simulate the stretching and shrink-fitting process. The inner pipe, with a length of 180 mm, has an inner and outer radius of 9 mm and 11 mm respectively. On the other hand, the outer pipe, which is 320 mm long, has an inner and outer radius of 11.5 mm and 13.5 mm respectively, with a 0.5 mm gap separating them. Table 1 presents the mechanical properties of stainless steel 316 L. Similar to the actual tensile process, one end of the pipe is fixed, and controlled tensile loads are applied on the other end for each assembly. In order to produce accurate stress distribution results in a reasonable analysis time, the structural meshing approach is utilized to mesh the model with hexahedral C3D8T (An 8-node thermally coupled brick, trilinear displacement, and temperature), which is illustrated in Figure 3.

Table 1: Mechanical properties of Stainless steel 316L [20]

Mechanical Properties	Type 316L stainless steel
Modulus of Elasticity, <i>GPa</i>	198
Poisson Ratio	0.25
Yield Strength, <i>MPa</i>	184
Strength at the break, <i>MPa</i>	240
Elongation at break, <i>mm</i>	25.5

After the removal of the tensile load, the residual stress in the radial direction along the wall thickness of the pipe is displayed in 4. The radial residual stress at the interface of pipe manufactured under 240 MPa tensile load is -15 MPa. It is also visible that radial stress is maximum at interface and reduces at both of its corners.

The residual stress represents the final contact pressure at the interface of the double-walled pipe in the radial direction.

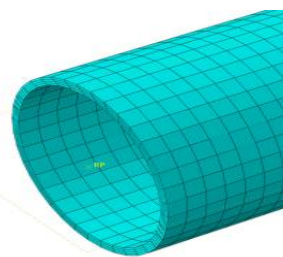


Figure 3: FE Model of test specimen with the hexahedral meshing model of the outer pipe

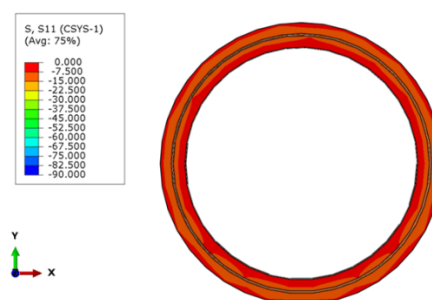


Figure 4: The distribution of residual stress in radial direction

3. EXPERIMENTAL SETUP

Based on prior research and the laboratory's foundational work, an electrical phase-sensitive transient thermal measurement method was developed, as illustrated in Figure 5. This method is tailored to the unique characteristics of the measurement object, which include millimeter dimensions, a cylindrical shape, and high thermal conductivity material. Similar to the principle of PSTTR, a radiant heating wire is used instead of laser heating to run through the center of the pipe. Multiple thermistor (PT100) temperature sensors are employed in place of non-contact optical detection via thermo-reflectance.

A periodic heating signal heats the pipe internally by adjusting the voltage across the heating wire at frequency f . This creates a heat flow that moves through the pipe wall to the outer surface and dissipates into the surroundings, resulting in a fluctuating temperature signal within the pipe wall at the same frequency. Due to the thermal resistance and heat capacity of the pipe wall, the temperature fluctuation on the outer surface lags in phase and decreases in amplitude compared to the inner surface. Temperature sensors attached to both the inner and outer surfaces of the pipe collect the phase signal of the temperature variations relative to the heating signal, thereby determining the phase lag between the surfaces.

This phase lag, which is related to the periodic heating frequency, contains information about the thermal properties of the object, such as thermal conductivity, specific heat, and thermal contact conductance at the interface. Since 316L stainless steel is a well-documented engineering material, its specific heat is known and used in the thermal model, while the thermal conductivity and thermal contact conductance at the interface are extracted by fitting the measured phase difference-frequency relationship. Details of the experimental setup and thermal model are provided in reference [13].

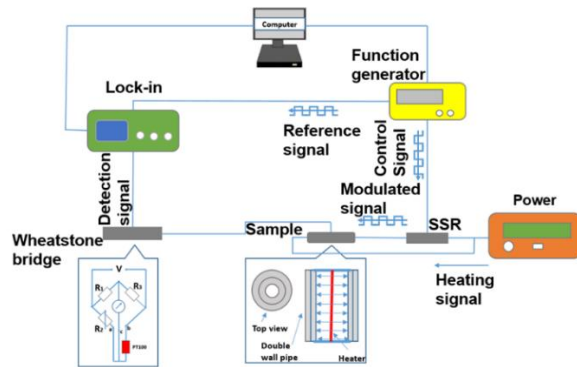


Figure 5: Schematic diagram of phase-sensitive transient thermal method

4. RESULT AND DISCUSSION

The double-walled pipe is produced using the shrink-fitting method, involving stretching displacement and applied force as detailed in Section 2.1. The pipe's thermal properties are examined using the phase-sensitive transient thermal measurement setup. The signal frequency range selected for this study is between 70 mHz and 230 mHz. Phase differences between four points on the outer surface and one point on the inner surface are measured as a function of the modulation frequency (ω). The heat transfer model is used for data fitting to determine the pipe's thermal properties, specifically thermal conductivity (k) and contact thermal conductivity (hc). Temperature signals are recorded at one point on the inner surface and four points on the outer surface to evaluate non-uniformity and variations in thermal properties around the pipe's perimeter. For each frequency point, 200 data points are collected, and the plot displays the average with error bars representing experimental uncertainties. The thermal conductivity (TC) and contact thermal conductivity (TCC) are obtained using the best-fitting method. Measurement errors are assessed by adjusting the best-fit result until the phase difference change exceeds the limit defined by the error bars. Detailed descriptions of the fitting process are available in the reference paper [13]. The thermal properties of the pipe are detailed in Figure 6 as a sample which indicates a thermal conductivity of 14 W/mK and a thermal contact conductance of 1×10^3 W/m²K.

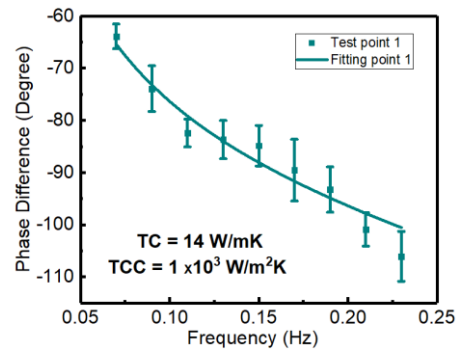


Figure 6: Phase lag between the outer and inner surface of the pipe

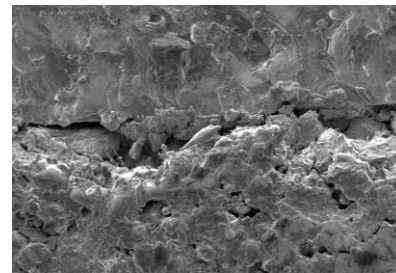


Figure 7: Scanning electron microscope image of interface of pipe

Figure 7 shows the scanning electron microscopic investigation at interface of double-walled pipes and some gaps are visible which effects the transfer of heat among walls. Figure 8 shows the thermal conductivity and thermal contact conductance measured at four points on a pipe. Point 1 has a thermal conductivity of 14 W/mK and a thermal contact conductance of 1×10^3 W/m²K. Point 2 shows a slight increase in both values, with a thermal conductivity of 14.2 W/mK and a thermal contact conductance of 1.3×10^3 W/m²K. Point 3 exhibits the highest values, with a thermal conductivity of 15 W/mK and a thermal contact conductance of 2.3×10^3 W/m²K. Point 4 has a thermal conductivity of 14.5 W/mK but the lowest thermal contact conductance at 0.7×10^3 W/m²K.

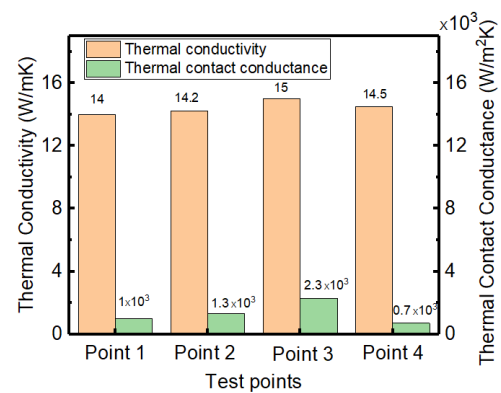


Figure 8: Thermal conductivity and thermal contact conductance results for 4 points of double-walled pipe.



These variations suggest differences in thermal properties along the pipe, potentially due to material inconsistencies or manufacturing processes.

5. CONCLUSION

This study demonstrates the effectiveness of using 316L stainless steel double-walled pipes for finding thermal contact conductance (TCC) in heat exchanger applications. The double-walled pipes were fabricated using a shrink-fitting method with a 25.31 mm stretching displacement. The phase-sensitive transient thermal measurement method, adapted for cylindrical geometries, proved to be a reliable technique for evaluating the thermal properties of this pipe. The experimental results showed that the thermal conductivity value is 14.43 ± 0.44 W/mK, while thermal contact conductance value is 1.33×10^3 W/m²K, when sample is prepared at 25.31 mm displacement of MTS machine. The findings underscore the potential of double-walled pipes to meet the dual requirements of high thermal and mechanical performance, making them suitable for use in various high-temperature and high-pressure industrial applications.

ACKNOWLEDGEMENTS

This research was funded by the National Key Research and Development Program of China (Grant No. 2022YFA1203604) and the National Natural Science Foundation of China (Grant No. 12172348). The author gratefully acknowledges the support from the CAS Key Laboratory of Mechanical Behavior and Design of Materials (LMBD) and the USTC Center for Micro and Nanoscale Research.

REFERENCES

1. K. Kumar, S. Kumar, H. S. J. J. o. F. A. Gill, and Prevention, "Role of surface modification techniques to prevent failure of components subjected to the fireside of boilers," vol. 23, no. 1, pp. 1-15, 2023
2. H. Ezuber, S. J. H. Zakir Hossain, and M. Transfer, "A review of corrosion failures in shell and tube heat exchangers: roots and advanced counteractive," vol. 59, no. 6, pp. 971-987, 2023.
3. W. Faes *et al.*, "Corrosion and corrosion prevention in heat exchangers," vol. 37, no. 2, pp. 131-155, 2019.
4. A. D. C. Simon Woodland, John W. Chew¹, "A New Method for Measuring Thermal Contact Conductance— Experimental Technique and Results," *Journal of Engineering for Gas Turbines and Power*, JULY 2011.
5. Y. Pei, H. Zhong, M. Wang, P. Zhang, and Y. Zhao, "Effect of Contact Pressure on the Performance of Carbon Nanotube Arrays Thermal Interface Material," *Nanomaterials (Basel)*, vol. 8, no. 9, Sep 17 2018.
6. M. G. B. a. M. Li, "Investigation of Pressure Dependence of Interface Thermal Resistance in Thermal Greases by Transient Thermoreflectance," *34th SEMI-THERM Symposium*
7. N. M. Yann Chalopin, Jiankuai Diao, Deepak Srivastava, and Sebastian Volz, "Large effects of pressure induced inelastic channels on interface thermal conductance," *Appl. Phys. Lett.*, 2012.
8. Y. Ohsone, "Optical Measurement of Thermal Contact Conductance Between Wafer-Like Thin Solid Samples.pdf," *Transactions of the ASME*, vol. Vol. 121, 1999.
9. W.-P. Hsieh, A. S. Lyons, E. Pop, P. Keblinski, and D. G. Cahill, "Pressure tuning of the thermal conductance of weak interfaces," *Physical Review B*, vol. 84, no. 18, 2011.
10. J. P. Gwinn and R. L. Webb, "Performance and testing of thermal interface materials," *Microelectronics Journal*, vol. 34, no. 3, pp. 215-222, 2003.
11. X. Feng, C. King, D. DeVoto, M. Mihalic, and S. Narumanchi, "Investigation of thermal interface materials using phase-sensitive transient thermoreflectance technique," in *Fourteenth Intersociety Conference on Thermal and Thermomechanical Phenomena in Electronic Systems (ITherm)*, 2014, pp. 1296-1307: IEEE.
12. R. Zhang *et al.*, "Stress analysis of double-walled pipes undergone mechanical drawing process," vol. 119, no. 3-4, pp. 2525-2535, 2022.
13. B. Hayat *et al.*, "Investigation of heat transfer performance of double-walled pipes of heat exchanger for power plant applications," vol. 149, p. 107115, 2023.

Structural and Thermal Numerical Investigation of Multiple Configurations of Super Insulated Cryogenic pipe for Liquid Nitrogen

Syed Yousaf Raza¹, Muzaffar Ali^{1,2}, Azhar Hussain¹, Guiqiang Li³

¹ Mechanical Engineering Department, University of Engineering and Technology Taxila,

² Energy Engineering Department, University of Engineering and Technology Taxila Pakistan

³ Thermal Science and Energy Engineering Department, University of Science and Technology of China

*syed.yousaff120@gmail.com

ABSTRACT

Vacuum-insulated cryogenic pipes play a critical role in industrial applications for the transportation of liquid nitrogen (LN₂). To maintain the temperature of the cryogenic fluid, effective thermal insulation and careful selection of pipe material are crucial. Failure to do so can result in the vaporization of LN₂. Extremely low temperature of LN₂ (-196°C) can cause material brittleness and loss of tensile strength, resulting in pipe cracking, corrosion, bending, issues. Even a tiny LN₂ leakage onto the pipe's surface can lead to frost or ice accumulation, which can cause structural failure. The objective of this study is to develop a model of super-insulated cryogenic pipe that prevents thermal losses and structural failure of cryogenic pipes. In the present work, initially, identification of the most appropriate materials for the cryogenic pipe, i.e. ASTM A312 SS304 and aluminized Mylar for insulation is made. Then, a cryogenic pipe of 1 meter length is designed by analytical modelling using the relevant governing equations. A 3D model is developed, followed. Afterward, detailed structural and thermal simulations are performed in ANSYS-Fluent to analyze the Performance of the multiple configurations (20, 40, 60 and 80 layers of insulation) of super-insulated cryogenic pipe in terms of structural and thermal behaviors under wide range of operating conditions. Through theoretical and numerical simulations, it has been determined that the ideal thickness for achieving minimal heat loss of LN₂ is 70 layers of Aluminized Mylar. It's worth noting that increasing the layer thickness beyond this point does not significantly improve thermal performance. It is concluded that the use of effective thermal insulation and Vacuum in these pipes, successfully addresses the challenges of heat gain from the environment, structural failure due to material brittleness, and frost or ice accumulation on the surface of pipes.

KEYWORDS: Vacuum Insulated Pipes, Cryogenic Pipes, Liquid Nitrogen, Multi-layer Insulation, Heat gain.

1. INTRODUCTION

Transporting cryogenic liquids safely and efficiently is critical for various industries. Cryogenic piping system utilizes super-insulated, high vacuum pipes for secure transportation of a wide range of liquids, such as Liquid Nitrogen, LOX, LAR, LNG, LHe, and LH₂. With vacuum-insulated piping, heat and gasification are minimized during transfer between cold points, resulting in minimal product loss, reduced energy consumption, and increased operational efficiency.

The application of cryogenic piping is greatly functional in the areas of LNG bunkering and transportation, liquid gas production and storage, cryobiology and medical research, aerospace and defence, food-based production and transportation, and energy and power generation. Vacuum-insulated pipes, which have achieved remarkable success in the thermal energy industry, are renowned for their superior isolation, durability and reliability [1].

Vacuum-insulated piping is proven to be a pioneering idea in heat retention, efficiency in heat loss, and retention of steady temperature. It serves in a risk-free and efficient manner during the transfer of cryogenic liquids, leading to a reduced spillage of products and energy conservation.

Conversely, vulnerable pipes will suffer from heat gain, equalling in higher energy costs, decline in fluid quality, and safety hazards. Similarly insulated pipes are meant to not only keep the fluid temperature but also protect the pipes from problems like condensation, corrosion and ice formation, all of which extend the lifespan of the pipes and reduce maintenance needs [3].

Of all the cryogenic or cold piping types of vacuum-jacketed piping tops the list due to its high insulation provided and the consistent safety measures. Vacuum Insulated Pipe comprises of the following components as shown in figure 1.

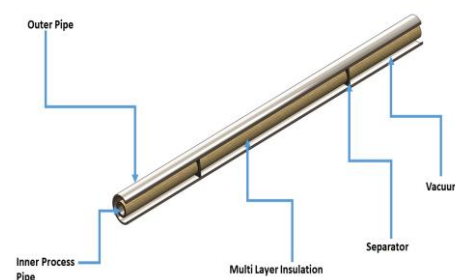


Figure 1: Vacuum Insulated Cryogenic Pipe

Inner pipe: In direct contact with cryogenic fluids, it withstands extremely low temperatures, Outer pipe: Provides an additional layer of protection and structural support, Vacuumed space: Between the two pipes, this evacuated region minimizes heat transfer and reduces thermal conductivity.

Spacers: Specially designed systems that prevent the inner and outer pipes from coming into contact, Insulation: Insulation of cryogenic pipes is a critical aspect for the safe and efficient transportation of cryogenic fluids. The insulation process aims to reduce heat transfer and minimize boil off. Cryogenic pipes have been developing since the 1940s with the introduction of new materials like stainless steel and fiberglass. Vacuum-insulated pipes were introduced in the 1960s, and advanced insulation materials like Multi-layer Insulation (MLI). Nowadays, cryogenic pipes have advanced with materials science and computer-aided design. Modern cryogenic pipes feature advanced insulation materials like aerogel and nanotechnology-based coatings, as well as optimized pipe geometries and joining techniques. They have applications in various industries, including energy, aerospace, and healthcare [1].

In cryogenic pipes, heat leaks are extremely problematic. Computational fluid dynamics simulations offer a way to investigate cryogenic systems. In this research study it is showed that small temperature changes from 77.0 K to 82.1 K in the intake for flow rates up to 2000 LPH, with VIP yielding the best results. Temperature variation in process pipes with thermal insulation protective layer is lower compared to those without insulation [2]. While transporting LNG through pipelines creates boil-off gas (BOG). Reducing BOG development is a major challenge that requires new ways. This research work uses thermal analysis to determine the temperature gain inside vacuum-insulated cryogenic pipelines with pipe type and diameter parameters [3].

The Layered Composite Insulation System for Extreme Conditions (LCX) solved the problem of a depleted or constrained regions. This approach works for both basic geometry (cylindrical pipelines, tanks, etc.) and complicated geometry that cannot be insulated by traditional ways [4]. This research describes insulating materials' conductivity under different conditions. The blanket aerogel composite utilized in this measuring instrument will keep thermal flow consistent between high and low temperatures. The study involved testing the blanket in different gases, such as Liquid Nitrogen (LN₂), helium, argon, and CO₂, at various pressures [5].

The thermal performance of a composite insulation system based on spray-on-foam-insulation (SOFI) and MLI/VDMLI for cryogenic fuel in spaceflights is examined in this study. The experimental findings showed that the composite system effectively reduces heat leakage and heat flux, but further research is necessary to enhance temperature distribution calculations [6]. In this research study different multi-layer insulating materials with

having different densities tested. The minimal heat leakages observed in two-plate support and MLI with 50 layers and 25 layers/cm were 0.200 W and 0.488 W, respectively. This approach can reduce heat leakage in cryogenic transfer lines, regardless of size, support, or MLI, and enhance system energy efficiency [7].

2. DESIGN OF CRYOGENIC PIPE

For the development of the best super insulated cryogenic pipe, important research is done on the previous techniques that are being used to develop vacuum super insulated cryogenic pipes. In this research study, first step is to find best suitable materials for inner and outer pipes i.e., ASTM A312 SS304 and then to find suitable material for insulation i.e., Aluminized Mylar. After the best suitable materials for Inner, outer pipes and insulation next step of this research study is the development of multiple configurations of cryogenic pipe for which purpose 20, 40, 60 and 80 layers of insulation material that is are used for 4 different configurations of pipe through Solid-works. Properties of ss304 are shown in table 1;

Table 1: Properties of SS304

Sr. No	Property	Value
1	Tensile Strength	620 MPa
2	Yield Strength	275 MPa
3	Thermal conductivity	16.2 W/m-K
4	Emissivity	0.85
5	Density	8.0 g/cm ³
6	Surface Roughness	0.1-0.5 μm
7	Specific Heat Capacity	500 J/kg-K

The necessity of the proper insulation to preserve the quality and performance of super insulated cryogenic pipes by keeping them not only safe from heat loss or heat gain also for effective working of cryogenic pipes. For this study Aluminized Mylar is used for the development of vacuum insulated cryogenic pipes because of its very low thermal conductivity as compared to other materials, low density and other properties. Properties of Aluminized Mylar are shown in table 2;

Table 2: Properties of Aluminized Mylar

Sr. No	Properties	Value
1	Tensile Strength	620 MPa
2	Yield Strength	275 MPa
3	Thermal Conductivity	16.2 W/m-K
4	Emissivity	0.85
5	Density	1.4-1.6 g/cm ³

The minimum thickness for pipe and insulation can be calculated from equation 1 and 2 can be calculated as:

$$t = \frac{PD_o}{2\sigma + P} \quad (1)$$

In the equation 1 P is the pressure, σ is the allowable stress for pipe material and D_o is the outer diameter for pipe.

$$d_{min} = \frac{k}{h} \quad (2)$$

In the equation 2 k is thermal conductivity of insulation material and h is the convective heat transfer coefficient for insulation material.

Pressure drop in the pipe can be calculated as:

$$\Delta P = f \left(\frac{L}{D} \right) \frac{\eta v^2}{2} \quad (3)$$

In the equation 3, f is the friction factor, L is the length of pipe, D is the diameter of the pipe, η is the density of fluid and v is the velocity of working fluid.

And this friction factor can be calculated through Colebrook white equation.

$$\frac{1}{\sqrt{f}} = -2 \log \left(\frac{\epsilon}{D} + \frac{2.51}{Re \sqrt{f}} \right) \quad (4)$$

In the equation 4, ϵ is the roughness of pipe material and Re is Reynolds number.

Reynolds number can be calculated as:

$$Re = \frac{\rho \times v \times D}{\mu} \quad (5)$$

In the equation 5, ρ is the density of Liquid Nitrogen, v is the velocity of liquid flowing and μ is the dynamic viscosity of LN_2 . By putting all values in equation 5 it is found that flow is turbulent.

Thermal expansion and contraction can be calculated from the below equation.

$$\Delta L = L \cdot \alpha \cdot \Delta T \quad (6)$$

In the equation 6, L is the original length of pipe, ΔT is the change in temperature and α is the coefficient of thermal expansion for material.

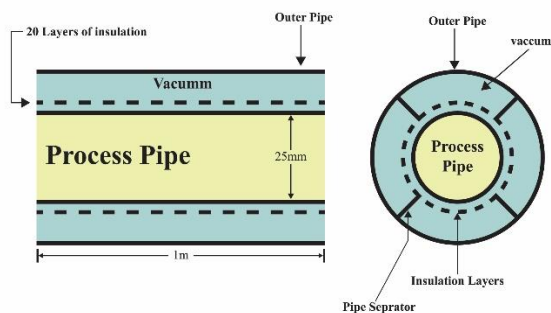


Figure 2: 20 Layer Insulation Configuration for Cryogenic Pipe

Figure 2 shows the 20-layer configurations for cryogenic pipe, other configurations that is 40, 60 and 80 layers will be same as figure 2, but the number of layers of insulation

materials will increase for other three configurations on inner process pipe which carries LN_2 . By increasing thickness or number of layers insulation material can limit temperature gain from surroundings and maintain LN_2 temperature.

Thermal and Structural Model for Cryogenic Pipe

After developing the model using SolidWorks, the next step is to perform a numerical analysis. ANSYS employs numerical methods such as finite element analysis to address complex issues across different fields. In this project, ANSYS will model the thermal behaviour of a cryogenic pipe that transports Liquid Nitrogen (LN_2) with various configurations of aluminized Mylar insulation. Specifically, the simulation will investigate the effects of 20, 40, 60, and 80 insulation layers on the pipe's thermal performance, providing valuable insights into the most efficient insulation setup for effective cryogenic fluid transport. Additionally, a structural analysis is conducted to predict the lifespan of the cryogenic pipe, stress and strain analysis to assess the pipe's mechanical strength and identify potential failure points under different operating conditions.

Thermal Model of Cryogenic Pipe

ANSYS is found to be the best for the present simulations by a critical analysis of the fact that it has a wide range of capability in handling thermal and mechanical problems. The simulation process can be divided into the following specific steps:

Engineering Data, Geometry, Model, Setup, Solution and finally Results. Materials were carefully assigned to each component, selected from the predefined materials listed in the Engineering Data section. The assigned materials are as follows: Outer Jacketed Pipe: ASTM A312 SS304, Process Fluid: Nitrogen Liquid, Inner Process Pipe: ASTM A312 SS304, Pipe Separator: ASTM A312 SS304, Reflective Layers: Aluminized Mylar (0.08 mm). After material assignment, named selections were created for each component to facilitate efficient mesh size. Meshing view for cryogenic pipe is shown in figure 3.

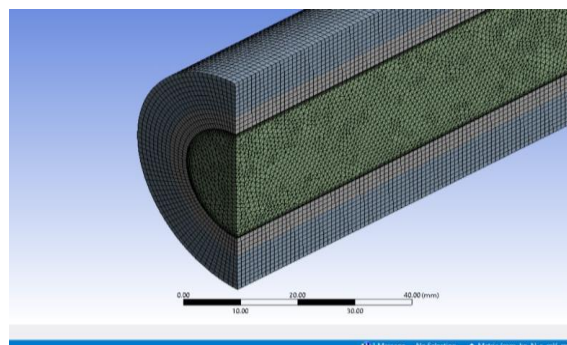


Figure 3: Meshing View for Cryogenic Pipe

The ANSYS Fluent utilized for this study, and the standard k-epsilon turbulence model was selected, a commonly used method for turbulent flow simulations. This model allowed for the representation of turbulent eddies and fluctuations in fluid flow, thereby improving the accuracy of the simulations. Due to doing this, the simulations became more accurate. The velocity was set at 1 m/s in the inlet boundary to grasp the dynamics of Liquid N₂ flow and find solutions to the problem, while on the other, the inlet temperature was kept at 77 Kelvin under no fluctuation conditions. Green-Gauss cell-based skin allowed us to adopt precise gradients and flux values, thus an exact and detailed depiction of the complex processes occurring. The basis of our momentum calculations allowed us to model the fluid momentum accurately, which in the end were suitable for the different cases of flow dynamics for the pipe system.

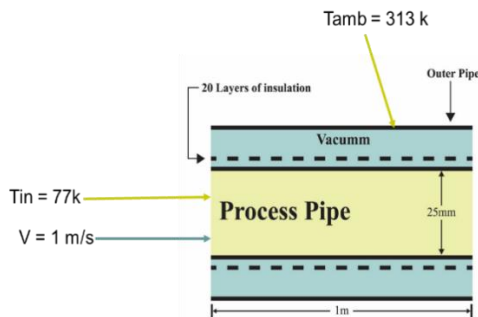


Figure 4: Boundary Conditions

After assigning properties to materials, meshing and giving boundary conditions as shown in figure 4 to cryogenic pipe, final step is to run simulations and get results. And before that a grid independence test performed so that changing the size of mesh and decreasing or increasing the number of elements does not affect the final results of simulation. From grid independence test it is found that 1mm is minimum size for element after that there are no change in simulation results. All the results are discussed in the discussion chapter.

Static Structural Analysis

The examination of the static structural behaviour of the super vacuum-insulated pipe under various loading conditions is analysed in a comprehensive manner which is another part of this study. Structural strength and stability of the pipe is the very first step towards developing an effective super insulated cryogenic pipe for the liquid nitrogen. The vacuum-insulated cryogenic pipe structure analysis commenced by applying an external load equivalent to atmospheric pressure, resulting in a pressure of 101325 Pascal. This load was imposed to replicate the environmental conditions surrounding the pipe structure. Also, a vacuum introduced between the insulation material and outer pipe. It was a 77 Kelvin temperature that we chose for the test inner part depending on the thermal analysis.

Investigations into the responses of the pipes to mechanical effects were conducted by using finite element analysis techniques in ANSYS Workbench and followed up by structural analysis. The results present analysis significant structural material failure and distribution of stress.

A fatigue tool analysis has been carried out to evaluate the fatigue life of each element within the assembly. Such comprehensive analysis comprised of is fatigue behaviour of the inner in-pipe as well as the outer insulating material at different cyclic loading stresses.

3. RESULTS AND DISCUSSION

Thermal Analysis

From thermal analysis results it is found that while using 20 layers of insulation layers on inner process pipe the liquid nitrogen temperature rises to 89.55 K. The rise in liquid nitrogen temperature indicate that the current insulation layers are insufficient to maintain the liquid nitrogen temperature throughout the pipe. For the second configurations of pipe i.e. 40 layers of insulation the temperature maintained at 83.3 K. While using 40 layers of insulation there is improved temperature for LN₂ but it's not sufficient. For 60 layers of insulation which is the third configurations of cryogenic pipe LN₂ temperature rises to 80.41 K. And for fourth configurations of pipe which uses 80 layers on inner process pipe the temperature rise for LN₂ is 77.72 K. After 80 layers of insulation, there were no improvements in controlling temperature. Temperature results for 20, 40, 60 and 80 layers of insulation are shown in figure 5.

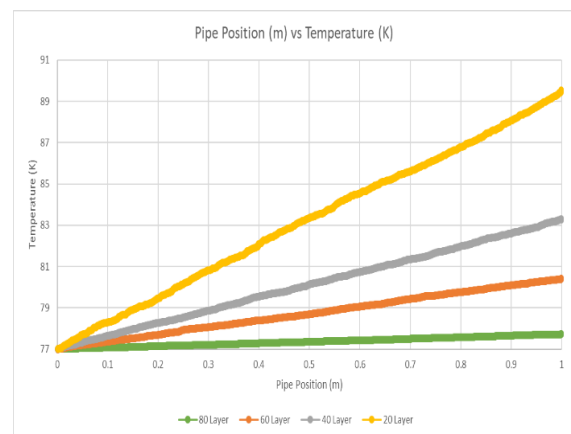


Figure 5: Temperature Graph for Multiple Configurations of Pipe

Critical Thickness Analysis

Critical thickness analysis, a crucial aspect of this study, revealed the optimal insulation thickness required to achieve optimal thermal performance in super-insulated cryogenic pipes. Through careful calculations,

considering the properties of the insulation material and layer thickness, it is found that the critical thickness to be 5.6 mm, equivalent to 70 layers of insulation. This study analysis also revealed that increasing the layer thickness beyond 70 layers does not yield further improvements in thermal performance, and instead, results in an unnecessary material excess, underscoring the importance of precise optimization in insulation design. Critical thickness result is shown in figure 6.

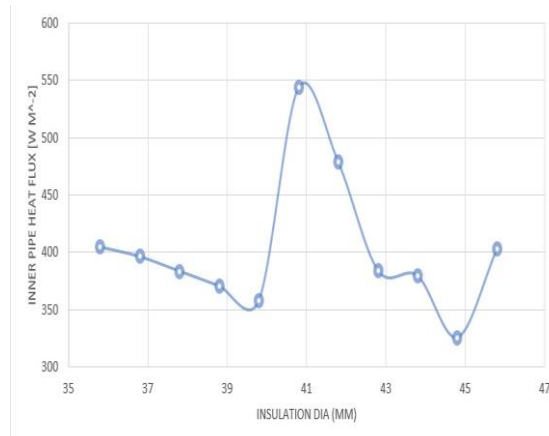


Figure 6: Critical Thickness Results

Static Structural Analysis

Static structural analysis performed to check the stability of structure such as stress strain in the cryogenic pipe assembly and life cycle analysis. Through deformation analysis it is found that maximum deformation in the cryogenic pipe is 0.74149 mm and the minimum deformation is 0.0823 mm as shown in figure 7.

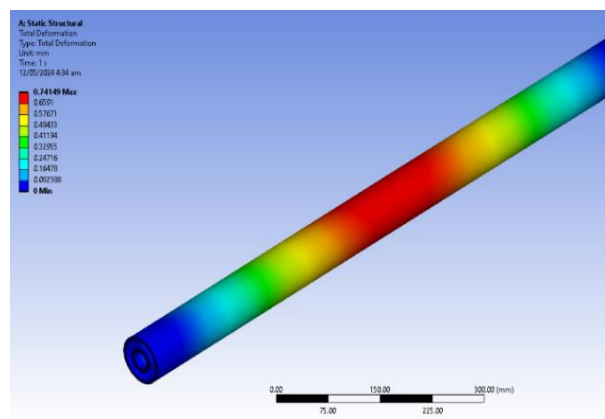


Figure 7: Deformation Analysis

A stress analysis is performed to check the stresses (hoop and thermal) developed in the inner process pipe due to extremely low temperature of LN₂. The developed stresses are within limit as shown in figure 8.

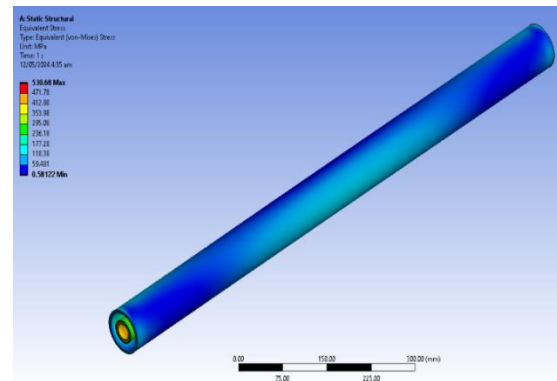


Figure 8: Stress Analysis

The life of whole assembly of cryogenic pipe found from life cycle analysis which also known as fatigue tool analysis. Life of inner pipe found to be 16.8 hours if LN₂ flows through continuously in the inner pipe as shown in figure 9.

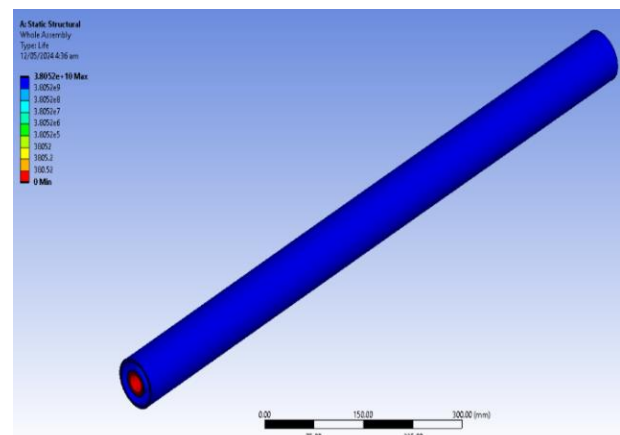


Figure 9: Life Cycle Analysis

4. MODEL VALIDATION

The developed model of the current study are qualitatively validated with another published work by Lim Chong Lye et al [2]. In which series of CFD simulations are conducted for cryogenic pipes Lim Chong Lye et al., in 2018 [2] uses SS304 for pipe materials and polyurethane as insulation materials. The research analysis shows that the pipe design was able to limit the temperature with vacuum insulation and polyurethane foam in the range of 77 to 82.1 K which was followed by the experimental fluid dynamics (EFD) data used for verification and validation of CFD simulations studies. This study uses same model that is used by Lim Chong Lye et al [2], but with different

insulation materials i.e. Aluminized Mylar with varying insulation of 20, 40, 60 and 80 layers. Therefore, qualitative validation is presented through Figure 10. The results showed that 80 layers of Aluminized Mylar can limit the maximum heat gain from the surroundings and the temperature of LN₂ rises to 77.78 K. So, it can be seen that the Aluminized Mylar insulation is able to limit more temperature compared to the polyurethane foam insulation. While using Polyurethane foam insulation rise of temperature was 82.1 K.

Figure 10 shows that the same trend is observed for temperature distribution curved as in the study done by Lim Chong Lye et al [2]. The resulted difference is around 4K due to different materials used by other study which show that the developed model is qualitatively in agreement with the published work.

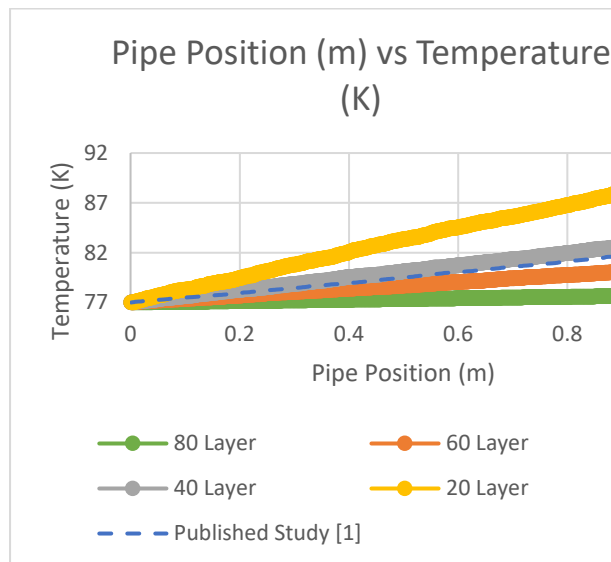


Figure 10: Temperature Based Model for Different Layers of Insulation layers

5. CONCLUSION

From thermal analysis it is concluded that while using 20 layers of insulation temperature of liquid nitrogen rises to 89K, when 40 layers of insulation rise of temperature of Liquid nitrogen limited to 83K, when we increased the layers of insulation to 60, temperature rise was limited to 80K and while using 80 layers of insulation temperature rises to only 77.72K. So 80 layers configurations is best choice to control liquid nitrogen temperature.

From critical thickness analysis it is found that after increasing the 70 layers of insulation does not improve in heat limitation. So, it is concluded that 70 layers configuration is the best configuration to limit heat gain. If we increased after 70 layers there is no improvement in heat limitation its only waste of material and money.

Structural analysis, life span of whole assembly especially inner pipe determined to be 16.8 hours. Also it is

concluded that maximum stress developed in inner process pipe i.e. 530 Mpa which is in limit for SS304.

REFERENCES

1. M. Ramezanizadeh, M. Alhuyi Nazari, M. H. Ahmadi, and E. Açıkkalp, "Application of nanofluids in thermosyphons: A review," *Journal of Molecular Liquids*, vol. 272, pp. 395–402, Dec. 2018, doi: 10.1016/j.molliq.2018.09.101.
2. C. L. Lim, N. M. Adam, and K. A. Ahmad, "Cryogenic pipe flow simulation for liquid nitrogen with vacuum insulated pipe (VIP) and Polyurethane (PU) foam insulation under steady-state conditions," *Thermal Science and Engineering Progress*, vol. 7, pp. 302–310, Sep. 2018, doi: 10.1016/j.tsep.2018.07.009.
3. J.-H. Lee, S.-P. Kim, and G.-H. Lee, "Numerical Analysis and Experimental Verification Based on Design Parameter Variation of Vacuum-Insulated Pipe for Cryogenics," in *Proceedings of the International Symposium on Mechanical Engineering and Material Science*, Jeju Island, South Korea: Atlantis Press, 2016. doi: 10.2991/ismems-16.2016.82.
4. J. E. Fesmire, "Layered composite thermal insulation system for nonvacuum cryogenic applications," *Cryogenics*, vol. 74, pp. 154–165, Mar. 2016, doi: 10.1016/j.cryogenics.2015.10.008.
5. J. E. Fesmire, J. B. Ancipink, A. M. Swanger, S. White, and D. Yarbrough, "Thermal conductivity of aerogel blanket insulation under cryogenic-vacuum conditions in different gas environments," *IOP Conf. Ser.: Mater. Sci. Eng.*, vol. 278, p. 012198, Dec. 2017, doi: 10.1088/1757-899X/278/1/012198.
6. J. Zheng et al., "Experimental study on composite insulation system of spray on foam insulation and variable density multilayer insulation," *Applied Thermal Engineering*, vol. 130, pp. 161–168, Feb. 2018, doi: 10.1016/j.applthermaleng.2017.11.050.
7. B. Deng, S. Yang, X. Xie, Y. Wang, and Q. Li, "Experimental Study of Minimizing Heat Leakage of Cryogenic Transfer Lines," *Energy Procedia*, vol. 158, pp. 4778–4784, Feb. 2019, doi: 10.1016/j.egypro.2019.01.721.



Design and Development of Solar Assisted Hybrid Bicycle

Mamoon Ahmad Khilji¹, Amar Ul Hassan Khawaja², Saad Ali Khan², Ismail Shahid¹,
Ebad Ullah Khilji³

¹University of Wah, Pakistan

²University Of Engineering and Technology Taxila, Pakistan

³University Of Engineering and Technology Peshawar

*mamoonkhilji93@gmail.com

ABSTRACT

Fossil fuel transportation is the most common type of transportation around the globe. Transportation in the developed countries consumes over one-third of all worldwide transportation energy and is a major source of the emission of pollutants like CO₂ which plays a great role in environmental pollution. To overcome the sustainability issue, a solar hybrid bicycle design is proposed as an alternative mode of transportation to address the ever-growing environmental pollution by minimizing CO₂ emissions as well as cost reduction. Hybrid Bicycle consists of a dual running mechanism such as solar energy and paddles. A BLDC motor is run with 12-volt dual batteries connected in series charged by a solar panel. In order to propel the Bicycle without physical human effort a 250-watt Brush Less DC motor is used. The motor is fitted in the rear wheel and relates to the help of a Chain Drive System. The design adopted in this study is to fit the panel as a roof of the vehicle due to the reasons that the load is equally distributed on the cycle, the roof is adjustable not just for a heightened person but also to avail maximum light intensity. The novelty of this research is that studies on e-bicycle existed but limited research on solar-powered e-bicycles and their influence on society, environment and cost were carried out. The analysis revealed that a solar e-bicycle is used as a sustainable way of transportation by meeting the requirements of local peoples with its greater occupancy rate, speed, and travel distance.

KEYWORDS: Solar Assisted Hybrid bicycle, E-bike, Transportation, sustainability

1. INTRODUCTION

Due to the excessive use of fossil fuel, there is a danger of its depletion because petrol and diesel are the products of these fossil fuels. Secondly the excessive use of these Fossil Fuels leads to high pollution rate in the environment which causes global warming and so greenhouse effect takes place. Therefore, there is a need of an alternative source of traveling. The alternative source of traveling is required not only due to the above-mentioned problems but also due to the high Fuel prices worldwide. In developing countries like Pakistan, the access to fuel for a poor man is almost unreachable. Therefore, we can adopt the alternative way of traveling that is Hybrid Bicycle. Hybrid system is any system which works by using two or more distinct fuels.

2. LITRATURE REVIEW

Ananda Paudel and Philipp Kreutzmann revised their paper in 2015 in which they stated that, as fossil fuel is the main source of traveling worldwide but it has few limitations. The main among them is the emission of Pollutants like Co₂ which can be very harmful to the environment therefore there was a need of an alternative way of traveling. The solar Tricycle has a greater occupancy rate, travel range, and speed to meet the needs

of local commuters. This paper discusses the solar Tricycle design, economics, sustainability, and performance analysis. This study proposes a sustainable mode of transportation. Solar-powered tricycles use very little energy and emit very little CO₂. The tricycle, while not ideal for high-speed highways, may be a second vehicle that can meet the needs of urban commuters.[1]

M. ReddiSankar 2013 stated in their paper that the solar assisted bicycle is equipped with a 250W DC hub motor mounted on the front axle of the bicycle and travels at a speed of roughly 25-30 km/h. In the case of a two-wheeler, this setup will replace the petrol engine, gearbox, and fuel tank; in the case of a traditional bicycle, this arrangement will replace the chain sprocket, chain, and gear shifting arrangement. A solar assisted bicycle is a bicycle that has been modified to run on solar energy. It can be used on cement, asphalt, or dirt roads in both cities and rural areas. The operational cost per kilometre is low, around Rs.0.70 per kilometer. In the event that the solar system fails, it can be powered by human pedalling.

3. METHODOLOGY

In order to propel the Bicycle without Physical human effort a 250-watt Brush Less DC motor is used. The motor is fitted in the rear wheel and relates to the help of a Chain Drive System. This motor is run with the help of 12-volt dual batteries which are connected in series and are

charged with the help of a solar panel as well as charged with help of an electrical charger. The main problem was fitting the solar panel. In reviewing the literature, it was noticed that the solar can be fitted on the carrier, on the front wheel and can also be fitted as a roof of the Bicycle.

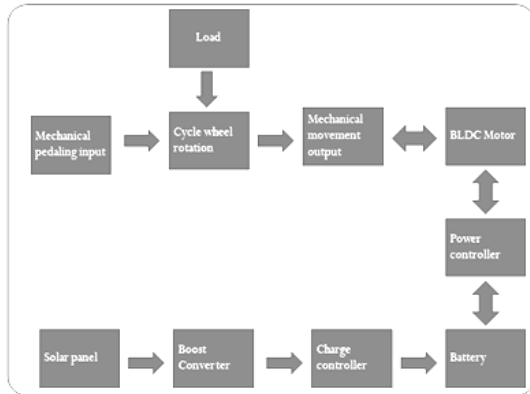


Figure 1: Methodology

The model that is adopted in this project is fitting the panel as a roof of the Vehicle. The main reason of this model is that the load is equally distributed in the cycle. Secondly it is comparatively easy to balance the Bicycle as the load is equally distributed throughout. Main reason of placing the solar at the roof is that the roof is adjustable not just for a heighted person but also the avail maximum light intensity.

The solar power bicycle's methodology aims to turn renewable solar energy into mechanical work. Solar panels, batteries, DC motors, and bicycle wheels are the components utilized in solar electrical energy. Solar panels are used to convert solar energy into electricity. The rechargeable battery stores this electrical energy. The DC motor attached to the bicycle's wheel rotates using the electrical energy stored in the battery.

4. FRAMEWORK

Connection of BLDC Motor

A 24-volt BLDC motor is used to propel the bicycle which is being operated with the help of solar panel along with 12 volts of two batteries connected in series.

Motor's Placement

Sprocket gear is welded on the axel of rear wheel and motor is also fitted on rear wheel. Motor and rear wheel is being operated through chain drive mechanism.

Parts installation/Assembling

Beginning with the installation of a BLDC motor on the rear wheel using a chain drive system, the power controller (which is powered by two 12-volt batteries

connected in series) stabilizes the alternating torques. All the components were precisely installed.

Throttle Placement

It is the most important component of a hybrid bicycle since it allows the bicycle to move. As a result, it is mounted on the right handle of the bicycle for convenience of use.

Solar Panel Installation

According to a detailed study based on historical data, the best location for a solar panel to achieve optimal efficiency is where it receives the most sunlight, so it takes less time to charge the batteries and drive the motor. Hence when the bicycle is ridded up or down hill (depending on the sunlight), the solar panel is mounted on the roof of the bicycle with (umbrella type design) with the help of an adjustable y-shape support for up and down movement of the solar panel.

WIRING AND ELECTRICAL CONNECTION

All wires of components used should be connected / tightened properly so that bicycle movement is not hindered at maximum speed and especially on uneven roads. The controller can be placed in any position that is as clean and dry as possible, and if necessary, protected from water and impurities with a cover. To ensure maximum output power, the controller should be screwed to a clean, flat metal surface. Proper heat sinking and circulation are essential to achieve the controller's full power capability.

Design calculations

Given Data

- Mass of Man = 80 kg
- Miscellaneous Weight = 40 kg
- Total Weight = 80 kg + 40 kg = 120 kg
- Diameter of Wheel = 60 cm = 0.6 m
- Radius of Wheel = 30 cm = 0.3 m
- Diameter of Wheel Sprocket = 8 cm = 0.08 m
- Radius of Wheel Sprocket = 4 cm = 0.04 m
- Number of teeth on Wheel Sprocket = 19
- Number of teeth on Motor Sprocket = 19
- Static Friction = $\mu_s = 0.03$
- Dynamic Friction = $\mu_d = 0.004$

Required Data

- Torque Calculation
- Power Calculation
- Motor Selection
- Solar Selection

TORQUE CALCULATION

$$\begin{aligned} \text{Total Load} &= m \times g \\ &= 120 \times 9.8 = 1176\text{N} \end{aligned}$$

$$\text{Total Load} = 1176\text{ N}$$

$$\sum F = m \times a$$

$$F \text{ applied} - 2F \text{ reaction} = m \times a$$

Table 1: Component Details

Sr. No.	Wattage	Voltage	Weight	Rpm	Torque	Capacity	Type	Current
DC Motor	250 W	24 V	3 kg	3000	18 Nm			-
Battery	-	12 V (in series)	3 kg	-		7 Ah	Dry Cell	-
Solar Panel	100 W	18 V	6 kg	-				6.5 A
Boost Converter	-	V _{in} = 10-32 V V _{out} = 10-35 V	-	-	-	-	-	I _{in} = 16 A I _{out} = 10 A

$$V2/1 = V2 - V1$$

$$V2/1 = V2 - 4.16 \text{ _____} A$$

$$\text{Dynamic Friction} = \mu d = 0.004$$

$$F \text{ applied} - 2(\mu d \times m \times g) = m \times \frac{vf - vi}{t}$$

Putting Values in equation

$$\begin{aligned} F \text{ applied} - 2(0.004 \times 120 \times 9.8) \\ = 120 \times \frac{4.16 - 0}{20} \end{aligned}$$

$$F \text{ applied} - 9.40 = 24.96$$

$$F \text{ applied} = 24.96 + 9.40 = 34.36\text{ N}$$

Now,

$$\text{Torque} = r \times F$$

$$\begin{aligned} \text{Torque} &= 0.3 \times 34.36 \quad \therefore r \\ &= \text{radius of wheel} \end{aligned}$$

$$\text{Torque} = 10.30\text{ N.m}$$

$$V = r \times \omega$$

$$\omega = \frac{V}{r}$$

$$\omega = \frac{4.16}{0.3}$$

$$\omega = 13.86\text{ rad/sec (Wheel)}$$

$$V = r \times \omega$$

$$\omega = \frac{V}{r}$$

$$\omega = \frac{4.16}{0.3}$$

$$\omega = 13.86\text{ rad/sec (Wheel)}$$

Using Wheel Sprocket,

As by taking relative velocity for wheel sprocket

For Rws:

$$Rws = R_w + R_s$$

$$Rws = 0.3 + 0.04$$

$$Rws = 0.34\text{ m}$$

Using Interpolation formula

$$y = y1 + \frac{(x - x1)}{(x2 - x1)} \times (y2 - y1)$$

Putting values

$$V2 = 4.16 + \frac{(0.34 - 0.3)}{(0.6 - 0.3)} \times (8.32 - 4.16)$$

$$V2 = 4.16 + \frac{(0.04)}{(0.3)} \times (4.16)$$

$$V2 = 4.16 + 0.54$$

$$V2 = 4.16 + 0.54$$

$$V2 = 4.71\text{ m/sec}$$

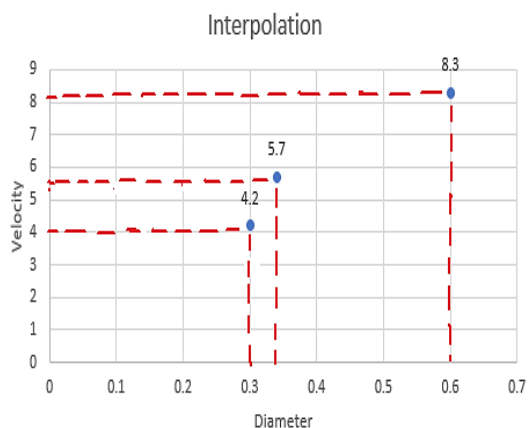


Figure 2: Interpolation

Put the value of V2 in Equation A

$$V2/1 = V2 - 4.16$$

$$V2/1 = 4.71 - 4.16$$

$$V2/1 = 0.55 \text{ m/sec}$$

As,

$$V = r \times \omega$$

$$\omega = \frac{V}{r}$$

$$\omega = \frac{0.55}{0.04}$$

$$\omega = 13.75 \text{ rad/sec (Sprocket)}$$

POWER CALCULATION

$$\text{Power} = \text{Torque} \times \omega$$

$$P = \tau \times \omega$$

$$P = 13.55 \times 13.75$$

$$P = 186.31 \text{ watt}$$

$$\text{Efficiency} = \frac{186.31}{0.80} = 233.75 \text{ watt}$$

Motor Selection

As per calculations over required was 234 watts at 80% efficiency.

Nearest available motor was 250 watt @ 78% which is suitable for our project.

Solar Selection:

When Cycle is at Rest:

For Charging Time:

$$\text{ChargingCurrent} = 6.5 \text{ A}$$

$$\text{BatteryRating(Current)} = 7 \text{ Ah}$$

$$\text{ChargingTime} = \frac{\text{BatteryRating}}{\text{ChargingCurrent}}$$

$$\text{ChargingTime} = \frac{7 \text{ Ah}}{6.5 \text{ A}} = 1.07 \text{ h}$$

So, Batteries will take 1 hour to get fully charged

When Cycle is in Motion:

$$\text{ChargingCurrent} = 6.5 \text{ A}$$

$$\text{BatteryRating(Current)} = 7 \text{ Ah}$$

$$\text{DischargedCurrent} = 10 \text{ A}$$

$$\text{DischargeTime} = \frac{\text{ChargingCurrent} + \text{BatteryRating}}{\text{DischargeCurrent}}$$

$$\text{DischargeTime} = \frac{6.5 \text{ A} + 7 \text{ Ah}}{10 \text{ A}} = 1.35 \text{ h}$$

Hence, Cycle can drive only 1.35 hours continuously after that battery will completely be discharged.

Table 2: Cycle at rest

	Motor Rating	Solar Panel Rating	Battery Rating
Power	250 Watt	100 Watt	-
Current	10 A	6.5 A	7 Ah
Voltage	24 V	18 V	24 V



Figure 3: Cad Model



Figure 4: Fabricated H

5. CONCLUSION AND FUTURE RECOMMENDATION

The goal of this review study was to document the current state and experiences with e-bicycles, specifically solar-powered e-bicycle. This study summarized previous research on e-bicycles and solar-powered e-bicycles, as well as the key technological characteristics of solar e-bicycles. It also based on literature and field research, introduced the solar e-bicycle as a sustainable way of transportation ideas about a specific kind of transportation. The literature analysis revealed a growing body of work on e-bicycle user studies, and, however, there are little research on solar-powered e-bicycles and their influence on users, health, mobility, and safety.

According to the research, individuals ride e-bicycles because they are less expensive and/or ecologically friendlier than other modes of transportation while also increasing physical activity. Motives for riding an e-bicycle depending on the age of the individual People over the age of 60 who use an e-bike for transportation are considered early adopters. Commuters and leisure trips users are drawn to solar e-bicycle because of their inexpensive cost and ease of use. When compared to a standard e-bicycle. Additionally, riding an e-bicycle has direct health benefits to consumers while lowering hazardous emissions including CO₂, NO_x, and other air pollutants.

Because fuel prices are rising across the world, including in Pakistan, there is a pressing need to find a substitute in order to protect these natural resources. As a result, a hybrid bicycle is an electric vehicle that provides that option by combining solar energy with battery charging to generate the desired power to drive the motor. Because Pakistan has an average of 12 month of sunshine every year, the idea of a hybrid bicycle is extremely appealing. A hybrid bicycle uses solar energy to charge the battery as well as pedalling to propel the bicycle forward.

Energy feasibility:

The answer to this question is that the solar panel used in this project is of 100W which provides enough power along with two batteries of 12V, connected in series to

run 250-watt motor that propels the bicycle forward. As the chosen design is roof (umbrella type) so during daytime bicycle is able to travel for long distances because it is continuously being charging and also increases the backup timing..

When the generated electricity of the on-bike PV prototype system is compared to the possible electricity generation of a stationary system, the latter clearly wins.

On-bike system versus Stationary system;

The stationary system is also a PV standalone system that uses a solar battery to store the energy produced during the day. The advantage is that the PV panel's tilt and alignment may be changed to maximize available and unshaded irradiation. The term "stationary system" implies that it is not carried on the bike but does not necessarily imply that it is fixed in one location. It may also be readily carried and placed in various locations. A stationary system could be used during a bike vacation where there is no access to the main grid. The on-bike system has a significant disadvantage in terms of the amount of electricity that can be generated as compared to the stationary system. The most significant benefit is that the on-bike system is portable and can generate electricity regardless of location. Electricity is generated as soon as the PV panel is turned on. If the bike is utilized in areas where there is no grid and no base camp to take use of a stationary system, this factor can be used. In any case, the higher the "time of park" to "time of ride" ratio, the more likely it is that even the on-bike system's lower electricity generation can provide enough energy to recharge the bike battery.

Key Features:

This research has lots of interesting elements. In comparison to an e-bike, this research makes this project more efficient. As this project has the potential to continuously charge the battery, whereas an electric bicycle requires a stationary charging station. It is economical and operates automatically (power controller) to provide smooth speed variations and maximum speed of 23 km/hr. is achieved and it can operate on battery for 1.5 hour. As a result, it requires less human intervention.

Limitations:

- The BLDC motor's initial required voltage to propel the hybrid bicycle is (24 volts), whereas the solar panel used is of (12 volts). As a result, a boost converter is utilized to raise the voltage from 12 to 26 volts. As a result, voltages are lost during conversion/boosting, affecting battery charge time and, as a result, cycling speed.
- In the absence of sunlight, the bicycle will not charge (it will not be able to travel a long distance).

Future work:

1. Installing a dynamo to reduce battery charging time by utilizing cycling energy.
2. Remove the boost converter by adding a solar charge controller.



3. Install a light weight (foldable) solar panel which increases the efficiency and charging time of bicycle.
4. Obtain a hub motor that can be fitted on 28-inch bicycles so that the hybrid bicycle can be built on larger bicycles and used by tall people comfortably.

We can also put effective solar panels on the wheels that can capture the majority of the sunshine

REFERENCES

1. A. M. Paudel and P. Kreutzmann, "Design and performance analysis of a hybrid solar tricycle for a sustainable local commute," *Renewable and Sustainable Energy Reviews*, vol. 41, pp. 473-482, 2015.
2. S. Johny, S. S. Kakkattil, S. Sunny, K. Sandeep, and V. Sankar, "Design and fabrication of foldable electric bicycle," *Materials Today: Proceedings*, vol. 46, pp. 9646-9651, 2021.
3. S. Kaplan, D. Wrzesińska, and C. Prato, "The role of human needs in the intention to use conventional and electric bicycle sharing in a driving-oriented country," *Transport Policy*, vol. 71, 09/01 2018, doi: 10.1016/j.tranpol.2018.09.010.
4. R. Bhukya and S. Duvvuri, *Solar Electric Bicycle using Permanent Magnet Direct Current Motor: A Realistic Prototype*. 2020.
5. T. Joshi, R. Sharma, V. Gupta, and O. Parkash, "Fabrication of Hybrid Bicycle for Minimizing Pollutant Emissions," *Journal of Physics: Conference Series*, vol. 1478, p. 012036, 04/01 2020, doi: 10.1088/1742-6596/1478/1/012036.
6. S. Kaplan, D. K. Wrzesinska, and C. G. Prato, "The role of human needs in the intention to use conventional and electric bicycle sharing in a driving-oriented country," *Transport policy*, vol. 71, pp. 138-146, 2018.
7. M. Sankar, T. Pushaveni, V. Bhanu, and P. R. Reddy, "Design and Development of Solar Assisted Bicycle," 2013.
8. P. Hazarathaiyah, A. K. Reddy, and P. V. B. Reddy, "Design and Fabrication of Hybrid Electric Bike," 2019.
9. M. R. Sankar, T. Pushaveni, and V. B. P. Reddy, "Design and development of solar assisted bicycle," *International Journal of Scientific and Research Publications*, vol. 3, no. 3, pp. 452-457, 2013.
10. P. Hazarathaiyah, K. Reddy, B. Reddy, and M. Sreenivasulu, "Design and Fabrication of Hybrid Electric Bike," *International Journal of Applied Engineering Research*, vol. 14, no. 4, pp. 930-935, 2019. [Online]. Available: http://ripublication.com/ijaer19/ijaerv14n4_13.pdf.
11. R. V. Jijith and S. Indulal, "Hybrid electric three-wheeler with ann controller," in *2018 International Conference on Circuits and Systems in Digital Enterprise Technology (ICCSDET)*, 2018: IEEE, pp. 1-5.
12. S. Pattanayak, M. Tirkey, P. Lakra, V. Ranjan, S. Ranjan Panda, and M. Ranjan Panda, "Electric Bicycle 1." Accessed: 2017.
13. S. Matey, D. R. Prajapati, K. Shinde, A. Mhaske, and A. Prabhu, "Design and fabrication of electric bike," *International Journal of Mechanical Engineering and Technology*, vol. 8, pp. 245-253, 03/01 2017.
14. "what is DC motor." <https://byjus.com/physics/dc-motor/> (accessed).
15. "PV solar Panel." <https://www.alternative-energy-tutorials.com/photovoltaics/photovoltaic-array.html> (accessed 20 April, 2022).
16. B. Smith. "Functionality of Dry Battery " <https://sciencing.com/wet-vs-dry-cell-battery-5510631.html> (accessed 20 April, 2022).
17. "PV Solar Panel." <https://www.alternative-energy-tutorials.com/photovoltaics/photovoltaic-array.html> (accessed).
18. "Throttle working." <https://www.bikeradar.com/advice/buyers-guides/bike-gears/> (accessed 22 April, 2022).
19. "Functionality of Power controller in Hybrid Bicycle." https://www.researchgate.net/publication/326637405_Power-assist_control_of_a_human-electric_hybrid_bicycle_with_energy_regeneration_and_cruise_control (accessed 18 April, 2022).
20. <https://www.embeddstudio.com/product/150w-boost-converter-dc-dc-10-32v-12-35v-step/> (accessed 20 April, 2022). <https://www.solar-electric.com/learning-center/solar-charge-controller-basics.html/> (accessed 18 April, 2022)



Wearable Data Acquisition System for Biomechanical Analysis

Maahad Ali^{1,*}, Abdullah¹ M. Hamza¹, Rizwan Khan¹, H. Farhan Maqbool^{1,2} and
Saqib Zafar¹

¹Department of Mechanical, Mechatronics and Manufacturing Engineering, University of Engineering and Technology
Lahore, FSD Campus

² Human Centered Robotics (HCR) Lab, University of Engineering and Technology Lahore

* maahadali.14@gmail.com

ABSTRACT

Gait is the essential function for humans, reflecting physical and cognitive status. This research aims to revolutionize clinical gait analysis, prosthetic design assessment, and human motion evaluation using the Wearable Data Acquisition System (WeDAQ). The system collects multi-parameter data, is capable of real-time transmission, and can be tailored for 90% less in cost than the average price for a standard 3D motion analysis set up. The wearable sensor modules include Force Sensitive Resistors (FSR) FSR402, Surface Electromyography Measurement (sEMG) MyoWare AT-04-001 and Inertial Measurement Unit (IMU), MPU6050. The configuration is scalable to handle input specifications, consequently lowering the design footprint and increasing ease of wear. Healthcare facilities can get it via the Data Logger GUI and WIFI- Enabled ESP microcontrollers. During thorough validation of the data, a correlation coefficient (R) between WeDAQ and SHIMMER® occupied 0.949.

KEYWORDS: Gait Analysis, WeDAQ, Biomechanics, Data Acquisition, IMU, FSR, sEMG, Human Activity Recognition

1. INTRODUCTION

Gait analysis is a systematic procedure that analyses the way we walk to measure, describe and assess parameters related to movement of human beings [1]. It has been used in sports [2], rehabilitation [3] and clinical assessment to detect athletic performance deficits monitor patient recovery and refine the ability of medial knee osteoarthritis sufferers which have a clinically significant presentation compared with those who are asymptomatic. Gait analysis has also been an important technology and clinical tool to study human body movement in biomedical engineering.

Conventional methods of gait analysis which utilizes the multi-camera motion capture systems [4] and force platforms in a lab environment using expensive equipment often leads to cumbersome set-up times. This research direction is cheaper and more flexible compared to the traditional technology in lab-based gait analysis over the past 20 years, which utilizes wearable sensors [5] for collecting data. In such devices, sensors that are used for function monitoring can include options such as inclinometers, goniometers (monitors joint angle), force sensors (gloves monitor the amount of pressure applied to a patient's hand and under feet for kinetic data) or accelerometers and gyro-sensors. A gait analysis is performed of the movement signals detected by these sensors.

WeDAQ (Wearable Data Acquisition System) provides the foundation for this study, which includes Inertial Measurement Unit (IMU), Surface Electromyography (sEMG), and Force Sensitive Resistor (FSR).

IMUs and sEMG sensors combined offer an all-encompassing image of human movement. The SEMG sensors measure muscle electrical activity while the IMUs capture movement kinematics in terms of direction and speed. The variety of other interesting applications for which FSRs have been considered causes them to be

evaluated in shoes, gloves and various other locations or garments (for example as impact detection, haptic feedback mechanisms; posture monitors & gesture identifiers) capable of detecting changes in pressure due a range different activity. FSRs are useful in detecting the gait events with applications in sports performance analysis, prosthetic control assistance, and rehabilitation input. The integration of muscle contraction to body motion provides a solution for wide range applications. The objectives of this study are.

- Design and develop low-cost wireless, multi-channel, multi-sensory Wearable Data Acquisition System (WeDAQ).
- Building a Data Logger GUI for operator control, focusing on data logging, parameter monitoring, and file handling.
- Validate data accuracy through benchmark data from the SHIMMER® apparatus using statistical techniques.

2. LITERATURE REVIEW

It is crucial to determine the optimal sensor placement to enhance data quality. This review presents a study that deals with the most suitable location of wearable sensors for gait analysis, and it is relevant in, e.g., health care system, fitness or security area. The three sensors include the surface electromyography (sEMG) [6], inertial measurement units (IMUs) [7] and force-resistive sensor [8]. A specialty of IMUs is movement analysis like measuring angular velocity and acceleration which makes them suitable for monitoring subject's motion in sports, cycling or running. They are also helpful in tracking the angles and movements of your joints. Force-sensitive sensor is a type of sensor that is used to measure the forces on it like pressure distribution and gait analysis, mostly force sensitive sensors are fitted underneath insoles

beneath your feet [9] or gloves foe grips etc., even inside a seat for chairs, cushions. The sensors must be positioned and accurately calibrated to take force data. Surface Electromyography (sEMG) sensors for monitoring electrical activity in the muscles, muscle function analyses can be performed. One study or application may utilize electrodes placed over up to three (triceps brachii) or four muscles. At different locations are an IMU, sEMG and FSR measurements in the Leg.

3. METHODOLOGY

WEDAQ is a wearable system that uses three different types of sensors to capture human movement patterns and activities. Foot pressure is measured with the aid of force-sensitive resistors (FSR 402) [10] and muscle electrical activity as surface Electromyography system, AT-04-001 [11]. The Inertial Measurement Unit (MPU 6050) combines an accelerometer and gyroscope to provide accurate measurement of acceleration: and Rotation rates [12]. The system is built with an effective Battery Management System (BMS) incorporated within custom PCBs and ESP 01 microcontrollers.

The hardest part was exploring exactly what microcontroller should be used, and how much space they would take, cost etc. The target audiences of the project were motion analysis labs, human-computer interaction spaces, sports science and healthcare industry. Extensive research was done on previous sensory systems and plans were made for the initial architecture of the system. The prototype of the sensory system comprises of integrating different type sensors such as FSR 402, AT04001 and MPU 6050.

Some major problems in data integrity are Signal filtering, Noise reduction and Calibration. Hence algorithms were developed to process sensor data which followed by interpretations of the same in an efficient way. Fast Fourier Transform FFT was used along with single-sided amplitude spectrum for cutoff frequency analysis. Butterworth filter was utilised as low pass and selective band applications. Optimized code for better performance and lesser latency, eliminating any bugs. Custom PCBs integrated with Efficient Battery management systems (BMS) and ESP 01 for communication.

System-level tests that sustained connectivity integrity and validated proper data transmission. It was tested in real life use cases and conditions based on accuracy, response time and user satisfaction. Usability and effectiveness at practical scenarios were evaluated based on feedback from stakeholders.

The data acquired from FSR was highly effective in the gait event detection. It made it easy to extract the exact gait cycle and the gait event-wise distribution.

Integrating WeDAQ System

To develop a complete sensory system, we concatenated our system with other sub-system composed of multiple heterogenous sensors including.

- Inertial Measurement Units (MPU6050)- 2 on right and 2 on left leg

- FSRs- 3 under right and 3 under left foot
- 2 sEMGs- 1 on Right leg Shank Soleus Muscle & 1 on Right leg Vastus Medialis Muscle.

Conceptual Sketch

After selecting the sensors, the next phase will be that of sensor placement to obtain better results of specific parameters. For example, while looking for the IMU position on thigh, the options are anterior or lateral side. Similarly, FSRs are to be placed in the sole of the shoes for event detection (heel strike/Toe off). Moreover, muscles for placing sEMG sensors are Lateral Muscles of Thigh and Posterior side of Shank. One Completer module Made in this research is shown in the Figure 1.



Figure 1: Complete Module having 3D printed body, PCB, ESP controller, MPU 6050 and BMS.

In the concatenated system, modules are mounted on both legs. On the right leg, One IMU module is mounted on the thigh and the other one is placed on the shank in the direction shown in Figure 2.

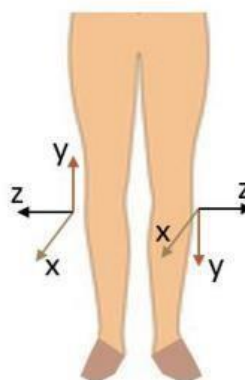


Figure 2: IMU Placement

Moreover, FSRs are placed at heel, Toe and Stride Position in the Right and Left Foot. Figure 3 shows the placement of FSRs in the shoe sole.

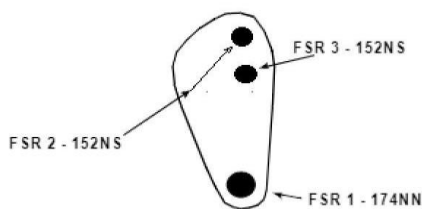


Figure 3: Placement of FSRs

FSR 1 is attached to the Heel, FSR 2 is attached to the first metatarsal bone While the FSR 3 is attached to the Toe of the foot, manufactured by Interlink Electronics Inc. Were used to measure forces generated by subject's heel, metatarsal bones and Toe bones during walking.

After going through sensor selection and conceptual sketch, hardware is designed in which 5 Modules are made. Each module can send data to one Master ESP Module wirelessly using Wi-Fi.

A complete hardware development of data acquisition system based on conceptual sketch is shown in Figure 4. Each module is attached at the lateral position of thigh & shank but sEMG electrodes are placed at soleus muscles of shank & second sEMG electrodes are attached to the Vastus Medialis Muscle.



Figure 4: Completer hardware DAQ system based on Conceptual Sketch

GUI Development

The following are the main goals of the GUI development:

- Offer a platform that enables users to easily connect to the ESP32 device.
- Enable data sent by the ESP32 through a serial link to be monitored in real-time.
- Make it simple for users to start and stop data logging sessions.
- Give users access to visualization tools so they can analyse and comprehend the logged data

more effectively. GUI Home Screen shows in Figure 5.

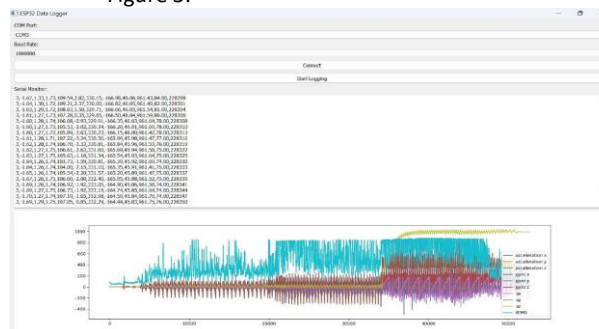


Figure 5: GUI Home Screen

4. RESULTS

VALIDATION

This study aimed to validate the data acquired by the WeDAQ system against the data acquired by the SHIMMER® system for lower limb motion analysis. Both systems were mounted side-by-side on the same participant's thigh and shank during ground walking activity. Extracted data channels included acceleration (sagittal plane), gyroscope (sagittal plane), and sEMG (medial gastrocnemius).

PROTOCOLS

This validation study adhered to the following protocols to ensure data quality and standardization:

PARTICIPANTS

- A healthy population sample with no reported lower limb injuries or gait abnormalities was recruited for the initial study.
- After a comprehensive description of the study's methods and any dangers, informed permission was acquired.

DATA ACQUISITION:

Participants performed a standardized overground walking task at a comfortable self-selected pace.

Data was continuously recorded from both systems throughout the walking trials.

Sampling frequency for all channels (gyroscope, accelerometer, sEMG) was set sufficiently high to capture the relevant signal dynamics (e.g., minimum 10 times the highest frequency of interest).

DATA PROCESSING:

A single gait cycle was extracted from each channel (gyroscope, accelerometer, sEMG) for both WeDAQ and SHIMMER® systems.

The extracted data segments were time-normalized to a common gait cycle duration (e.g., 100% of the gait cycle). The accelerometer and gyroscope data were cleaned up of noise and high-frequency distortions using a low-pass filter with a 100 Hz cut-off frequency.

A Bandpass filter with a band of (1 to 20 Hz) was applied to the sEMG data as it captures muscle activity with noise and other disturbances.

STATISTICAL ANALYSIS:

Correlation coefficients were calculated to assess the level of agreement between the corresponding channels from the WeDAQ and SHIMMER® systems.

VALIDATION RESULTS:

The validation results were highly promising, demonstrating strong correlations between the corresponding channels from both systems. The correlation coefficients were shown in Table 4.1.

Table 7: Correlation Results

Channel	Correlation Results
Shank Gyroscope	0.97351
Shank Accelerometer	0.904853

WEDAQ VS SHIMMER® GC PLOTS

SHANK GYRO

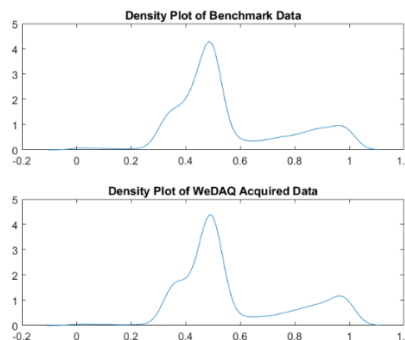
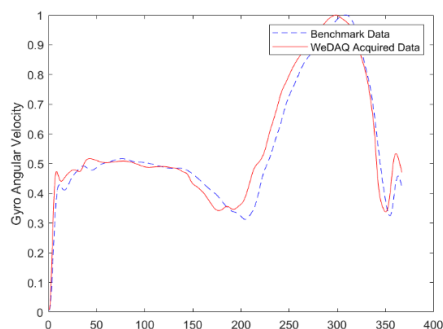


Figure 6: Shank Gyro Plots

SHANK ACCELERATION

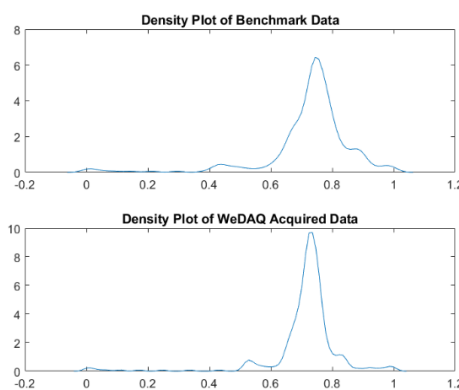
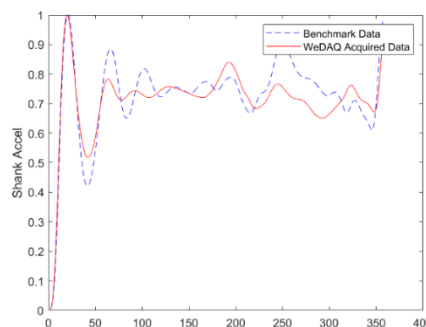


Figure 7: Shank Acceleration Plots

5. CONCLUSIONS

The validation results provide compelling evidence that the WeDAQ system can acquire data comparable to the SHIMMER® system for lower limb motion analysis during ground walking. The strong correlations observed across gyroscope, accelerometer, and sEMG channels demonstrate a high level of compatibility between the two systems. These findings suggest that the WeDAQ system can be a reliable and accurate tool for researchers and clinicians investigating lower limb biomechanics.

The WEDAQ project holds significant promise for applications in sports science, biomechanics, rehabilitation, and even fall detection in the senior population. WEDAQ is a serious competitor to replace the existing data collection systems because to its affordability, wearability, and data accuracy. The WEDAQ project has the potential to become an invaluable resource for researchers, doctors, and developers involved in human movement analysis by tackling the suggested future works.

Future work

Advancements planned for this project involve:

- Extensive data acquisition of healthy subjects while performing different activities.
- Extensive data validation against any benchmark device.
- Implementation of Human Activity Recognition algorithm HAR utilizing machine learning techniques such as:
 - Decision Trees
 - KNN
 - SVM
- GUI enhancement for seamless data transfer.
- Enhance Battery Management System BMS for long lasting use.
- PCB enhancements for power efficiency.
- Data acquisition of patient category subjects.

REFERENCE

1. Cicirelli, G., et al., *Human gait analysis in neurodegenerative diseases: a review*. IEEE Journal of Biomedical and Health Informatics, 2021. **26**(1): p. 229-242.
2. Xu, D., et al., *A new method proposed for realizing human gait pattern recognition: Inspirations for the application of sports and clinical gait analysis*. Gait & Posture, 2024. **107**: p. 293-305.
3. Marin, J., et al., *Is my patient improving? Individualized gait analysis in rehabilitation*. Applied Sciences, 2020. **10**(23): p. 8558.
4. Palermo, M., et al., *A multi-camera and multimodal dataset for posture and gait analysis*. Scientific data, 2022. **9**(1): p. 603.
5. Saboor, A., et al., *Latest research trends in gait analysis using wearable sensors and machine learning: A systematic review*. Ieee Access, 2020. **8**: p. 167830-167864.
6. Sutherland, D.H., *The evolution of clinical gait analysis part I: kinesiological EMG*. Gait & posture, 2001. **14**(1): p. 61-70.
7. Seel, T., J. Raisch, and T. Schauer, *IMU-based joint angle measurement for gait analysis*. Sensors, 2014. **14**(4): p. 6891-6909.
8. Achanta, S.D.M., *A wireless IOT system towards gait detection technique using FSR sensor and wearable IOT devices*. International journal of intelligent unmanned systems, 2020. **8**(1): p. 43-54.
9. Park, J.S., et al., *Gait phase detection using force sensing resistors*. IEEE Sensors Journal, 2020. **20**(12): p. 6516-6523.
10. Negi, S., S. Sharma, and N. Sharma, *FSR and IMU sensors-based human gait phase detection and its correlation with EMG signal for different terrain walk*. Sensor Review, 2021. **41**(3): p. 235-245.
11. Wei, P., et al. *Different sEMG and EEG features analysis for gait phase recognition*. in *2020 42nd Annual International Conference of the IEEE Engineering in Medicine & Biology Society (EMBC)*. 2020. IEEE.
12. Mazzà, C., et al., *Technical validation of real-world monitoring of gait: a multicentric observational study*. BMJ Open, 2021. **11**(12): p. e050785.

FEM Based Complex Multivariate Random Vibration Fatigue Life Prediction of a Tracked Vehicle Balance Arm Using Various Road Surface Profiles

Ayaz Mahmood Khan², Shahid Khalil², Yasir Hamid¹, Syed Waheed Ul Haq¹

¹ Department of Mechanical Engineering, HITEC University, Taxila Cantt 47070, Pakistan

² Department of Mechanical Engineering, University of Engineering and Technology, Taxila 47070, Pakistan.

*enr.ayyazz@gmail.com

ABSTRACT

Probabilistic random vibration can speed up wear and tear on several components of the tracked vehicle, including the track system, drivetrain, and suspension. Extended exposure to high levels of vibration can cause structural damage to the vehicle frame and other critical components. Assessing random vibration in track vehicles requires a comprehensive approach that considers both the root causes and potential consequences of the vibrations. This Random vibration significantly influences the structural performance of balance arm which is key component of tracked vehicle. The current research article investigates the fatigue damage characteristics of a tracked vehicle balance arm considering the dynamic loads induced by traversing on smooth and rough terrain. The analysis focusses on assessing the damage and stress response Power spectral density (PSD) ground based excitation which is termed PSD-G acceleration. Quasi Static Finite Element Method based approach is used to simulate the operational conditions experienced by the balance arm. Through comprehensive numerical simulations, the fatigue damage accumulation patterns are examined, providing insights into the structure integrity and performance durability of the balance arm under varying operational scenarios. The obtained stress response PSD data and fatigue damage showed that the rough terrain response exhibits higher stresses in balance arm. The accumulated stresses in case of rough terrain may prompt to brittle failure at specific critical locations. This research contributes to the advancement to the design and optimization strategies for tracked vehicle components enhancing their reliability and longevity in demanding operational environment.

KEYWORDS: Fatigue Life, FEM, Balance Arm, Power Spectral Density (PSD), Probabilistic, Fast Fourier Transform

1. INTRODUCTION

Tracked suspension vehicles are vehicles equipped with continuous tracks (also known as caterpillar tracks) instead of wheels. These tracks provide better traction and weight distribution, allowing the vehicles to move efficiently over challenging terrains such as mud, sand, snow, and rough ground. High-mobility tracked vehicles, such as armored battle tanks and armored personnel carriers, are designed to move over difficult off-road terrain, which subjects them to severe excitations. Their performance is normally limited by the operator's ability to withstand transmitted shocks and vibrations and to retain control. The maximum allowable speed depends upon the roughness of the terrain and is primarily determined by the design characteristics of the suspension system [1]. In view of detrimental effects of ride vibration on health and safety of vehicle drivers and on vehicle mobility, the ride quality of wheeled vehicles has drawn considerable. However, the present trend is towards the use of hydrogas and passive suspension configurations (balance arm) to maximize the ride limiting speeds [2-3]. These high-mobility tracked vehicles are usually fitted with passive suspension systems that include torsion bars with shock absorbers to dampen terrain-induced shocks and vibrations [4]. A balance arm is a structural element of the tracked suspension system connecting the road wheels to the chassis of the vehicle [5-7]. The balance arms help in equalizing the weight of the vehicle upon the tracks, therefore providing better grip and stability in

changing surfaces and adaptability on uneven terrain. Under such uniform pressure on the track, the balance arm works to help the vehicle overcome rough ground with greater ease and allows movement with more comfort by shock and vibration absorption. Investigation of stresses and damage in the balance arm is done through Computer simulation using an analytical vehicle model, which is commonly employed to Predict and quantify the effects of the above-mentioned excitations in the balance arm with various road surface profiles before final design and testing. The analytical predictions should be experimentally validated to gain confidence in the use of the computer model. Historically, the Suspension dynamics of track laying vehicles have been investigated with the aid of mathematical models of variable complexities. Numerical analysis and computer simulations are then used to determine the overall stress and damage in the balance arm.

NOMENCLATURE

Symbol	Description
$S_x(f)$	Power Spectral Density
$x(t)$	acceleration time series
$X(f)$	Fourier transform
T	Total observation time
K	Stiffness Matrix
u	Displacement vector

F	Applied load vector
S_y(f)	PSD of the response
H(f)	Frequency response function
α	Scaling factor
S_{xy}(f)	cross-spectral density matrix
S_σ(f)	Stress spectrum
X_x(f), X_y(f)	Fourier Transform of Vibration signal

Abbreviations	
ISPSD	Input Smooth Power Spectral Density
IRPSD	Input Rough Power Spectral Density
SSRPSD	Smooth Stress Response Power Spectral density
RSRPSD	Rough Stress Response Power Spectral density
FRF	Frequency Response function

GOVERNING EQUATIONS

The Power Spectral Density of the ground-based excitation can be used to describe the random vibration input [8-10]. For an acceleration time series $x(t)$, the PSD is given by:

$$S_x(f) = \frac{1}{T} |X(f)|^2 \quad (1)$$

For the quasi-static FEM approach, the equilibrium equations are:

$$K \cdot u = F \quad (2)$$

The response of the model to the random vibrations can be characterized using the Frequency Response Function (FRF), which relates the input PSD to the output PSD:

$$S_y(f) = |H(f)|^2 S_x(f) \quad (3)$$

The stress spectrum in the model due to random vibrations can be obtained from the response PSD:

$$S_\sigma(f) = \frac{1}{\alpha} |H(f)|^2 S_x(f) \quad (4)$$

For complex scenarios, multivariate random vibrations have to be considered which involve multiple correlated vibration sources. This can be represented by a cross-spectral density matrix $S_{xy}(f)$:

$$S_{xy}(f) = \frac{1}{T} \langle X_x(f) \cdot X_y^*(f) \rangle \quad (5)$$

where $X_x(f)$ and $X_y(f)$ are the Fourier transforms of different vibration signals, and $\langle \cdot \rangle$ denotes the expected value.

DESCRIPTION OF PHYSICAL MODEL

The 3d model of the Balance arm is developed and used in this study to assess the fatigue damage and structural integrity. The tracked vehicle's balance arm is studied under various dynamic loading conditions, focusing on the effects of probabilistic random vibrations.

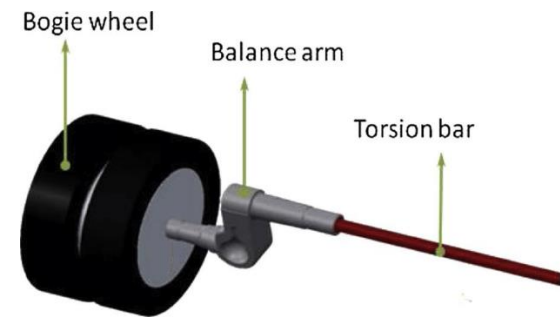


Figure 1: Mounting Location of Balance Arm [6]

The mounting locations of the balance arm are shown in Figure 1. This model incorporates several critical parts such as torsion bar on one side and bogie wheel on the other side. The model accounts for dynamic loads induced by random loads and the traversal of different terrains, including both smooth and rough surfaces. Power Spectral Density (PSD) data, specifically PSD-G acceleration, is used to represent the ground-based excitation forces acting on the balance arm.

2. COMPUTATIONAL ANALYSIS

A Quasi-Static FEM approach is employed to simulate the operational conditions that the balance arm experiences. The data was collected over time for simulation input, and was treated as a multivariate time series to allow for analyzing the interdependencies and temporal patterns between the different load variables. This method allows for the accurate representation of stress and damage responses under the defined loading conditions. The model calculates the stress response of the balance arm under different terrain conditions, using PSD data to assess how vibrations impact stress distribution. The model evaluates the fatigue damage of the balance arm by analyzing damage accumulation patterns over time. It considers both high-stress scenarios and the potential prediction for brittle failure at critical locations.

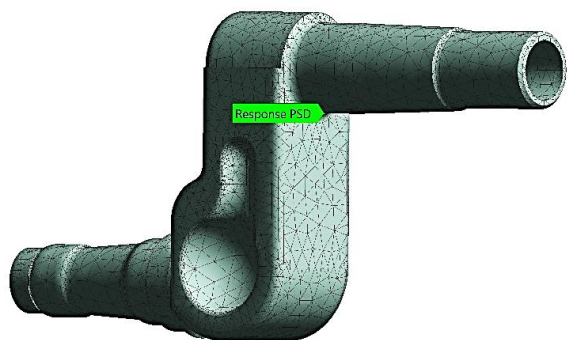


Figure 2: Response PSD location 1

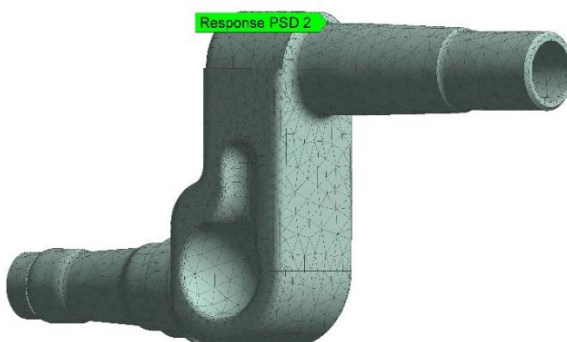


Figure 3: Response PSD location 2

Two points have been chosen for analyzing the vibration response of the the model. Both the locations are shown and marked in Figure 2 and 3 respectively. The simulation uses 2 operational scenarios to understand how different terrains impact the balance arm's performance. Specifically, it compares the stress and fatigue damage outcomes for smooth versus rough terrain. The simulation results further used to assess the ground-based excitation (PSD-G) and its impact on the balance arm. PSD helps in understanding how different frequency components contribute to the overall vibration response. This method simulates the operational conditions and stress responses experienced by the balance arm. FEM is essential for capturing detailed stress distributions and damage patterns. Comprehensive numerical simulations are employed to evaluate the fatigue damage accumulation in the balance arm. These simulations account for dynamic loads, and terrain interactions (both smooth and rough). The research focuses on how different operational scenarios affect the fatigue damage and structural performance of the balance arm. The computational results reveal that rough terrain causes higher stress and reduced fatigue life due to increased fatigue damage. Overall, the research contributes to understanding how random vibrations affect tracked vehicle components and aims to improve design and optimization strategies to enhance component reliability and durability.

3. RESULTS & DISCUSSION

This section presents results and a comprehensive discussion for Vibration response obtained on smooth and rough terrain. The vibration data is applied to the balance arm model in the form of Power spectral density. The response is obtained for 2 locations (shown in Figure 2 and 3). The stress response is utilized for analyzing both locations to understand the location which is more critical. The results also discuss which frequencies are expected to cause more damage both on the smooth and rough terrain. As an initial step the balance arm has been analyzed for its fatigue life under smooth and rough terrain vibration plots. The S-N approach was employed for find out the fatigue life in terms of specific number of cycles. This represents the expected number of cycles the arm can endure under the given loading conditions before fatigue failure is expected. By understanding the fatigue life of critical components, maintenance schedules can be efficiently optimized. Knowing the expected life in cycles helps predict mean time between failure (MTBF), allowing proactive replacement or reinforcement. This lessens unexpected breakdowns in the field, where repairs can be challenging and costly. The fatigue life contour plots are presented in Figure 4 and Figure 5.



Figure 4: Fatigue Life of Balance arm for smooth terrain

The fatigue life contour presented in Figure 4 shows that The maximum life cycles of the balance arm are expected to be $2E+7$ cycles whereas the minimum expected life is expected to be 4082.5 cycles. It is indispensable to mention here that the lowest fatigue life is expected to be at the edge present at the inner side of the balance arm which is prone to failure under current loading state.

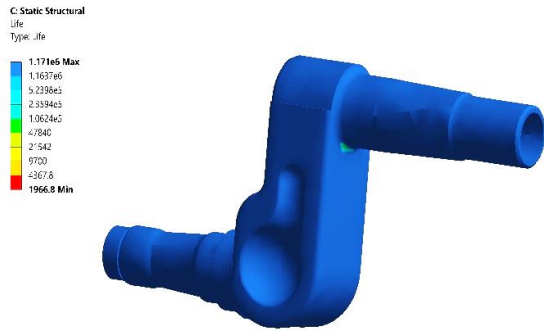


Figure 5: Fatigue Life of balance arm for rough terrain

The fatigue life contour presented in Figure 5 shows that the maximum life cycles of the balance arm are expected to be 1.171E+6 cycles whereas the minimum expected life is expected to be 1966 cycles. The next step was carried out to assess and analyze damage in the balance arm.

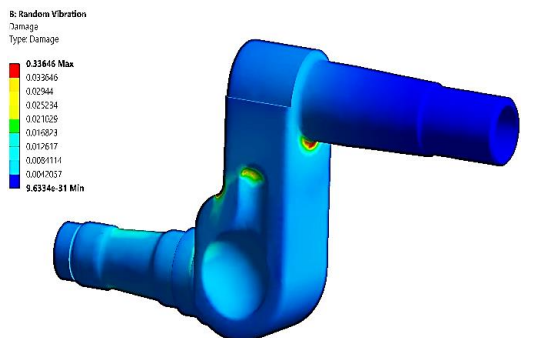


Figure 6: Damage Contour smooth terrain response

The Figure 6 presents damage contour plot obtained in the ANSYS random vibration analysis environment. The balance arm contour shown in the figure exhibits damage characteristics in the balance arm for smooth terrain traverse of the tracked vehicle. The maximum damage is expected at the edge of the arm which can be attributed to high stress concentration.

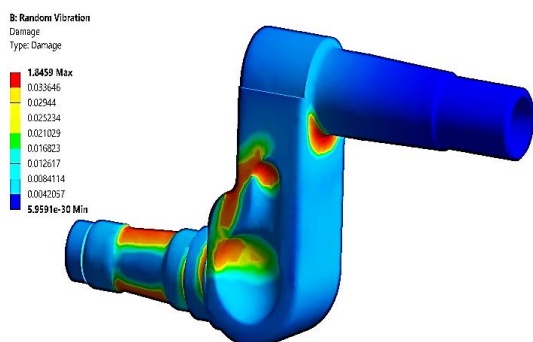


Figure 7: Damage Contour rough terrain response

The simulation contour in figure 7 shows result in ANSYS environment to assess expected damage due to random loading. The balance arm contour shown in the figure displays damage in the balance arm when the tracked vehicle traverses on the rough terrain. The maximum

damage is anticipated at the edge of the arm but it is expected to spread in further areas as well.

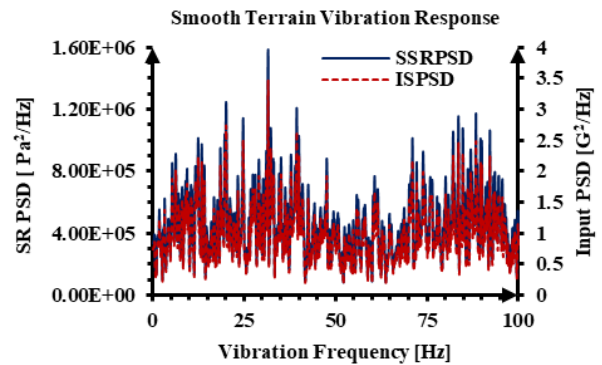


Figure 8: Location 1 Smooth Vibration Response PSD

The Figure 8 presents plot of Stress response PSD obtained for balance arm for smooth terrain for Location 1. The primary axis represents the stress response PSD (blue color) whereas the secondary axis represents the input PSD applied to the model (red color). Both the axis are plotted against the vibration frequency. It is pertinent to mention here that the maximum stress response PSD is 1.57E + 06 Pa²/Hz at a frequency of 32.031 Hz. This indicates that under smooth terrain conditions, the system experiences vibrations or accelerations predominantly at this frequency.

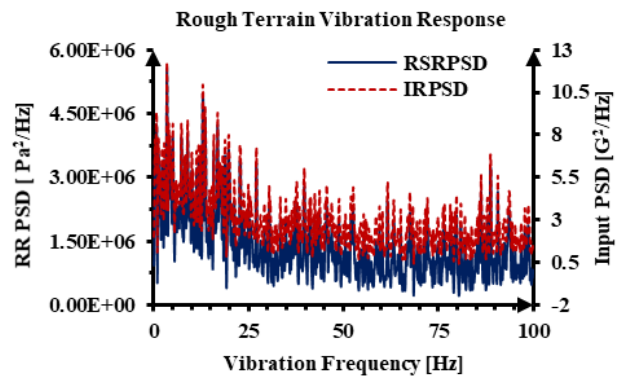


Figure 9: Location 1 Rough Vibration Response PSD

The Figure 9 presents plot of Stress response PSD obtained for balance arm for rough terrain at Location 1. The primary axis represents the rough terrain stress response PSD (blue color) whereas the secondary axis represents the PSD applied as an input to the 3d balance arm model (red color). Both the axis are plotted against the vibration frequency. It is pertinent to mention here that the maximum stress response PSD is 5.54 E + 06 Pa²/Hz at a frequency of 3.5156 Hz.

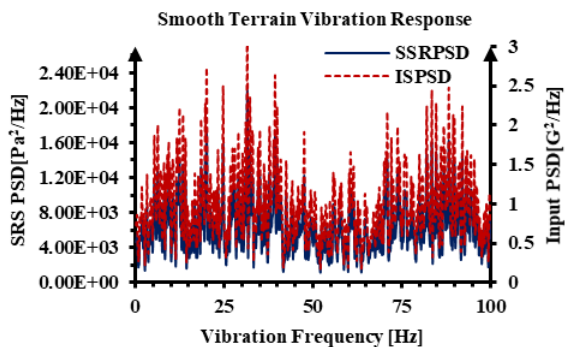


Figure 10: Location 2 Smooth Vibration Response PSD

The Figure 10 shows plot of Stress response PSD obtained for balance arm for smooth terrain for Location 2. The Left side y-axis represents the stress response PSD (blue color) whereas the secondary y-axis represents the input PSD applied to the model (red color). Both the axis is plotted against the vibration frequency. It is observed that the maximum stress response PSD is $2.17 \text{ E} + 04 \text{ Pa}^2/\text{Hz}$ at a frequency of 31.543 Hz.

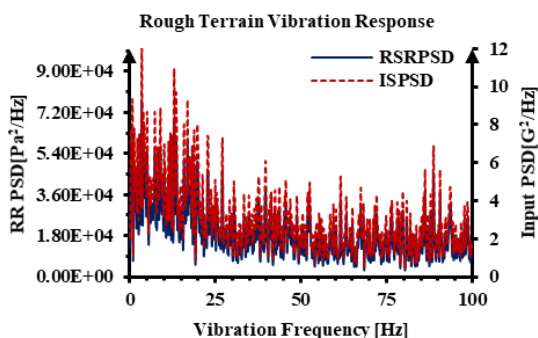


Figure 11: Location 2 Rough Vibration Response PSD

Figure 11 depicts Stress response PSD plot obtained for balance arm for rough terrain for Location 2. The Left side y-axis represents the rough stress response PSD (blue color) whereas the secondary y-axis represents the PSD input applied to the balance arm model (red color). The primary and secondary axis are plotted against the vibration frequency. The plot exhibits the maximum stress response PSD at $7.68 \text{ E} + 04 \text{ Pa}^2/\text{Hz}$ at a frequency of 3.5156 Hz.

The bar chart presented in Figure 12 shows the mean response PSD (Log scale) on the y-axis. The horizontal axis represents the PSD input as well as stress response PSD for Location 1 and location 2 for both smooth and rough terrains. Location 1 is seen to exhibit higher mean values of stress response PSD as compared to Location 2. The rough terrain showcases response PSD of $6.14 \text{ Pa}^2/\text{Hz}$ as compared to $5.66 \text{ Pa}^2/\text{Hz}$ for smooth terrain on Location 1.

The bar chart in Figure 13 presents the maximum fatigue damage for smooth and rough terrains. The primary axis shows minimum fatigue damage whereas the secondary (right side) axis presents the scale for maximum fatigue damage. The rough terrain exhibits an overall damage of

1.8549 as compared to smooth terrain maximum damage of 0.33646. This can be attributed to the unpredictable and random nature of vibrations during the rough terrain traverse.

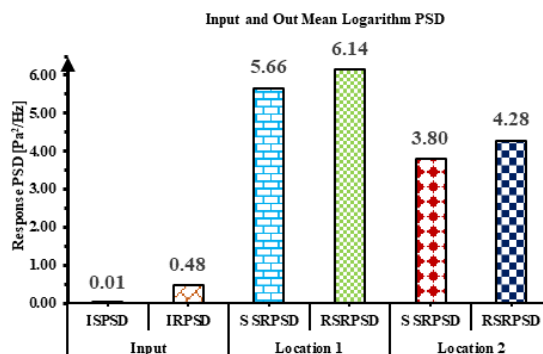


Figure 12: Mean Vibration Response PSD at Different Locations

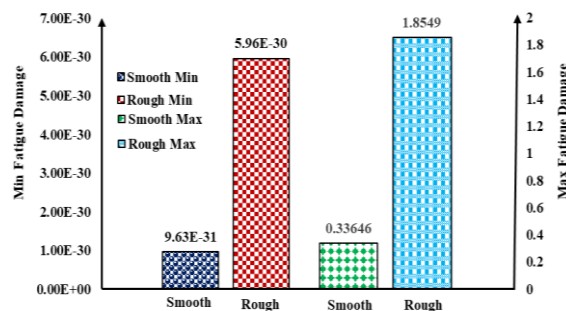


Figure 13: Min and Max Fatigue damage

4. CONCLUSIONS

The analysis focusses on ascertaining the damage and stress response Power spectral density (PSD) ground-based excitation which is termed PSD-G acceleration. Random Vibration FEA was used to simulate the operational conditions experienced by the balance arm. Through comprehensive numerical simulations, the damage accumulation patterns, and stress response PSDs were examined at 2 locations on the balance arm. Location 1 was observed to be more critical under the influence of rough terrain conditions. The conclusions of the current research made are as following:

1. The fatigue life contour has been found for both smooth and rough terrains in ANSYS environment. The fatigue life is seen to reduce by 51.8 percent for rough terrain as compared to smooth terrain.
2. The fatigue damage observed in the case of rough terrain is about 81.8 percent higher as compared to smooth terrain damage.
3. The mean vibration response in case of rough terrain for location 1 is about 7.82 percent higher than for smooth terrain.



- The FEA results highlight that the overall PSD stress response for location 1 exhibits higher values as compared to response obtained for location 2. This can lead to crack development and early failure.
- The peak stress response PSD valued at $5.54 \text{ E} + 06 \text{ Pa}^2/\text{Hz}$ is obtained at Location 1 for rough terrain at a frequency of 3.5156 Hz.
- The elevated stress response PSD value suggests more powerful vibrations under rough terrain conditions, and the shift in frequency reflects a variate dynamic response of the system due to terrain irregularities.

random Loading. International Journal of Mechanical Engineering & Robotics Research, 3(4), 533-541.

- You, T., Zhou, J., Gong, D., Sun, Y., Li, B., & Chen, J. (2022). Synthesis of random vibration environment spectra for the fatigue analysis and optimization of railway vehicles. International Journal of Fatigue, 159, 106752.
- Xiang, P., Zhao, Y., Lin, J., Kennedy, D., & Williams, F. W. (2016). Random vibration analysis for coupled vehicle-track systems with uncertain parameters. Engineering Computations, 33(2).

REFERENCES

- Dhir, A., & Sankar, S. (1994). Ride dynamics of high-speed tracked vehicles: simulation with field validation. *Vehicle System Dynamics*, 23(1), 379-409.
- Maclaurin, B. (1983). Progress in British tracked vehicle suspension systems (No. 830442). SAE Technical Paper.
- Dhir, A., & Sankar, S. (1995). Assessment of tracked vehicle suspension system using a validated computer simulation model. *Journal of Terramechanics*, 32(3), 127-149.
- Rakheja, S., Afonso, M. F. R., & Sankar, S. (1992). Dynamic analysis of tracked vehicles with trailing arm suspension and assessment of ride vibrations. *International Journal of Vehicle Design*, 13(1), 56-77.
- Z.P. Hao, F.Y. Han, J.Q. Lin, Z.X. Yu, Wear characteristics and wear control method of PVD-coated carbide tool in turning Inconel 718, *Int. J. Adv. Manuf. Technol.* 78 (2015) 1329–1336.
- Khan, A. M., Mahmood, K., ul Haq, S. W., Choudhry, R. S., & Khan, S. M. (2017). Root cause failure analysis of a tracked vehicle balance arm. *Case studies in engineering failure analysis*, 9, 112-117.
- Rakheja, S., Afonso, M. F. R., & Sankar, S. (1992). Dynamic analysis of tracked vehicles with trailing arm suspension and assessment of ride vibrations. *International Journal of Vehicle Design*, 13(1), 56-77.
- NC, S. C., & Subbaratnam, B. (2014). Finite element analysis and fatigue analysis of spur gear under

Simulation of Collaborative Controlled Collision Avoiding Robot

Muhammad Arqum Razzaq^{1,2}, Ahsan Ali², Kashif Bilal¹

¹Department of Mechatronics Engineering, University of Chakwal, Chakwal, Pakistan

²Air University, Islamabad, Pakistan

*arqum.razzaq@uoc.edu.pk

ABSTRACT

Vehicle robots have become part of our daily life, from household tasks to military operations. Typically, these robots are controlled autonomously, semi-autonomously, or manually via remote control, but each method has limitations, including sensor failures, communication errors, and processing delays. To remove such issues, this study introduces a collaborative control method for vehicle robots that combines the strengths of tele-operated and fully autonomous systems to provide better navigation for the vehicle robot. A simulation environment is created using MATLAB® that contains multiple dynamic, circular shaped obstacles that move linearly and reflect off walls. The robot's position is specified by its x and y coordinates, and its trajectory is predicted based on its steering direction. Obstacles are detected at the robot's corners and edges. When a collision is anticipated, the collaborative control system activates to provide avoidance recommendations, selecting the safest option with minimal or no collision risk. If no obstacles are detected, the robot remains under manual control. The results show that the collaborative control system allows the vehicle robot to reach its destination faster and with fewer collisions compared to fully manual or autonomous modes. The proposed system significantly improves safety and operational efficiency while avoiding very few dynamic obstacles.

KEYWORDS: Collaborative control, vehicle robot, obstacle avoidance, robot safety, recommendation, robot navigation.

1. INTRODUCTION

The vehicle robot has gained the attention of researchers in various fields due to its simple control algorithms and the extensive literature available. Tele-operated robots are being used for surgery and rehabilitation [1][2][3]. Robots have become an important part of agriculture, where smart farms are being developed, adopting features of industrial robots [4]. The adoption of these robots has also increased in nuclear environments, where conditions are harsh and tasks are dangerous [5]. Tele-operated robots are also being used domestically to care for older adults, providing physical assistance in daily routine activities such as monitoring, feeding, and dispensing medication [6][7][8].

When designing and navigating vehicle robots, collision avoidance and path planning are crucial steps. The robot must generate an accurate map of the environment, and timely responses are essential for effective operation [9][10]. Challenges arise when the robot operator has limited knowledge of the environment, or when communication delays or sensor failures occur [11]. This limited environmental knowledge can lead to unavoidable collisions, which may damage the robot and pose risks to the surroundings.

Key obstacle avoidance algorithms like Dijkstra, Ant Colony Optimization, A*, and artificial potential field algorithms are discussed in [12]. Obstacle avoidance and motion planning algorithms are further defined in [13]. A combination of the Rapidly Exploring Random Tree (RRT) ROS navigation system and the YOLOv7 object detection model is used in [14] to avoid obstacles and drive the robotic vehicle. The concept of shared control for tele-operated robots originated in [15], where a

multilevel collaborative driving framework was developed for real-time autonomous vehicle control. Human participation in robot driving can enhance safety and robustness. A similar driving framework was developed in [16], where six-degree-of-freedom haptic devices and Electromyography (EMG) signals were used to control the robot. Another study in [17] explores how users interact with the robot through virtual force and visual feedback to control the robot's dynamic response.

In light of the above discussion, this paper presents the concept of a collaborative control robot, where control is shared between the human operator and the robot. The simulation provides recommendations, and the safest and most secure option is applied to the robot's controller.

2. METHODOLOGY

A compromise between tele-operated robots and fully autonomous robots has been proposed to control vehicle robots. MATLAB® has been used to generate an environment with multiple dynamic obstacles of specified size and circular shape, moving linearly. Obstacles that collide with the walls of the environment can reflect back. The position of the front-wheel-drive robot can be specified by the x and y coordinates (center of gravity) in the environment. The prediction of the robot's placement can be foreseen by tracing the robot forward according to the current direction of the steering wheels. Obstacles can be detected at the corners or side edges of the robot. In collaborative control, if a collision is anticipated, a recommendation is applied to avoid it. If no collision is anticipated, the robot is controlled manually.

Working of Vehicle Robot

The vehicle robot operates by executing input commands provided by a human operator. These inputs control various movements, such as acceleration, deceleration, moving forward, and reversing. The robot's direction is controlled based on the position of a cursor on a screen, which can indicate forward, backward, or diagonal directions (e.g., right-forward, left-backward) as shown in Fig. 1. When the cursor is positioned directly in front or behind, the robot adjusts its velocity without changing direction, either accelerating or decelerating according to a constant acceleration. The velocity is calculated using the equation of motion:

$$V_f = V_i + at \quad (1)$$

Where the requested acceleration can be positive or negative, affecting the robot's speed. The relationship between the cursor position and robot movement is visualized, showing how the robot steers and adjusts its velocity accordingly.

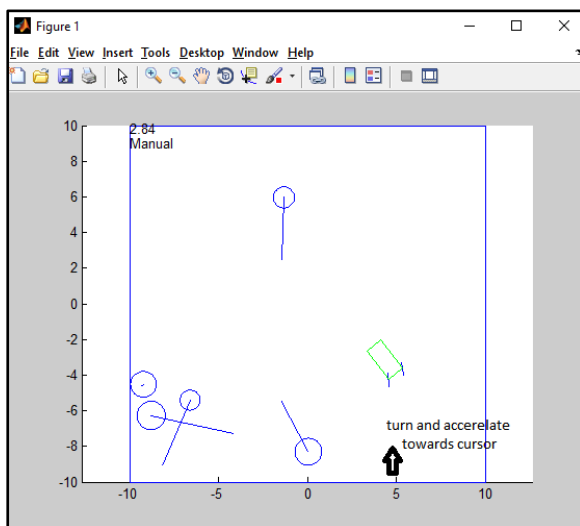


Figure 1: Robot accelerating or decelerating towards cursor

Dynamic Environment Generation

In the simulation, the environment is populated with dynamic obstacles that the robot must navigate around. For simplicity, the obstacles are modelled as circles with varying sizes, directions, and speeds, all randomly generated within predefined limits as shown in Fig. 1. The formula used to generate obstacle is given by:

$$output = min * (1 - r) + max * (r) \quad (2)$$

These circles represent different obstacles that move throughout the environment. The size of each obstacle is constrained to ensure they are neither too small (which would make them resemble a point) nor too large (which would dominate the entire simulation space). Although the simulation environment may have prior knowledge of all obstacles, the collaborative control focuses on real-time

decision-making where human input can adjust for unexpected changes that makes it highly relevant for practical applications. The direction of the obstacle is shown through the line, while the speed is proportional to the length of the line. The robot avoids a collision using available techniques developed for detecting and navigating the circular obstacles. This method allows for a dynamic and unpredictable setting that can effectively simulates real-world navigation challenges.

Obstacle Detection

Two methods are available for obstacle detection for a robot: Edge Collisions and Corner Collisions. These two methods have been designed to increase the effectiveness of detecting obstacles that allows detection at both the edges and at the corners of the robot. If an obstacle is not detected by the corner, the system ensures that it can still be identified at the robot's edge. This dual-method approach significantly improves the robot's ability to identify obstacles in its path, ensuring a more reliable collision avoidance process. These detection methods are deployed to tackle the dynamic nature of the simulated environment. This will improve the robot's responsiveness to obstacles.

Obstacle Avoidance using Collaborative Control

The robot can be controlled through three different modes of operation, that are, fully autonomous, pure manual and the collaborative mode. In the fully autonomous mode, the robot navigates without any human input. This mode is typically used in situations where the path is predefined, such as line-following or wall-following robots. In pure manual mode, all commands are executed as directed by the human operator, similar to the control of a teleoperated vehicle or remote-controlled car. The control mode is shown on the top left corner as shown in Fig. 1. In the collaborative control mode, obstacle avoidance is achieved by combining human input with automated safety recommendations from the robot. When a potential collision is detected, either through corner or edge collision detection, the system generates recommendations based on human perception and situational awareness. These recommendations are evaluated and, if safe, then applied to the robot. This ensures that even if the human operator's commands lead to a potential collision, the robot can override those commands with safer alternatives. The collaborative control mode, therefore, increases safety and preventing accidents while maintaining human control. All recommendations are tested before execution to ensure effectiveness in avoiding obstacles. The implemented algorithm has been shown in Fig. 2.

Robot Representation in Simulation

The vehicle robot used in simulation is a point vehicle with front wheel steering dynamics. Refer to the Fig. 3, the position (x, y) of a robot at any time instant can be found by:

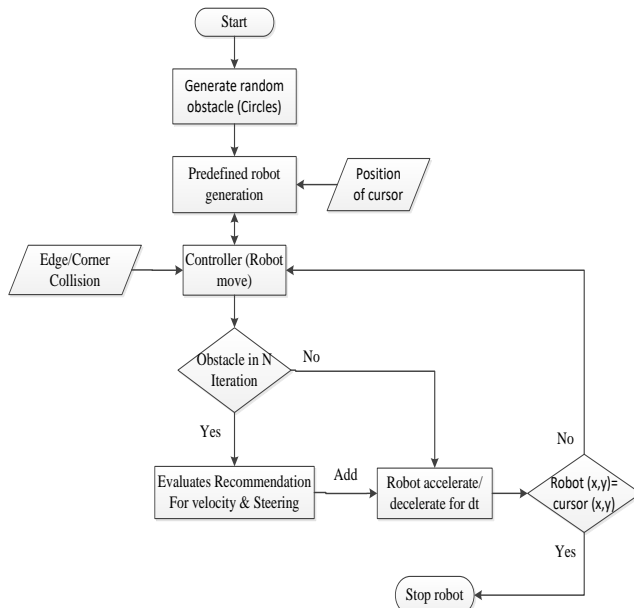


Figure 2: Implementation of collaborative control mode

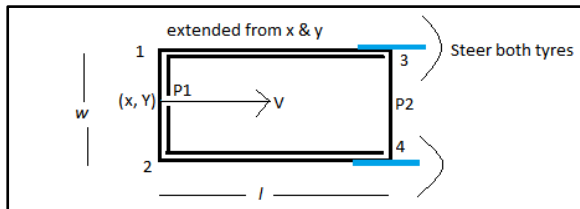


Figure 3: Schematic of a robotic vehicle

$$x = x + v \cos(\theta) * dt \quad (3-a)$$

$$y = y + v \sin(\theta) * dt \quad (3-b)$$

The represented point robot (x, y) is a point at the mid of the back edge of the robot as shown in Fig. 3. The length and the width of the robot are given, so all corner can be evaluated by solving the robot rectangle. Fig.4 shows the four corners of the robot that can be evaluated by:

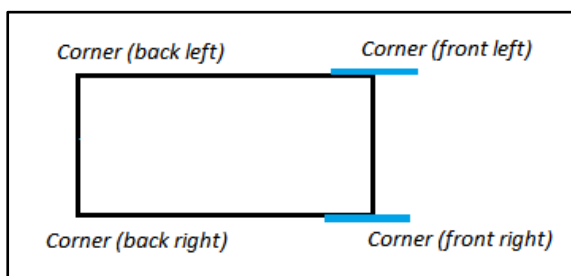


Figure 4: Corner computation of the robot rectangle

$$\begin{aligned} \text{corner}(\text{back left}(x)) &= \text{robot}(x) + \frac{w}{2} * \sin(\theta) = a \\ \text{corner}(\text{back right}(x)) &= \text{robot}(x) - \frac{w}{2} * \sin(\theta) = b \\ \text{corner}(\text{front left}(x)) &= a + l * \cos(\theta) \\ \text{corner}(\text{front right}(x)) &= b + l * \cos(\theta) \\ \text{corner}(\text{back left}(y)) &= \text{robot}(y) - \frac{w}{2} * \cos(\theta) = c \\ \text{corner}(\text{back right}(y)) &= \text{robot}(y) + \frac{w}{2} * \cos(\theta) = d \end{aligned}$$

$$\begin{aligned} \text{corner}(\text{front left}(y)) &= c + l * \sin(\theta) \\ \text{corner}(\text{front right}(y)) &= d + l * \sin(\theta) \end{aligned} \quad (4-a \text{ to } h)$$

Corner and Edge collision detection

A corner collision occurs when the robot's corner comes too close to an obstacle. To detect this, the distance between the robot's corner and the obstacle's center is calculated, and a collision is going to occur if this distance is less than 1.2 times the obstacle's radius. The obstacle's diameter is enlarged by 20% to ensure that a potential collision is detected before the robot makes contact. This method checks all four corners of the robot, and if any corner detects a collision, it triggers the system to avoid it. If the obstacle approaches from the side of the robot, a corner collision may not occur, but an edge collision might. Edge collisions are detected by checking if the obstacle intersects with any of the robot's sides (represented as lines). If the circle intersects the line at two points, an edge collision is detected. If only one point of intersection is found, it would have already been captured by the corner collision detection. The system prioritizes corner collisions first, and if none are detected, it checks for edge collisions. Both corner and edge collisions are described in Fig. 5.

Although the simulation environment has access to all obstacle data, the collaborative control system allows for dynamic human input, compensating for potential limitations in fully autonomous systems such as sensor failures or unanticipated obstacle behaviour. This reflects real-world scenarios where such challenges are common.

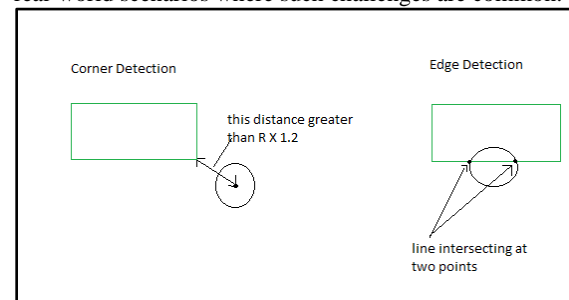


Figure 5: Corner and Edge Collision Detection

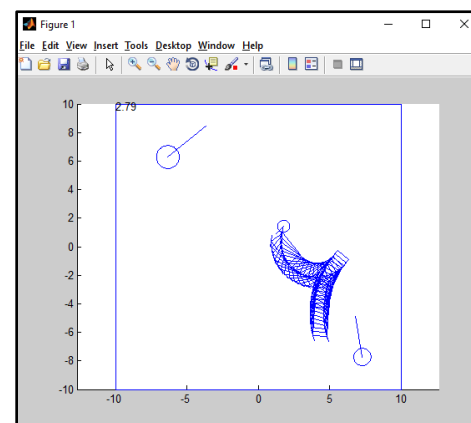


Figure 6: Foreseen trajectory of the robot

Recommendation to avoid collision

The robot's foreseen trajectory is shown in Fig. 6. In the collision avoidance process, the main file, **RobotStep2**, handles the collaborative mode by detecting possible edge and corner collisions and generating recommendations to avoid them. The function **Collides2** identifies collisions by computing the robot's corners through **ComputeCorners**, then sends this information back to **RobotStep2**, which integrates the recommendations with human inputs to avoid obstacles. If no collisions are detected, the robot proceeds using the **ManualControl** function. The **AnticipateCollision** function checks if collisions are expected, and if not, the recommendations are applied through **ApplyRecommendation**. Collision detection occurs not in real-time but by projecting the robot and obstacles into a future environment, allowing the system to foresee potential collisions based on the robot's trajectory, as visualized by the **RobotPlot2** function.

If there's a risk of a corner or edge collision, the collaborative control algorithm adjusts the robot's steering, speed, and acceleration to avoid it. These adjustments are based on both human perception and the velocity obstacle method, which looks at the relative speed between two objects. Table 1 shows that these adjustments resemble how a person would react when they sense a possible collision.

Table 1: Cases of collision avoiding

Sr. #	Occurred Collision	Recommendation Added
1	Right corner	Positive steer, reduce speed
2	Left corner	Negative steer, reduce speed
3	Right/ left back corner	Same steer, reduced speed
4	Front edge	Reduce speed

3. RESULTS AND DISCUSSION

The simulation results demonstrate that the vehicle robot successfully navigates from one point to another within the simulation environment. The robot is controlled by positioning the cursor in the simulation interface, which directs the robot's steering and acceleration towards the cursor's location. In scenarios where a collision is imminent, the system highlights the potential collision point with a small circle around the corner. The control automatically shifts to the collaborative control mode, named as 'autopilot,' to avoid the anticipated collision. These results are illustrated in Fig. 7 and Fig. 8.

In the simulation where density of obstacles is high, the vehicle robot have no boundary constraints and the freedom to move anywhere on the screen. Despite the simulation's knowledge of obstacles, collaborative control simulates real-time interactions that would occur in environments with incomplete or changing information, demonstrating the system's adaptability and relevance in complex real-world scenarios. Various experiments has been conducted where the robot was guided along specific trajectories using either manual or collaborative control modes. Table 2 summarizes some of the results of these experiments, demonstrating the effectiveness of the

collaborative control mode in different scenarios. Each result corresponds to different no of obstacles, proving the adaptability and efficacy of the collaborative control.

The collaborative control method for the vehicle robot has been successfully implemented and tested using MATLAB® simulation. The simulation includes randomly moving circular obstacles that do not respawn, and the robot's ability to avoid the collision was evaluated. When the trajectory of the vehicle robot intersects with moving obstacles, and a collision is foreseen during the simulation, the collaborative control mode is activated. The recommendation from the robot and input command from the human operator is combined to avoid any foreseen collision. The control system provides safer recommendations that minimize the risk of potential collision, which are then applied collaboratively. The results indicate that the collaborative control mode enhances the robot's ability to navigate safely in dynamic environments.

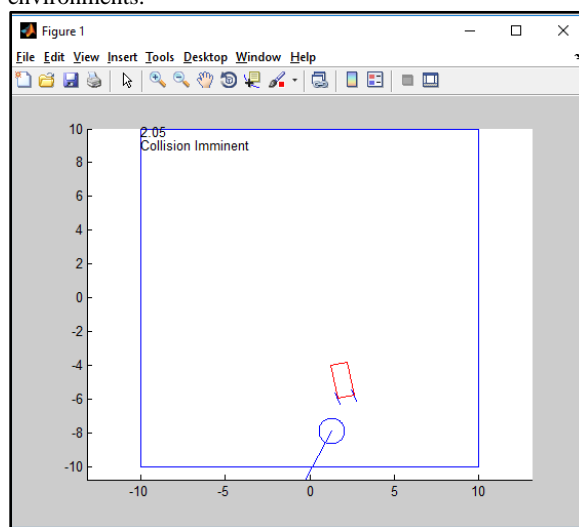


Figure 7: Collision imminent of a robot with obstacle

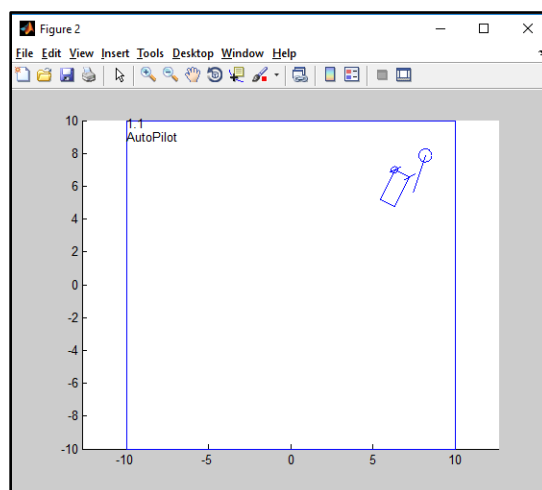


Figure 8: Enabling collaborative control mode and corner which is going to collide

Table 2: Simulation testing

Mode of operation	Time	No. of collision
Manual (obstacles=1)	7.36	1
Collaborative (obstacle=1)	7.00	0
Manual (obstacles=2)	7.08	0-1
Collaborative (obstacle=2)	6.67	0

4. CONCLUSIONS

Robot applications have been increased significantly over the years, including transportation of materials and humans in various industries. Examples of robot application include domestic purpose socially active mobile robots, military war robots, fire fighting robot and agricultural robots. These robots can be autonomous or operated manually through operators (or teleoperated). Fully autonomous robots usually face challenges like sensor failures, unable to see the real scenario, which can lead to incorrect data and information, and operational issues. In case of image processing, the images could be unclear or similar in colour, affecting obstacle avoidance. On the other hand, teleoperated robots can suffer from time delays and range limitations, leading to loss of control that can create the disastrous situation.

To solve these issues, a collaborative control approach was implemented in the research, combining both manual and autonomous control. If a sensor or image processing system gets fail, the human operator can take over, while the robot's intelligence assists if the operator lacks expertise.

There are certain limitation in the collaborative control mode. Dynamic obstacles can create problem; for instance, if a fast-moving obstacle approaches the robot, a collision might be unavoidable despite maximum acceleration or steering adjustments (tested in the simulation). Solving these issues requires collision probabilities evaluation and dependent planning accordingly. The current research uses basic equation of motion to predict robot and obstacle positions. Future work can include factors like maximum acceleration, skidding, and smooth velocity changes for improved performance. Further experimentation and research can help compare autonomous, manual, and collaborative modes, to show that collaborative control often results in fewer collisions with the reduced travel time.

ACKNOWLEDGEMENTS

I would like to express my deepest gratitude to ALMIGHTY ALLAH for bestowing us with the capability to complete this project. My heartfelt thanks go to my supervisor, Dr. Mohsin Rizwan, Associate Professor, UET Lahore for his invaluable guidance and support. I also appreciate my colleagues at UET Taxila, especially Engr. Muhammad Asif, for their encouragement and advice. Lastly, I am profoundly grateful to my family for their unwavering support.

REFERENCES

1. S. Mehrdad, F. Liu, M. T. Pham, A. Lelevé, and S. Farokh Atashzar, "Review of advanced medical telerobots," *Appl. Sci.*, vol. 11, no. 1, pp. 1–47, 2021, doi: 10.3390/app11010209.
2. M. Shahbazi, S. F. Atashzar, and R. V. Patel, "A Systematic Review of Multilateral Teleoperation Systems," *IEEE Trans. Haptics*, vol. 11, no. 3, pp. 338–356, 2018, doi: 10.1109/TOH.2018.2818134.
3. A. Peretti, F. Amenta, S. K. Tayebati, G. Nittari, and S. S. Mahdi, "Telerehabilitation: Review of the state-of-the-art and areas of application," *JMIR Rehabil. Assist. Technol.*, vol. 4, no. 2, pp. 1–9, 2017, doi: 10.2196/rehab.7511.
4. P. Gonzalez-De-Santos, R. Fernández, D. Sepúlveda, E. Navas, L. Emmi, and M. Armada, "Field robots for intelligent farms—inhering features from industry," *Agronomy*, vol. 10, no. 11, 2020, doi: 10.3390/agronomy10111638.
5. R. Smith, E. Cucco, and C. Fairbairn, "Robotic development for the nuclear environment: Challenges and strategy," *Robotics*, vol. 9, no. 4, pp. 1–16, 2020, doi: 10.3390/robotics9040094.
6. J. M. Beer and L. Takayama, "Mobile remote presence systems for older adults," pp. 19–26, 2011, doi: 10.1145/1957656.1957665.
7. K. Dautenhahn, S. Woods, C. Kaouri, M. L. Walters, K. L. Koay, and I. Werry, "What is a robot companion - Friend, assistant or butler?," *2005 IEEE/RSJ Int. Conf. Intell. Robot. Syst. IROS*, pp. 1488–1493, 2005, doi: 10.1109/IROS.2005.1545189.
8. C. D. Kidd, W. Taggart, and S. Turkle, "A sociable robot to encourage social interaction among the elderly," *Proc. - IEEE Int. Conf. Robot. Autom.*, vol. 2006, no. January 2006, pp. 3972–3976, 2006, doi: 10.1109/ROBOT.2006.1642311.
9. K. Berntorp and K. Berntorp, "(handig voor motion planning en variational methods) Path Planning and Integrated Collision Avoidance for Autonomous Vehicles," 2017, [Online]. Available: <http://www.merl.com>
10. S. Glaser, L. Nouveliere, S. Glaser, B. Vanholme, S. Mammam, and D. Gruyer, "Maneuver-Based Trajectory Planning for Highly Autonomous Vehicles on Real Road With Traffic and Driver Interaction. Said Mammam Université d'Évry-Val-d'Essonne Maneuver based trajectory planning for highly autonomous vehicles on real road with traffic and driver interaction," *Ieee Trans. Intell. Transp. Syst.*, p. 1, 2010, [Online]. Available: <https://www.researchgate.net/publication/220109062>



11. D. G. MacHaret and D. A. Florencio, "A collaborative control system for telepresence robots," *IEEE Int. Conf. Intell. Robot. Syst.*, pp. 5105–5111, 2012, doi: 10.1109/IROS.2012.6385705.
12. K. Katona, H. A. Neamah, and P. Korondi, "Obstacle Avoidance and Path Planning Methods for Autonomous Navigation of Mobile Robot," *Sensors*, vol. 24, no. 11, 2024, doi: 10.3390/s24113573.
13. K. F. Tang SH and K. W. Zulkifli N, "A Review on Motion Planning and Obstacle Avoidance Approaches in Dynamic Environments," *Adv. Robot. Autom.*, vol. 04, no. 02, 2015, doi: 10.4172/2168-9695.1000134.
14. N. Adiuku, N. P. Avdelidis, G. Tang, and A. Plastropoulos, "Improved Hybrid Model for Obstacle Detection and Avoidance in Robot Operating System Framework (Rapidly Exploring Random Tree and Dynamic Windows Approach)," *Sensors*, vol. 24, no. 7, 2024, doi: 10.3390/s24072262.
15. J. Wei and J. M. Dolan, "A multi-level collaborative driving framework for autonomous vehicles," *Proc. - IEEE Int. Work. Robot Hum. Interact. Commun.*, pp. 40–45, 2009, doi: 10.1109/ROMAN.2009.5326205.
16. J. Luo, Z. Lin, Y. Li, and C. Yang, "A Teleoperation Framework for Mobile Robots Based on Shared Control," *IEEE Robot. Autom. Lett.*, vol. 5, no. 2, pp. 377–384, 2020, doi: 10.1109/LRA.2019.2959442.
17. Y. Deldjoo, *Enhancing Video Recommendation Using Multimedia Content*. 2020. doi: 10.1007/978-3-030-32094-2_6.

Performance Analysis of V-Trough Concentrators

Amnah Kamran¹, Azan Ijaz Yousufzai¹, Ubaid Ur Rehman¹, Ibrahim Raza¹ Mumtaz A. Qaisrani^{1,*}, Muhammad Umar Farooq¹, Muhammad Khalid²

¹Institute of Mechanical and Manufacturing Engineering, Khwaja Fareed University of Engineering and Information Technology, Rahim Yar Khan, Pakistan.

²Balochistan University of Information Technology, Engineering and Management Sciences, Quetta, Pakistan.

* mumtazqaisrani@yahoo.com

ABSTRACT

This research endeavor holds immense importance, particularly in regions like Pakistan, where the energy crisis presents formidable obstacles to both economic progress and daily existence. Our study explores the performance of monocrystalline solar panels with V-trough concentrators made of simple reflective mirrors. A comprehensive CAD model was simulated in Trace Pro for advanced ray tracing. The cooling system, designed with copper tubes arranged in a spiral pattern beneath the panel, enhances heat dissipation. Experiments measured surface temperature and electrical output under varying solar irradiance conditions. Results indicated that panels with V-trough concentrators experienced significantly higher surface temperatures, particularly during peak sunlight hours, resulting in an electrical output increased by up to 20% as compared to those without the trough. Theoretical efficiency was calculated at 92%, practical efficiency was 35% due to heat and other losses. Effective thermal management is essential to mitigate overheating risks and optimize overall system performance, highlighting the importance of balancing enhanced solar concentration benefits with thermal regulation.

KEYWORDS: Solar Energy, V-Trough Concentrators, Monocrystalline Solar Panels, Renewable Energy Efficiency, Energy Crisis Solutions.

1. INTRODUCTION

Humans have a long history of harnessing solar energy in different forms for varying reasons [1]. Now that we're entering 21st century, it is visible that the energy landscape is facing multiple challenges, in third world countries such as ours, where an energy crisis alters progress and development. Pakistan struggles with heavy power shortages, and increasing energy costs, that affect economic stability, industrial advancements, and our routine lives. The crisis also awakens social and environmental issues, because of their reliance on fossil fuels. However, solar energy offers a promising solution. Pakistan has significant solar potential having required sunlight and an average daily solar irradiance of 5.5 kWh/m². [2] Effective harnessing of solar energy can provide a sustainable energy source.

Photovoltaic modules are extensively employed to avoid fossil dependence, yet their deployment is hindered by the challenge of low solar intensity, primarily due to the accumulated heat generated during operation [3]. The primary focus revolves around enhancing the efficiency of harnessing solar energy, given its renewable nature [4]. It is believed that V-trough concentrators can significantly increase the amount of sunlight incident on solar panels, increasing electrical output.

The primary objective of our research is to increase the electrical output of solar panels by using V-trough concentrators made of simple reflective mirrors, in order to overcome the traditional limitations of solar power conversion. By investigating both electrical and thermal

aspects, we find a balance between maximizing energy output and managing excess heat to improve overall system performance.

We have introduced a novel approach by integrating simple V-trough concentrators with an innovative spiral-patterned cooling system beneath solar panels. This combination is designed to enhance solar concentration while mitigating the associated thermal losses. Unlike conventional methods, we have used advanced ray tracing simulations in TracePro to find the optimal angle for maximum solar concentration. This theoretical modeling helps guide the experimental setup for real-world application.

V-trough concentrators enhance radiation for higher thermal system temperatures [5]. This makes them a cost-effective solution for improving overall system efficiency without needing precise sun-tracking mechanisms. V-troughs boost energy yield by 86% annually versus flat-plate systems [6]. Their geometric configuration offers flexibility for optimized performance, enhancing both energy capture and heat dissipation for reliable long-term use. Despite weak dependence on vertex angle, cost-benefit analysis may favor larger trough angles for a given concentration ratio [7]. Cheaper flat-plate technology is key to a significant reduction in PV energy costs [8].

Shaltout et al. (1995) optimized the V-trough concentrator design for solar modules using ray tracing in OptisWorks, achieving a concentration ratio of 1.6. This design is effective, affordable, and easy to construct [9]. Al-Shohani et al. (2016) investigated vertex angles to achieve the highest concentration ratio, minimal irradiance non-uniformity, and lower reflector slant height, considering

reflective materials and different concentration ratios in their simulations [10]. Künemeyer et al. (2014) analyze V-trough concentrators using mean reflections and angular acceptance to approximate optical efficiency. For concentration ratios (C) ≤ 2.5 , the errors are less than 2% for diffuse radiation and 3.4% for beam radiation. A simpler method yields reliable results with a 5% error margin for diffuse radiation. Increasing the concentration ratio from 0.74 to 0.59 decreases optical efficiency for a one-third vertex angle, converting solar energy into both heat and electrical energy [11].

Therefore, our research addresses the need for an integrated approach that combines the optimization of V-trough concentrators with effective thermal management solutions. It also aims to bridge the gap between theoretical simulations and experimental validations, providing a comprehensive understanding of the practical efficiency of concentrated solar power systems.

2. METHODOLOGY

The system is built around V-trough concentrators on a sturdy panel framework, as sunlight hits the PV cells, it generates heat, which is efficiently managed by a sophisticated thermal system. This system uses circulating water, a network of pipelines, a high-performance pump, and a strategically placed water tank to capture and transfer heat, maximizing efficiency.

Thus, an extension of this concept is illustrated in Figure. This modification aims to further optimize the collection and concentration of sunlight onto the photovoltaic cells, thereby enhancing the overall efficiency and performance of the system.

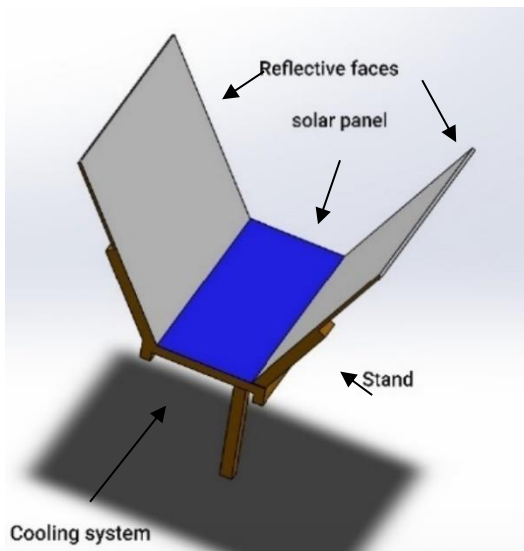


Figure 1: A panel with V trough concentrators showcasing proper arrangements

Theoretical analysis of V-trough concentrator

The V-trough photovoltaic absorber was inclined at 28.4 degrees, matching the local latitude, to maximize solar energy collection year-round. To adapt to seasonal solar declination, V-troughs were designed with a half-angle of 25 degrees, ensuring consistent sunlight capture.

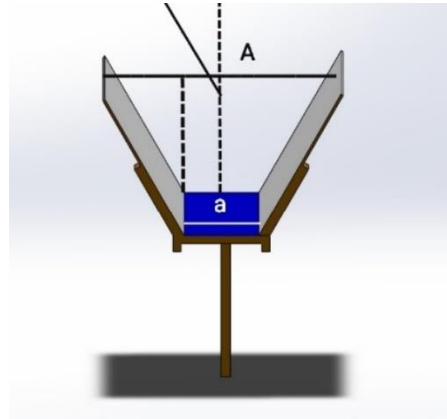


Figure 2: V-trough cross-section

A concentration ratio of 2.36, as shown in Figure, optimizes solar energy collection, ensuring the absorber receives maximum sunlight while minimizing energy losses.

The concentration ratio directly influences the efficiency and performance of the system.

$$\frac{A}{a} = 2.36 \quad (1)$$

where, (A) is aperture area and (a) trough area showing the concentration ratio.

$$P_o = \begin{cases} \frac{1}{C} + \frac{C-1 \sin(-|\theta_i| + \varphi)}{2C \cos\theta_i \sin\varphi}, & \varphi < |\theta_i| \leq \alpha_o \\ \frac{1}{C'}, & |\theta_i| \leq \varphi \\ 0, & \text{otherwise} \end{cases} \quad (2)$$

where, (P_o) is proportion of radiation directly reaching the absorber at the trough's base without reflection, θ_i the angle of the incident radiation with respect to the trough normal and φ is V-trough half angle.

$$P_R = \begin{cases} \frac{C-1 \sin(\theta_i + \varphi)}{2C \cos\theta_i \sin\varphi}, & -\varphi \leq \theta_i \leq \alpha_2 \\ \frac{\cos(\theta_i + 2\varphi)}{C \cos\theta_i}, & \alpha_2 < \theta_i \leq \alpha_o \\ 0, & \text{otherwise} \end{cases} \quad (3)$$

$$P_L(\theta_i) = P_R(-\theta_i) \quad (4)$$

where, (P_R) is proportion of reflected radiation that reaches the absorber from the right-hand wall and (P_L) is from the left-hand wall.

Formulae for acceptance angles are taken from this reference [11]

To evaluate thermal performance of V-trough, a one-dimensional steady-state thermal model for an unglazed solar collector was used.

$$Q_t = AF_R[(\tau\alpha) \cdot G'' - U_L(T_i - T_a)] \quad (5)$$

where, (Q_t) is heat gain, (A) is collector area, (F_R) is heat removal efficiency factor, ($\tau\alpha$) is transmittance-absorptance of collector (G'') is solar irradiance, (U_L) is collector heat loss coefficient and (T_i) is inlet temperature while (T_a) is ambient temperature.

Equations for the remaining parameters are adapted from this reference [11]

$$\eta_e = 0.145[1 - 0.045(T_{pm} - NOCT)] \quad (6)$$

Electrical output can be given by,

$$Q_e = \eta_e AG'' \quad (7)$$

Overall efficiency is given by the ratio between energy gain to solar irradiance falling on the absorber area Q/AG''

To determine total heat gain

$$Q = Q_t - U_{loss} \quad (8)$$

where, U_{loss} is the sum of U_{Top} and U_{Back}

Coefficient of radiation

$$h_r = \sigma \epsilon_p (T_{pm}^2 + T_s^2)(T_{pm} + T_s) \quad (9)$$

where, (h_r) is radiation heat transfer coefficient (T_s) is sky temperature and (T_{pm}) is mean collector plate temperature, the plate emissivity (ϵ_p), and the Stefan-Boltzman constant (σ)

$$T_s = 0.037536T_a^{1.5} + 0.32T_a \quad (10)$$

Additionally, it is essential to consider losses from both natural and forced convection.

Heat transfer coefficient (h_c)

$$h_c = (h_w^3 + h_{nat}^3)^{\frac{1}{3}} \quad (11)$$

Heat transfer coefficients (h_w) and h_{nat} could be determined using by this reference [11].

We can calculate the overall top loss heat transfer coefficient (U_{Top}) for the unglazed collector by considering both convection and radiation losses together.

Thus, the back loss (U_{Back}) can also be expressed using equation. Therefore, the overall heat loss coefficient (U_{loss}) for the collector can be determined by summing the top (U_{Top}) and back (U_{Back}) losses.

Experimental analysis of V-trough concentrators

Experimental thermal efficiency can be represented by,

$$\eta_{th} = \frac{Q_c}{AG''} \quad (12)$$

$$Q_c = \dot{m}C_p(T_i - T_o) \quad (13)$$

where, T_i is water inlet temperature and T_o is water outlet temperature.

Experimental electrical efficiency is shown as

$$\eta_{el} = \frac{P}{AG''} \quad (14)$$

where, P is the power output obtained experimentally while A is area and G'' is irradiance

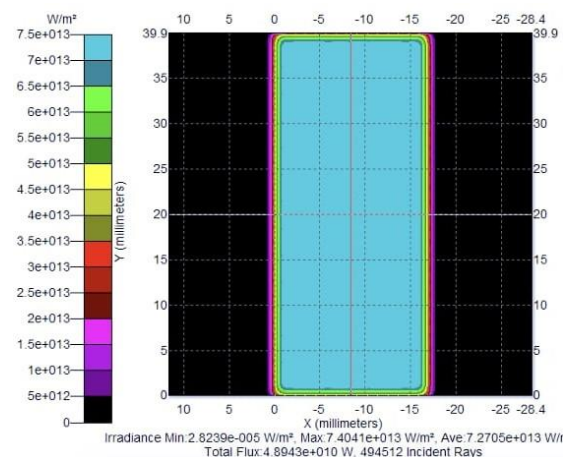
Overall experimental efficiency

$$\eta_{PV} = \eta_{el} + \eta_{th} \quad (15)$$

Ray Tracing

A CAD model was then imported into TracePro for advanced ray tracing simulations, which meticulously traced light rays' interactions within the system.

The reflective trough surfaces direct radiation towards each other, ensuring convergence onto the absorber. This behavior is governed by the acceptance angle (α_o), which depends on the panel's dimensions. A wider panel reduces this angle, while a narrower one increases it, with a calculated value of approximately 71.56 degrees. The spectrum graph reveals color-coded regions indicating varying radiation absorption levels, with blue showing maximum absorption and purple showing minimum. Notably, these regions extend no more than 5mm from the panel edges. The accompanying line graph shows that horizontally incident rays (blue line) remain consistent, while vertically incident rays (green line) vary, with vertical radiation diminishing towards the edges.



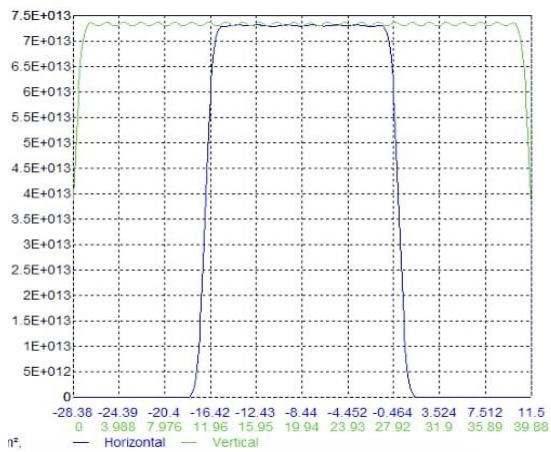


Figure 3: Simulation using TracePro was conducted to determine the optimal angle for maximizing the number of incident ray. Graph obtained in response of ray tracing

Experimental Setup

The setup includes a monocrystalline PV panel with simple reflective mirrors in a V-trough configuration for sunlight concentration. In our investigation, we explored various options for reflective materials, visiting local stores to identify suitable candidates. The most readily available and effective material we found were mirrors made of transparent glass plates with a thin reflective silver layer on the back. They have a reflectivity of 85%, making them the most efficient for this application. The thickness of the mirrors was 5mm, providing a balance between structural integrity and optical performance.

This material selection impacts the optical efficiency of the V-trough concentrators, as the high reflectivity of silver allows for greater concentration of sunlight onto the photovoltaic cells.

Beneath the panel, a cooling system with copper tubes arranged in a spiral pattern effectively dissipates heat. The V-trough mirrors focus sunlight onto the PV panel, enhancing efficiency. The cooling system, using water flowing through copper tubes, maintains optimal panel temperatures, preventing overheating and maximizing energy conversion.

3. RESULTS

To evaluate effectiveness, we conducted a series of experiments comparing the electrical output and temperature of solar panels with and without V-trough concentrators. The experiments were designed to measure the efficiency gains and thermal behavior under controlled conditions. Readings were taken for both configurations over a period of four days, from 6:00 AM to 6:00 PM.

Once the mathematical description of the concentration ratio was developed, it was decided to validate it against experimental results.



Figure 4: Experimental setup

Comparative analysis of panels with and without V-trough in Figure concentrators reveal stark differences in thermal behavior. Panels lacking V-troughs show a predictable diurnal temperature pattern, while panels with it exhibit significantly higher temperatures, especially from noon to early afternoon, they also demonstrate markedly higher voltage outputs as illustrated in Figure during peak sunlight hours, showcasing the concentrators' effectiveness in intensifying solar radiation.

In Figure panels without V-troughs follow a diurnal current pattern, while those with V-trough show boosted midday currents underscoring their role in enhancing solar energy capture. Advanced concentrator technologies can optimize photovoltaic efficiency, meeting higher energy demands effectively. Those with V-trough exhibit enhanced power outputs as seen in Figure, peaking consistently higher during midday compared to panels without concentrators. This highlights the concentrators' effectiveness in maximizing solar energy capture and improving overall energy yield. However, managing increased heat from higher solar radiation is crucial, emphasizing the need for effective thermal management strategies.

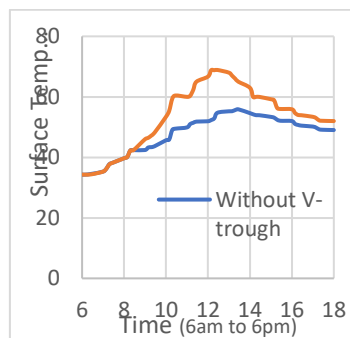


Figure 5: Surface temperature: With vs Without V-trough

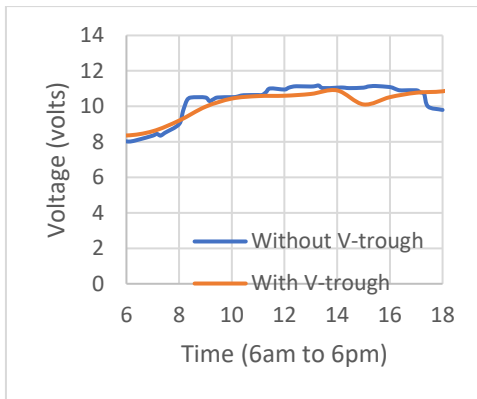


Figure 6: Voltage: With vs Without V-trough

In Figure inclusion of V-trough concentrators led to a 20% increase in electrical output compared to panels without concentrators. This increase aligns with the primary purpose of the V-trough system, which is to concentrate sunlight onto the solar panel, thereby enhancing the incident solar radiation and boosting the electrical power generated.

However, the observed electrical efficiency was significantly lower than the calculated theoretical efficiency, the discrepancy arises from multiple factors such as; concentrating sunlight not only increases the electrical output but also raises the panel's surface temperature. Elevated temperatures adversely affect the performance of solar cells, reducing their conversion efficiency. Although the V-troughs are designed to maximize light concentration, not all incident rays are perfectly directed onto the absorber.

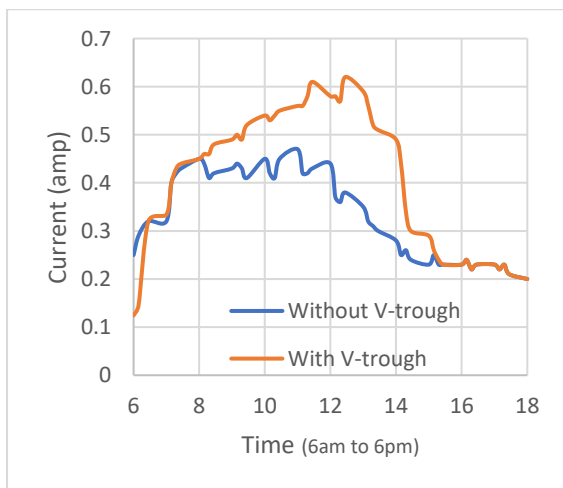


Figure 7: Current: With vs Without V-trough

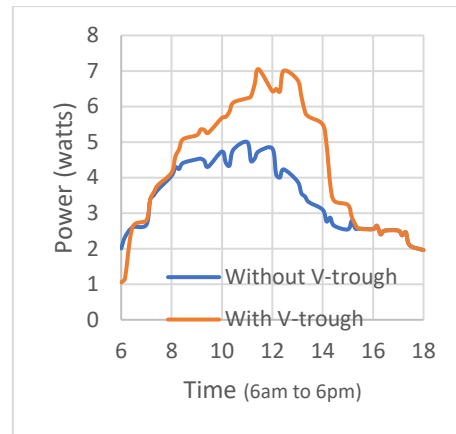


Figure 8: Power: With vs Without V-trough

Some rays may undergo multiple reflections within the trough and eventually escape or scatter, contributing to optical losses. This effect reduces the actual sunlight reaching the panel, thereby affecting the electrical output. The efficiency graph in Figure for solar concentrators typically peaks around midday reflecting sunlight intensity and system performance. The overall theoretical efficiency was calculated at 92%, assuming near-perfect energy concentration and conversion. However, the practical overall efficiency was much lower, at 35%. The overall efficiency accounts not just for the electrical output but also for the thermal losses within the system.

While V-trough concentrators significantly enhance electrical output by focusing more sunlight on the panel, they also introduce challenges related to heat buildup. The findings underscore the need for more effective cooling strategies, such as improved heat exchangers or phase-change materials, to mitigate thermal losses and optimize overall system performance.

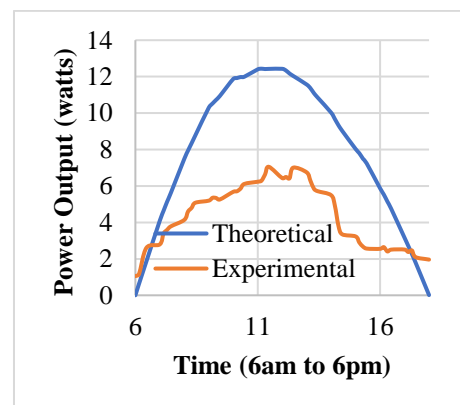


Figure 9: Experimental and theoretical electrical output of concentrator

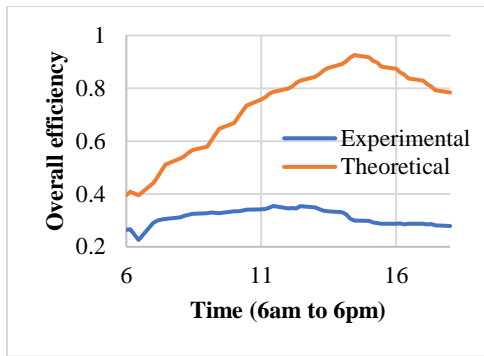


Figure 10: Overall efficiency

4. CONCLUSION

The study showed that the V-trough concentrator affects both thermal and electrical performance of monocrystalline solar panels. With the concentrator, the panel produced 4 watts, compared to 5 watts without it. The theoretical efficiency was 92%, but the actual efficiency was 35%, highlighting significant losses due to heat and other factors. Effective thermal management is essential to improve efficiency and longevity of solar panels with V-trough concentrators.

Future research in solar concentrator technology should focus on improving material robustness and thermal management to enhance efficiency and reliability. Interdisciplinary efforts in materials science and electrical engineering will drive innovations for more sustainable solutions. Addressing these challenges can significantly advance global renewable energy goals.

ACKNOWLEDGEMENTS

We are grateful to our mothers for their unwavering support, and the Department of Mechanical Engineering for providing a conducive research environment.

REFERENCES

1. M. Taguchi, A. Suzuki, N. Ueoka, and T. Oku, "Effects of poly(methyl methacrylate) addition to perovskite photovoltaic devices," *AIP Conf Proc*, vol. 2067, 2019, doi: 10.1063/1.5089451.
2. S. Orangezab et al., "Potential Assessment and Economic Analysis of Concentrated Solar Power against Solar Photovoltaic Technology," *Int J Energy Res*, vol. 2023, pp. 1–26, Jun. 2023, doi: 10.1155/2023/3611318.
3. Y. Wang, G. Xia, R. Li, Q. Li, and Z. Yan, "Heat transfer enhancement in porous wall mini-channel heat sinks utilizing electric field: An experimental study," *Int J Heat Mass Transf*, vol. 203, p. 123803, Apr. 2023, doi: 10.1016/J.IJHEATMASSTRANSFER.2022.123803.
4. N. Zhao et al., "Experimental analysis of the optical loss of a dusty Fresnel lens with a novel solar flux test system," *Sustainable Energy Technologies and Assessments*, vol. 48, p. 101656, Dec. 2021, doi: 10.1016/J.SETA.2021.101656.
5. T. N. Anderson, "Natural convection heat transfer in V-trough solar concentrators," *Solar Energy*, vol. 95, pp. 224–228, Sep. 2013, doi: 10.1016/J.SOLENER.2013.06.022.
6. F. Reis, M. C. Brito, V. Corregidor, J. Wemans, and G. Sorasio, "Modeling the performance of low concentration photovoltaic systems," *Solar Energy Materials and Solar Cells*, vol. 94, no. 7, pp. 1222–1226, Jul. 2010, doi: 10.1016/j.solmat.2010.03.010.
7. N. Fraidenraich and G. J. Almeida, "Optical properties of V-trough concentrators," *Solar Energy*, vol. 47, no. 3, pp. 147–155, Jan. 1991, doi: 10.1016/0038-092X(91)90073-6.
8. S. Nann, "Potentials for tracking photovoltaic systems and V-troughs in moderate climates," *Solar Energy*, vol. 45, no. 6, pp. 385–393, Jan. 1990, doi: 10.1016/0038-092X(90)90160-E.
9. M. A. M. Shaltout, A. Ghetas, and M. Sabry, "V-trough concentrator on a photovoltaic full tracking system in a hot desert climate," *Renew Energy*, vol. 6, no. 5–6, pp. 527–532, Jul. 1995, doi: 10.1016/0960-1481(95)00055-O.
10. W. A. M. Al-Shohani, R. Al-Dadah, S. Mahmoud, and A. Algareu, "Optimum design of V-trough concentrator for photovoltaic applications," *Solar Energy*, vol. 140, pp. 241–254, Dec. 2016, doi: 10.1016/J.SOLENER.2016.11.012.
11. R. Künnemeyer, T. N. Anderson, M. Duke, and J. K. Carson, "Performance of a V-trough photovoltaic/thermal concentrator," *Solar Energy*, vol. 101, pp. 19–27, Mar. 2014, doi: 10.1016/J.SOLENER.2013.11.024.



Experimental Comparative Investigation of EGR and Water Injection for Lean and Rich Combustion in Turbocharged Diesel Engine

Asad Asghar Janjua¹, Waqas Khalid¹, Samiur Rahman Shah¹, Xavier Tauzia²

¹School of Mechanical & Manufacturing Engineering, National University of Sciences & Technology, Islamabad, Pakistan

²Ecole Centrale de Nantes, France

*asadasghar.phd@smme.edu.pk

ABSTRACT

Emission reduction in diesel engines is crucial due to their widespread use and environmental impact. Exhaust Gas Recirculation (EGR) and Water Injection (WI) are used for emission reduction. This study compares the efficacy of Low-Pressure Exhaust Gas Recirculation (LP-EGR) and Indirect Water Injection (IWI) in modifying combustion modes, focusing on lean and rich combustion using lambda values. A high-speed, turbocharged automotive diesel engine, fitted with an indirect water injection system, was tested under three distinct speed and loading (operating) conditions, with a total of 20 different rates of water injection and EGR for each condition. WI resulted in lambda value decreases of 5%, 3%, and 3% for respective operating conditions, while EGR showed more significant decreases of 43%, 27%, and 18%. Both methods showed lower reductions in lambda values at higher speeds, but EGR consistently led to richer combustion over the entire range of operating conditions. The study concluded that WI better maintains lean combustion, making it a more favorable option for sustaining leaner combustion modes in high-speed automotive diesel engines.

KEYWORDS: Diesel Engine, Indirect Water Injection, Low-Pressure Exhaust Gas Recirculation, Lean Combustion, Rich Combustion, Lambda

1. INTRODUCTION

The automotive sector will continue to rely on high-speed diesel engines with modern modifications to meet environmental standards and customer needs [1-4]. Diesel engines are preferred by manufacturers and customers for their efficient speed-torque characteristics, lower fuel consumption, and reduced carbon emissions [5-6]. These targets are achieved by maintaining lean combustion in diesel engines [7]. Therefore, the effectiveness of any new modification in a diesel engine can be gauged by its ability to maintain lean combustion.

Exhaust Gas Recirculation (EGR) is one of the most widely used techniques to reduce exhaust emissions in diesel engines. EGR recirculates a portion of the exhaust gas back into the engine cylinders, diluting the incoming air. This reduces the available oxygen for combustion and lowers the combustion temperature, thereby inhibiting the formation of NO_x, which mainly occurs at high temperatures due to the reaction between nitrogen and oxygen in the air. Besides NO_x reduction, EGR also reduces engine knocking by promoting a more uniform burn of the air-fuel mixture [8-11]. There are two main types of EGR systems which are high-pressure EGR (HP-EGR) and low-pressure EGR (LP-EGR). HP-EGR takes exhaust gas before the turbocharger and reintroduces it at high pressure. LP-EGR takes exhaust gas after the turbocharger, reintroducing it at lower pressure [12].

Water injection is an innovative technique developed to reduce NO_x emissions in diesel engines. This approach involves injecting water to mix with the inlet air in order to lower the combustion temperatures. This cooling effect reduces NO_x formation. Moreover, water injection can mitigate the risk of engine knocking and pre-ignition [13-15].

There are two main types of water injection systems which are direct and indirect injection. Direct Water Injection (DWI) delivers water straight into the combustion chamber. In contrast, Indirect Water Injection (IWI) mixes water with the inlet air before it enters the combustion chamber, ensuring a more uniform distribution of water vapor [16]. Although the advantages of water injection are significant, the technology is still under research and development.

As both EGR and water injection (WI) are utilized to reduce NO_x emissions in diesel engines, comparing their effectiveness can be insightful, particularly in their ability to maintain lean combustion. Diesel engines typically operate on lean combustion, which is essential for fuel efficiency and reducing carbon emissions. Therefore, assessing the performance of EGR and WI can be effectively done by comparing their impacts on lambda values.

The lambda value (λ) is a measure of the air-fuel ratio relative to the stoichiometric mixture, where $\lambda = 1$ indicates the ideal stoichiometric ratio. When $\lambda > 1$, the combustion is lean, meaning there is excess air compared

to fuel, which is desired for diesel engines. Conversely, when $\lambda < 1$, the combustion is rich, indicating a higher proportion of fuel to air, which can lead to increased emissions and decreased fuel efficiency [17]. By analysing how EGR and WI influence lambda values under various operating conditions, we can determine which method better sustains lean combustion, thereby optimizing the diesel engine's performance and emission characteristics. This comparative study on the impact of EGR and WI on lambda values in diesel engines, focusing on their ability to maintain lean combustion, has not been conducted before, making this research a novel contribution to the field.

2. EXPERIMENTATION

In this study, a test-bed mounted turbocharged automobile diesel engine was tested through speed and load variations using a dynamometer of eddy current type. The engine was installed with an LP-EGR and IWI systems that can run independently. Both installed systems have the ability to vary EGR and WI levels. The same system has also been utilized previously in similar researches [18]. The detailed engine parameters and their quantities are represented in Table 1. The line diagram and actual testbed settings are shown in the Figures 1 and 2 respectively.

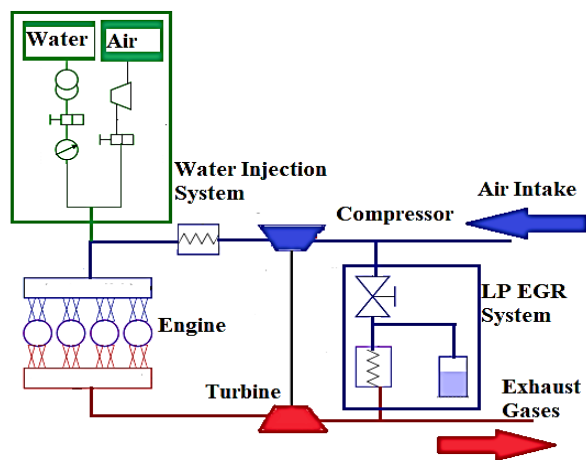


Figure 1: Line Diagram of Testbed

Table 1: Engine Parameters

Engine Parameter	Parameter Quantity
Engine Size	1.998 L
Cylinders	04
Bore and Stroke	85 mm and 88 mm
Compression	18
Engine Speed Range	750 to 5100 rpm
Max Power	100 kW
Max Torque	320 Nm
Turbine Type	Variable Geometry

WI Pressure	6 bars
-------------	--------

The study conducted experimentation on three tests named as Test-A, B, and C respectively. Each test was assigned an operating speed and torque setting accompanied with variable EGR (measured in percentage) and WI (measured in kg/hr) levels. The lambda values were measured at each test for every EGR and WI level. The lambda values were measured using real-time air and fuel flow measurements as a ratio between actual air-fuel ratio and stoichiometric air-fuel ratio.

Table 2: Speed and Torque Settings

Test	Test-A	Test-B	Test-C
Speed (rpm)	1510	1662	1996
Torque (Nm)	44	114	198

At the start of each test, the value of lambda was measured with zero EGR and WI level at designated speed and torque settings. Thereafter, successive levels of EGR were added and lambda values were measured. Similarly, lambda values were measured using varying WI levels. The speed and torque settings for all three tests are shown in Table 2 while EGR and WI levels at corresponding tests are tabulated in the Table 3.

Table 3: WI and EGR levels at each Test

Test-A	WI (kg/hr)	EGR (%)
	0	0
	3.12	6.85
	4.36	15.68
	5.69	24.26
	5.79	31.25
	7.47	39.23
	9.12	45.10
Test-B	WI (kg/hr)	EGR (%)
	0	0
	3.28	1.14
	5.15	1.86
	7.13	2.70
	8.89	3.39
10.48	4.26	
Test-C	WI (kg/hr)	EGR (%)
	0	0
	3.22	3.48
	4.95	7.64
	7.36	11.54
	9.05	13.42
	13.12	16.34
16.96	17.73	

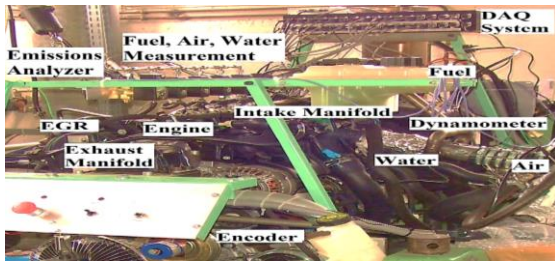


Figure 2: Actual Testbed Picture

3. RESULTS AND DISCUSSION

The results for Test-A are shown in the Figure 3. The results indicate that variation in WI did not influence the lambda values which only changed from 3.15 to 3.01 over entire WI level from zero to 9.12 kg/hr which indicates that combustion remains lean. Whereas, lambda values show a considerable decrease from 3.15 to 1.80 over entire EGR level from zero to 45.10% which shows that although combustion remains lean but the overall behaviour of the combustion has moved towards the richer side. This indicates that WI is better at maintaining the leaner combustion of the diesel engine than EGR.

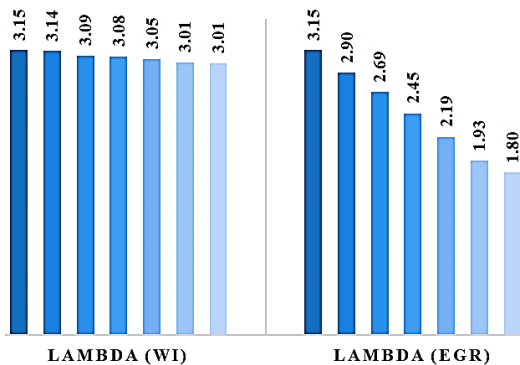


Figure 3: Test-A results for Lambda values

The results for Test-B are shown in the Figure 4. The results show that lambda values remain almost constant for the entire range of WI from zero to 10.48 kg/hr. The lambda values changed from 1.54 to 1.50 only which means that WI has maintained the leaner operation of the diesel engine. In comparison to WI, the value of lambda has shown a decrease from 1.54 to 1.13 when EGR is applied from 0 to 4.26% which indicates the overcoming of richer operation with the use of EGR.

The results for Test-C are shown in the Figure 5. The results again indicated that WI did not change the lambda values. The lambda values remained within the range of 1.33 to 1.30 for WI levels from zero to 16.96 kg/hr. This showed that leaner mode of operation of the diesel engine

was not affected by the use of WI. The lambda values showed the decrease from 1.33 to 1.09 for the EGR levels from 0 to 17.73% which again indicate that EGR tends to shift the diesel engine operation towards the richer side.

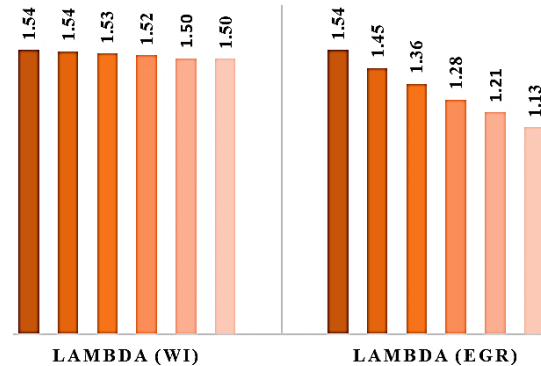


Figure 4: Test-B results for Lambda values

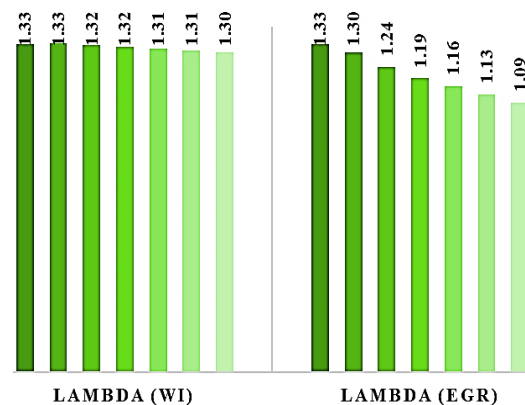


Figure 5: Test-C results for Lambda values

The percent change in the lambda values at all tests for WI and EGR are shown in the Table 4. The tabulated data shows that overall lambda values have decreased with the use of both WI and EGR. This shows that presence of water and exhaust gases in the air-fuel mixture do tend to reduce the amount of air molecules which reduces the actual air-fuel ratio.

But, this reduction in air molecules is very less when WI is used in comparison to the EGR. This is proved by the fact that lambda values have only reduced by 5, 3, and 3 % for all three tests with the use of WI whereas the lambda values have decreased in large amount i.e. 43, 27, and 18 % for all three sets with the use of EGR. The reason for this difference is that water makes a mist in the inlet manifold without greatly changing the quantity of inlet air molecules consequently maintaining the air quantity and leaner combustion. Whereas, EGR consists of compressed exhaust gases routed back to the inlet air manifold replacing the inlet air molecules in large quantity as

compared to the reduction caused by WI. Consequently, air quantity is reduced by EGR and combustion tends to shift towards richer behaviour.

Table 4: Percent Change in Lambda values

Test	Percent Change in Lambda for WI	Percent Change in Lambda for EGR
Test-A	-5%	-43%
Test-B	-3%	-27%
Test-C	-3%	-18%

4. CONCLUSION

The aim of this study was to conduct a comparative investigation on the use of EGR and WI in diesel engines. This comparison was decided upon the sustenance of the lean combustion of the diesel fuel. For this purpose, a test-bed installed diesel engine having independent LP-EGR and IWI systems was used. Three tests were conducted each having its own set speed and torque conditions. At each test, the EGR and WI levels were varied and corresponding lambda values were obtained. The lambda values for WI system showed an overall percent decrease of 5, 3, and 3 percent for each test respectively while for the EGR system, the percent decrease in the lambda values was 43, 27, and 18% respectively for each test. The experimental results concluded that WI tried to maintain the actual air-fuel ratio of the diesel engines during its operation which in-turn maintains the quantity of inlet air thus, maintaining the leaner combustion of the diesel engine. This further concludes that the WI system is more beneficial than EGR system due to its potential of sustaining the leaner combustion of diesel engine at same operating conditions.

REFERENCES

1. IJER Editorial, *The future of the internal combustion engine*. International Journal of Engine Research, 2019. **21:** 1–8. <https://doi.org/10.1177/1468087419877990>
2. Johnson, T. and A. Joshi, *Review of vehicle engine efficiency and emissions*. SAE International Journal of Engines, 2018. **11(6):** 1307–1330. <https://doi.org/10.4271/2018-01-0329>
3. A. Joshi, *Review of vehicle engine efficiency and emissions*. SAE Technical Papers, 2021. <https://doi.org/10.4271/2021-01-0575>
4. Crosignani, P., et al., *The effect of non-compliance of diesel vehicle emissions with euro limits on mortality in the city of Milan*. Atmosphere, 2021. **12:** 342. <https://doi.org/10.3390/atmos12030342>
5. Sahin, Z., M. Tuti, and O. Durgun, *Experimental investigation of the effects of water adding to the intake air on the engine performance and exhaust emissions in a DI automotive diesel engine*. Fuel, 2014. **115:** 884–895. <http://dx.doi.org/10.1016/j.fuel.2012.10.080>
6. Lu, X., et al., *Simultaneous reduction of NOx emission and smoke opacity of biodiesel-fueled engines by port injection of ethanol*. Fuel, 2008. **87:** 1289–1296. <http://doi:10.1016/j.fuel.2007.07.006>
7. Tsolakis, A., A. Megaritis, and M.L. Wyszynski, *Low temperature exhaust gas fuel reforming of diesel fuel*. Fuel, 2004. **83:** 1837–1845. <https://doi:10.1016/j.fuel.2004.03.012>
8. Maiboom, A., X. Tauzia, and J.F. Hetet, *Influence of EGR unequal distribution from cylinder to cylinder on NOx-PM trade-off of a HSDI automotive Diesel engine*. Applied Thermal Engineering, 2009. **29:** 2043–2050. <doi:10.1016/j.applthermaleng.2008.10.017>
9. Agrawal, A.K., et al., *Effect of EGR on the exhaust gas temperature and exhaust opacity in compression ignition engines*. Sadhana, 2004. **29(3):** 275–284.
10. Agarwal, D., S.K. Singh, and A.K. Agarwal, *Effect of Exhaust Gas Recirculation (EGR) on performance, emissions, deposits and durability of a constant speed compression ignition engine*. Applied Energy, 2011. **88:** 2900–2907. <doi:10.1016/j.apenergy.2011.01.066>
11. Maiboom, A., X. Tauzia, and J.F. Hetet, *Experimental study of various effects of exhaust gas recirculation (EGR) on combustion and emissions of an automotive direct injection diesel engine*. Energy, 2008. **33:** 22–34. <doi:10.1016/j.energy.2007.08.010>
12. Zheng, M., G.T. Reader, and J.G. Hawley, *Diesel engine exhaust gas recirculation – a review on advanced and novel concepts*. Energy Conversion and Management, 2004. **45:** 883–900. [https://doi:10.1016/S0196-8904\(03\)00194-8](https://doi:10.1016/S0196-8904(03)00194-8)
13. Shah, S.R., et al., *Experimental study of Inlet Manifold Water Injection on a Common Rail HSDI automobile Diesel Engine, compared to EGR with respect to PM and NOx Emissions and Specific Consumption*. SAE Technical Paper, 2009. **2009-01-1439**. <https://doi.org/10.4271/2009-01-1439>
14. Tauzia, X., A. Maiboom, and S.R. Shah, *Experimental study of inlet manifold water injection on combustion and emissions of an automotive direct injection Diesel engine*. Energy, 2010. **35:** 3628e3639. <doi:10.1016/j.energy.2010.05.007>



First International Conference on Advances in Mechanical, Materials, Mechatronics, and Energy Engineering (ICAME-24)



15. Zhu, S., et al., *A review of water injection applied on the internal combustion engine*. Energy Conversion and Management, 2019. **184**: 139–158. <https://doi.org/10.1016/j.enconman.2019.01.042>
16. Janjua, A.A., et al., *Simplistic Comparative Analytical Methodology for Accuracy Determination of In-Cylinder Convective Heat Transfer Coefficient Models of Diesel Engine Operating with Water Injection using Experimental Pressure Signals*. Arabian Journal for Science and Engineering, 2023. **48**: 12177-12190. <https://doi.org/10.1007/s13369-023-07627-w>
17. Heywood, J.B., *Internal Combustion Engine Fundamentals*, Indian ed. McGraw Hill Education (India) Private Limited, New Delhi, India, 2011. p. 68–72.
18. Shah, S., *Experimental study and Thermodynamical analysis of water injection in the intake manifold of an automotive Diesel Engine, for pollutant emission reduction*. PhD Thesis, Ecole Centrale de Nantes, France, 2011.



Experimental Investigation of Mechanical Properties of Biodegradable Polymer Composite for Artificial Orthopedic Implants

Muhammad Faisal¹, Zulkarnain Abbas^{1,*}, Saqlain Abbas², Maryam Fatima³,

¹Department of Mechanical Engineering, National Fertilizer Corporation (NFC), Institute of Engineering and Technology, Multan, Pakistan

²Department of Mechanical Engineering, University of Engineering and Technology Lahore, Narowal Campus, Pakistan

³Allied Health Department, Bakhtawar Amin Medical and Dental College Multan, Pakistan

* zulkarnain@nfciet.edu.pk

ABSTRACT

Poly(lactic acid) (PLA) is a biodegradable polymer material with mechanical properties similar to bone. However, its use is limited due to low biocompatibility and mechanical properties. To address this, tricalcium phosphate (TCP) can be used to improve biocompatibility, while metal oxide reinforcements can enhance mechanical properties. In this research, novel PLA/ZnO/TCP composites were developed using TCP and ZnO to improve biocompatibility and mechanical properties. The samples were prepared using solution casting. Mechanical and degradation studies were performed to investigate the performance of the composites. Ultimate tensile strength and Young's modulus of PLA-based nano-composite membranes were determined using a Universal Testing Machine. The mechanical strength of PLA was increased up to 17.03% after adding 1 wt.% ZnO nanoparticles. Additionally, the biodegradation behavior of PLA was maintained by adding tricalcium phosphate (TCP). The improvement in mechanical properties and degradation behavior of composite membranes suggests their potential use in tissue engineering applications.

KEYWORDS: Biocompatibility, ultimate tensile strength, scanning electron microscope, composite membranes.

1. INTRODUCTION

Polyester-based biodegradable polymers show better properties such as better biocompatibility, better biodegradability, and mechanical characteristics and are used for several biomedical applications [1]. Polylactide, or poly(lactic acid) (PLA), is one of the most prominent biodegradable polymers derived from renewable resources, making it a key player in sustainable material development [2]. PLA is synthesized primarily from lactic acid, which is produced through the fermentation of natural sources like sugarcane, corn starch, or other carbohydrate-rich crops. Due to its adaptability, PLA can be used in a wide range of applications, from packaging materials and disposable items to medical devices such as sutures and implants, owing to its biocompatibility and ability to degrade safely in the body [3]. This thermoplastic polymer offers several advantages, including biodegradability, meaning it breaks down into natural components like water and carbon dioxide under industrial composting conditions [4]. PLA is also known for its excellent mechanical properties, including high tensile strength and toughness, which make it a strong competitor to traditional petroleum-based plastics [5]. Its processability is another key feature, as it can be easily molded or extruded into films, fibers, and 3D printing filaments. Moreover, PLA provides high optical clarity, making it ideal for applications requiring transparency, and is cost-effective due to its reliance on abundant, renewable resources [6].

The issues associated with biodegradable polymers are incompatibility, volatility, low biodegradability, and immunogenicity. After modifying their properties these polyester-based polymers offer better applicability. These polymers have been neglected for use in biomedical applications for their hydrophobic effect, low resistance to antibacterial activity, and less biocompatibility [7]. To use these polymers in clinics there is a need to improve their mechanical properties. The most frequently used metal alloys for orthopedic applications are titanium alloys, steel alloys, and cobalt-chromium alloys, chosen for their superior mechanical properties compared to ceramics and polymers. However, orthopedic implants made from metal alloys typically require a second surgery for removal. To achieve the desirable properties, copolymers and blends of PLA are fabricated. The study focuses on the composite of biodegradable polymer PLA and additives, their essential functions, and other factors in detail. The studies will be conducted to predict the degradation and mechanical failure behavior of prepared composites.

Polymers and composites can be processed using various methods, including injection molding, blow molding, and thermoforming. PLA films, in particular, can be produced through processes like extrusion, thermo-compression, and solution casting [7]. It is important to note that the properties of PLA films are influenced by the processing techniques used due to the varying degrees of thermo-mechanical history involved. In a study by Jong-Whan Rhim et al., PLA films were prepared using two different methods: thermo-compression and solvent casting. The films produced by thermo-compression exhibited high

strength but brittle behavior, while those made using solvent casting were more ductile.

2. MATERIALS AND METHODS

The reinforcement materials for fabricating the PLA/nZnO/TCP nanocomposite include zinc oxide (nZnO) nanoparticles and tricalcium phosphates (TCP). Tetrahydrofuran was employed as a solvent to dissolve PLA and the reinforcement materials, while chloroform was used as an alternative solvent to improve sample quality. In this research, nano-grade zinc oxide powder with a particle size of 20-30 nm was utilized. PLA pellets served as the base material for the composite fabrication, and commercially sourced TCP was used as a filler in the composite preparation.

SAMPLE PREPARATION

A pure PLA solution was prepared by dissolving 4 g of PLA granules in 100 mL of THF at room temperature with 24 hours of magnetic stirring. The solution was sonicated for 30 to 45 minutes to improve its solubility. It was then poured into Petri dishes and left to evaporate the solvent for 24 hours. The pure PLA was dried, cured, and packed. PLA/nZnO nanocomposite films were prepared by mixing various concentrations of ZnO into the PLA solution. The solution was sonicated for 2 to 3 hours at room temperature. The homogeneous suspension of PLA was then poured into Petri dishes for evaporation. The dried samples were cured and packed. For the PLA/TCP samples, 10 to 30 wt.% of TCP was mixed into the PLA solution. The samples were sonicated, then dried in Petri dishes. For the preparation of PLA/ZnO/TCP composites, both ZnO and TCP were mixed in THF. The samples were sonicated for 30 to 45 minutes. The PLA granules were then added to the TCP/ZnO suspension and stirred for 24 hours. After preparing the solutions, they were sonicated again and carefully poured into Petri dishes. The schematic of the fabrication of PLA/ZnO/TCP composites is shown in Figure 1, and the details of sample preparation in the laboratory are shown in Figure 2.

MORPHOLOGICAL STUDIES

Scanning electron microscope (SEM) was used for the surface analysis of prepared samples. The samples were cut in 10 × 10 mm dimensions for SEM analysis. Sputter coater was used for gold coating. Microscopic images of samples is shown as in Figure 3. The micrograph of pure PLA was recorded at 20 K magnification, while the images of composites were recorded at 100 K magnification.

3. RESULTS AND DISCUSSION

This section presents the results of the mechanical tests on the prepared samples, including ultimate tensile strength and Young's modulus, along with their comparison. Degradation results are also included in this section

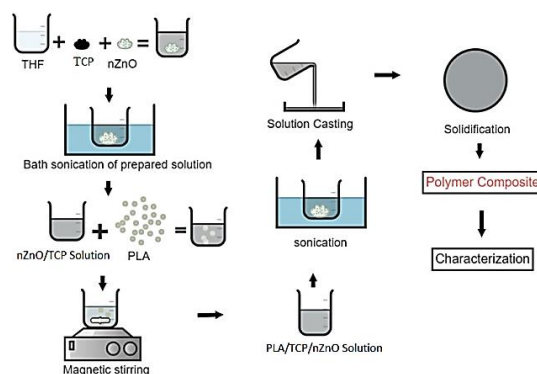


Figure 1: Fabrication method for the preparation of PLA/ZnO/TCP composites

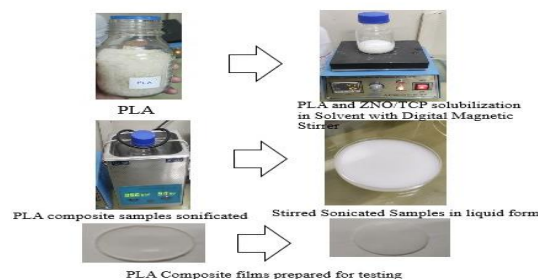


Figure 2: Preparation method for the preparation of PLA-based composites

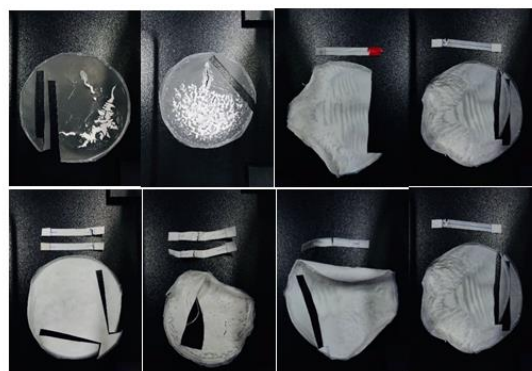


Figure 3: Microscopic images of samples fabricated in THF

MECHANICAL RESULTS

The results of PLA, PLA/TCP, and PLA/ZnO/TCP composites prepared in THF can be noticed in Figure 4. Pure PLA exhibits the maximum stress upon mechanical testing which is 13.9 MPa and the strain produced in it is 2.5mm. The addition of TCP into the PLA decreased strength to 8.8 MPa. The addition of 1 wt.% ZnO and 20 wt.% TCP into PLA decreased the mechanical strength to 12.4 MPa and with that value of strain was also decreased and has come down to 1.5 mm.

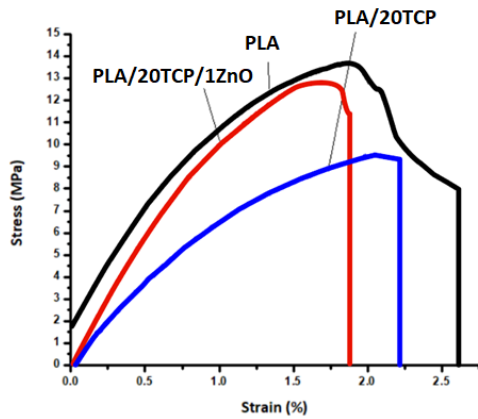


Figure 4: Tensile test results for the samples fabricated in THF

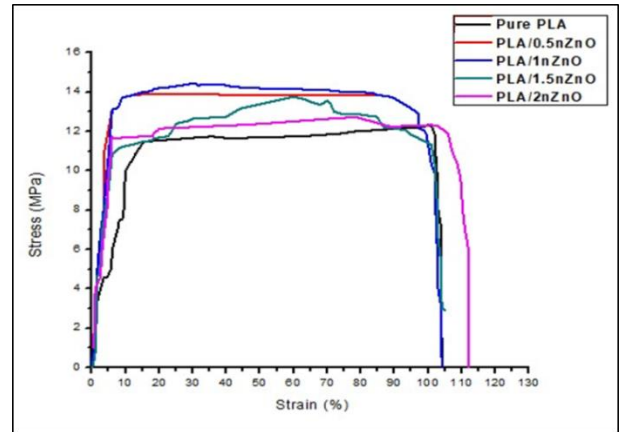


Figure 5: Tensile test results for the PLA/ZnO composites fabricated in Chloroform

The tensile testing results of Pure PLA, PLA/nZnO, PLA/TCP composite films are presented in Figure 5 and Figure 6. The ultimate tensile strength of PLA/ZnO composites increased to some extent with the addition of ZnO nanoparticles. The ultimate tensile strength of Pure PLA was 12.13 MPa, it was increased to 13.87, 14.45, 13.75, and 12.72 MPa after 0.5, 1.0, 1.5, and 2 wt. % addition of ZnO. As compared to Pure PLA the maximum 17.03% increase in ultimate tensile strength was noticed for 1 wt % of nZnO. However, when the concentration of nZnO was exceeded, ultimate tensile strength was decreased, which might be due to the accumulation of Zinc oxide particles. The Young Modulus of Pure PLA was 66.67MPa it notably increased to 72.3, 75.4, 71.6, 68.3 MPa after the 0.5, 1.0, 1.5, and 2wt % incorporation of ZnO nanoparticles. The highest increase in Young Modulus was recorded at 13.02 % for PLA/0.5nZnO as compared to Pure PLA. Reinforcement of TCP was carried out using different concentrations. PLA/TCP films revealed declined behavior in UTS and Young Modulus this might be due to stress concentration at the different portions of the sample. The non-uniform thickness of the sample having a rough surface could cause a loose grip and many more defects during tensile testing.

The addition of TCP makes the samples more brittle and the difference between both images showed that the PLA, PLA/ZnO samples exhibit the maximum value of tensile strength until the failure of samples. While PLA/TCP samples showed a decline in strength after the reach of maximum strength

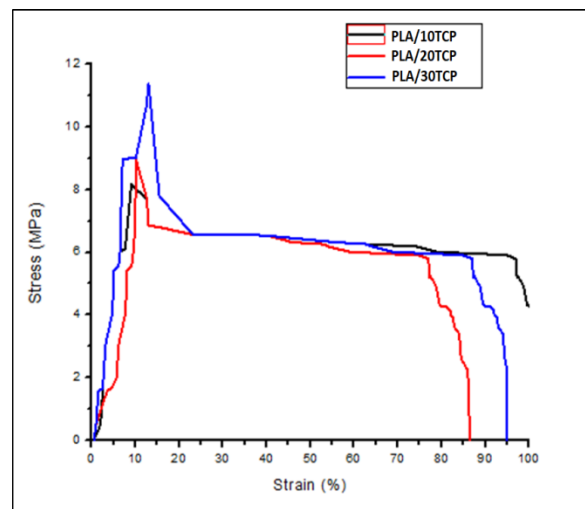


Figure 6: Tensile test results for the PLA/TCP composites fabricated in Chloroform

Table 1: Mechanical results of PLA and their composites

Sample	Ultimate Tensile Strength (MPa)	Young Modulus (MPa)
Pure PLA	12.318	66.6
PLA/0.5nZnO	13.870	72.3
PLA/1.0nZnO	14.45	75.4
PLA/1.5nZnO	13.75	71.6
PLA/2.0nZnO	12.72	68.3
PLA/10TCP	8.177	50.3
PLA/20TCP	8.97	53.3
PLA/30TCP	9.01	53.7
PLA/20TCP/1ZnO	13.796	71.9

According to the literature, the effectiveness of the reinforcement and the dispersion of nano fillers within the polymer matrix are the primary parameters that regulate the stress at the interface between the matrix and the filler, ultimately enhancing the mechanical properties of the

polymeric materials. The processing temperature of the solvent may also affect the strength of the composite films. The values of ultimate tensile strength and Young's modulus are presented in Table 1.

The results of PLA/20TCP/1ZnO are presented in Figure 7. The ultimate tensile strength for PLA/20TCP/1ZnO composites was recorded at 13.796 MPa. The graph showed the variation in behavior as compared to pure PLA and other samples. The PLA/20TCP/1ZnO samples failed after attaining the maximum load, while other samples gained maximum load or stress in the starting stage.

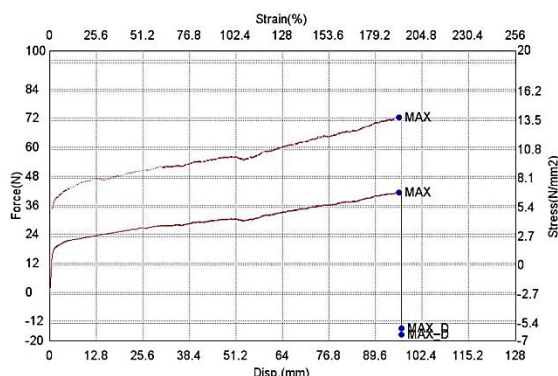


Figure 7: Tensile test results for the PLA/TCP/ZnO composite samples

Results for Degradation Test

Samples of Pure PLA, PLA/nZnO, PLA/20TCP/1ZnO and PLA/TCP were dipped in “PBS Solution” to check their degradability, the weight of the sample was observed after some days, the degradability of membranes was observed by its weight loss, and it was noticed that the composite loses its weight after few days of immersion presented in Table 2. The degradation rate calculated using the “Coupon Method” was recorded in Table 3. The corrosion rates graph is presented in Figure 8. PLA/1.5nZnO film exhibited a maximum degradation rate after 30 days. A degradability test is performed to ensure that the scaffold can provide vital support for cells to regenerate. If the degradation rate is too rapid, the hydrogel scaffold may be encapsulated by fibrous tissue when implanted into the body, hindering overall cellular regeneration. If the degradation rate is too slow, a prolonged inflammatory reaction may occur, which can lead to further damage to the body.

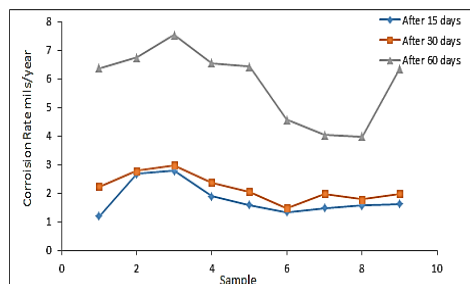


Figure 8. Degradation test results

Morphological Studies

SEM images of the pure PLA, PLA/ZnO, and PLA/ZnO/TCP are presented in Figure. The surface of the pure PLA sample is shown in Figure 9 (a). It looks more compact and smoother as compared to other samples. Figure 9 (b) shows the surface of the PLA/ZnO composite. The surface of PLA/ZnO samples looks rough as compared to pure PLA samples due to the presence of nanoparticle reinforcements. However, these SEM results confirm the presence and distribution of nanoparticles at higher magnification. The uniform dispersion of ZnO nanoparticles is probably due to the breakage of nanoparticles as a result of sonication. Few cracks found on the surface are due to the effect of gold sputtering. The surface of PLA/ZnO/TCP composites is shown in Figure 9(c). The addition of TCP makes the composites rougher as compared to other samples.

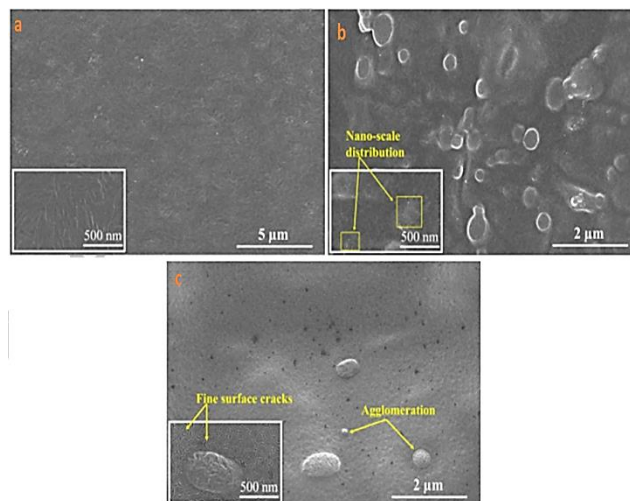


Figure 9. SEM results of best samples

4. CONCLUSIONS

Biodegradable PLA/nZnO, PLA/TCP, and PLA/TCP/ZnO nanocomposites were successfully fabricated. Favourable parameters were obtained at 1.0 wt. % nZnO, 24 hours of stirring time, and 3 to 4 hours of sonication time. The concentration of nZnO was found to be a highly significant parameter compared to other independent variables.

The samples fabricated in THF were brittle. When the solution was stirred for 24 hours and sonicated for 3 to 4 hours the samples were of better quality. Chloroform was used to make the ductile and elastic samples of PLA and its composites. The difference in the quality of samples in both solvents was probably due to the difference in the solubility index of PLA.

The mechanical strength of PLA was increased with the addition of ZnO nanoparticles. 17.03 % increase in strength was recorded with the addition of 1 wt. % ZnO



nano-particles. The mechanical strength of PLA was decreased by adding TCP. The biodegradation behavior of PLA was maintained by adding TCP. The addition of TCP and ZnO makes the samples with moderate strength and degradation. SEM micrographs confirm the presence and uniform dispersion of nanoparticles.

ACKNOWLEDGEMENTS

The authors would like to gratefully acknowledge the support received from the National Fertilizer Cooperation Institute of Engineering and Technology, Multan (NFC IET, Multan, Pakistan), University of Engineering & Technology Lahore and Allied Health Department Bakhtawar Amin Medical and Dental college to accomplish this research work.

REFERENCES

1. Zhao, C., Wu, H., Ni, J., Zhang, S., and Zhang, X., "Development of pla/mg composite for orthopedic implant: tunable degradation and enhanced mineralization", *Composites Science and Technology*, v. 147, pp. 8–15, 2017.
2. Lee, J. et al., "Fabrication of poly(lactic acid)/ti composite scaffolds with enhanced mechanical properties and biocompatibility via fused filament fabrication (fff)-based 3d printing", *Additive Manufacturing*, v. 30, p. 100883, 2019.
3. Li, X., Cong, Y., Sui, J., and Li, X., "An investigation on the degradation behaviors of mg wires/pla composite for bone fixation implants: influence of wire content and load mode", *Science and Engineering of Composite Materials*, v. 28, pp. 39–47, 2021.
4. Zhang, Y. et al., "Investigation on the microstructure, mechanical properties, in vitro degradation behavior and biocompatibility of newly developed zn-0.8%li-(mg, ag) alloys for guided bone regeneration", *Materials Science and Engineering: C*, v. 99, pp. 1021–1034, 2019.
5. Wang, T., Lin, C., Batalu, D., Zhang, L., Hu, J., and Lu, W., "In vitro study of the plla- mg65zn30ca5 composites as potential biodegradable materials for bone implants", *Journal of Magnesium and Alloys*, 2021.
6. Boro, U., Kashyap, N., and Moholkar, V. S., "Sonochemical synthesis of poly(lactic acid) nanocomposites with zno nanoflowers: effect of nanofiller morphology on physical properties", *ACS Engineering Au*, v. 2, pp. 46–60, 2021.
7. Shankar, S., Wang, L. F., and Rhim, J. W., "Incorporation of zinc oxide nanoparticles improved the mechanical, water vapor barrier, uv-light barrier, and antibacterial properties of pla-based nanocomposite films", *Materials science & engineering. C, Materials for biological applications*, v. 93, pp. 289–298, 2018.



Evaluating the Influence of SiC coating on Surface Characteristics of UHMWPE

Muhammad Tahir^{1*}, Rizwan M. Gul¹, Ahmed Nawaz¹, Mohsin Hayat¹, Muhammad Ali Kamran¹, Rashid Ali², Muhammad Kaleem Ullah Khalil¹

¹University of Engineering and Technology, Peshawar

²Ghulam Ishaq Khan Institute of Science and Technology, Topi, Pakistan

tahiribrar@uetpeshawar.edu.pk

ABSTRACT

Ultra-high Molecular Weight Polyethylene (UHMWPE) is a highly versatile polymer known for its exceptional properties, however, its limited life as an implant material in biomedical applications necessitates surface modification to lessen wear debris formation. Silicon Carbide (SiC) is extensively employed as a coating material due to its exceptional corrosion resistance, resistance to significant temperature fluctuations, and effective wear resistance. This study aims to investigate surface properties of UHMWPE through application of SiC coating. Magnetron sputtering in RF mode was used to deposit thin film with thickness 500 nm on UHMWPE substrate. The surface characteristics, such as, surface roughness, uniformity, elemental composition, nano-hardness and adhesion of coated and uncoated samples were analyzed through Atomic Force Microscopy (AFM), Scanning Electron Microscopy (SEM), Energy Dispersive X-ray Spectroscopy (EDX), Nano Indentation and mechanical adhesion tests, respectively. The finding showed no significant difference in surface topography comparatively. Nano-indentation reveals that the hardness increases by 167%. The adhesion test also confirms that a strong adhesive film of class 4B was obtained. It was concluded that SiC exhibits good properties confirming magnetron sputtering as a reliable method that can result in enhanced life span of UHMWP.

KEYWORDS: UHMWPE, Biomaterial, Thin film deposition, SiC coating Characterization, Nano indentation

1. INTRODUCTION

UHMWPE, a semi-crystalline polymer, exhibits remarkable mechanical and chemical properties [1]. It is a type of polyethylene, a commonly utilized plastic material. UHMWPE distinguishes itself through its remarkably high molecular weight, typically falling within the range of 3.5 to 6 million g/mole for medical-grade variants, with a density of 0.930-0.935 g/cm³ [2]. It has outstanding impact strength, low friction coefficient, extraordinary abrasion resistance, and nonreacting to a wide range of chemicals and solvents. Due to these characteristics, UHMWPE is a very popular material across many industries. It is widely used as implants in orthopaedics including hip and knee replacements due to its biocompatibility [3].

Silicon Carbide (SiC) is a well-known ceramic material having good biocompatibility, high thermal stability, high wear resistance, and high corrosion resistance [4]. SiC ceramic is extensively employed as a coating for safeguarding against oxidation due to its exceptional anti-oxidation properties, resistance to significant temperature fluctuations, high corrosion resistance, and effective wear resistance [5]. Although it is used as a filler material in UHMWPE but no research has yet documented the deposition of SiC films on UHMWPE. This study addresses this gap by investigating the deposition of SiC film on UHMWPE using Magnetron Sputtering.

Several coating techniques has been developed and used for the same applications including Pulsed-laser deposition [6] plasma CVD [7], electron beam Physical Vapor Deposition (PVD) [8], Thermionic Vacuum Arc method [9], and magnetron sputtering [10]. Magnetron sputtering is used for film deposition because of the promising results in enhancing surface properties like wear resistance, hardness and producing uniform high-quality films.

The morphology, stoichiometry, nano hardness and adhesion of SiC thin films with thicknesses 500nm deposited on medical-grade UHMWPE utilizing unbalance magnetron sputtering with radio frequency power supply (MS), a PVD technique, is presented in this paper. The purpose is to determine the influence of coating thickness on UHMWPE using AFM, SEM, EDX, Nano-indentation and adhesion

2. MATERIAL AND METHODS

Sample preparation

Using a compression molding machine (QINGDAO China), a 10 cm diameter disc with 0.5 cm thickness was prepared from GUR 1050 UHMWPE (Ticona, UK). The sample was then cut into small pieces for subsequent experiments. Prior to any experiment, the cleaning

protocol was followed in isopropanol for 10 minutes in an ultrasonic bath.

SiC Coating

The SiC coating was deposited on Control UHMWPE surface using Multi-Target magnetron Sputtering (MS) unit (Xiamen OLLITAL Technology Co. Ltd. China) in Argon atmosphere. Prior to deposition, the samples were plasma treated for 5 minutes with base pressure of 0.002 Pa, argon flow rate of 350 SCCM and biased voltage of 300 V. Utilizing RF power supply, the coating was then performed with vacuum pressure of 0.002 Pa, working pressure of 1.33 Pa, argon flow rate of 50 SCCM and RF power supply of 120 watts. The substrate was mounted on a rotatory disc (100 rpm) positioned at a distance of 6cm from the target surface. The parameters of deposition were adjusted in order to obtain a continuous plasma plume and a suitable deposition rate. Film with thickness 500nm was deposited on the controlled surface measured by a Quartz crystal equipped in the same MS unit.

Coating Characterization

The surface roughness was measured for control and coated UHMWPE using AFM (Nanosurf C3000, Switzerland). The analysis was carried out in air at room temperature. To analyse the uniformity of the coating, the micrograph images of the deposited film were captured using a Zeiss EVO 15 SEM at magnification of 10,000X focusing on the film's top surface. To analyse the elemental composition of the coated samples, EDX equipped with the SEM was performed. The nano-hardness was then analysed using a nano-indenter (iMicro, Nano mechanics, Oak Ridge, TN, USA) at room temperature according to the computational procedure based on the Oliver-Parr method. During the nano-indentation test, a three-sided Berkovich tip in depth control mode was used to measure the hardness of the coated and uncoated surface. The indentations were made at a constant strain rate of 0.05s⁻¹ with a maximum depth of 100 and 150nm in depth control mode. Five or six indentations were made in each sample and the results presented are an average of these indentations. Cross hatch tape test was employed to evaluate the adhesion between the film and substrate according to ASTM standard D3359.

3. RESULTS AND DISCUSSION

Surface roughness

AFM images of the control, coated samples with a scan area of 40µm × 40µm are shown in Fig. 1. Using Gwydion-a free SPM (scanning probe microscopy) data analysis software, the average surface roughness (R_a) was assessed. The R_a values for both coated and uncoated samples were found to be 32.45±14.13 and 31.25±11.21 nm respectively aligning with the maximum threshold define for tribological applications [11].

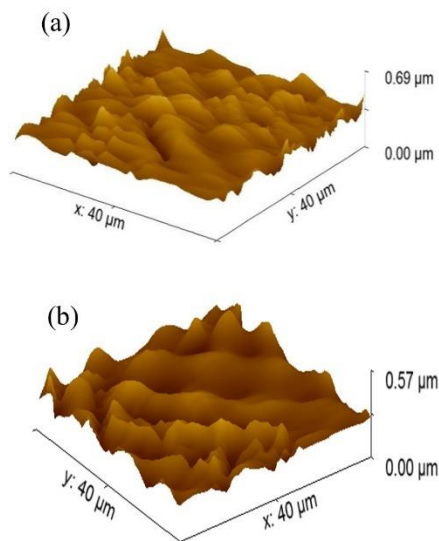


Figure 1: AFM images of (a)Control UHMWPE and (b) Coated UHMWPE

Scanning Electron Microscopy

The in-depth morphology of the SiC thin film was analysed with an SEM. The micrographs of the coated surface after plasma treatment are shown in figure 2. Small spherical grains that are characteristic of films deposited by magnetron sputtering are visible on the film surface [12]. The results clearly show some voids formation as well as some agglomerates of the deposited sputtered particles represented by rectangular and circular marks respectively. It was due to the lower energy of the ejected particles from the target which result in the lack of mobility on the substrate surface and hence the formation of agglomerate and voids as depicted in figures below [13]. The wear debris formation can originate from these agglomerates and can be therefore avoided by optimizing the deposition parameters.

Elemental Composition

The elemental composition of the deposited film was analysed using EDX equipped with Zeiss EVO 15 SEM. The comprehensive results are briefly presented in Table 1 offering a detailed insight into the elemental constituents of the coatings. Atomic ratios of Silicon to Carbon was found to be 1:3. This data serves as a definitive confirmation of the successful deposition of the film, thereby validating the effectiveness of the coating process. The same ratio was also achieved when SiC film was deposited by DC magnetron sputtering with lowest CH₄ flow rate along with Argon flow rate [14].

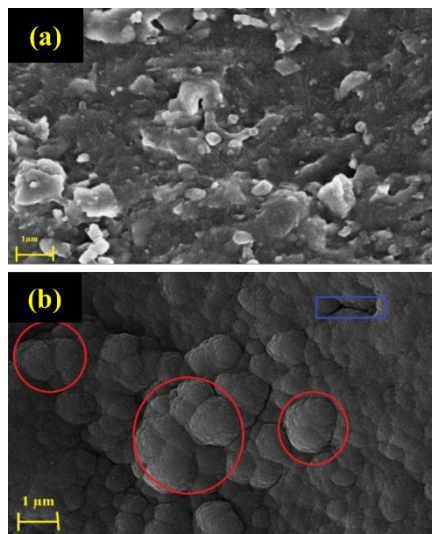


Figure 2: SEM images of (a) Control UHMWPE and (b) Coated UHMWPE at 10K X

Table 8: Elemental analysis of the coated Sample

Element	Weight %	Atomic %
C K	12.14	24.42
Si K	87.86	75.58

Nano-hardness

During nano-hardness analysis, the thumb rule used was that the maximum depth of indentation taken was the 20% and 30% of the whole thickness of the film only [15]. Hence the correlation of hardness was found out at two different depth i.e. 100 and 150 nm for film thickness of 500 nm at a constant strain rate of $0.05s^{-1}$ and at a holding time of 10s. The P-h curves are shown in figure 4 that show a considerable difference in plastic deformation. The load and stiffness recorded as a function of indentation depth were used to calculate the hardness and modulus in GPa of the film which are presented in table 2 below. The hardness of the coated sample increases up to 167% as SiC being a hard ceramic material and can absorb a lot of stresses [16].

Mechanical Adhesion

The adhesion analysis revealed a strong interface between the two surfaces. After following the standard procedure according to ASTM D3359 for cross hatch tap test, and after analysing the lattice of 100 squares of 1 mm^2 each through optical microscopy, the area that get detached from the sample was found 5% of the whole area, thus depicting a coating adhesion of class 4B.

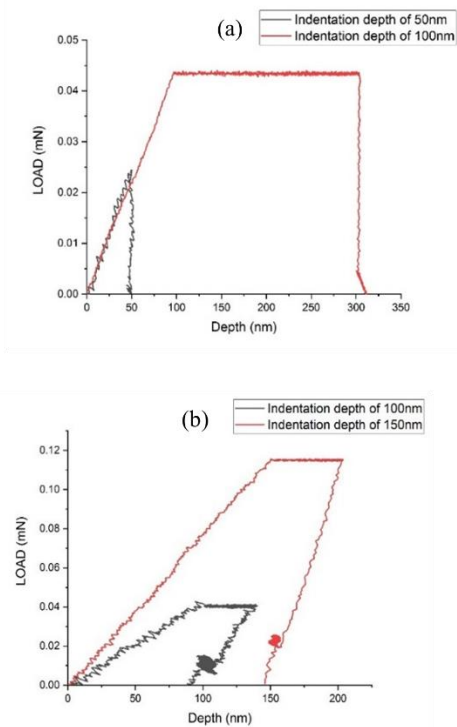


Figure 3: P-h curve of (a) Control UHMWPE and (b) Coated UHMWPE

Table 9: Nano-hardness of the samples

Control UHMWPE	At 50nm Depth	At 100nm Depth	Average Hardness (GPa)
	Hardness	Hardness	0.256±0.063
	0.315±0.073	0.197±0.053	
PTCU-500	At 100nm Depth	At 150nm Depth	0.685±1.163
	Hardness	Hardness	
	0.618±0.117	0.753±2.209	

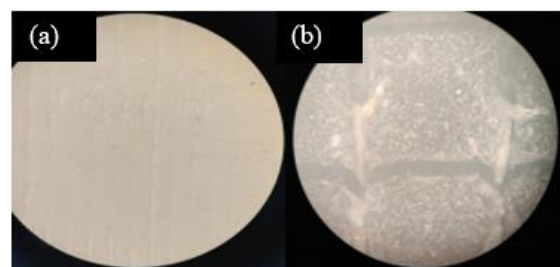


Figure 4: Large view of cross cut array and detail near the cross cut of coated UHMWPE

(The sample dimension is 1 cm * 1 cm with each square of 1 mm * 1 mm)

4. CONCLUSIONS

In this study the surface morphology, elemental composition and nano hardness of SiC coated UHMWPE through radiofrequency unbalance MS unit after plasma treatment was investigated. From the findings it was concluded that the surface roughness was found below the maximum threshold define for tribological applications. However, a little discontinuity in the uniformity of the film as depicted in SEM micrograph was due to the insufficient diffusion of the sputtered particles on the substrate surface. A considerable variation in the hardness between the coated and control surface was observed. A strong adhesive film of class 4B was obtained showing magnetron sputtering process to be a useful method for deposition.

ACKNOWLEDGEMENTS

The research was funded by NRP grant #20-16020 of Higher Education Commission (HEC).

REFERENCES

1. Sobieraj, M. C., & Rimnac, C. M. (2009). Ultra high molecular weight polyethylene: mechanics, morphology, and clinical behavior. *Journal of the Mechanical Behavior of Biomedical Materials*, 2(5), 433-443.
2. Simis, K., Bistolfi, A., Bellare, A., & Pruitt, L. (2006). The combined effects of crosslinking and high crystallinity on the microstructural and mechanical properties of ultra high molecular weight polyethylene. *Biomaterials*, 27(9), 1688-1694.
3. Technavio. (2017). *Global Ultra-High Molecular Ployethylene Market 2017-2021*. London: Technavio.
4. Anma, H., Yoshimoto, Y., Warashina, M., & Hatanaka, Y. (2001). Low temperature deposition of SiC thin films on polymer surface by plasma CVD. *Applied Surface Science*, 484-489.
5. Yi, J., He, X., Sun, Y., & Li, Y. (2007). Electron beam-physical vapor deposition of SiC/SiO₂ high emissivity thin film. *Applied Surface Science*, 253(9), 4361-4366.
6. Katharria, Y., Kumar, S., Choudhary, R., Prakash, R., Singh, F., Lalla, N., . . . Kanjilal, D. (2008). Pulsed laser deposition of SiC thin films at medium substrate temperatures. *Thin Solid Films*, 516(8), 6083-6087.
7. Anma, H., Yoshimoto, Y., Warashina, M., & Hatanaka, Y. (2001). Low temperature deposition of SiC thin films on polymer surface by plasma CVD. *Applied Surface Science*, 484-489.
8. Yi, J., He, X., Sun, Y., & Li, Y. (2007). Electron beam-physical vapor deposition of SiC/SiO₂ high emissivity thin film. *Applied Surface Science*, 253(9), 4361-4366
9. . Vladoiu, R., Ciupina, V., Lungu, C., Dinca, V., Contulov, M., Mandes, A., . . . Prodan, G. (2012). Investigation of the SiC thin films synthesized by Thermionic Vacuum Arc method (TVA). *The European Physical Journal D*, 99, 66: 99.
10. Oladijo, O., Sanjay, M., Collious, L., Siengchin, S., Moloisane, L., & Oladijo, S. (2022). Effects of deposition time and RF power on the film characteristics of magnetron sputtered silicon carbide thin films. *Materials Today: Proceedings*, 52, 2432-2438.
11. Fisher, J., Dowson, D., Hamdzah, H., & Lee, H. (1994). The effect of sliding velocity on the friction and wear of UHMWPE for use in total artificial joints. *Wear*, 219-225.
12. Oladijo, O., Sanjay, M., Collious, L., Siengchin, S., Moloisane, L., & Oladijo, S. (2022). Effects of deposition time and RF power on the film characteristics of magnetron sputtered silicon carbide thin films. *Materials Today: Proceedings*, 52, 2432-2438.
13. Salunkhe, P., Muhammed, A., & Kekuda, D. (2021). Structural, spectroscopic and electrical properties of dc magnetron sputtered NiO thin films and an insight into different defect states. *Applied Physics A*, 127(5), 390.
14. Tavsanoğlu, T., Zayim, E., Agirseven, O., Yildirim, S., & Yücel, O. (2019). Optical, electrical and microstructural properties of SiC thin films deposited by reactive dc magnetron sputtering. *Thin Solid Films*, 1-6.
15. Kurtz, S. M. (2016). *UHMWPE Biomaterials Handbook (Third edition)*. Norwich, NY: William Andrew.
16. Ault, N. (2001). Silicon Carbide Ceramics, Structure and Properties of. In N. Ault, *Encyclopedia of Materials: Science and Technology (Second Edition)* (pp. 8502-8508). Amsterdam: Elsevier.



Estimation of Creep Behaviour of CFRP Composite under Hoop Stress through ASTM D2290 and Accelerated Testing Methodology

Azaz Ullah*, Muhammad Ali Kamran

¹University of Engineering & Technology Peshawar

*engr.azazullah@gmail.com

ABSTRACT

Polymer composites are used in almost every industry from automotive, aerospace, sports and defense industries. Like other materials, composites also undergo creep. Finding the creep behavior of composites is crucial because unlike other defects, we cannot see if the material is undergoing creep as the strains are very small. After reaching a certain limit, the strain maximizes, and the material fails catastrophically. The goal of this research was to review the previous work done on the creep behavior and perform experiments to conduct our research on the basis of which we can estimate the creep behavior of the CFRP composite. For the experimental setup, we used the ASTM D2290 standard which is used for hoop tensile tests and Accelerated Testing Methodology which is used for creep testing at elevated temperatures. The pre-stressed samples were then placed in the thermal chamber at 80°C for 40 days. The strain data at different time periods at 80°C temperature from the experiments were used to obtain the creep behavior of the composite. The knowledge gained about the creep behavior of the CFRP composites through the experimentation can be applied by the mentioned industries in their products.

KEYWORDS: Creep, Composite, CFRP, ASTM D2290, Accelerated Testing Methodology

1. INTRODUCTION

The late 20th and 21st centuries are the centuries of developing and using composites. Composites are being used in every industry like medical, sports, aerospace and military etc. Composites include metal matrix composites (MMCs), ceramic matrix composites (CMCs) and polymer matrix composites (PMCs) which are the most used composites. In this research, our main area of composites is PMCs specifically carbon fiber reinforced polymer composites (CFRP). This specific composite was chosen because of its high strength to weight ratio and its use in a variety of applications.

CFRP composites consist of a matrix which is the polymer part, usually epoxy and the reinforcement part, which is made up of carbon fibers. The matrix gives shape to the composites and protects the fibers while the main load is carried out by the fibers. CFRPs are very good in tensile and longitudinal loading but not good in compression and transverse loading. The strength of the composite depends on the volume fraction of matrix and fibers, type of polymer, and angle of fibers to the applied load.

There are different types of failures that may occur in a composite like:

Delamination: in which the two or more layers of the composite are separated.

Fiber pullout: in which the bond between the fiber and the matrix breaks and fibers are pulled from the matrix.

Interface breakage; in which the interface between the fiber and the matrix breaks resulting in the uneven distribution and transfer of the load from the matrix to the fibers.

Chemical reaction: in which the composite reacts with the environment resulting in the decay or dissolving of the matrix.

The failure that we discussed in this research is the failure due to creep and on the basis of that we found out the estimated creep life of the composite by experimentation and using the data obtained to find the creep behavior of the CFRP composite.

Creep is defined as; when a component is subjected to a constant load for a longer period of time, a deformation is produced in that component which may be permanent and the component may fail catastrophically due to that deformation. Creep is time dependent but can be accelerated at high temperatures. Materials like polymers can go under creep even at room temperature.

As shown in Figure 1, creep has three stages. The first stage is called primary creep which is a transient stage. In this stage, the strain rate is high and requires less time compared to the second stage. The second stage is called the secondary creep in which the strain rate is almost constant. This stage requires the longest time. The third one is called tertiary creep in which the strain rate is again high and leads to sudden failure.

Therefore, finding the creep life of a composite is important because, after a certain amount of time, we may never know when the component will fail

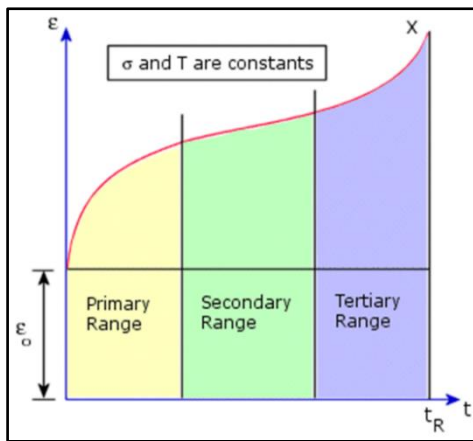


Figure 1: Stages of Creep

2. LITERATURE REVIEW

[1] The authors used the statistical tensile strengths and creep failure times of the CFRP strands obtained from the tension tests in the longitudinal direction of the composite to predict the creep life of the composite using the Weibull distribution method which is a statistical method used to describe the failure time of physical entities. The author has found that there will be a failure probability of 0.1 after 100 years if the ratio of Creep load and ultimate tensile strength is 0.8 at a temperature of 25°C.

[2] The authors used the Time-Temperature Superposition Principle (TTSP) method to predict the durability strength of the CFRP composites and those predictions from the models were then validated by experiments. In this method, short-term tensile tests are carried out with an increase in temperature in every subsequent test. The graphs from these tests are then combined together to form a master curve and that curve then gives us the behavior/life of the composite under that specific loading conditions

[3] The authors created master curves of strength for a glass/epoxy composite by using time-temperature superposition. Modulus data was used to generate the shift factors for the master curves. Even though the actual strength values varied, they discovered that the shift factors for the composite strength were unaffected by the kind, orientation, or loading method of the glass filler.

[4] The authors developed an accelerated test methodology for composite creep rupture. This methodology made the additional assumption that the strain to failure during the rupture test would be constant and that the shift factors for rupture would be the same as for compliance. They achieved good results when they compared the model to the outcome of a graphite epoxy composite. Additionally, they examined the Larson-Miller parameter and found that it did not correlate well with the experimental results.

[5] The authors examined unidirectional carbon epoxy composite laminates with fiber angles of 10°, 15°, 30°, 45° and 90° under a constant load for creep rupture test under 100°C for 10 hours. They noticed that there was no tertiary stage for the off-axis composite laminates during the creep rupture test like ductile materials. As the fiber orientation angle increases, the off-axis creep rupture strength decreases. Regardless of the fiber orientations, the creep

rupture time decreases with increasing creep stress. The off-axis creep rupture strength and the static strength both depend on fiber orientation. The morphology of macroscopic creep failure is comparable to that of static tensile failure. There is practically no difference between them.

[6] The authors used the accelerated testing methodology to forecast the statistical failure life of CFRP under tension loading was done for CFRP in unidirectional with a heat-resistant resin epoxy matrix. The outcomes are explained below:

Using the authors' devised ATM, the strength of creep failure vs the virgin and heat degraded composite strands' failure time at 110°C working temperature was forecasted and the reliability was quantified. The results of this investigation made it clear that creep loading for ten years at 110°C followed by ten years of heat degradation treatment at 110°C reduced the composite strand's creep strength to 74% at probability of failure $P_f = 10\%$ and time of failure $t = 1$ min.

[7] The variation in mechanical characteristics along horizontal and vertical directions is caused by the distribution of fibers. Because the load is supported by the fibers, the vertical specimen has exceptional mechanical qualities. The resin and interface bear the weight of the horizontal specimens, which results in the inferior qualities. The vertical specimens fracture by resin cracking, fiber withdrawal, and fiber breaking. The cracking of the resin and the debonding of the fiber-resin contact are the fracture mechanisms of the horizontal specimen. First and second stages of creep were experienced by every specimen during the long-term creep process. As the load rises, the creep rate increases. In the long-term creep test, the vertical specimens exhibit better creep resistance. Predicting the creep curves of the vertical specimen under 2 MPa–10 MPa and the horizontal specimen under 2 MPa–6 MPa, the Modified Time Hardening model can fit the experimental data with accuracy.

3. METHODOLOGY

For the experimental setup, we used the ASTM D2290 standard which is used for hoop tensile tests and Accelerated Testing Methodology ATM in which we perform creep tests at elevated temperatures. The fixture and the sample setup are given below.

Force is applied through the brackets which are connected with the split disks through pins as shown in Figure 2b. The samples were stressed in a universal testing machine by applying a tensile force to induce a stress of 700Mpa. After applying force on the split disk, a small space was created between the split disks. Spacers were then inserted in those spaces to retain the stress in the samples

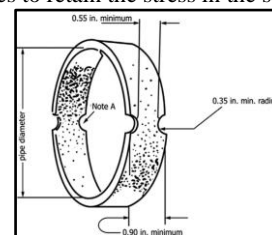


Figure 2a. Ring shaped CFRP Sample

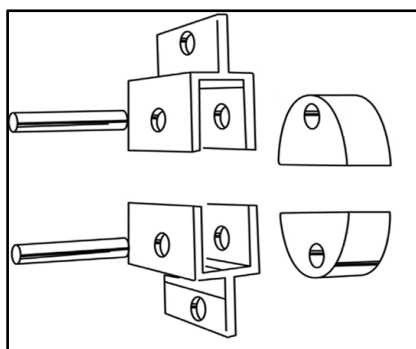


Figure 2b. Split Disks with Brackets

. The split disk along with the samples were then taken out from the machine and fixture. Strain gauges were then installed on the samples to note the strain produced under the application of a constant load as shown in the Figure 3a.

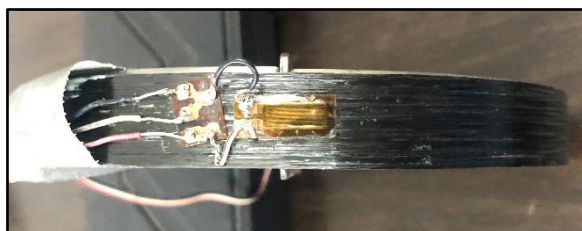


Figure 3a. Strain Gauge installed



Figure 3b. Sample wrapped around split disk

The fixture shown in Figure 3b consists of a split disk (silver color, made of mild steel) as and a ring sample (black color, CFRP) wrapped around the split disk while in middle between the two holes there is a spacer.

5. EXPERIMENTATION

The pre-stressed samples with strain gauges installed were then kept in the thermal chamber. The experiments were

carried out at a temperature of 80°C at a constant load of 700MPa for 40 days as shown in Figure 4.

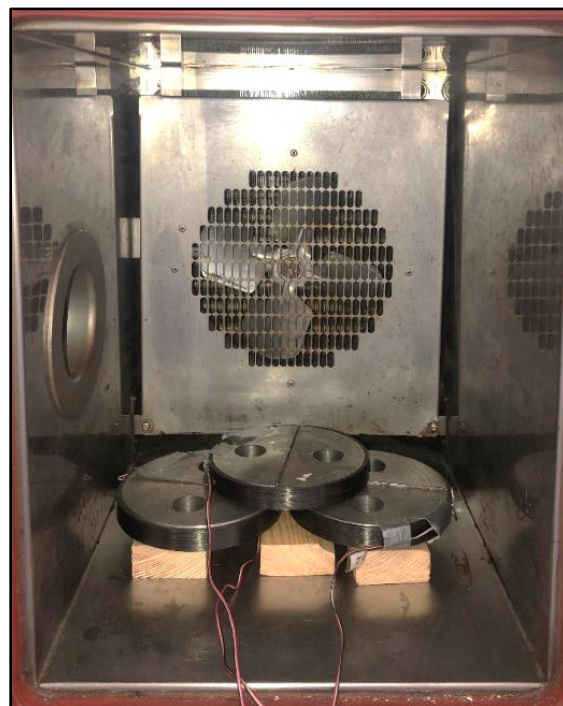


Figure 4. Samples in Thermal Chamber

Data Collection

The following strain data in Table 1 was obtained after performing experiments for 40 days at 80°C. The strain was recorded after every 24 – 48 hours. The strain units are in microns.

Table 2: Strain Data after 40 days

Days	Strain	Days	Strain
1	71	16	122
2	88	17	128
3	97	18	129
4	105	19	129
5	105	20	130
6	110	21	132
7	114	22	132
8	117	23	134
9	116	24	135
10	119	25	131
11	120	26	134
12	120	27	137
13	122	28	134
14	122	29	134
15	114	30	135

6. RESULTS

Creep Graph

Based on the strain data from Table 1 the following creep graph has been generated. From the graph in Figure 5, it can be seen that the trend of the creep graph is going in a positive expected direction.

The stages of creep are shown in the figure as “Primary Creep” and “Secondary Creep”. The “Tertiary Creep” is not attained as it is the last stage of the creep in which the strain rate is high and requires a very long time to reach after which the material fails.

Life Estimation

After 40 days the maximum strain produced was 138 microns. To find the percent strain for 138 microns:

$$138 \times 10^{-6} = \frac{138}{1000000} \times 100 \quad (1)$$

$$\text{Percent Strain} = 0.0138 \%$$

We know that the material fails at 2% strain, so to produce 2% strain, we have to find out how much strain would be produced in the material to reach 2% strain.

$$\frac{x}{1000000} \times 100 = 2 \quad (2)$$

$$x = 2 \times 10000$$

$$\text{Strain} = x = 20000$$

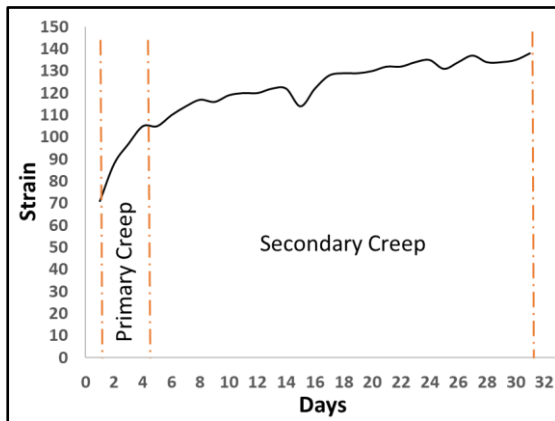


Figure 5. Strain vs Time at 80°C

When a strain of 20000 is produced then the material will reach 2% strain after which the material will fail.

For 40 days, the average increment of the strain was 2.23 microns which means that each day the strain was increasing with an average rate of 2.23.

If we want to know how many days or years will be needed for the material to reach 20000 strain, then we have the following formula:

$$\text{No. of days} = \frac{\text{Final strain} - \text{Initial strain}}{\text{Average strain}} \quad (3)$$

$$\text{No. of days} = \frac{20000 - 71}{2.23}$$

$$\text{No. of days} = 8936$$

$$\text{No. of years} = \frac{8936}{365}$$

$$\text{No. of years} = 24.5$$

This number is just an approximation, so to be on the safe side we can double the average strain from 2.23 to 4.46. After putting the new average strain value in the equation we get:

$$\text{No. of years} = 12.25$$

So the material will be safe for 12.5 years in service with FOS of 2.

7. CONCLUSIONS

In conclusion, we used the accelerated testing methodology to find the creep behaviour of the CRFP composite and estimated the life of the composite under the ASTM D2290 at elevated temperature for 40 days at 700Mpa. The results of this research in the form of the strain data, creep graph and life estimation of the CFRP composite can be used by those industries which use CFRP composite in their products mainly pressure vessels and storage tanks like submersible vehicles and spacecrafts.

REFERENCES

- Nakada, M., Miyano, Y., Morisawa, Y., Nishida, H., Hayashi, Y., & Uzawa, K. (2019). Prediction of statistical life time for unidirectional CFRTP under creep loading. *Journal of Reinforced Plastics and Composites*, 38(19–20), 938–946. <https://doi.org/10.1177/0731684419854213>
- Miyano, Y., & Nakada, M. (2020). Accelerated testing methodology for durability of CFRP. *Composites. Part B, Engineering*, 191, 107977. <https://doi.org/10.1016/j.compositesb.2020.107977>
- Moehlenpah, A. E., Ishai, O., & Dibenedetto, A. T. (1971). The effect of time and temperature on the mechanical behavior of epoxy composites. *SPE Transactions/Polymer Engineering and Science*, 11(2), 129–138. <https://doi.org/10.1002/pen.760110208>
- Brinson, H. F., Griffith, W. I., & Morris, D. H. (1981). Creep rupture of polymer-matrix composites. *Experimental Mechanics*, 21(9), 329–335. <https://doi.org/10.1007/bf02326232>
- Kawai, M., Masuko, Y., & Sagawa, T. (2006). Off-axis tensile creep rupture of unidirectional CFRP laminates at elevated temperature. *Composites. Part*



First International Conference on Advances in Mechanical, Materials, Mechatronics, and Energy Engineering (ICAME-24)



a, *Applied Science and Manufacturing*, 37(2), 257–269.

<https://doi.org/10.1016/j.compositesa.2005.08.002>

6. Miyano, Y., Nakada, M., Morisawa, Y., Matsuno, J., & Kageta, S. (2024). Prediction of creep failure life for unidirectional CFRP with heat-resistant epoxy resin as matrix exposed to high temperature under tension load. *Journal of Composite Materials*, 58(8), 1051–1062.

<https://doi.org/10.1177/00219983241234578>

7. Li, J., Liu, Z., Liu, Y., Zhao, Y., Wang, M., Wang, H., & Chen, X. (2023). Tensile and long-term creep properties of structurally and functionally integrated carbon fiber reinforced plastic at room temperature. *International Journal of Pressure Vessels and Piping*, 206, 105017.

<https://doi.org/10.1016/j.ijpvp.2023.105>

Enhancing Mint Yield through IoT-Integrated Vertical Hydroponic Systems: A Sustainable Solution for Future Agriculture

Sardar Muhammad Aneeq Khan¹, Yasir Hamid¹, Shahbaz Ali¹, Ahmed Zaheer¹,
Muhammad Hanzala¹, Muhammad Kashif¹

¹ Department of Mechanical Engineering, HITEC University, Taxila Cantt 47070, Pakistan

* aneeq.khan@hitecuni.edu.pk

ABSTRACT

The purpose of this study is to highlight the challenges inherent in traditional irrigation systems, such as lower yields, higher resource consumption, extensive land requirements, and lengthy growth cycles. Moreover, traditional methods put constraints due to environmental factors and are more likely to be attacked by the pests. The proposed system is a hydroponic system, which can maximize mint yield in a confined indoor space utilizing less resources. This study provides insights and shows the advantage of hydroponic systems over traditional agriculture by providing validation on how vertical plant cultivation can achieve three times the growth over conventional methods. The hydroponic structure is designed with optimal vertical dimensions, ensuring adequate sunlight exposure and spatial growth for mint plants. Given the increasing population and decreasing agricultural land, hydroponics presents a sustainable method for future food production. This research also incorporates an Internet of Things (IoT) based data collection system, using an Arduino Uno microcontroller to monitor and control environmental conditions and nutrient delivery in real-time. The system includes sensors for light intensity, temperature, humidity, and nutrient solution quality. An automated control system maintains optimal growing conditions to enhance the growth efficiency. Experiments conducted at HITEC University Taxila with a vertical hydroponic setup demonstrated that mint could be successfully grown with controlled pH and nutrient levels, achieving full growth in 24 days. The findings suggest that hydroponics is a viable alternative for urban and barren land agriculture, offering a high yield from a small area, though initial setup costs are higher compared to traditional methods.

1. INTRODUCTION

Hydroponics is the process of growing plants without soil directly from water by giving them specific nutrients that increase the production and reduce the growth time. It is a cleaner method for growth when natural resources and land are scarce. Through hydroponics, plants grow inside enclosures that control temperature, light, water, and nutrition [1].

Hydroponics has been recognized as a viable method of producing crops using liquid nutrient solution instead of soil. Hydroponics can be used in places where natural gardening is not possible, using less water and nutrients. Eliminating the risk of soil insects, growth occurs in controlled environment which increases the crop yield. Multiple techniques can be used to grow crops hydroponically, such as the flood-and-drain system, solution culture method, media culture method etc., which conserves water and nutrients without compromising the requirements of the plant [2], [3], [4].

Hydroponics system is the best method from which food production can be increased because a specific site for the system is not needed, and the yield also nearly doubles as compared to traditional agricultural methods. The Food

Agriculture Organization (FAO) of United Nations defines food security as four-dimensional issue focusing on availability, stability, access and safety. In the future, the world's agriculture will face a great challenge as farmers have to produce enough food for the rapid population growth [5]. Plants require intensive care for healthy growth, which includes many key aspects i.e. watering, fertilizer, rejuvenation and others. In hydroponic systems, water is the main resource of life for plants to photosynthesize [6]. Hydroponic cultivation is generally evaluated with pH and electrical conductivity that may not provide complete information regarding imbalance in cultivation process that cause poor yield and wastage of resources to overcome these limitations, Internet-of-Things (IoT) measurement system has to be implanted in this cultivation process, where sensors and actuators may measure the corresponding reading when need. Therefore, imbalance in attaining nutrients is eliminated by constant monitoring of resources towards plant cultivation. Fruits and vegetables are healthy when they are non-pesticides and not contaminated by chemicals. The automated system provides timely based nutrients and water which increases the growth rate as compared to the normal soil [7].

A study by Sundgren focused on monitoring the data of hydroponic plants sent to smart phone through IoT simultaneously displaying the data in real time using

Arduino microcontroller with LCD display. The plants were placed in a specialized vessel and the nutrients were directly sent to their roots. Arduino Uno microcontroller was used to control the flow of water towards the vessel. This microcontroller could be controlled by a smartphone and also by program module, which was embedded in the system. Water flow (carrying nutrients) was controlled by the microcontroller and alarms were used to activate the pumps when necessary. Two sensors were used to monitor the water level and the temperature of surrounding environment. Use of a relay with microcontroller helped to irrigate the vessels with the help of pump [8].

In a study by Santos et al., an automated hydroponics controller which measured air temperature, water temperature, humidity, pH and electrical conductivity (EC) was constructed. In a hydroponics system monitoring of pH and EC is very essential for healthy growth. The constant monitoring was achieved by using computerized systems, requiring knowledge of electronics and programming. Hardware included Arduino microcontroller, pH interface, EC interface, temperature and humidity sensors, DC motor, SD module and LCD display [9]

A study by Mishra et al. found that low light intensity could devalue a plant. It could affect the sugar content of a fruit, the external colors and taste of a fruit. Temperature changes could reduce the growth rate and quality of a crop. High humidity could cause different diseases in vegetables by spreading pathogens (it was the difficult factor to be controlled). With the increase of carbon dioxide concentration in the greenhouse, there was an increase in plant leaves, dry weight of plant and plant height. The water used for the irrigation was recommended to be contamination free as contaminated water could cause different diseases to the crops [10], [11].

A study by Khan considered different flow rates of water to the plants and checked their effects. It was found that when the water flow rate increased, the plant growth decreased. The different flow rates considered were 10, 20, and 30 liters/hour to three growth trays containing the plants. The authors used the Nutrient Film Technique (NFT) technique in which the growth tray was set on a specific slope of 2-3% so that the water flows backward to water tank using gravity. All the other parameters were the same for all of the three growth trays. After collecting the data and analysing it, the optimum flow rate for the plants was found to be 20 L/h; the height of the plants receiving this flow rate reached the highest height of 28 cm. The author also measured the weight of the plants and checked whether the flow rate also affected the weight of plant [12].

2. METHODOLOGY

Experimental investigation was carried out at HITEC University, Taxila. The normal environmental

temperature was measured as 28oC. The average altitude of the area was found to be 590 m. The mean annual precipitation was found to be 90.86 m. Experimental design consisted of a vertical hydroponic system having three channels in which we can grow multiple plants.

I. Design of Structure: In this section major components of the hydroponic system have been outlined. After reviewing numerous research papers and visiting different hydroponic farms in the local vicinity, a new design for small scale hydroponic structure was devised which can be placed in both indoor and outdoor areas. The design of structure is dual side step shaped, containing three layers. Dimensions of the structure are: length (L) is 1100 mm, width (W) is 1600 mm, and height (H) is 1500 mm. Structure is supported by wheels, which help in the movement of the structure and increases the height of structure by approximately 100 mm. Material used for fabrication of structure is angle iron.

Table 1: Geometric Properties of Hydroponic System

Name	Symbol	Value	Units
Height	H	1500	mm
Width	W	1600	mm
Length	L	1100	mm
Thickness of Iron pipe	T	20	mm
Vertical distance between two channels	V	400	mm

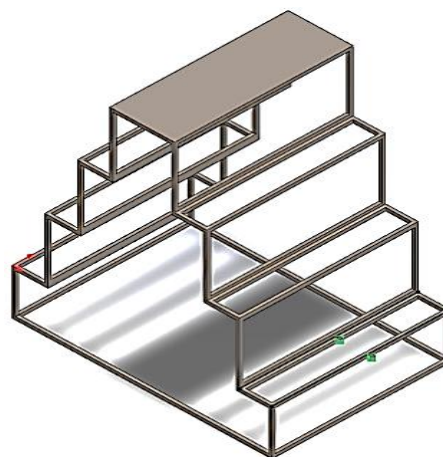


Figure 1: Frame Design of Hydroponic System

II. Design of Channels: Channels have been designed in such a way that the plants are soaked up in nutrient solution. The channels have been made using PVC pipes of diameter 76.2 mm (3 inches). Three growth channels were placed on the structure. Holes were drilled of diameter 50.8 mm (2 inches) in every channel, having centre to centre distance of 100 mm. Elbows were connected on all the ends of each channels to ensure that

nutrient solution flows inside without leaking. These elbows aid in rapid drainage of nutrient solution if required and also allow for cleaning of the channels from the inside. Vertical distance between two channels is 400 mm, providing maximum length for the growth of each plant. Due to the difference in width of each channel, the number of holes in channel is different. The first channel contains 16 holes, the second channel contains 20 holes, and the third channel contains 24 holes.

Table 2: Specification of the Channel

Name	Symbol	Value	Units
Length of each channel	l	1200	mm
Width of 1 st channel	w ₁	400	mm
Width of 2 nd channel	w ₂	800	mm
Width of 3 rd channel	w ₃	1200	mm
Diameter of holes	d	65	mm
End-End distance b/w holes	c	100	mm



Figure 2: Channel Design of Hydroponic System

III. Design of Water Circulation System: Coco peat was added into 80 mL disposable glasses, which were placed in the holes made into the channels. Six to eight holes of diameter 5 mm were made in lower half of each glass so that the coco peat could soak nutrient solution from the growth channel (if the diameter of holes in the glass exceed a certain limit, coco peat would start to leak into the nutrient solution and can choke the water circulation system). Plants selected for investigation require the same amount of nutrient solution, therefore, we modified our initial basic design. We drilled holes of diameter 25.4 mm (1 inch) in each channel on both sides. This allowed us to use only one water pump, pumping the water from the upper reservoir tank to the first channel. We linked all three channels using hollow anal plug of diameter 12.7 mm (0.5 inch) and water pipes of diameter 12.7 mm (0.5

mm). The combination of hollow plug and water pipe halted the nutrient solution leakage. Water pipes were inserted in each channel at a height of 40 mm from the bottom, maintaining a constant nutrient solution level and flowing the excess solution to the other channel.

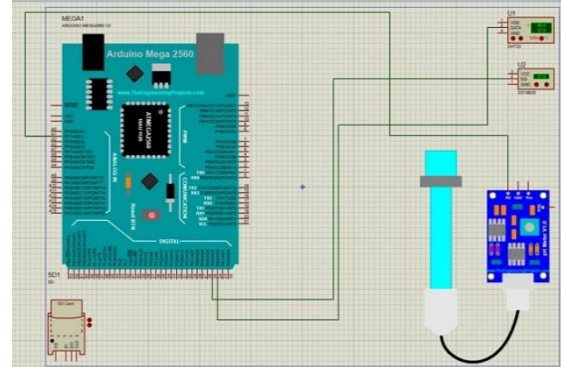


Figure 3: Schematic of the control system

IV. Design of Control System: The control system was made for surveillance of data and saved the daily data of the plants and the environment. The Arduino Mega 2560 microcontroller board was used for the control system. All the values of the attached sensors are displayed on a LCD connected with the control system; the module's dimensions are 146 x 62.5 mm.

A light intensity sensor (BH1750) was used to measure the intensity of light in the environment, ensuring that the plants getting the necessary light for their growth; the range of this sensor is up to 65,535 lux with an input voltage of 4.5 V. Another sensor, the DHT22 was used to measure relative humidity and ambient temperature of the surrounding environment; the temperature range of this sensor is up to 40oC, and the humidity range is humidity 0 – 100% relative humidity (RH), with an input voltage of 3 – 6 V. A liquid solution temperature measuring sensor (DS18B20) was used to measure the temperature of the nutrient solution, having a temperature range of -55oC – 125oC with an input voltage of 3 – 5.5 V.

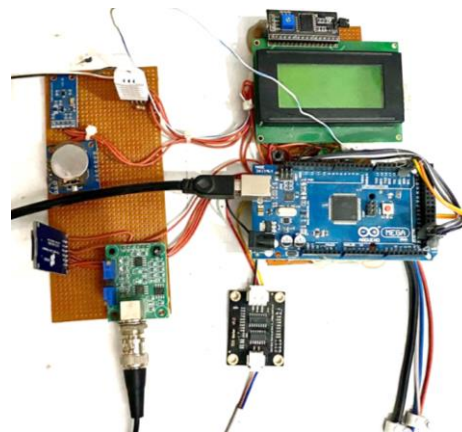


Figure 4: Process Parameters Control System

For measuring the Total Dissolved Solids (TDS) in the nutrient solution, the TDS Module (SEN0244) was used to measure the concentration in parts-per-million (ppm) of the nutrient solution, with a range up to 1000 ppm, and input voltage. A PH Module (SEN0161) was used to measure the pH of the nutrient solution, with a range of 0 – 14, and input voltage of 5 V. These five sensors mounted on a circuit board (measuring 43 x 32 mm) and connected to the control system through wires.

A Time Clock module (DS1307) was used to save to the data at that time and date so that after the experiments, during analysis, the data could be separated with the help of date and time. A 16 GB SD Card module was used to store data of every sensor. The data was saved in the card in excel sheet and everyday a new excel sheet was created with date as its name. A power supply of 5 V was supplied to the control system.

V. Plant Seeds Selection: The plants seeds are purchased from Islamabad (Awan Garden Centre, Ayyub Market, Sector F-8 Markaz). The seeds were germinated in growth tray for three weeks, and when the seeds developed roots and gained height of 2 - 3 inches above the grown medium, they were transferred to the hydroponic system.



Figure 5: Initial Stage of Mint Production



Figure 6: Final Stage of Mint Production

The nutrient solution was prepared using the Potassium nitrate, Magnesium sulphate, Mono potassium phosphate, Calcium nitrate, Boric acid, Ammonium molybdenum, Copper sulphate, Manganese sulphate, Zinc sulphate, and Iron EDTA. In order to maintain the nutrient solution, pH and TDS were monitored. The pH of solution was kept between 6 – 6.5 and the TDS was kept between 1100 – 1200 ppm [13]. Photos of the plants were taken daily to measure progress of their growth, and the control system saved the sensors' data hourly and stored into the SD card.

The hydroponic system design was selected based on findings from earlier studies, which emphasize the significance of optimized flow rates and bifurcation angles for plant growth. Following the work of Khan et al. and others, the system was tailored to investigate 10, 20, and 30 liters/hour as optimal flow rates to identify their impact on mint growth. The step-shaped structure ensures even water distribution, while the inter-channel connections prevent leakage and ensure nutrient flow consistency. This design builds upon previous studies by incorporating gravity-fed channels that allow for natural water flow through varying angles, simulating slopes like those used in Nutrient Film Technique (NFT) systems.

3. RESULTS AND DISCUSSION

In this research, the author gathered a data of 24 days of growth. Author has observed different environmental conditions such as ambient temperature, nutrient solution temperature, and relative humidity. The graphs presented here show the daily data of environmental conditions and temporal dynamics of plant health.

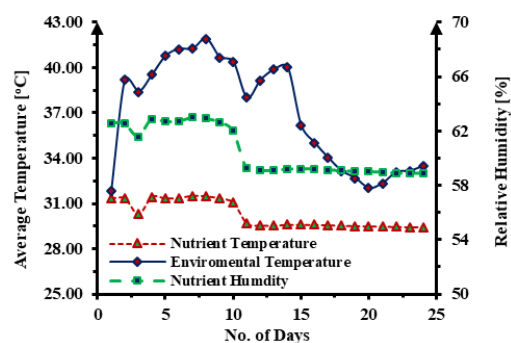


Figure 7: Nutrient Temperature Based on Environmental Temperature and Humidity

Figure 7 indicates the temporal dynamics of plant health and the effect of environmental temperature on the nutrient temperature and relative humidity as shown in Figure 6. Maximum environmental temperature achieved was 41.89oC at day nine of the implantation. It was observed that as the environmental temperature increases and decreases, both the nutrient temperature and relative humidity rise and fall accordingly. Maximum nutrient temperature and relative humidity achieved were 31.43oC and 62.99%. It was observed that after day fourteen of

implantation, corresponding decrease in environmental temperature did not significantly affect the nutrient temperature and relative humidity. Decrease in nutrient temperature and relative humidity was found with the decrease in environmental temperature at day three.

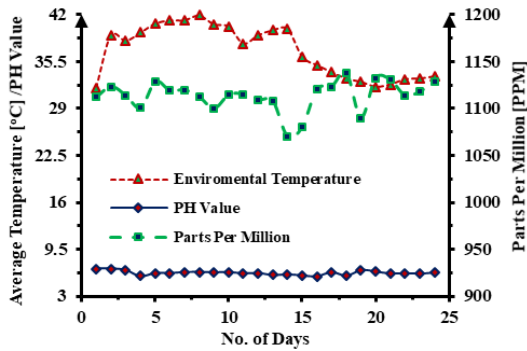


Figure 8: PH Value Based on Environmental Temperature and PPM

Figure 8 shows pH value and parts per million (ppm) of the nutrient solution. Parts per million (ppm) is a way to provide direct indication of very dilute concentrations of substances. It specifies how many parts of a constituent are existing in one million parts of a solution or blend. Results indicated that average environmental temperature did not significantly affect the pH value of the solution. Maximum pH value measured through experimentation was 6.3097 while maximum value of ppm was 1138.267. Experimentation in published articles indicated that maintaining a pH level between 5.5 and 6.5 is good for optimal nutrient uptake [14]. While mint is a form of herb, the optimal value for ppm published in articles found to be 800 to 1200 [15].

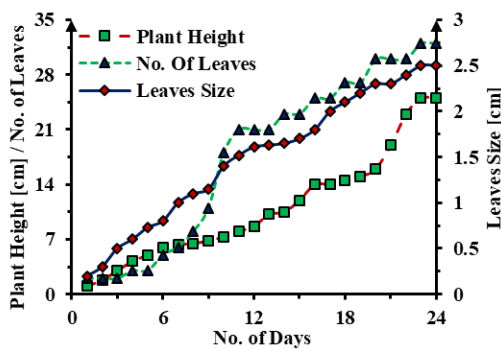


Figure 9: Temporal Dynamics of Plant Health

Figure 9 shows the temporal dynamics of plant health. Results shows that plant height, number of leaves, and leaves' size increase with the passing number of days of implantation. Maximum height of the mint obtained was 25 cm, while number of leaves were 32 at day 24 of the implantation. Faster growth of the plant observed on between the sixth and tenth day of the experimentation. The maximum size of the leaves was found to be 2.4 cm.

This study distinguishes itself by introducing a novel umbrella-like design, characterized by its step-shaped vertical structure and enhanced mobility. Unlike recent studies, which lack such a configuration, the dual-purpose structural innovation ensures optimal sunlight exposure and nutrient delivery

4. CONCLUSION

Experiments conducted at HITEC University Taxila with a vertical hydroponic setup demonstrated that mint could be successfully grown with controlled pH and nutrient levels, achieving full growth in 24 days. The findings suggest that hydroponics is a viable alternative for urban and barren land agriculture. Current full length research article-based conclusions made as are following:

Maximum nutrient temperature and relative humidity achieved are 31.43oC and 62.99%.

With fluctuations in environmental temperature, the nutrient temperature and relative humidity also increase and decrease in response.

The pH value of nutrient solution measured through experimentation is 6.3097, while its maximum concentration is 1138.267 ppm.

Faster growth of the plant observed between 6th to 10th days of the experimentation.

Future works:

While this study has demonstrated the effectiveness of an IoT-integrated vertical hydroponic system for enhancing mint yield, there remain several avenues for further exploration that are highlighted below:

Extended Crop Variety: Investigate how the proposed hydroponic system performs with other crops besides mint

Advanced IoT Integration: Focus on enhancing the IoT system with advanced predictive algorithms or AI-based models to optimize nutrient delivery in real-time, reducing energy and resource consumption further.

Comparative Study with Other Hydroponic Techniques: Future work can include a comparative study between different hydroponic techniques (like aeroponics or aquaponics) to evaluate which system is most efficient for different plants and environments.

ACKNOWLEDGEMENT

The authors are in debt to HITEC University Taxila Cantt, Pakistan for supporting this study by providing financial support.

REFERENCE

1. A. Razzaq Al-Tawaha et al., "Effect of water fl ow



- rate on quantity and quality of lettuce (*Lactuca sativa* L.) in nutrient film technique (NFT) under hydroponics conditions Abstract,” 2018.
2. D. Savvas and N. Gruda, “Application of soilless culture technologies in the modern greenhouse industry - A review,” Oct. 01, 2018, International Society for Horticultural Science. doi: 10.17660/eJHS.2018/83.5.2.
 3. A. Joseph and I. Muthuchamy, “Productivity, Quality and Economics of Tomato (*Lycopersicon esculentum* Mill.) Cultivation in Aggregate Hydroponics-A Case Study from Coimbatore Region of Tamil Nadu,” *Indian J Sci Technol*, vol. 7, no. 8, pp. 974–6846, 2014, [Online]. Available: www.indjst.org
 4. A. Shrouf and A. Alshrouf, “Hydroponics, Aeroponic and Aquaponic as Compared with Conventional Farming,” *American Scientific Research Journal for Engineering*, [Online]. Available: <http://asrjetsjournal.org/>
 5. P. Sihombing, N. A. Karina, J. T. Tarigan, and M. I. Syarif, “Automated hydroponics nutrition plants systems using arduino uno microcontroller based on android,” in *Journal of Physics: Conference Series*, Institute of Physics Publishing, Mar. 2018. doi: 10.1088/1742-6596/978/1/012014.
 6. T. Y. Kyaw and A. K. Ng, “Smart Aquaponics System for Urban Farming,” in *Energy Procedia*, Elsevier Ltd, 2017, pp. 342–347. doi: 10.1016/j.egypro.2017.12.694.
 7. N. A. Heredia, “DESIGN, CONSTRUCTION, AND EVALUATION OF A VERTICAL HYDROPOINIC TOWER,” 2014.
 8. A. Sundgren, “Tampereen ammattikorkeakoulu Degree Programme in Environmental Engineering.”
 9. J. Santos et al., “Comparative Analysis on Lettuce Quality Produced From Urban Agriculture and Organic Farming,” 2016.
 10. P. Mishra, L. Jimmy, G. A. Ogunmola, T. V. Phu, A. Jayanthiladevi, and T. P. Latchoumi, “Hydroponics Cultivation Using Real Time Iot Measurement System,” in *Journal of Physics: Conference Series*, IOP Publishing Ltd, Dec. 2020. doi: 10.1088/1742-6596/1712/1/012040.
 11. M. Esa, M. Abu Bakar, P. E. Pg Abas, L. De Silva, and F. Metali, “IoTs Hydroponics System: Effect of light condition towards plant growth,” *European Alliance for Innovation n.o.*, Feb. 2019. doi: 10.4108/eai.24-10-2018.2280609.
 12. F. A. KHAN, “A review on hydroponic greenhouse cultivation for sustainable agriculture,” *International Journal of Agriculture Environment and Food Sciences*, vol. 2, no. 2, pp. 59–66, Apr. 2018, doi: 10.31015/jaefs.18010.
 13. G. S. Brar, A. Kumar, G. Singh, . Ishika, . Shubham, and S. Kaushal, “Optimisation of Advanced Nutrient Solutions for Escalating Crop Production under Hydroponic Systems: A Comprehensive Review,” *Int J Plant Soil Sci*, vol. 36, no. 6, pp. 165–177, Apr. 2024, doi: 10.9734/ijpss/2024/v36i64618.
 14. H. M. Resh, “Hydroponic Food Production : A Definitive Guidebook for the Advanced Home Gardener and the Commercial Hydroponic Grower,” *Hydroponic Food Production*, Apr. 2022, doi: 10.1201/9781003133254.
 15. R. Pandey, V. Jain, and K. P. Singh, “Hydroponics Agriculture: Its Status, Scope and Limitations.”



Assessment of Erosive Wear Resistance Characteristics of 3D Printed Polymers Agitator Blade

Muhammad Haris Yazdani¹, Muhammad Rehan Khan^{1*}, Suleman Qamar¹

¹Department of Mechanical Engineering, College of Electrical and Mechanical Engineering, National University of Sciences and Technology, Islamabad, Pakistan

* mrehan.khan@ceme.nust.edu.pk

ABSTRACT

Erosion, the wearing away of material, is quite common in 3D-printed PLA plastic specimens and can be classified into various types, including abrasive, chemical, microbial, and hydrolytic erosion. Given the extensive use of 3D-printed materials in daily applications, understanding this process holds significant importance. In this experiment, the erosion of a 3D-printed PLA plastic agitator blade, mounted on a slurry pot erosion test rig and spun in a slurry solution, was investigated. The slurry mixture, containing water, sand, and other particles, is the primary cause of erosion in PLA specimens. Microscopic analysis after the experiment revealed varying erosion rates across different points on the blade. The maximum erosion occurred at the center of each blade, likely due to factors such as velocity distribution. Although tangential velocity increases with distance from the center, turbulence and secondary flow patterns may cause higher velocities at the blade's center, increasing erosion. Additionally, as the blade spins, material is thrown outward, but the highest erosion remains at the center. Furthermore, 3D printing properties significantly influence the specimen's erosion. Improper printing or asymmetrical blade dimensions can exacerbate wear. Lastly, the size of particles in the slurry affects the surface erosion. Heavier particles, which have greater momentum, often strike the blade's center with greater force, rather than the outer edges, causing increased erosion.

KEYWORDS: 3D printing, impact resistance, polymers, mechanical properties, additive manufacturing

1. INTRODUCTION

Additive manufacturing is a revolutionary process that has transformed daily life in numerous ways. It involves creating an object, part, or device from a digital model, such as a CAD model, by fusing layers of material, typically plastic. This method allows for the development of complex designs that are difficult to achieve through traditional manufacturing processes [1]. A 3D printer adds material layer by layer, progressively forming the final shape.

The practical applications of 3D printing span various industries, including healthcare, aviation, and automotive sectors. In healthcare, it is used for manufacturing prosthetics and artificial limbs, while the aerospace and automotive industries apply 3D printing to produce high-strength components that enhance fuel efficiency [2]. Ongoing advancements in additive manufacturing suggest even greater possibilities for its future applications.

In industrial settings, steel blades are commonly used in agitators; however, they can be problematic. Abrasive wear is a significant and costly issue faced by many industries, as it reduces component lifespan, increases maintenance frequency, and diminishes efficiency [3]. Enhancing the resistance of materials to abrasive wear is crucial for improving product longevity. The corrosion rate of stainless steel primarily depends on its passive

oxide layer, which protects the material from chemical attacks [4]. However, abrasion can remove this protective layer, exposing the material to chemical degradation [5].

In recent studies, researchers have explored 3D printing as an innovative method to produce impeller blades, emphasizing the advantages of using ceramic materials in the manufacturing process. For example, Kim et al. [6] demonstrated the fabrication of ceramic cores for impeller blades using 3D printing techniques such as selective laser sintering (SLS) and powder bed binder jet printing (BJP). Their findings indicated that SLS produced a higher-strength core with a lower coefficient of thermal expansion compared to BJP, making it more suitable for precision casting applications.

The objective of this project is to design a specialized system that can test and evaluate the performance of PLA 3D-printed blades in agitators. This research aims to address the challenges posed by erosion in industrial settings and explore the potential of alternative materials, such as PLA, to enhance the durability and safety of blade components. Through experimentation and analysis, we seek to develop effective strategies for erosion management, ultimately contributing to improved reliability of blades and reduced operational costs.

In the context of biodegradable polymers, Dananjaya et al. [7] have presented an in-depth review of the use of biodegradable polymers and their composites in 3D

printing, highlighting the integration of machine learning for optimizing future manufacturing processes. Their work underscores the potential of biodegradable materials in diverse applications, ranging from biomedical implants to sustainable packaging, emphasizing the need for material preparation and post-processing techniques to achieve structural integrity.

Blade erosion is a significant and complex challenge in materials science, costing the global economy billions of dollars annually. Erosion-corrosion of blades is a common issue across various industries, regardless of the type of equipment or materials used. Consequently, research in this area has grown over the last decade, with ongoing efforts to identify solutions. This literature review aims to systematically present various aspects related to the mechanisms, causal factors, and countermeasures for erosion-corrosion in blades. It synthesizes current knowledge, highlighting key areas of importance and gaps that warrant future investigation.

Furthermore, Dizon et al. [8] explored the importance of post-processing in 3D printing, particularly for polymers. Their research examined various methods for enhancing the mechanical, chemical, and aesthetic properties of 3D-printed components, which is crucial for industrial applications where precision and durability are essential. They noted that post-processing can significantly improve the geometrical accuracy and surface quality of 3D-printed parts, contributing to their long-term performance and reliability.

This study employed the Eulerian-Lagrangian method to analyse the performance and wear characteristics of a centrifugal slurry pump under varying slurry flow rates. Numerical analysis indicated that the pump's performance declined with increased sediment concentration, while the average erosion rates of the impeller blades and volute casing increased proportionally. Transitioning from a mono-sized to a broader particle size distribution (PSD) reduced impeller surface erosion by 20%, although it increased volute surface erosion by 30%. Interestingly, angular particles, although smaller than spherical ones, tend to cause higher erosion rates in blades and volutes.

Understanding impact resistance is crucial due to its practical applications in ensuring reliability, durability, and performance. In sectors such as healthcare, automotive, and aerospace, objects are often exposed to sudden forces and impacts. Knowledge of impact resistance allows researchers to optimize design and material properties, ensuring that materials can withstand specific loads and stresses [5]. Furthermore, strict international safety regulations necessitate the use of materials with substantial strength.

2. EXPERIMENTATION

The agitator blade was 3D printed using an Ender-3 Pro 3D printer, following the dimensions depicted in Figure 1. The printing method employed was Fused Deposition Modelling (FDM). In this technique, the 3D printer extrudes the polymer layer by layer onto the build plate, allowing the layers to fuse together and form the complete 3D object. The agitator blade was printed with a layer thickness of 0.8 mm, a build temperature of 70°C, and an infill density of 100%.

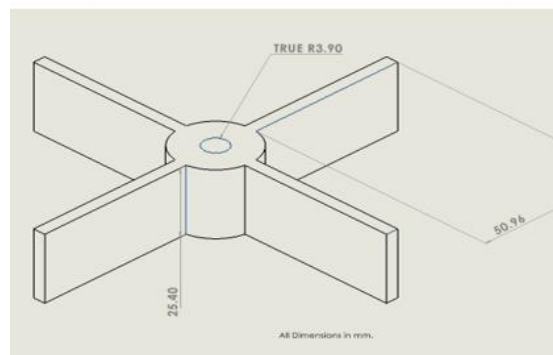


Figure 1: Dimensions of agitator blade

A bucket measuring 9 inches in diameter and 12 inches in height was constructed from 26-gauge (0.45 mm) sheet metal, secured with rivets. Four baffle plates, each 18 mm long with a 4.5 mm offset to facilitate slurry flow, were also made from the same material, extending throughout the bucket's height. Subsequently, due to leakage issues and the flexibility of the baffle plates, the bucket was reconstructed using 16-gauge (1.5 mm) galvanized sheet metal and fitted with a 220-volt AC induction motor. The 3D-printed agitator blade was then mounted within the assembly, as illustrated in Figure 2.

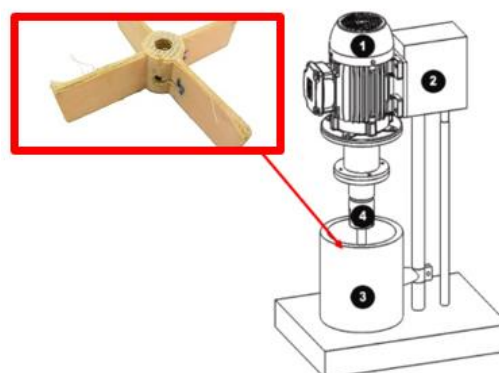


Figure 2: Agitator blade mounted in the assembly

Tests were conducted for six hours, with breaks to allow the motor to cool down. The slurry contained 25% sand by weight. After the testing, wear was evident along the edges and corners of the blades, which was later

confirmed through microscopic imaging and scanning electron microscopy.

MICROSCOPY ANALYSIS

Microscopic imaging (Figure 3) was performed using a digital microscope from Eakin. The blades exhibited deformation at the midpoint. Micro-perforation sites—tiny holes at the microscopic level—were observed on the blades. Ploughing, a condition where material is removed from the surface but remains in place rather than being blown away, was noted at the centre. Additionally, micro-level cracks were observed at the centre of the blades. Scanning Electron Microscopy (SEM) was employed to examine the nano-level abrasion patterns on the PLA blades.

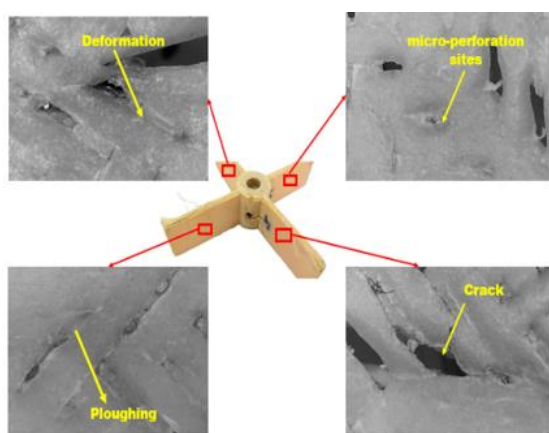


Figure 3: Microscopy analysis after erosion test

3. RESULTS AND DISCUSSION

Thickness loss was measured using a micrometre screw gauge. The condition of the blades after testing is illustrated in Figure 4 (a) and (b). The maximum wear occurred at the midpoint of the blade, facing the direction of flow, approximately 40 mm from the central shaft, while minimal wear was observed near the shaft due to higher particle velocity. The graph in Figure 5 (a) displays the erosion rate at various locations on the agitator blade.

The erosion observed at the center of the agitator blade (Figure 5 (b)) can be attributed to several factors. The abrasive nature of sand plays a significant role; when spun in a slurry with a 25% sand concentration, the sand particles behave like sandpaper, contributing to the erosion. Additionally, the center of the agitator blade is subjected to high-velocity gradients and turbulence, which further exacerbates wear. Furthermore, the rotational motion of the blade generates increased hydrodynamic forces at the center, leading to higher stress concentrations and, consequently, greater erosion in this area.

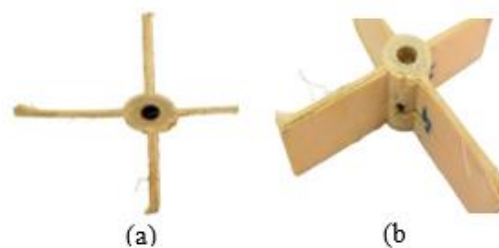


Figure 4: (a) Top view and (b) Side view of the blade after the erosion test

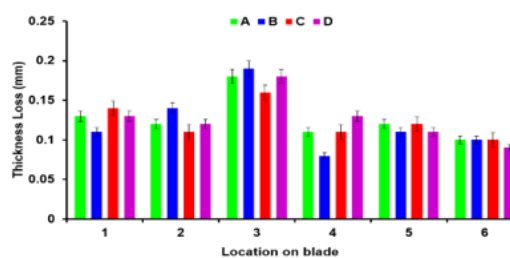


Figure 5: (a) Thickness Loss vs. location (b) Locations about the erosion in blade

4. CONCLUSION

In this study, the erosion of 3D-printed PLA The erosion of plastic blades has been discussed. This wear can be attributed to the abrasive nature of sand, the higher stress concentration at the centre of the blade, and the effects of turbulence on the blades. The lifespan of the agitator blade can be enhanced through various techniques, such as applying protective coatings to the blade propellers, adjusting the rotational velocity of the shaft, and optimizing the design of the agitator blade. Future advancements in these areas could prove highly beneficial in the field of mechanical engineering and positively impact various aspects of daily life.

REFERENCES

1. Khan, R., et al., Experimental and numerical investigation of hydro-abrasive erosion in the Pelton turbine buckets for multiphase flow. *Renewable Energy*, 2024. 222: p. 119829.
2. Popa, C.F., et al., Numerical and experimental study for FDM printed specimens from PLA under IZOD impact tests. *Materials Today: Proceedings*, 2023. 78: p. 326-330.
3. Hodžić, D., et al., Strength comparison of FDM 3D printed PLA made by different manufacturers. *TEM J*, 2020. 9(3): p. 966-970.
4. Khan, R., et al., Experimental and numerical



First International Conference on Advances in Mechanical, Materials, Mechatronics, and Energy Engineering (ICAME-24)



- study of erosive wear of t-pipes in multiphase flow. *Engineering Science and Technology, an International Journal*, 2024. 52: p. 101683.
5. Khan, R., et al., Erosion-corrosion failure analysis of the elbow pipe of steam distribution manifold. *Engineering Failure Analysis*, 2024: p. 108177.
 6. Kim, E.-H., Choi, H.-H., & Jung, Y.-G. (2020). Fabrication of a ceramic core for an impeller blade using a 3D printing technique and inorganic binder. *Journal of Manufacturing Processes*, 53, 43–47. <https://doi.org/10.1016/j.jmapro.2020.01.055>
 7. Dananjaya, S. A. V., Chevali, V. S., Dear, J. P., Potluri, P., & Abeykoon, C. (2024). 3D printing of biodegradable polymers and their composites – Current state-of-the-art, properties, applications, and machine learning for potential future applications. *Progress in Materials Science*, 101336. <https://doi.org/10.1016/j.pmatsci.2024.101336>
 8. Dizon, J. R. C., Gache, C. C. L., Cascolan, H. M. S., Cancino, L. T., & Advincula, R. C. (2021). Post-Processing of 3D-Printed Polymers. *Technologies*, 9(3), 61. <https://doi.org/10.3390/technologies9030061>

Experimental Identification of Campbell Diagram of a Flexible Rotor Supported by Active Magnetic Bearings

Muhammad Saad Fasih^{1,2}, Tobias Gorbach¹, Dušan Lapadatovic¹, Fadi Dohnal¹

¹Fachhochschule Vorarlberg, ²UMIT, Tirol

Muhammad.Fasih@edu.umat-tirol.at

ABSTRACT

Resonances of a rotor system could lead to dangerous vibrations or even mechanical failure. To identify these resonance frequencies, a Campbell diagram is usually employed which visualizes the relationship between the discrete natural frequencies and the excitation frequency. This diagram helps to identify rotor response frequencies resulting from typical excitation mechanisms like unbalance or alignment issues of the rotor. The experimental identification of the Campbell diagram of a flexible rotor supported by two active magnetic bearings is performed in the current study. An additional excitation is introduced in the active bearings during the rotation of the rotor in order to measure the speed-dependent natural frequencies. These frequencies are then collected and combined in the final Campbell diagram. The process is implemented in a rotor test rig. The results are benchmarked against the system response during run-up and run-down. The results show the lack of variation of the natural frequencies of the rotor plotted at different rotational speeds which is as expected. Due to simple configuration of the flexible rotor, there is not many variations in the natural frequencies. The maximum difference in natural frequency is 1.1% (2nd mode) from the perspective of stationary position of rotor. This approach helps to analyze flexible rotor systems in operation.

KEYWORDS: rotor dynamics, Campbell diagram, active magnetic bearings, flexible rotor

1. INTRODUCTION

The Campbell diagram is a graphical representation of natural frequencies of a rotating system plotted against its rotating speed. It provides the spectral response at specific speeds. It is commonly used in the vibration analysis of rotating systems. In rotor dynamics, the natural frequencies naturally depend on the rotation speed in terms of gyroscopic effects, variable hydrodynamic coefficients in fluid-film bearings or a centrifugal force causing an elastic deformation of large blades.

The research has been extensive for exploiting active magnetic bearings (AMBs) for identifying a Campbell diagram experimentally. AMBs can control and monitor rotor positions effectively and precisely which makes them a string tool to measure and analyses rotodynamic behavior. How AMBs can be utilized effectively to generate the Campbell diagram is explained in detail in [1]. The impact of AMB stiffness and damping coefficients and how they influence the rotodynamic behavior is briefly demonstrated in [2]. A methodology for rotodynamic analysis using AMBs is presented in [3]. The use of AMBs for system identification in rotor dynamics analysis is found in [4]. The study particularly

focuses on Campbell diagram generation using AMBs to help identify natural frequencies and critical speeds. In

[5], the authors have demonstrated the dual role of AMBs: vibration control and Campbell

diagram mapping. Details on applying a controlled excitation to record the response of the rotor have been outlined. Campbell diagrams can be useful in analyzing rotor defects as well. Campbell diagram analysis was used in recent past to detect open crack in a rotor [6]. In [7], Campbell diagram is utilized to optimize the performance of a complex rotor bearing system.

In the present work, these ideas are followed experimentally identify the Campbell diagram during operation of a flexible rotor levitated by two AMBs.

2. EXPERIMENTAL SETUP

The experimental setup consists of a steel rotor of diameter 8 mm and a total length of 760 mm which is supported by two active magnetic bearings. In the center of the two bearings and mounted on the rotor is a rigid disc (Figure 1).

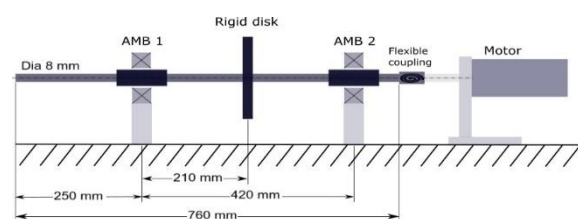


Figure 1: Sketch of the rotor configuration (taken from [8]).

The rotor is connected to the motor (ESP-Pollmeier) by flexible coupling. The motor is shown in Figure 3. This whole setup is mounted on a solid foundation plate which is supported by two I-beams placed on four low

frequency supports. There is a protective hood covering the rig to protect from any unwanted event. The AMBs play the main role in levitation of the rotor while providing stiffness and damping to the rotor until its nominal speed and the coast down. These AMBs (Fig. 2) are powered by MECOS power amplifier which help in the levitation of rotor by applying a current of 2 A to 8 A in the coils as defined by control input voltage. A self-made analog filter (MagLev) is used to process the signal and improve the signal quality. The sensitivity and offset of each individual sensor can be adjusted from the front panel of the MagLev using spindle potentiometers. A real time target machine (Speedgoat) is used to implement the control loop as shown in Fig. 5. MATLAB Simulink is used to design the controller.



Figure 2: AMB (taken from [8]).



Figure 3: Motor (taken from [8])

Two additional proximity sensors are installed in the test rig to measure the displacement of the centre disc. For the identification of the Campbell diagram, eight proximity sensors from the AMBs and the two sensors from the central disc (Fig. 4)



Figure 4: Rigid disc (taken from [8])



Figure 5: Speedgoat (taken from [8])

will be used to measure the displacement as the frequency changes in the sweep. The control loop of the system is shown in Figure 6. The overall setup is displayed in Figure 7.

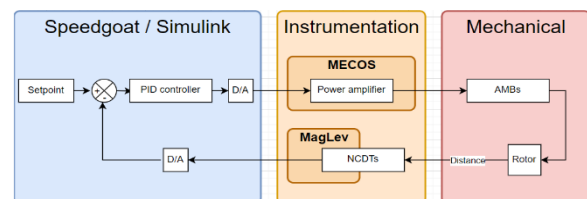


Figure 6: Control loop of the system (taken from [8]).



Figure 7: Test rig with foundations and cover (taken from [8]).

3. METHODOLOGY

For the identification of the natural frequency during rotor operation, a constantly accelerated frequency sweep is applied via one or both AMBs. The direction of excitation is chosen to be in a fixed, non-rotating plane. For the excitation, a sinusoidal function $y(t)$ is defined as a

frequency sweep which changes its frequency with a constant acceleration α such that

$$y_{AMB}(t) = \sin\left(\frac{\alpha}{2}t^2 + 2\pi f_0 t\right), \quad (1)$$

where, α is the angular acceleration in rad/s^2 , f_0 the start frequency of the frequency sweep and t the time in s.

To calculate α for a frequency increase from f_0 to f_e , the simple calculation is performed below. Basic physics [9, 10] provides

$$\begin{aligned} 2\pi f(t) &= \Omega(t) = \alpha(t - t_0) + \Omega_0 \\ &= \alpha(t - t_0) + 2\pi f(t_0), \end{aligned} \quad (2)$$

where $\Omega(t)$ is the instantaneous angular velocity in rad/s and $f(t)$ the instantaneous frequency in Hz of the AMB excitation. t_0 is the starting time of the frequency sweep, such that $f(t_0) = f_0$ is the initial frequency of the frequency sweep. Rewriting eq. (2) results in

$$\alpha = \frac{2\pi}{t-t_0} (f(t) - f(t_0)). \quad (3)$$

For example, for a starting frequency of 30 Hz and achieving 60 Hz in 10 s, the angular acceleration α becomes 6π . In the present study of this flexible rotor system, a frequency sweep from 0 Hz to 180 Hz is applied during 30 seconds in the flexible rotor bearing system.

4. RESULTS

While applying the frequency sweep excitation for 30 s, the displacement is measured at one of the proximity sensors of the AMB 1. The resulting time history is collected, filtered and converted to the frequency domain by applying FFT in MATLAB. Raw time histories at the position of AMB 1 are plotted in Figures 9 and 10. The x-axis shows the time in seconds whereas the y-axis has the displacement on it as a function of time in mm. The corresponding FFT spectra has the speed in rpm on x-axis and amplitude of the signal on y-axis and highlight that the present noise level is too high for a robust identification of the natural frequencies. This is why a low-pass filter of half power frequency 0.05 is applied in both time and frequency domains using a Butterworth filter characteristic of order 12, i.e. the frequency dependent filter gain is [11],

$$G(\omega) = \frac{1}{\sqrt{1 + \left(\frac{\omega}{\omega_c}\right)^{12}}}, \quad (4)$$

with ω_c being the low-pass filter frequency. For the present study, 0.05 is chosen. Since a live filter is not being used, the phase does not have too much effect on the information and performance of the AMBs. Examples of filtered and processed time histories at 0, 250, 500 and 1000 rpm are collected in Figures 11, 12, 13 and 14. For the unfiltered time history in Figure 10, sharp peaks

between 0 and 2000 rpm are clearly seen. These are the harmonics of rotational speed (250 rpm).

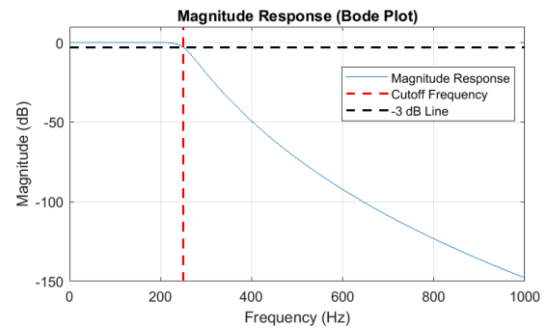


Figure 8: Filter magnitude response.

These sharp peaks due to unbalance excitations are strongly reduced by the filter and enable the spectra in Figures 11 to 14. The results highlight that the chosen filter characteristics as shown in Figure 8, allow for a robust identification of resonance peaks.

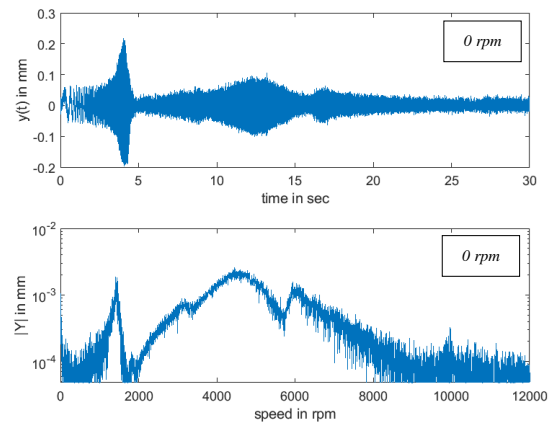


Figure 9: Unfiltered rotor response at AMB1 for rotor at rest.

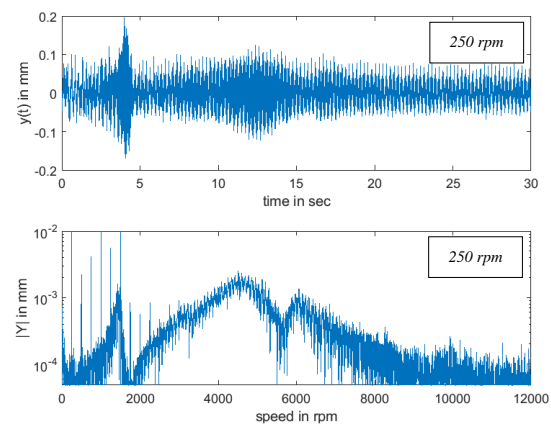


Figure 10: Unfiltered rotor response at AMB1 at 250 rpm.

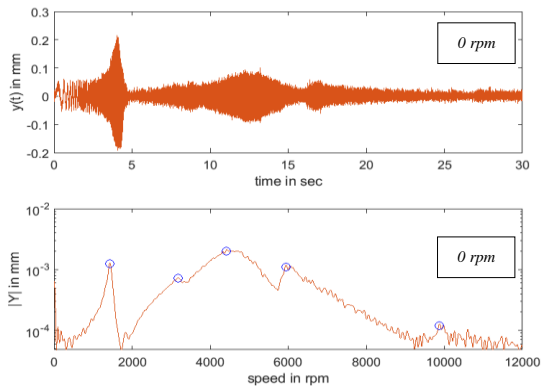


Figure 11: FFT of filtered time history at AMB1 for rotor at rest.

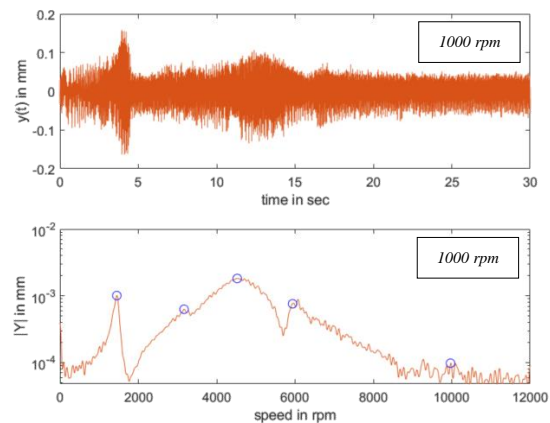


Figure 14: FFT of filtered time history at AMB1 at 1000 rpm.

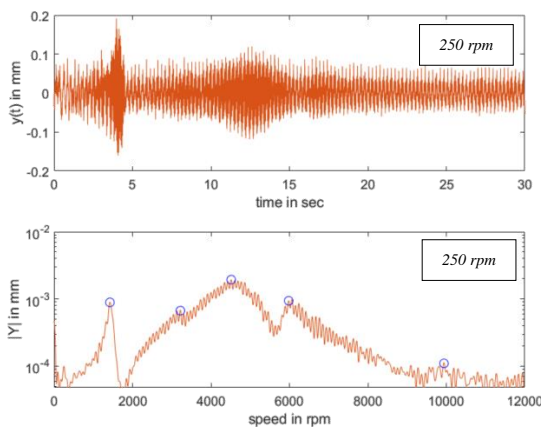


Figure 12: FFT of filtered time history at AMB1 at 250 rpm.

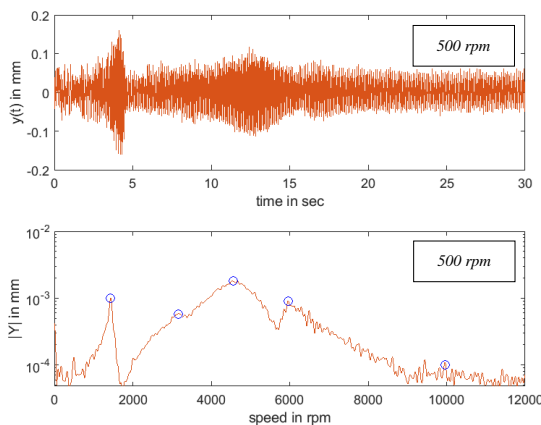


Figure 13: FFT of filtered time history at AMB1 at 500 rpm.

The resonance peaks in the frequency spectra indicate the dominant natural frequencies at each rotor speed. The identified resonances are summarized in Table 1. The values show a marginal dependency on the speed. This is expected for the present rotor configuration which is very close to a Jeffcott rotor with a central disc and symmetric AMBs. The natural frequencies are plotted against the corresponding rotor speed resulting in the experimentally identified Campbell diagram in Fig. 15.

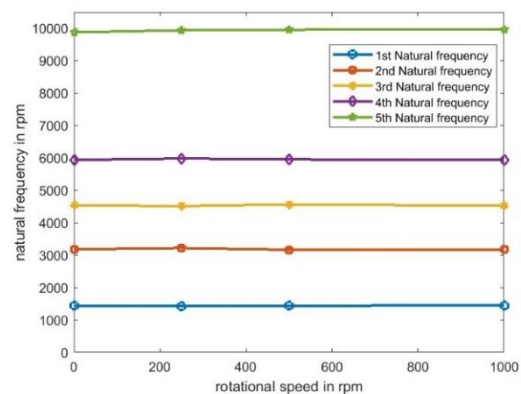


Figure 15: Campbell diagram of the flexible rotor supported by AMBs in Figure 7.

The corresponding mode shapes can be extracted by evaluating the displacements at AMB 1, the central disc and AMB 2 at the identified natural frequencies.

Table 1: Natural frequencies of the rotor at different rotational speeds.

Rotating speed (rpm)	Modes (rpm)				
	1 st	2 nd	3 rd	4 th	5 th
0	143 6	3182	4538	5940	9876

250	142 4	3220	4516	5982	9940
500	143 4	3166	4566	5956	9958
1000	145 0	3168	4524	5944	9968
Max. difference from 0 rpm	1%	1.1%	0.6%	0.7%	0.9%

5. CONCLUSION

By applying a frequency sweep in situ in the rotor system via an active magnetic bearing is capable of exciting the rotor during operation at its natural frequencies. It is possible to excite the rotor sufficiently via the AMB along with the position control of the PID-controllers of each AMB. The level of excitation creates sufficient response levels in terms of noise and overlays with unbalanced response. A low-pass filter is applied for increasing the robustness in the identification of the resonance peaks that eventually results in the experimentally identified Campbell diagram during rotor operation. In the speed range up to 1000 rpm, five distinct natural frequencies are identified clearly within the frequency range up to 180 Hz or 10,800 rpm. For the present Jeffcott-like configuration, the Campbell diagram shows straight horizontal lines. The maximum percent deviation from the natural frequencies at stationary position of the rotor is 1 percent (1st mode), 1.1 percent (2nd mode), 0.6 percent (3rd mode), 0.7 percent (4th mode) and 0.9 percent (5th mode). As explained earlier, it is an expected result for the current rotor configuration with a centre disc and symmetric AMBs. Hence, the gyroscopic effect is rendered negligible, and the bearing coefficients do not depend on the speed. In a future step, a second disc will be introduced to realize a rotor with an overhang disc which shows usually strong gyroscopic effect.

REFERENCES

1. G. Schweitzer and E. H. Maslen, Active Magnetic Bearings: Theory, Design, and Application to Rotating Machinery, Springer, 2009.
2. T. R. Fuhrmann and K. P. Hollkamp, "Influence of Magnetic Bearing Characteristics on the Campbell Diagram of a

- Rotor," *ASME Journal of Turbomachinery*, vol. 126, no. 4, pp. 504--510, 2004.
3. P. Nyberg and G. Schweitzer, "Rotordynamic Analysis Using Active Magnetic Bearings," *IEEE Transactions on Magnetics*, vol. 33, no. 5, pp. 4002--4008, 1997.
4. D. J. Gunter and A. K. Gupta, "Rotordynamic System Identification Using Active Magnetic Bearings," *Mechanics of Machine Theory*, vol. 45, no. 5, pp. 682--694, 2010.
5. M. E. Karamanci and B. F. Wissa, "Application of Active Magnetic Bearings for Vibration Control and Campbell Diagram Mapping of Rotating Machinery," *Journal of Vibration and Acoustics*, vol. 136, no. 3, p. 031008, 2014.
6. R. Tamrakar and N. Mittal, "Campbell diagram analysis of open cracked rotor," *Engineering Solid Mechanics*, vol. 4, no. 3, pp. 159-166, 2016.
7. T. G. Ritto, R. H. Lopez, R. Sampaio and J. E. Souza de Cursi, "Robust optimization of a flexible rotor-bearing system using the Campbell diagram," *Engineering Optimization*, vol. 43, no. 1, pp. 77-96, 2011.
8. M. S. Fasih, J. Van Baren and F. Dohnal, "Experimental verification of periodic control during run-up of a flexible rotor," 2024.
9. D. Halliday, R. Resnick and J. Walker, *Fundamentals of Physics*, Hoboken, NJ: Wiley, 2014.
10. P. A. Tipler and M. Gene, *Physics for Scientists and Engineers*, New York: W. H. Freeman and Company, 2008.
11. A. V. Oppenheim, A. S. Willsky and S. H. Nawab, *Signals and Systems*, Prentice Hall, 1996.

Study on the Impact of Ozone and Humidity on the Aging of Polymeric Composite Materials

Fatma Gül Yiğit¹, Mehmet Karahan²

¹Uludag University/ Institute of Science/Mechanical Engineering

²Uludag University /Vocational School of Technical Sciences

mkarahan@uludag.edu.tr

ABSTRACT

Polymer composites tend to degrade over time, resulting in a reduction in their mechanical properties. This degradation can be caused by various internal and external factors, including high temperature, humidity, ultraviolet rays, ozone, chain structure, combination, and aggregation. To counteract the aging of polymer matrix composite materials due to moisture and ozone, chemical fillers have been utilized. The aim of this study is to show, through experimental studies, tests, and analyses, that incorporating aging-retarding or preventive agents in composite production can prolong the lifespan and enhance the safety of composite materials. The study examines how carbon/epoxy composites age under different humidity and ozone concentrations and assesses the impact of adding ZnO to the epoxy resin on the material's aging process. The findings revealed that ZnO, used as a filler, reacted with ozone and enhanced the mechanical properties of the composite material.

KEYWORDS: carbon/epoxy composites, ozone aging, humidity, mechanical properties, ZnO

1. INTRODUCTION

Composites have an important role in many industries such as automotive, marine, construction, packaging, etc. due to their resistance to abrasion, chemicals and better mechanical properties such as high strength-to-weight ratios [1]. Aging in polymer matrix composite materials can occur due to factors like exposure to ultraviolet rays, high temperature, humidity, ozone, as well as internal factors such as chain structure, composition, and aggregation [2]. When subjected to high temperatures, polymer materials degrade rapidly. Furthermore, thermal cycling can lead to cracks in laminates and accelerate crack growth in oxidative atmospheres [3]. Several studies have been conducted to examine the effects of thermal aging on composites, with a focus on issues such as changes in shear strength and impact performance, deteriorations in the morphology between fiber/resin, and alterations in mechanical properties [5,6,7].

Moisture exposure is a significant factor contributing to the aging of composites. Polymer matrix composites are prone to instability when exposed to high temperatures and humidity during service. In humid environments, these composites absorb moisture and expand [7]. This expansion leads to a change in their mechanical properties, resulting in decreased damage tolerance and structural durability in the designed components. Several studies have explored the impact of moisture on the aging of polymer matrix composites. While some studies have focused on understanding the changes in mechanical properties and the mechanisms of composite materials due

to humidity, others have specifically investigated the material's response in marine environments by simulating exposure to salt water [8,9,10].

One of the factors that affect the properties of polymer-based composite materials under atmospheric conditions is ozone. Depending on its location, ozone can be either beneficial or harmful. Ozone can react with organic or inorganic compounds to form harmful products such as hydroxides or hydroperoxides [11,12]. Middleton examined the characterization of aging of hybrid composite rods and pure resin in ozone and high temperature [13]. The study revealed that residual stresses after aging at 140°C for one year were minimal but significant at temperatures above 160°C. The obtained results showed that laminated composites tested at room temperature yielded 17% lower tensile strength for ozone-conditioned laminated composites alone and 26% lower tensile strength when immersed in water.

Composite materials have their own set of advantages and disadvantages. However, some fillers can be added to eliminate these disadvantages or to give the composite new properties. By doing so, the composite material can meet high performance demands and the quality of the material increases. One such filler is ZnO, a metal oxide that has both inorganic and semiconductor properties and can be found in various structures. Gull et al. conducted a study where they produced glass fiber reinforced polyester (GFRP) composites with varying concentrations of ZnO filler [14]. They investigated the mechanical and thermal behavior of these composites and found that the bending strength of the GFRP composite with 3 wt% ZnO filler

was improved up to 62.12% compared to the unfilled composite. Furthermore, the hardness, impact strength, and thermal stability were found to increase with increasing ZnO concentration. They measured the dielectric constants and losses of the composites in the frequency range of 1-10 MHz. The results showed that modified w-ZnO had a remarkable effect on the dielectric properties of the composites. They reported that the dielectric constants and losses increased as the w-ZnO content increased.

It has been observed that atmospheric conditions can cause aging in composites, leading to a decrease in mechanical properties. There has been a lack of research aimed at improving this situation. To address this, experimental studies were conducted to examine the use of anti-aging agents in composite production, with the aim of ensuring safer and longer-lasting use of composite materials. The study focused on the aging effect of carbon/epoxy composites at different humidity and ozone concentrations and investigated the effects of adding ZnO into epoxy resin on the aging life and mechanical properties of the composite material.

2. MATERIAL AND METHODS

In this study, carbon-epoxy composites were produced by using certain proportions of ZnO as an anti-ageing agent. The fiber type and properties used in the production of carbon-epoxy composites are given in Table 1.

Table 1: Properties of 3K Carbon Fiber

Parameters	3K Carbon (200 tex)
Fiber diameter, mm	7
Fiber Young modulus, GPa	238
Fiber strength, MPa	3950
Fiber ultimate elongation, %	1,7
Areal density , g/m ²	245
Fiber density, g/cm ³	1,76

Samples Preparation

The composite material was produced by the vacuum infusion method using the reinforcement and matrix material whose properties are given in Table 1. In the production of the samples, the fiber arrangement was made so that the warp directions were in the same direction. A homogeneous mixture was obtained by adding certain proportions of ZnO to the resin. The prepared resin was immersed into the fiber reinforcement

using the vacuum infusion method, and the composite plate was allowed to cure at 23 °C for 24 hours. The presence of ZnO in the structure was also proved by optical microscope images. As seen in Figure 1, the presence of ZnO is clearly seen in the cross-section view taken from 2 different samples. In order to better understand the reaction of the composite samples as a result of their interaction with ozone, elemental analysis was performed, and SEM images were examined.

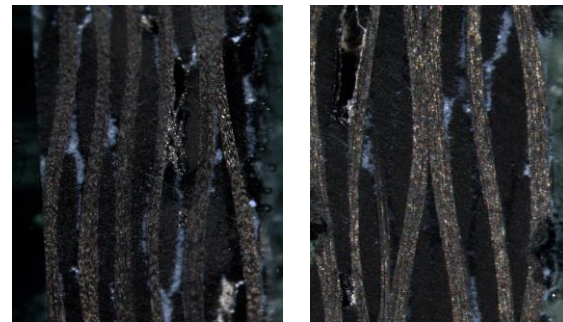


Figure 1. Cross-sectional optical microscope image of the carbon-epoxy sample

Ozonization Condition

While some of the pure samples containing 1%, 2%, and 4% ZnO additive by weight of the resin were left untreated, some were subjected to ozone-induced ageing. The effect of chemical additive on ozone degradation of polymer matrix composites was examined under 3 different ozone concentrations and 2 different humidity amounts. The samples were carried out in the ANSEROS SIM7300-TH model ozone test chamber at 300, 500 and 700 pphm ozone concentrations.

Tensile Strength Tests

The samples cut from the composite plate were prepared with a 25mm*225mm diamond-tipped cutter, and 40mm*25mm aluminum endtabs were glued to both ends of the samples with Araldite 2015 two-component epoxy adhesive. Samples of 2 different fiber materials were tested according to ASTM D 3031 standard.

3. RESULTS AND DISCUSSION

The main issues to determine the effects of ageing on an industrial scale are changes in physical properties such as tensile strength, hardness or modulus of elasticity. While evaluating these changes, the homogeneous distribution of ZnO mixed into the resin and the reactions and products resulting from the interaction of O₃ with ZnO were also taken into account. Tensile tests were applied to the samples before and after processing, and the tensile test results are presented in Tables 3 and 4.

Table 2. Tensile Strength of Untreated Samples

		σ (MPa)	E(GPa)
Untreated	No added	498,7	57,565
	% 1 ZnO	332,498	42,645
	% 2 ZnO	370,153	45,224
	% 4 ZnO	407,575	44,255

Table 3. Tensile Strength of Treated Samples

		%40 Humidity	
		σ (MPa)	E(GPa)
300 pphm	No added	329,0225	55,84
	% 1 ZnO	336,64	38,526
	% 2 ZnO	368,1458	49,77
	% 4 ZnO	411,7213	44,83
500 pphm	No added	369,9098	54,32
	% 1 ZnO	376,5307	53,41
	% 2 ZnO	472,6988	49,59
	% 4 ZnO	511,9791	43,26
700 pphm	No added	341,9015	55,02
	% 1 ZnO	314,0613	42,78
	% 2 ZnO	391,3848	45,88
	% 4 ZnO	408,9014	43,06

An additive added to the composite by adding it to the resin plays an important role in reducing the strength of the composite material. This situation is clearly seen in the values given in the untreated group in Table 5. All untreated and treated samples were compared among themselves. While the tensile strength value was 494.1 MPa in the pure and untreated sample, this value decreased by 32.7%, 25% and 17.5%, respectively, when the additive was added at different rates. In addition, the tensile strength values of samples exposed to ozone and without additives showed a decrease compared to the initial value. These values are 34.02%, 25.82% and 31.14% lower than the tensile strength values of the pure and untreated sample given above, respectively.

All processed samples were compared among themselves. Under 300 pphm ozone concentration, the tensile strength value of the pure sample was measured as 329.0225 MPa. It was observed that with the addition of ZnO as an additive at different concentrations, this situation was in the opposite direction to the untreated group.

The change in tensile strength was also calculated for the samples under 500 and 700 pphm ozone. For 40% humidity, the percentage changes of samples below 500 pphm ozone increased by 1.75%, 21.75% and 27.75%, respectively. In samples under 700 pphm ozone, unlike other conditions, an 8.14% decrease in tensile strength was observed between the pure sample and the 1% added sample.

The elemental analysis of the pure and untreated carbon-epoxy sample was performed, SEM images were examined. As a result of the analysis, it was determined that the oxygen rate in the pure and untreated sample was 11.1%.

After this process, SEM images of the untreated and doped composite sample were examined and element ratios were analyzed for an accurate comparison. the O ratio of the sample was found to be 11.9%, while the Zn ratio was found to be 0.4%.

O element showed an initial decreasing trend and then an increasing trend. While the oxygen element ratio shows a decreasing and increasing trend, the strength value is constantly increasing. As the O% wt ratio increases, ZnO in the composite sample reacts with O₃.

4. CONCLUSION

The tensile strength of untreated and pure carbon-epoxy composite samples is at least 18% higher than composites with additives and without treatment. However, this changes when composites are subjected to ozone conditioning. The tensile strength of pure and treated composite increases as additives are added to the composite. As the additive concentration increases, the tensile strength also increases. This result is confirmed by tests and analyses.

Tensile testing was applied to all samples, and all tests were repeated 3 times for each group to ensure reliability. The results showed that as the additive was added to the samples under 300 parts per million (ppm) ozone concentration, the tensile strength increased by a maximum of 20%. For samples under 500 and 700 ppm ozone concentration, tensile strength values respectively increased by 27% and 16.4%.

Exposure to ozone reduces the strength of composite materials. To minimize this disadvantage, ZnO can be considered as a substance that reacts with O₃, therefore, minimizing ozone's direct effect on the material.

18-22.

ACKNOWLEDGEMENTS

This study was carried out by students in the tübitak 2244 program. The materials and equipment we used in our study were provided by Bursa R&D and Coordination Center (BUTEKOM). We would also like to thank BUTEKOM for their support during production and experiments.

REFERENCES

1. Kumar, S., & Balachander, S. (2020). Studying the effect of reinforcement parameters on the mechanical properties of natural fibre-woven composites by Taguchi method. *Journal of Industrial Textiles*, 50(2), 133-148. Maxwell, A. S., Broughton, W. R., Dean, G. D., & Sims, G. D. (2005). Review of accelerated ageing methods and lifetime prediction techniques for polymeric materials.
2. Dede, F., Kalay, O., Yılmaz, T., & Karpat, F. Experimental and numerical analysis of mechanical properties of carbon fiber-reinforced polymer gears. *Acta Technica Corviniensis – Bulletin of Engineering* 2023, 16(1), 25-28.4
3. Akay, M., Spratt, G. R., & Meenan, B. (2003). The effects of long-term exposure to high temperatures on the ILSS and impact performance of carbon fibre reinforced bismaleimide. *Composites science and technology*, 63(7), 1053-1059.
4. Zhang, M., Sun, B., & Gu, B. (2016). Accelerated thermal ageing of epoxy resin and 3-D carbon fiber/epoxy braided composites. *Composites Part A: Applied Science and Manufacturing*, 85, 163-171.
5. Zuo, W., Luo, Q., Li, Q., & Sun, G. (2023). Effect of thermal and hydrothermal ageing on the crashworthiness of carbon fiber reinforced plastic composite tubes. *Composite Structures*, 303, 116136
6. Burks, B., & Kumosa, M. (2012). The effects of atmospheric ageing on a hybrid polymer matrix composite. *Composites Science and Technology*, 72(15), 1803-1811.
7. Shi, Z., Zou, C., Zhou, F., & Zhao, J. (2022). Analysis of the Mechanical Properties and Damage Mechanism of Carbon Fiber/Epoxy Composites under UV Ageing. *Materials*, 15(8), 2919.
8. Ray, B. C. (2006). Temperature effect during humid ageing on interfaces of glass and carbon fibers reinforced epoxy composites. *Journal of colloid and interface science*, 298(1), 111-117.
9. Liu Jianhua, Zhao Liang, Hu Jianping, & Gong Zhaohe. (2007). Effect of salt spray on mechanical properties of glass fiber reinforced polymer composites. *Journal of Composite Materials*, 24(3), 18-22.
10. Liao, K., Schultheisz, C. R., & Hunston, D. L. (1999). Effects of environmental ageing on the properties of pultruded GFRP. *Composites Part B: Engineering*, 30(5), 485-493.
11. Karahan, M., Ozkan, F., Yildirim, K., & Karahan, N. (2016). Investigation of the properties of natural fibre woven fabrics as a reinforcement materials for green composites. *Fibres & Textiles in Eastern Europe*, (4 (118), 98-104.
12. Von Gunten, U. (2003). Ozonation of drinking water: Part I. Oxidation kinetics and product formation. *Water research*, 37(7), 1443-1467.
13. Middleton, J. M. (2014). Ageing of a Polymer Core Composite Conductor under combined ozone and temperature conditions (Doctoral dissertation, University of Denver).
14. Gull, N., Khan, S. M., Munawar, M. A., Shafiq, M., Anjum, F., Butt, M. T. Z., & Jamil, T. (2015). Synthesis and characterization of zinc oxide (ZnO) filled glass fiber reinforced polyester composites. *Materials & Design*, 67, 313-317

Evaluating Capillary Pressure and Relative Permeability Models for Enhanced Reservoir Management

Muhammad Arslan¹, Khurram Zahoor², Ahmed Nouman³

¹University of Chakwal, muhammad.arslan@uoc.edu.pk

²UET, Lahore, mkzahoor@yahoo.com

³Örebro University,

* ahmed.nouman@oru.se

ABSTRACT

Accurate characterization of petrophysical properties is essential for optimizing hydrocarbon extraction for reservoir management. Capillary pressure and relative permeability are key factors that influence fluid distribution and flow within reservoirs. This study investigated the implications of these properties on reservoir simulations, focusing on the Brooks-Corey and Van Genuchten models. Significant variations between these models, particularly near the endpoint saturation, can lead to inaccurate predictions and inefficient recovery strategies. This research refines these models by integrating real field data, enhancing their practical applications. The methodology involved data analysis, model testing, and comparison of predictions with field results. By generating capillary pressure and relative permeability curves, the study evaluated the recovery efficiencies and explored the effects of endpoint saturation variations. The results indicate substantial differences between the models, especially at saturation endpoints, necessitating careful history matching with field data. This study underscores the importance of incorporating geological heterogeneity in modelling for more accurate forecasts. Advanced models that consider geological features are required to optimize hydrocarbon recovery. Improving these models can enhance reservoir management strategies, align with global energy demands and sustainability goals, and improve the petroleum industry's strategic planning.

KEYWORDS: capillary pressure models, relative permeability, endpoint saturation, reservoir simulation, geological heterogeneity.

1. INTRODUCTION

Reservoir management is a pivotal element in the petroleum industry, demanding precise characterization of petrophysical properties to maximize hydrocarbon extraction efficiency. The understanding of capillary pressure and relative permeability within reservoir rocks is essential for optimal fluid distribution and flow modelling [1,2]. Capillary pressure describes the force required to displace fluids within the porous media of the reservoir, a crucial factor in determining fluid saturation and distribution [3,4]. Relative permeability measures the ability of the reservoir rock to transmit fluids when multiple fluid phases are present, directly influencing recovery strategies and the efficiency of hydrocarbon production [5–7].

Analytical models, particularly the Brooks-Corey and Van Genuchten models, are fundamental in predicting the behaviour of these fluids under varying conditions [8,9]. These models are most widely accepted and used in the petroleum industry. Initially, they were developed for soil science but have a relevant application in reservoir engineering, adopted for assessing fluid controlling parameters in the petroleum industry for forecasting the flow within porous media. The Brooks-Corey model is particularly valued in the petroleum industry for its ability to describe flow in heterogeneous and high-permeability reservoirs, which are common in many oil and gas fields. Its simplicity and effectiveness in modeling multiphase flow make it a standard for evaluating porous media

behavior. While the Van Genuchten model is known for its ability to fit a wide range of data due to its flexible S-shaped curves. It provides a more accurate description of capillary pressure and fluid distribution in low-permeability or tight reservoirs, which are becoming increasingly important with the development of unconventional resources. The Brooks-Corey model is well-suited for reservoirs with a broad range of permeability, providing reliable results for water and gas injection strategies. The Van Genuchten model is often used for fractured reservoirs and low-permeability formations, where fluid flow behavior is more complex. Their usage in the petroleum industry helps to refine predictions of fluid behavior under various saturation levels. These models in conjunction with real reservoir data, offering a more nuanced evaluation of capillary effects and fluid flow dynamics over a wide range of reservoirs. These models are critical tools in the petroleum industry for evaluating the relationship between capillary pressure, saturation, and relative permeability, which are essential parameters for reservoir characterization and fluid flow predictions. Understanding these relationships is vital for improving recovery techniques, optimizing production, and managing reservoirs more effectively.

By using these models, engineers can simulate how fluids move through the reservoir over time, informing decisions related to primary, secondary, and tertiary recovery methods. In EOR techniques such as water flooding, gas injection, or chemical flooding, these models provide a better understanding of how injected fluids interact with



existing reservoir fluids. By predicting residual oil saturation and capillary pressure effects, both models help optimize the design of EOR projects, improving recovery factors.

The Brooks-Corey model is typically used for reservoirs where water-wet conditions dominate, while the Van Genuchten model is preferred for reservoirs with mixed-wet or oil-wet characteristics, common in more complex geological settings. Additionally, in cases where detailed experimental data are limited, these models serve as effective tools for generating reasonable initial estimates of capillary pressure and relative permeability. Their simplicity, ease of use, and integration into industry-standard simulation tools ensure that they continue to play a role in reservoir evaluation and management.

These models facilitate the construction of capillary pressure and relative permeability curves, which are indispensable tools for engineers. By utilizing these curves, professionals can simulate how changes in pressure and saturation levels impact fluid flow, enabling more accurate predictions and informed decision-making in reservoir management [10]. The accuracy of these models directly correlates with the effectiveness of the strategies employed for hydrocarbon recovery, reducing both financial costs and engineering risks.

The current study aims to delve into the implications of capillary pressure and relative permeability on reservoir simulations, with a specific focus on the recovery efficiencies predicted by the Brooks-Corey and Van Genuchten models. Additionally, this research investigates the effects of endpoint saturation variations on flow distribution within porous media [11]. Despite the substantial body of research already existing, this area remains ripe for further exploration [12–14]. Variations in saturation levels can significantly alter fluid distribution and flow dynamics, necessitating a deeper understanding to optimize recovery techniques.

To enhance the comprehensiveness of the models used in reservoir simulations, this study will also explore the integration of real field data into the Brooks-Corey [8] and Van Genuchten [9] models. By comparing the theoretical predictions with actual field results, this research aims to refine the models for more realistic and practical applications in reservoir management. This approach will not only validate the existing models but also identify potential areas for modification and improvement, contributing to more robust and accurate predictive tools in the petroleum industry.

Through rigorous data analysis and model testing, this study seeks to contribute to the broader understanding of petrophysical properties in reservoir engineering. By improving the accuracy of capillary pressure and relative permeability models, the petroleum industry can achieve more efficient and economical hydrocarbon recovery, aligning with global energy demands and sustainability

goals. The findings of this research could offer significant implications for future technological developments and strategic planning in reservoir management.

Reservoir management, a pivotal element in the petroleum industry, requires the precise characterization of petrophysical properties to maximize hydrocarbon extraction efficiency. Capillary pressure and relative permeability, two key factors, are essential for optimal fluid distribution and flow modelling. Capillary pressure describes the force required to displace fluids within the porous media of the reservoir, a crucial factor in determining fluid saturation and distribution. Relative permeability measures the ability of a reservoir rock to transmit fluids when multiple fluid phases are present, directly influencing recovery strategies and the efficiency of hydrocarbon production.

Accurately determining petrophysical properties is critical at any reservoir exploration and management stage. Capillary pressure and relative permeability are essential parameters in reservoir engineering calculations that play vital roles in reservoir development. The capillary pressure provides insights into the irreducible saturation of the displaced fluid, indicating the pressure at which destruction begins. On the other hand, relative permeability expresses a rock's ability to allow fluid flow in the presence of multiple fluids. These parameters are particularly significant in unconventional rocks and unique fluid systems where mass or phase transfer occurs owing to pressure changes, impacting the fluid distribution and recovery processes.

Analytical models, particularly the Brooks-Corey and Van Genuchten models, are fundamental in predicting the behaviour of these fluids under varying conditions [8,9]. These models facilitate the construction of capillary pressure and relative permeability curves, which are indispensable tools for engineering. By utilizing these curves, professionals can simulate how changes in pressure and saturation levels impact fluid flow, enabling more accurate predictions and informed decision-making in reservoir management. The accuracy of these models directly correlates with the effectiveness of the strategies employed for hydrocarbon recovery, reducing both the financial and engineering costs.

The current study aims to investigate the implications of capillary pressure and relative permeability on reservoir simulations, specifically focusing on the recovery efficiencies predicted by the Brooks-Corey and Van Genuchten models. Additionally, this study investigated the effects of endpoint saturation variations on the flow distribution within porous media. Despite substantial research, this area remains ripe for further exploration [11,12,15–17]. Variations in saturation levels can significantly alter the fluid distribution and flow dynamics, necessitating a more profound understanding to optimize recovery techniques.

This study also explores integrating real field data into the Brooks-Corey and Van Genuchten models to enhance the comprehensiveness of the models used in reservoir simulations. By comparing the theoretical predictions with actual field results, this research aims to refine the models for more realistic and practical applications in reservoir management. This approach will validate the existing models and identify potential areas for modification and improvement, contributing to more robust and accurate predictive tools in the petroleum industry. Through rigorous data analysis and model testing, this study aims to contribute to a broader understanding of the petrophysical properties of reservoir engineering.

Ultimately, the potential of significantly enhancing hydrocarbon recovery processes lies in improving the accuracy of capillary pressure and relative permeability models. By aligning these models with the global energy demands and sustainability goals, the petroleum industry can achieve more efficient and economical hydrocarbon extraction. The findings of this study could offer significant implications for future technological developments and strategic planning in reservoir management. Enhanced modelling techniques can lead to better prediction accuracy, reduced uncertainties, and optimized recovery strategies, ensuring a more sustainable and economically viable approach to reservoir development and management.

2. METHODOLOGY

In this research, we developed a detailed approach to assess how capillary pressure and relative permeability affect reservoir simulations, specifically focusing on the utilization of the Brooks-Corey and Van Genuchten models as shown in Figure 8: Block Diagram of our Methodology. Our initial step involved gathering capillary pressure and saturation data from field experiments as well as existing literature, which formed the basis for constructing the necessary curves that illustrate the behaviour of these petrophysical properties under different reservoir conditions.

For the Brooks-Corey model, we adopted a log-log plotting technique to establish the model parameters, which facilitated the graphing of capillary pressure against effective saturation using the equation.

$$P_c = P_d S_e^{\frac{-1}{\lambda}}$$

In contrast, we applied a semi-log plotting method for the Van Genuchten model to identify its essential constants from the equation.

$$P_c(S_e) = \frac{1}{\alpha} \left(S_e^{\frac{-1}{m}} - 1 \right)^{\frac{1}{n}}$$

These methodologies were vital in accurately developing the models to reflect the real physical processes within the reservoir.

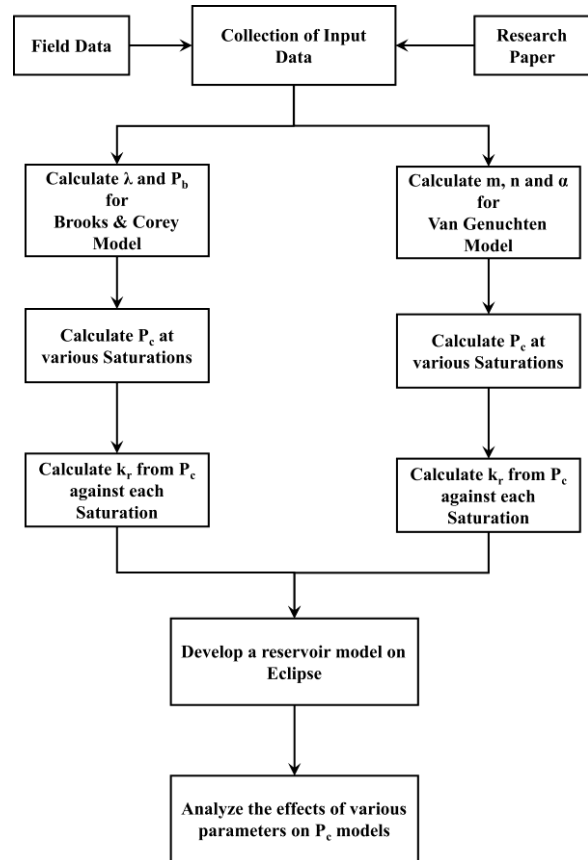


Figure 8: Block Diagram of our Methodology

Our study further examined how changes in endpoint saturation influence the performance of these models. Through this investigation, we produced curves for relative permeability of both the wetting and non-wetting phases. This phase of analysis is crucial for a deeper understanding of the fluid mechanics within the reservoir, particularly in terms of how various fluids move and interact within the rock's porous structure.

We then applied our findings on capillary pressure and relative permeability to model and forecast the performance of the reservoir under different operational conditions. This phase involved analysing key factors like oil production rates and water cuts, which are crucial for maximizing hydrocarbon recovery and enhancing the efficiency of reservoir management. Our integrated approach not only broadened our comprehension of fundamental petrophysical properties but also improved the predictive accuracy of our simulations.

This methodology enabled a comprehensive examination of the critical factors that influence fluid dynamics in reservoirs, helping to refine the simulation models used in the petroleum industry. By integrating both field data and

theoretical models, our study offers significant insights into optimizing reservoir management strategies, contributing to more effective and economically viable hydrocarbon recovery processes.

3. RESULTS AND DISCUSSION

In this comparative analysis of field oil production rates and field water cuts, notable discrepancies were observed between the outputs predicted by the Brooks-Corey and Van Genuchten models as shown in Figure 9: Comparison of the field oil production rate (FOPR) and the field water cut (FWCT). The Brooks-Corey model yielded significantly lower production rates compared to the Van Genuchten model. This variance primarily stemmed from the differences in the relative permeability calculated for the wetting phase by each model, where the Brooks-Corey model demonstrated lower fluid mobility that negatively impacted production rates.

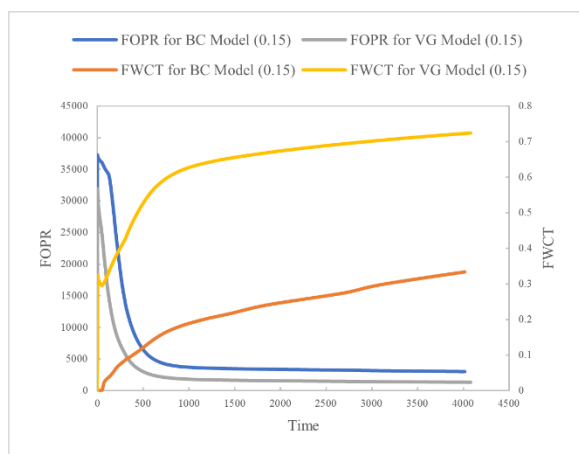


Figure 9: Comparison of the field oil production rate (FOPR) and the field water cut (FWCT)

The analysis also revealed that both models deviated from actual field data, indicating a gap in their ability to accurately replicate reservoir performance. This gap highlights the inherent limitations of these models, particularly their failure to incorporate geological heterogeneity. The complex interplay of rock properties and reservoir characteristics, which significantly influence fluid dynamics, was not adequately represented.

The need for more advanced modelling techniques that can integrate detailed geological features—such as fractures, faults, and varied rock types—is evident from this study. Incorporating these elements into reservoir models is crucial for enhancing the accuracy of predictions concerning oil and water production rates. More sophisticated models would allow for a more realistic simulation of the physical and chemical interactions occurring within the reservoir.

These findings suggest that while the Brooks-Corey and Van Genuchten models are useful for basic predictions and educational purposes, their practical application is limited in scenarios involving complex geological settings. To address this limitation, future research should focus on developing models that more accurately reflect the geological diversity and complexity of reservoir environments. Ultimately, enhancing reservoir models to accurately incorporate geological heterogeneity will bridge the theoretical and practical discrepancies observed in field data comparisons. This improvement is essential for optimizing hydrocarbon recovery strategies, leading to more efficient and economically viable production outcomes in the petroleum industry.

4. CONCLUSION

In this study, it was examined that the performance of the Brooks-Corey and Van Genuchten capillary pressure models in predicting relative permeability and production rates in petroleum reservoirs. These findings indicate that while both models perform similarly at higher wetting phase saturation, their predictions diverge significantly at lower saturation close to endpoint values. Particularly, changes in endpoint saturation had a more pronounced impact on the relative permeability curves for the non-wetting phase. These results underscore the importance of integrating actual field production data and geological heterogeneity into these models to enhance their accuracy. The study highlights the need for careful history matching and suggests refining model forecasts to mitigate uncertainties, ensuring more reliable predictions in reservoir management.

REFERENCES

1. Gang T, Kelkar M. A more general capillary pressure curve and its estimation from production data. SPE Rocky Mountain Petroleum Technology Conference/Low-Permeability Reservoirs Symposium, SPE; 2007, p. SPE-108180-MS.
2. Hassler GL, Brunner E. Measurement of capillary pressures in small core samples. Transactions of the AIME 1945;160:114–23.
3. Ahmed T. Fundamentals of Reservoir Fluid Behavior. Reservoir Engineering Handbook, Elsevier; 2010, p. 1–28. <https://doi.org/10.1016/B978-1-85617-803-7.50009-2>.
4. Purcell WR. Capillary pressures-their measurement using mercury and the calculation of permeability therefrom. Journal of Petroleum Technology 1949;1:39–48.
5. Zahoor MK, Haris M, Akhtar J. Predictive modeling using capillary pressure models and fluid densities and their effect on reservoir fluid distribution and dynamics. Journal of faculty of engineering & technology 2017;24:73–81.



First International Conference on Advances in Mechanical, Materials, Mechatronics, and Energy Engineering (ICAME-24)



6. Zahoor MK. Brooks & corey model and extended analysis to develop a new correlation. PAKISTAN ACADEMY OF SCIENCES 2011:197.
7. Li K, Horne RN. Comparison of methods to calculate relative permeability from capillary pressure in consolidated water-wet porous media. Water Resources Research 2006;42.
8. Brooks RH. Hydraulic properties of porous media. Colorado State University; 1965.
9. Van Genuchten MT. A closed-form equation for predicting the hydraulic conductivity of unsaturated soils. Soil Science Society of America Journal 1980;44:892–8.
10. BÓDI ÁP-T. Determination of capillary pressure and relative permeability curves with a novel ultra rock centrifuge. Geosciences and Engineering 2012;1:75–86.
11. Manthey S. Two-phase flow processes with dynamic effects in porous media-parameter estimation and simulation. 2006.
12. Sun Y, Buscheck T, Lee K, Hao Y, James S. Modeling thermal-hydrologic processes for a heated fractured rock system: impact of a capillary-pressure maximum. Transport in Porous Media 2010;83:501–23.
13. Shen B, Li Z, Zheng Z, Li C, Lei H, Zhang L, et al. Status and relative content of water in shale determined by thermogravimetry-mass spectrometry analysis. Journal of Petroleum Science and Engineering 2021;196:107739. <https://doi.org/10.1016/j.petrol.2020.107739>.
14. De Falco MC, Adduce C, Negretti ME, Hopfinger EJ. On the dynamics of quasi-steady gravity currents flowing up a slope. Advances in Water Resources 2021;147:103791. <https://doi.org/10.1016/j.advwatres.2020.103791>.
15. Li K. Generalized Capillary Pressure and Relative Permeability Model Inferred from Fractal Characterization of Porous Media, 2004, p. SPE-89874-MS. <https://doi.org/10.2118/89874-MS>.
16. Matthai S, Bazrafkan S, Lang P, Milliotte C. Numerical Prediction of Relative Permeability in Water-Wet Naturally Fractured Reservoir Rocks. ECMOR 2012 - 13th European Conference on the Mathematics of Oil Recovery 2012. <https://doi.org/10.3997/2214-4609.20143167>.
17. Mehmani A, Prodanović M. The effect of microporosity on transport properties in porous media. Advances in Water Resources 2014;63:104–19. <https://doi.org/10.1016/j.advwatres.2013.10.009>.

Investigating Public Opinion to Overcome Energy Policy Hurdles in Pakistan

Hamza Babar¹, Ahmed Nouman²

¹ University of Management and Technology Lahore, eng.hamzababar@gmail.com

² Örebro University,

ahmed.nouman@oru.se

ABSTRACT

Energy policies in Pakistan are critical for addressing the country's severe energy crisis; however, their effective implementation faces significant challenges. The reliance on fossil fuels, inadequate infrastructure, and policy mismanagement have led to persistent energy deficits. Key obstacles include the scarcity of renewable energy sources, widespread corruption, and political instability, all of which exacerbate energy shortfalls. This study utilized a comprehensive survey methodology to capture public opinion and engage various consumer sectors to identify preferences for affordable energy and flat-rate billing. Our analysis indicates that a strategic shift towards renewable energy could mitigate this crisis, providing a cost-effective and sustainable solution. This study advocates policy revisions that emphasize transparent governance, infrastructure improvements, and public awareness campaigns. By incorporating consumer feedback into policy formulation and addressing systemic issues, Pakistan can enhance energy security and economic stability. The findings offer actionable recommendations for policymakers, suggesting targeted investments in renewable energy and robust regulatory frameworks to overcome existing challenges, thus paving the way for a more resilient and sustainable energy future. Additionally, this study underscores the importance of addressing corruption and political instability, which are critical to the success of any energy policy reform. These results highlight that consumer involvement and transparency are crucial for achieving public trust and cooperation. Pakistan can transition toward a more sustainable and reliable energy system through a comprehensive approach that includes technological advancements, regulatory support, and active public engagement.

KEYWORDS: renewable energy, energy policy, public perspective, sustainable development, energy crisis, consumer perspective

1. INTRODUCTION

Energy plays an important role in sustaining modern civilization's social and economic demands. Consequently, an uninterrupted supply of energy is crucial to the development and sustainability of countries. Developed nations today enjoy reliable energy supplies, which underpin their industrial progress and overall socioeconomic stability. In contrast, many developing countries have needed help to secure a reliable and sustainable source of electrical energy [1–3]. Approximately 25% of the world's population lives without electricity, which has remained relatively unchanged since the 1970s. This disparity underscores the need for effective energy policies in developing nations, including Pakistan.

Pakistan is currently facing a severe energy crisis that directly and indirectly affects all sectors of the economy [1,4,5]. Presently, the energy sector is grappling with a significant demand-supply gap that needs to be addressed [6–8]. Enhancing the energy mix to include more cost-effective and sustainable energy sources is crucial for mitigating this crisis [9–11]. The country's over-reliance

on fossil fuels is evident from its energy generation statistics. As of 2020, Pakistan's installed power generation capacity has reached 37,402 MW. However, the transmission and distribution infrastructure can only handle approximately 22,000 MW, leading to a substantial deficit during the peak demand periods [12–14].

This mismatch between the installed capacity and actual transmission capability highlights the inefficiencies within Pakistan's energy system, which hinders national development and economic growth. Despite the theoretical capacity to meet demand, practical limitations in infrastructure mean that the country experiences a deficit of approximately 3,000 MW during peak times. This deficit severely affects the residential, industrial, and other sectors, necessitating immediate and effective policy interventions to bridge the gap.

Effective energy policies are essential for addressing these challenges; however, their implementation in Pakistan needs to be improved by several factors. Key obstacles include inadequate power distribution systems, widespread corruption, over-reliance on fossil fuels, and a lack of renewable energy sources [15–17]. Furthermore, political instability exacerbates these issues, making it

difficult to execute long-term sustainable energy strategies [18,19]. Researchers have pointed out that countries incorporating public opinion into their energy policy formulations tend to develop more effective policies [20–22]. In Pakistan, defining energy policies based on public opinion is particularly critical, given the country's unique socioeconomic dynamics.

This study employed a comprehensive survey methodology to gather and analyse public opinion on energy policies to address these issues by engaging various consumer sectors—household, industrial, agricultural, commercial, and others—the survey aimed to identify the preferences and priorities of different stakeholders. The findings revealed a strong preference for affordable energy solutions and flat-rate billing, reflecting Pakistani consumers' economic pressures. These insights are crucial for informing policy revisions that are aligned with public needs and expectations.

Our analysis indicates that a strategic shift towards renewable energy could significantly mitigate the energy crisis in Pakistan. Renewable energy sources not only offer a sustainable and environmentally friendly alternative to fossil fuels but also have the potential to reduce the financial burden associated with energy production. This study advocates policy revisions that emphasize transparent governance, significant infrastructure improvements, and robust public awareness campaigns to facilitate the adoption of renewable energy technologies. Pakistan can enhance its energy security and economic stability by incorporating consumer feedback into policy formulation and addressing systemic issues, such as corruption and inadequate infrastructure.

In conclusion, this study provides actionable recommendations for policymakers, suggesting targeted investments in renewable energy and enhanced regulatory frameworks to overcome existing challenges. These steps are essential for creating Pakistan's more resilient and sustainable energy future. By adopting a comprehensive approach that includes technological advancements, regulatory support, and active public engagement, a country can transition to a more reliable and sustainable energy system, ultimately contributing to its broader socioeconomic development goals.

2. SURVEY METHODOLOGY AND PARTICIPANTS INSIGHT

The primary objective of this comprehensive survey was to investigate Pakistan's energy policies through the lens of public opinion from different energy consumers. The survey was designed to identify the key factors hindering effective energy policies and to gather consumer preferences, with the goal of informing future policy directions. The survey was distributed online to a diverse group of 793 individuals using Microsoft Forms. It can be found online [here](#). The participants were categorized by consumer type as domestic, commercial, industrial,

agriculture, and transportation, following the categorization suggested by Poudyal et al. (2019) [2]. Of the total invitations, 526 individuals responded, providing a substantial dataset for analysis.

The distribution of the respondents revealed a diverse representation, with predominant participation from domestic consumers, constituting 65% of the responses. Commercial consumers accounted for 10.5%, industrial consumers for 13.5%, agricultural consumers for 4%, and others for 6.5%. This varied representation across different sectors ensures a comprehensive understanding of energy challenges and preferences from multiple perspectives. Table 1 details the number of participants by consumer type and provides a clear overview of survey demographics.

The survey was structured into multiple sections to explore various aspects of energy consumption and policy impact thoroughly. The first section, titled "Introduction", played a crucial role in gathering the participants' basic demographic and professional details. This included questions regarding their name, education, consumer type, job specifications, and experience. This foundational information was crucial for contextualizing subsequent responses and ensuring the data could be analysed effectively across different consumer categories.

The second section, "Proposed Energy Strategy," consisted of four categorical questions aimed at identifying factors that could help address Pakistan's energy deficit. Participants were asked which energy sector should be prioritized in future policies, their preference for cheaper versus uninterrupted energy supply, their preferred billing policy, and their views on the potential of renewable energy sources to alleviate the current energy crisis. These questions were designed to gather insights into consumer priorities and expectations, essential for shaping effective and sustainable energy policies.

The third section, 'Factors Hindering Current Energy Policies,' focuses on identifying the underlying barriers to effective energy policy implementation in Pakistan. Fifteen factors were presented as shown in Table 10: Factor hindering energy policies, ranging from overpopulation to corruption and energy wastage. The participants rated these factors using a Likert scale ranging from 1 (low) to 7 (high) to gauge their perceived severity. This section is significant because it highlights global challenges identified by the World Bank and unique local issues that impact Pakistan's energy sector.

Table 10: Factor hindering energy policies

Sr. No.	Factors
1	Accidents/Disasters

2	Corruption
3	Delays in projects
4	Discontinuity of energy projects
5	Financial mismanagement
6	Government subsidies
7	Incompetent IPPs
8	International politics
9	Lack of dams and renewable energy
10	Lack of regular energy audits
11	National politics
12	Over consumption and wastage
13	Overpopulation
14	Poor infrastructure and distribution
15	Power theft

The survey findings provide several critical insights, shedding light on the significant barriers to effective energy policy implementation in Pakistan. Many participants highlighted the lack of renewable energy sources, corruption, and inadequate infrastructure as major hurdles. The preference for cheaper energy solutions over uninterrupted supply is evident, reflecting the economic pressures faced by Pakistani consumers. Additionally, there was a strong inclination towards flat-rate billing, suggesting the need for more predictable and manageable energy costs. These findings not only inform but also enlighten us about the current energy landscape in Pakistan.

One key aspect of the survey was the examination of public opinion regarding the role of renewable energy in addressing the energy crisis. An overwhelming majority of respondents believed that renewable energy sources could play a crucial role in mitigating current energy shortfalls. This sentiment underscores the importance of transitioning towards more sustainable energy solutions and the need for policy revisions that prioritize investments in renewable energy technologies.

The Survey was designed to provide a comprehensive understanding of the challenges and preferences related to Pakistan's energy policies. By incorporating public opinion and addressing systemic issues, our findings offer actionable recommendations for policymakers. These include targeted investments in renewable energy, infrastructure improvements, and enhanced public awareness campaigns. The insights gathered from the survey underscore the critical role of consumer feedback

in shaping effective energy policies, empowering the public to influence the direction of the energy sector and paving the way for a more resilient and sustainable energy future in Pakistan.

3. ANALYSIS OF CONSUMER RESPONSES TO ENERGY POLICY QUESTIONNAIRE

The survey on Pakistan's energy policies revealed a significant finding—a uniform preference across various consumer sectors, including the Domestic, Commercial, Industrial, Agriculture, and Transportation sectors. This widespread agreement on the critical aspects of energy policies suggests that future policies can be streamlined to effectively address common concerns. It reflects the collective stance of Pakistani consumers on pivotal energy issues, providing crucial insights for policymakers.

Participants were asked to prioritize sectors for future energy policies. Nearly half of the respondents (46%) identified the industrial sector as a priority, underscoring its perceived importance to Pakistan's national development. In contrast, 22% of the participants highlighted the domestic sector, demonstrating significant but less emphasis than industrial needs. The statistical analysis through chi-square tests validated these preferences, emphasizing a clear preference for boosting industrial energy support in future policies.

Preferences for energy-supply options also showed distinct trends. A majority (64%) of the respondents opted for cheaper energy rates over the reliability of an uninterrupted supply, which was chosen by 32% of the participants. This indicates that the cost of energy is a more critical issue for most consumers than is the consistency of its supply. The statistical significance of these findings, confirmed via chi-square tests, reaffirms the need for policies that focus on reducing energy costs to address consumer concerns effectively.

The survey further examined opinions on billing policies and the potential of renewable energy. 47% of respondents favored a flat rate billing approach, indicating a preference for simpler and more predictable charges. Meanwhile, 92% believed in the potential of renewable energy sources to mitigate Pakistan's energy crisis, a sentiment strongly supported by statistical evidence. These results suggest key areas for policy adjustment, including adopting flat-rate billing and increased investment in renewable energy to meet public expectations and enhance energy sustainability in Pakistan.

In the section on factors hindering the implementation of energy policies, participants rated 15 factors using a Likert scale ranging from 1 (low) to 7 (high). The results showed that the participants rated "Lack of Dams & Renewable Energy" as the highest contributor to the energy crisis of Pakistan, followed by "Corruption," "National Politics," and "Discontinuity of Energy Projects." Conversely,

“Accidents/Disasters” was the lowest-ranked contributing factor. The Friedman test showed that the difference in the ratings was significant, $X^2(14, n=164) = 583.9, p < 0.001$. The mean ranking of the top-rated factors, as revealed by Friedman’s test, is presented in Table 2.

A post-hoc Wilcoxon signed-rank test was performed to compare the top-rated factors. The test showed a non-significant difference between “Lack of Dams & Renewable Energy” and “Corruption,” with 53 participants rating the former higher, 40 rating it lower, and 88 rating them equally. However, a significant difference was found between “Corruption” and “National Politics” ($Z = 2.04, p < 0.05$), indicating that these factors are distinctly perceived in their impact on energy policy implementation.

The analysis did not observe any significant differences in opinion between the different consumer types regarding the top-rated factors. The Kruskal-Wallis Test was conducted to establish non-significance, which revealed no significant effect of consumer type on any top-rated factor (i.e., lack of energy storage, corruption, and discontinuity of energy projects). This consistency across various consumer groups further underscores the uniformity of public perceptions regarding hindrances to effective energy policies.

The survey results underscore critical areas that require policy interventions. The emphasis on industrial energy needs, preference for cheaper energy, and support for renewable energy all indicate the necessity for comprehensive policy revisions. These revisions should focus on reducing energy costs, ensuring predictable billing, and investing in renewable energy infrastructure. By aligning with these public preferences, policymakers can effectively address the identified barriers and guide Pakistan towards a more resilient and sustainable energy future.

In conclusion, the survey findings offer actionable insights for policymakers. The clear consensus on the importance of addressing corruption, improving infrastructure, and investing in renewable energy sources provides a roadmap for effective policy formulation. By incorporating these public preferences and addressing the identified barriers, Pakistan can enhance its energy security and economic stability, paving the way for a more resilient and sustainable energy future.

4. DISCUSSION

The findings of this study highlight the critical obstacles affecting the implementation of effective energy policies in Pakistan. The lack of dams and renewable energy sources is particularly prominent, reflecting a broader issue in the country’s infrastructure that limits energy storage and sustainable energy generation. This aligns with global trends, where transitioning to renewable sources is increasingly viewed as both an environmental

necessity and an economic opportunity. Corruption and political factors exacerbate the energy crisis by undermining trust and efficiency in policy execution. Addressing these issues requires a comprehensive strategy that includes strengthening governance and regulatory frameworks, promoting transparency, and ensuring policies are resilient to political changes.

The consumer preferences revealed through the survey indicate a strong demand for cheaper, flat-rate energy solutions, highlighting the economic pressures average consumers face. These preferences should guide future policy decisions, ensuring they align with public needs and contribute to socioeconomic stability. By focusing on renewable energy, Pakistan can not only alleviate the cost burdens associated with fossil fuels but also reduce the environmental impact, setting a foundation for sustainable growth. It is crucial to recognize that public opinion is not just a factor to consider, but a key driver in shaping the future of Pakistan’s energy policies.

Our results show that the “Lack of Dams and Renewable Energy” is a key factor hindering Pakistan’s effective implementation of energy policies. This finding is consistent with Pakistan’s 2030 vision for the energy mix, which aims to shift 30% of its energy needs to renewable sources by 2030. However, according to the Pakistan Economic Survey 2020, the share of renewable energy has declined, indicating a gap between policy intention and execution. The inability of the government to effectively implement its energy policies stems mainly from mismanagement and corruption, as highlighted by the Federal Investigation Agency of Pakistan’s report on Independent Power Producers. This aligns with our survey findings, in which corruption was rated a significant hindrance.

5. CONCLUSIONS

In conducting this research, we utilized the IBM SPSS software to analyze and interpret the survey data, enabling us to identify significant trends and preferences among the respondents. SPSS was instrumental in performing statistical tests, such as chi-square tests, Friedman tests, and Wilcoxon signed-rank tests, to validate the relationships and differences across various sectors and factors influencing energy policies in Pakistan. By leveraging SPSS for these analyses, we ensured the robustness and reliability of the results, providing a solid foundation for the study’s conclusions and recommendations. This methodological approach allowed us to objectively assess consumer preferences and identify key areas for policy intervention.

The study emphasizes the urgent need to revise Pakistan’s energy policy, with a strong focus on incorporating renewable energy to address both the supply deficit and consumer demand for affordable energy. The transition to

renewable sources is critical for achieving sustainable energy security and economic resilience. By integrating public opinion into policy formulation and addressing systemic issues, such as corruption and inadequate infrastructure, Pakistan can pave the way for a more sustainable and equitable energy future.

Implementing these changes will require coordinated efforts across all government and private sector levels, underpinned by a commitment to transparency and innovation. The urgency of this coordinated effort cannot be overstated, as it is crucial for the successful execution of energy policies and the transition to a sustainable energy system. Future research should focus on enhancing renewable energy infrastructure, promoting public-private partnerships, and developing robust regulatory frameworks to ensure the effective execution of energy policies. Additionally, raising public awareness of the benefits of renewable energy and engaging consumers in the policy-making process is crucial for the successful transition to a sustainable energy system.

REFERENCES

1. World Bank. The World Bank Annual Report 2020. World Bank, Washington, DC; 2020. <https://doi.org/10.1596/978-1-4648-1619-2>.
2. Poudyal R, Loskot P, Nepal R, Parajuli R, Khadka SK. Mitigating the current energy crisis in Nepal with renewable energy sources. *Renewable and Sustainable Energy Reviews* 2019;116:109388. <https://doi.org/10.1016/j.rser.2019.109388>.
3. Awan AB, Khan ZA. Recent progress in renewable energy – Remedy of energy crisis in Pakistan. *Renewable and Sustainable Energy Reviews* 2014;33:236–53. <https://doi.org/10.1016/j.rser.2014.01.089>.
4. Arshad F, Shamshad M. Energy Crisis in Pakistan: Socio-Economic Implications and the Way Forward. *Annals of Social Sciences and Perspective* 2022;3:105–15.
5. Abbas MN. Energy crisis in Pakistan 2015.
6. KHATRI S, Mirjat N, Harijan K, Uqaili M, Syed F, Shaikh P, et al. An Overview of the Current Energy Situation of Pakistan and the Way Forward Towards Green Energy Implementation. *Energies* 2022;16:423. <https://doi.org/10.3390/en16010423>.
7. Khan D. Impact of energy crisis on economic growth of Pakistan. *International Journal of African and Asian Studies* 2015:33–42.
8. Qureshi MN. Energy crisis in Pakistan: a threat to national security. Islamabad: ISSRA 2009.
9. Azhar MI, Sultan A, Nouman A, Javed A. Energy dynamics of Pakistan. Pakistan: International Islamic University, Faculty of Engineering and Technology, Islamabad; 2011.
10. Kaygusuz K. Energy for sustainable development: A case of developing countries. *Renewable and Sustainable Energy Reviews* 2012;16:1116–26. <https://doi.org/10.1016/j.rser.2011.11.013>.
11. Babar H, Chaudhry IA, Saleem MK, Nouman A. Energy Policy of Pakistan: A Consumer Perspective. 2022 5th International Conference on Energy Conservation and Efficiency (ICECE), Lahore, Pakistan: IEEE; 2022, p. 1–6. <https://doi.org/10.1109/ICECE54634.2022.9758961>.
12. Zafar R, Mahmood A, Razzaq S, Ali W, Naeem U, Shehzad K. Prosumer based energy management and sharing in smart grid. *Renewable and Sustainable Energy Reviews* 2018;82:1675–84. <https://doi.org/10.1016/j.rser.2017.07.018>.
13. Raza MY, Cuculelli M. Sustainable energy changeover in Pakistan: prospects, progress, and policies. *Environmental Science and Pollution Research* 2024; 31:6610–27. <https://doi.org/10.1007/s11356-023-31766-0>.
14. Asif M. Energy Crisis in Pakistan: Origins, Challenges, and Sustainable Solutions 2008.
15. Raheem A, Abbasi SA, Memon A, Samo SR, Taufiq-Yap Y, Danquah MK, et al. Renewable energy deployment to combat energy crisis in Pakistan. *Energy, Sustainability and Society* 2016;6:1–13.
16. Khan AN, Begum T, Sher M. Energy crisis in Pakistan: causes and consequences 2012.
17. Harijan K, Uqaili MA, Memon M. Renewable energy for managing energy crisis in Pakistan, Springer; 2009, p. 449–55.
18. Javaid MA, Hussain S, Maqsood A, Arshad Z, Arshad A, Idrees M. Electrical energy crisis in Pakistan and their possible solutions. *Int J Basic Appl Sci* 2011;11:38–52.
19. Bhatti AG, Bhatti AR, Chaudhary IA, Javed MN. Energy crisis in Pakistan, adaptation and mitigation measures. *Journal of Faculty of Engineering & Technology* 2012;19:67–82.
20. Bergquist P, Konisky DM, Kotcher J. Energy policy and public opinion: patterns, trends and future directions. *Prog Energy* 2020;2:032003. <https://doi.org/10.1088/2516-1083/ab9592>.
21. Farhar BC. Trends: Public Opinion About Energy. *The Public Opinion Quarterly* 1994;58:603–32.
22. Anderson B, Böhmelt T, Ward H. Public opinion and environmental policy output: a cross-national analysis of energy policies in Europe. *Environ Res Lett* 2017;12:114011. <https://doi.org/10.1088/1748-9326/aa8f80>.

Enhancing the Accuracy of SSVEP Target Frequency Detection: A User-Friendly Approach

Adeel Wahab¹, Umar S. Khan^{1,2}, Tahir Nawaz^{1,2}, S.T. Hussain¹, Naveed Anjum¹

¹Department of Mechatronics Engineering, National University of Sciences and Technology (NUST), Islamabad, 44000, Pakistan

²National Centre of Robotics and Automation (NCRA), College of Electrical and Mechanical Engineering (CEME), National University of Sciences and Technology (NUST), Islamabad, 44000, Pakistan

adeel.whb@ceme.nust.edu.pk

ABSTRACT

The steady-state visual evoked potential (SSVEP) is a brain signal induced by flickering visual stimuli, which usually originates in the occipital region. SSVEP detection methods often employ multichannel setups, which, despite their effectiveness, can be complex and uncomfortable. On the other hand, single-channel setups offer a simpler and more comfortable alternative, although achieving high accuracy can be challenging. To this end, this paper proposes an effective and robust single channel SSVEP-based method that relies on the improved complete ensemble empirical mode decomposition with adaptive noise (ICEEMDAN) method as a preprocessor. The ICEEMDAN decomposes the signal into various modes known as intrinsic mode functions (IMF). To accurately detect target frequencies, we utilize the Pearson correlation coefficient to select the most relevant IMFs. Our evaluation using the publicly available AVI-SSVEP dataset demonstrated the method's effectiveness, achieving an average accuracy of 91.97% and an information transfer rate of 62.98 bits per min, outperforming several existing methods. This robust single-channel approach enhances user comfort, making it a user-friendly choice. Additionally, it is adaptable to a variety of applications, including human-robot collaboration and controlling wheelchair.

KEYWORDS: SSVEP, ICEEMDAN, single-channel, Pearson correlation coefficient.

1. INTRODUCTION

Brain-computer interface enables communication between the brain and the outside world using electrical signals [1]. Eeg-based devices are commonly used for measuring brain activity due to their ease of use and affordability [2]. Steady-state visual evoked potential (ssvep) is an eeg paradigm generated in the occipital cortex in response to visual stimuli. Ssvep is popular for its high signal-to-noise ratio (snr) and quick response time. Ssvep-based bcis are applied to various real-world applications like controlling wheelchairs [3], human-robot collaboration [4] and automatic feeding robots [5].

Ssvep feature extraction methods are divided into training-free and training-based approaches [6]. Training-based methods are tiring and lengthy due to the requirement of additional data from multiple targets [1], while training-free methods are more practical and convenient, as they do not rely on prior data. Ssvep-based detection methods often use multichannel setups, making them complex and uncomfortable [7]. Alternatively, single-channel methods are preferred for their simplicity and comfort. Emd is an adaptive and training-free method used for preprocessing single-channel ssveps effectively

[8] but has issues with mode mixing which distorts the signal [9]. Eemd, an evolution of emd, addresses mode aliasing but introduces endpoint distortion due to added white noise. Ceemdan, an improved version of eemd, enhances mode separation and signal reconstruction [10] but still has residual noise and spurious modes in the reconstructed signal which affect the classification performance of the signal. The improved ceemdan (iceemdan) effectively addresses these issues, providing enhanced performance by eliminating residual noise and reducing spurious modes in decomposed signals [11], resulting in better performance.

Ssvep detection accuracy is influenced by the number of channels, frequency detection algorithms, and the snr of eeg signals [12]. Multi-channel setups can improve accuracy, but they can be complex and uncomfortable, especially for patients with conditions like neuromuscular paralysis [13]. On the other hand, single-channel setups are simpler and more comfortable, making them preferable for reducing algorithm complexity. However, accurate classification of ssvep response using the single channel electrode is quite challenging.

This study aims to develop a training-free, accurate, and robust algorithm for single-channel ssvep datasets. We use

the iceemdan method to identify the target frequency by selecting the effective imf with the highest pearson correlation coefficient (pcc) relative to the parent signal.

2. MATERIALS AND METHODS

Dataset

The dataset comprises four subjects aged between 27 and 32 years, known as the avi-ssvep dataset [14]. Each subject participated in trials targeting seven different frequencies: 6 hz, 6.5 hz, 7 hz, 7.5 hz, 8.2 hz, 9.3 hz, and 10 hz. As per the 10-20 international standard, the single electrode was located at the oz position. Each trial duration was 30sec and was recorded at a 512 hz sampling rate. Data was recorded at least three times per person at each frequency, resulting in a total of 92 trials across the four subjects.

An ssvep signal comprises a fundamental frequency, its harmonics (integral multiples of the fundamental frequency), and noise components. Figure 1 shows the normalized ssvep signal at 10 hz for subject 1, along with its psda. To enhance classification accuracy, it's essential to suppress the noise components in the ssvep signal. We first applied a 6th-order butterworth bandpass filter, ranging from 4 hz to 16 hz [8], to eliminate irrelevant, noisy frequencies and improve the classification accuracy. Since noise can degrade the performance of iceemdan, the filtering step is essential before iceemdan application.

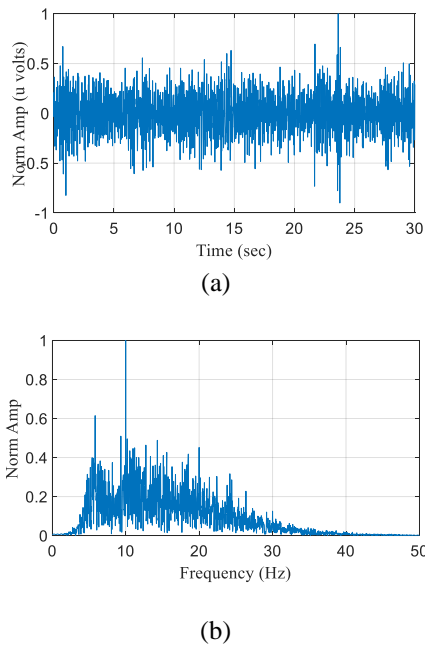


Figure 1.: (a) Normalized SSVEP signal at 10 Hz for subject 1; (b) PSD of the signal

ICEEMDAN

It is important to understand EMD, EEMD, and CEEMDAN, as they are the predecessors of ICEEMDAN. The EMD method decomposes the non-stationary and nonlinear signal into oscillating modes known as intrinsic mode functions (IMFs). The original signal IMFs should meet two conditions: (i) The extrema, such as maximum and minimum points, must be equal or differ by one. (ii) The average of the maximum and minimum values should be zero. It is the shifting technique that fulfills the above two conditions [8].

While EEMD reduces mode mixing, it introduces challenges like residual noise in the reconstructed signal and inconsistent modes across different trials. To overcome these issues, Complete EEMD with Adaptive Noise (CEEMDAN) was developed.

Like EEMD, CEEMDAN adds opposite white noise signals to the original signal before decomposing it with EMD. However, unlike EEMD, which independently decomposes each realization, CEEMDAN applies progressive decomposition. A CEEMDAN algorithm iteratively adds noise to the residual signal from the current IMF, which improves spectral separation of the modes as well as signal reconstruction accuracy, at a lower computational cost [10].

CEEMDAN overcomes some of the limitations of EEMD but still faces two main problems: residual noise within the modes and the occurrence of spurious modes. ICEEMDAN overcomes these limitations. During each step of ICEEMDAN decomposition, the noise is adjusted to optimize IMF extraction. As a result, the decomposition becomes more precise with less noise interference. The ICEEMDAN algorithm is as follows [11]:

Let x is the original EEG signal, σ_0 is the standard deviation of the zero mean and unit variance of white Gaussian noise $H^i(n)$ (where $i= 1, 2, \dots, M$) and an operator represented as $P_j(\cdot)$, that provides the j th EMD mode. Let $N(\cdot)$ is represented an operator defines the signal local mean.

1. The first residue is obtained to calculate the local mean of I realization by EMD $x^i = x + \sigma_0 P_1(H^i)$.

$$r_1 = \langle N(x^i) \rangle \quad (1)$$

2. The first mode r_1 is found as

$$\tilde{I}_1 = x - r_1 \quad \text{for } (k=2)$$

The second residue is estimated, which is the average of the local mean of the realization $r_1 + \sigma_1 P_2(H^i)$ and the second mode is defined as

$$\tilde{I}_2 = r_1 - r_2 = r_1 - \langle N(r_1 + \sigma_1 P_2(H^i)) \rangle \quad (3)$$

3. The k th residue is calculated by K as

$$r_k = \langle N(r_{k-1} + \sigma_{k-1}P_k(H^i)) \rangle \quad (4)$$

4. Repeat step 4 for the next k

$$\tilde{I}_k = r_{k-1} - r_k \quad (5)$$

We use $\sigma_{k-1}P_k(H^i)$ gaussian white noise instead of noise during signal plus noise realization such as $\sigma_{k-1}(H^i)$. From iteration to iteration, noise mode amplitude σ_k changes as given by $\sigma_k = \varepsilon_0 \text{std}(r_k)$. Where, $\text{std}()$ represent the signal standard deviation.

Where v_j and S_j represent the sample points for IMF and parent restored signal, while \bar{v}_i and \bar{S}_i denote their respect mean. If PCC value close to 1 indicates a strong correlation, whereas a value near 0 signifies a weak correlation [16].

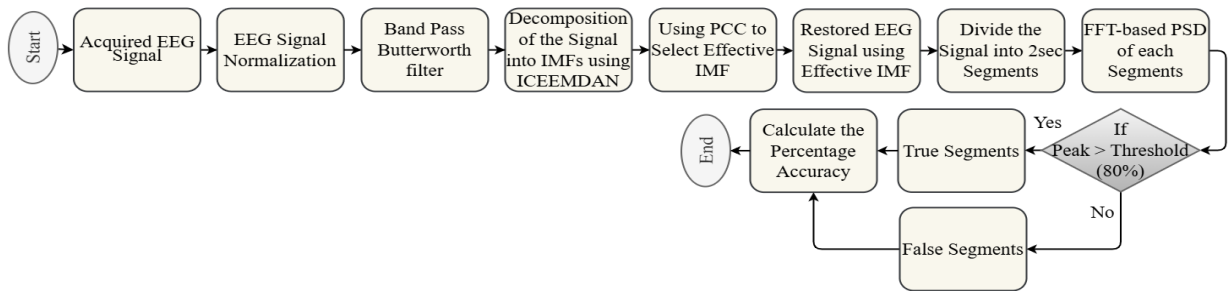


Figure 2:. Flow chart of the proposed methodology

Proposed Methodology

The flowchart of the proposed method is shown in Figure 2. First, the EEG signal is normalized to its maximum absolute amplitude [8] to distinguish significant signal components from smaller ones. A bandpass filter then removes irrelevant and noisy components. A filtered signal is decomposed into various IMFs using ICEEMDAN, such as effective and noisy IMFs. as shown in Figure 3, We select the effective IMF as IMF-1 (containing the target frequency) based on the maximum PCC, a measure of its correlation with the parent signal. SSVEP's signal is reconstructed by isolating this effective IMF, dividing it into 15 segments, and calculating PSDA for each segment. The amplitude of segments matching 80% of the target frequency is classified as true; otherwise, it is classified as false.

The goal of ICEEMDAN is to reduce noise in the EEG signal and isolate the effective and most related IMF containing valuable information from the parent signal. Despite its advantages, the ICEEMDAN method faces a challenge in identifying the most effective IMFs among all the decomposed components. To achieve this, we use the PCC to evaluate the correlation between each IMF and the parent signal, ensuring the selection of the most informative components. The PCC between the IMF and the parent EEG signal is defined by the following expression [15]:

$$\rho_i = \frac{\sum_{j=1}^N (v_j - \bar{v}_i)(S_j - \bar{S}_i)}{\sqrt{\sum_{j=1}^N (v_j - \bar{v}_i)^2 \sum_{j=1}^N (S_j - \bar{S}_i)^2}} \quad (6)$$

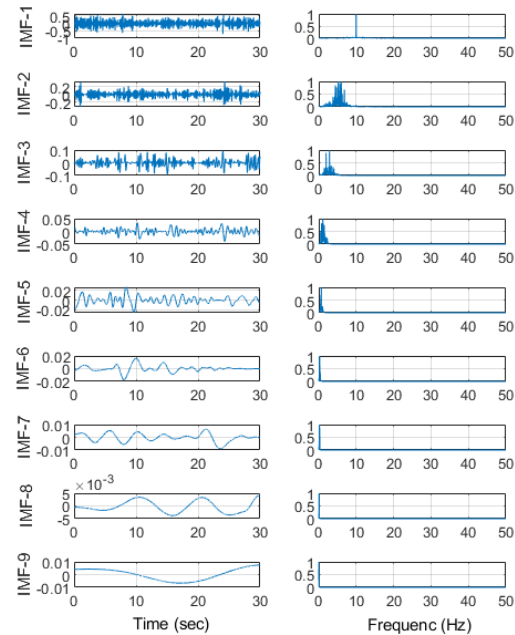


Figure 3: (a) ICEEMDAN decomposed the signal into 9 IMFs; (b) their PSDA.

PCC's theoretical foundation and high efficiency enable effective correlation of time series data. Table 1 presents a comparison of nine IMFs to determine which ones can fully capture the required information from the parent EEG signal. According to the analysis, IMF-1's PCC is 92.1% higher than the other IMFs, as shown in Table 1. Based on this, it indicates that it is highly correlated and contains more information about the parent signal

regarding the target frequency than other IMFs. Consequently, we refer to IMF-1 as an effective IMF.

Table 1. PCC value of 9 IMFs

IMF	1	2	3	4	5	6	7	8	9
PCC x 10 ²	92.1	42.2	6.0	0.4	0.1	0.1	0.08	0.03	0.0

3. RESULTS AND DISCUSSION

In this paper, we evaluate the efficacy of the proposed method in detecting SSVEP target frequencies using publicly available AVI-SSVEP datasets. SSVEP frequency detection involves data preprocessing, feature extraction, and signal classification. The first step involves subjecting the normalized EEG signal to the Butterworth bandpass filter, which suppresses the irrelevant noisy component and increases the signal's SNR.

After that, the ICEEMDAN is used to decompose the signal into 9 IMFs with a standard deviation of 0.2 and 25 realizations, as shown in Figure 3. This method decomposes the EEG signal into effective and noisy IMFs. We identify the effective IMF containing the target frequency based on the maximum PCC value. The PCC calculates the correlation between each IMF and the parent signal. As shown in Table 1, IMF-1 has the highest PCC value among the remaining IMFs, indicating that it retains the necessary information (target frequency) of the parent signal, making it an effective IMF. After this selection process, it is essential to use indicators that compare IMF-1 to the parent EEG signal. This ensures that IMF-1 captures all the necessary information of the parent signal without mode mixing [15]. To achieve this, we calculated the standard deviation, variance, and absolute mean of both the parent signal and IMF-1, as detailed in Table 2. We found that IMF-1 effectively captures the essential information from the parent EEG signal and enhances the SNR. This method also mitigates the mode aliasing typically seen with EMD decomposition [9].

The effective IMF signal is converted into 15 segments (each lasting 2sec), and the PSDA of each segment is obtained to segregate true and false segments. Segments that have more than 80% of the target frequency amplitude are classified as true segments; others are classified as false segments.

Table 2: Comparison of parent signal and IMF-1 in terms of statistical indicators.

Signal	Std deviation	Variance	Abs. mean
Parent Signal	0.1945	0.0378	0.0002

IMF-1	0.1769	0.0313	0.0002
-------	--------	--------	--------

SSVEP signal performance is measured by two parameters: classification accuracy and information transfer rate (ITR). Classification accuracy (C_a) is the ratio of correctly identified segments to the total number of segments, calculated as follows [8]:

$$C_a = \frac{T_s}{T_s + F_s} \quad (7)$$

Where T_s and F_s are the number of true and false segments, respectively. Whereas the ITR indicates the communication speed of the BCI system and mainly depends upon the number of classes (O), classification accuracy, and processing time (T). the ITR can be expressed as [17]:

$$ITR = \frac{60}{T} \left[\log_2 O + C_a \log_2 C_a + (1 - C_a) \log_2 \left(\frac{1 - C_a}{O - 1} \right) \right] \quad (8)$$

We evaluated the proposed method's performance by comparing it with other relevant methods, such as PSDA, DWT-PSDA, EMD-PSDA [8], EEMD-PSDA, and CEEMDAN-PSDA, using the AVI-SSVEP dataset, as shown in Table 3. The proposed method achieved an average accuracy of 91.97% and an ITR of 62.98 bits per min for AVI-SSVEP dataset. From the Table 3, it is found that the proposed method outperforms the other comparable methods. The ICEEMDAN method preprocesses the SSVEP signal, effectively denoising it by eliminating irrelevant and noisy IMFs and accurately selecting the effective IMF through the PCC method. Furthermore, the ICEEMDAN significantly reduces mode mixing and residual noise in the modes with low computational costs. Therefore, the proposed method utilized a single-channel setup that made it a user-friendly approach. This study used an offline dataset to evaluate SSVEP in single-channel setups. Future research will use more datasets and different time windows to further improve accuracy and ITR of SSVEP signal.

4. CONCLUSION

This study proposes ICEEMDAN-PSDA, an efficient and robust method for classifying SSVEP frequencies using a single-channel setup. The ICEEMDAN method effectively splits the EEG signal into useful and noisy IMFs, while the PCC method accurately identifies the effective IMF that retains valuable information from the parent signal, avoiding mode aliasing and residual noise. We use the reconstructed SSVEP signal from the effective IMF for feature extraction with PSD and then for classification. This approach improves the proposed methods. Performance by focusing on the most relevant IMF component of SSVEP signal. The proposed ICEEMDAN-PSDA method outperformed existing

related methods, with an average accuracy of 91.97% and an ITR of 62.98 bpm. The results illustrate the effectiveness of the proposed method, which utilizes data from a single channel rather than multiple channels and provides greater comfort for paralyzed patients or

individuals requiring extended use. As a result, this method is user-friendly, robust and suitable for a variety of real-world BCI applications.

Table 3: Comparison of proposed method with relevant method in term of accuracy and ITR

Subject	Segment length (sec)	PSDA		DWT-PSDA		EMD-PSDA		EEMD-PSDA		CEEMDAN-PSDA		ICEEMDAN-PSDA	
		Ca (%)	ITR (bpm)	Ca (%)	ITR (bpm)	Ca (%)	ITR (bpm)	Ca (%)	ITR (bpm)	Ca (%)	ITR (bpm)	Ca (%)	ITR (bpm)
1	2	84.70	53.92	88.88	60.43	91.66	65.42	90.30	59.24	92.43	62.85	92.62	63.18
2	2	78.90	45.62	86.15	56.14	89.23	61.10	88.01	55.19	90.34	58.48	90.51	58.76
3	2	80.64	47.96	78.73	45.33	85.71	55.42	85.13	53.24	89.71	60.48	90.96	62.60
4	2	87.30	57.90	87.93	58.99	92.06	66.06	91.54	63.31	93.18	66.27	93.79	67.41
Average value		82.88	51.35	85.42	55.22	89.66	62.00	88.75	57.75	91.42	62.03	91.97	62.98

NOMENCLATURE

Abbreviation	Definition
SSVEP	Steady-state visual evoked potential
EMD	Empirical mode decomposition
EEMD	Ensembled empirical mode decomposition
CEEMDAN	Complete ensembled empirical mode decomposition with adaptive noise
ICEEMDAN	Improved complete ensembled empirical mode decomposition with adaptive noise
IMF	Intrinsic mode function
PSDA	Power spectral density analysis
PCC	Pearson correlation coefficient

ACKNOWLEDGEMENTS

The authors acknowledge support received from the National Centre of Robotics and Automation (NCRA) at College of Electrical and Mechanical Engineering, NUST Islamabad, Pakistan.

REFERENCES

1. R. Zerafa, et al., To train or not to train? A survey on training of feature extraction methods for SSVEP-based BCIs, *J Neural Eng*, 2018, 15(5), pp. 1-25.
2. G. Placidi, et al., A modular framework for EEG web based binary brain computer interfaces to

recover communication abilities in impaired people, *J Med Syst*, 2016, 40(1), p.1-14.

3. W. Chen, et al., An Electric Wheelchair Manipulating System Using SSVEP-Based BCI System, *Biosensors*, 2022, 12(10), p. 1-20.
4. Yevheniy Dmytriiev, et al., “Brain–Computer Interface and Hand-Guiding Control in a Human–Robot Collaborative Assembly Task,” *machines*, 2022, 10(54), pp. 1-161.
5. Trung-Hau Nguyen, et al., A Single-Channel SSVEP-Based BCI Speller Using Deep Learning, *IEEE Access*, 2019, 7, p.1752-1763.
6. Yue Zhang, et al, “Data Analytics in Steady-State Visual Evoked Potential-Based Brain–Computer Interface: A Review”, *IEEE Sens.*, 2021, 21(2), p.1124-1138.
7. S. C. Chen, et al., Applying fuzzy decision for a single channel SSVEP-based BCI on automatic feeding robot,” *Microsystem Technologies*, 2018, 24(1), pp. 199–207.
8. M. K. Ojha, et al., A Novel Approach Based on EMD to improve the Performance of SSVEP Based BCI System, *Wirel Pers Commun*, 2021, 118(4), p.2455-2467.
9. Z. Wu and N. E. Huang, “Ensemble Empirical Mode Decomposition: A Noise-Assisted Data Analysis Method, *World Sci.*, 2009, 01(1), p.1-41.
10. M. E. Torres, et al., A complete ensemble empirical mode decomposition with adaptive noise,” in *ICASSP, IEEE International Conference on Acoustics, Speech and Signal Processing*, 2011, pp. 4144–4147.



11. M. A. Colominas, et al., Improved complete ensemble EMD: A suitable tool for biomedical signal processing, *Biomed Signal Process Control*, 2014, 14(1), p. 19–29.
12. Z. Lin, et al., Frequency recognition based on canonical correlation analysis for SSVEP-Based BCIs,” *IEEE Trans Biomed Eng*, 2007, 54I(6), p. 1172–1176.
13. C. Farnaki, et al., Single-channel SSVEP-Based BCI for robotic car navigation in real world conditions,” in *IEEE 19th Int Conf on Bioinformatics and Bioengineering*, 2019, pp. 638–643.
14. <https://www.setzner.com/avi-ssvep-dataset>, 2022.
15. B. Liu, et al., A chatter detection method in milling based on gray wolf optimization VMD and multi-entropy features,” *Int. Jou. of Advanced Manufacturing Technology*, 2023, 125(2), p. 831–854.
16. . Zhou, et al., Estimating the mean cutting force of conical picks using random forest with salp swarm algorithm, *Results in Engineering*, 2023, 17, p. 1-12.
17. J. R. Wolpaw, et al., Brain-computer interfaces for communication and control, *Clinical Neurophysiology*, 2002, 113, p.771-791.

ANALYSIS OF VERTICAL AXIS WIND TURBINE UTILIZING DISSIMILAR AIRFOIL BLADE COMBINATION

Asif Khan^{1*}, Babar Hayat², Adil Loya¹, Muhammad Zia Ullah Khan², Fahad Aziz⁵,
Emad Uddin³, Muhammad Asfandyar Arshad⁴, Muntazir Abbass¹, Imran¹

¹National University of Sciences and Technology, PNEC, Karachi, Pakistan

²University of Science and Technology of China

³COMSATS University Islamabad, Sahiwal

⁴Institute of Space Technology, Islamabad

⁵PAF Karachi Institute of Economics and Technology, Karachi

Asif.khan@pnec.nust.edu.pk

ABSTRACT

Vertical Axis Wind Turbine (VAWT) is widely being used nowadays due to its capability of operating through the wind on any side, low maintenance, and simple blade design. Computational techniques have increased technological advancement related to VAWT. This study introduces a new design of four bladed VAWT as an augmentation to previous models. In this study VAWT with fix pitch blades were used for assessing performance dependent on power and torque coefficients using numerical simulations and effect of design on self-starting capability was also analyzed.

Keywords: Power Coefficient; Torque Coefficient; CFD; Fluent; Java Foil

1. INTRODUCTION

The energy requirement of the world is increasing rapidly due to which energy harnessing devices and fuels to operate them are of great concern. As time passes by, organic fuels are getting scarce, leaving no other choice to utilize renewable energy resources like wind, solar, geothermal, biogas and wave energy resources. The only problem with renewable resources is to develop efficient machinery, to harness different energy forms and convert them into utilizable means. Moreover, the Social Development Goals (SDG) set by the United Nation is a main concern and for which they have set SDG 7 to overcome the clean energy crisis existing around the world. Therefore, the majority of the developed countries and including under developed nations are all gradually adopting renewable means of energy generation.

efficiency of four-bladed VAWT were predicted using RANS turbulence modeling by selecting transient flow conditions with STD $k-\omega$ approach. Different cambered blade combinations were studied to predict the optimum combination for four bladed wind turbines while maintaining solidity, and extracting data after twelve rotations for each turbine combination. Results demonstrated a 32% increase in performance when NACA 3421 and NACA 4421 airfoils were employed as a hybrid airfoil based VAWT.

On an axis basis, wind turbines are divided into two types; horizontal axis and vertical axis wind turbines. Vertical Axis Wind Turbine (VAWT) is further divided into lift-based wind turbine known as Savonius and drag-based turbine known as Darrieus. The advantage of Darrieus is

its capability to accept wind from any side [1], low noise and confined operational area.

In early times, wind powered machinery was used for windmills, water pumping and crop irrigation stated by Bennett and Elton [2], [3, 4]. Horizontal Axis Wind Turbine (HAWT) was developed in 1908 at the Danish State of Askov[5] whereas, curved and straight blade Darrieus VAWT was invented and patent in 1931 by a French engineer George Jeans [6]. M Takao et al. investigated Darrieus type wind turbine having three blades [7]. Rotor blades and guide vanes were

provided with gaps as well as angles. In this study he studied about starting behavior and power coefficient of the turbine. His conclusion involved performance increases when gap between the rotor blade and vanes was increased.

B Newman in 1973 designed and tested two sails of three-bladed VAWT [8], as a double cloth sail and a single cloth sail rather than a solid airfoil and found out that power output was less but design was cost efficient. V Morcoa and O. Abdul Hafez in 1997 conducted an experiment on an arrowhead VAWT at different wind speed with rectangular and airfoil blade [9] and after studying power and torque coefficient, concluded that arrow head VAWT perform best with rectangular blades. His results demonstrated that the angle of attack increases performance parameters.

M Marini et al. in 1992 compared performance of different two blade design VAWT by varying airfoil section and length [10]. He performed performance calculations using momentum stream tube and free wake vortex models; concluding that momentum model is less computational

but vortex provides the best accuracy. J Baker in 1983 proposed methods to improve the self-start capability of VAWT [11]. His solution involved varying geometry and using airfoil sections like NACA 0012, GO 420 and FX 63-137 having low post stall drag with laminar separation bubble exhibiting capability. The inability of self-starting and boundary attachment is the main concern of discussion among researchers studying wind turbines [12, 13]. F Ponta et al. have made a unique design VAWT in which blades slide instead of rotating. Due to the sliding of the blades electricity was generated through the wheels on which they were connected [14].

T Wakui et al. designed a prototype of combined Darrieus and Savonius VAWT by employing them on a single shaft. His observation came up as a result of high starting torque, an efficiency, but design complexity made it only to the prototype stage [15]. D Gorelov and V Krivospitsky developed straight blade two tiers 900 shifted VAWT capable of generating 3KW power [16]. Its main feature was the capability of self-starting, but it was only for low power applications.

R Gupta and A Biswas developed three-bladed twisted Darrieus VAWT model with a shape of airfoil twisted at 300 at the trailing edge [17]. He concluded better aerodynamics efficiency due to a decrease in flow separation, but the power coefficient was low. Tim developed a design specifically for buildings [18]. The design consists of multiple Darrieus VAWT connected at the same frame. He concluded that the design provided good efficiency, but it was suitable for high buildings. Daegyoun Kim investigated the power output of two VAWT by placing deflectors on the upstream side and concluded that power output increases when each of VAWT is placed outside the near wake region [19].

A. Loya et al. investigated performance augmentation of VAWT using a computational method by varying camber of model and found out that at certain camber performance surged [20]. SO Akansu et al. compared NACA 0021, NACA015, NACA5520 and Clark-Y airfoil for VAWT based on performance coefficient and concluded that NACA 0021 outperformed other airfoils [21]. Nguyen compared NACA0012, NACA 0015, NACA 0018 and NACA 0021 and stated that NACA 0012 showed lowest self-starting capability, whereas NACA 0021 had the highest.

Blades of VAWT are of the same airfoil whether the turbine has two, three or four blades. Due to the surge in popularity of VAWT depending upon its low cost and ability to install it anywhere, this study will investigate the performance of VAWT using hybrid airfoil model design by considering torque coefficient, power coefficient, and self-starting capability.

In this study, base airfoil NACA 0021 will be used and combinations with varying camber will be made to notifying influence on the performance of Darrieus-type

VAWT. NACA 0021 is preferred in the study of VAWT due to high performance coefficient and high self-starting capability compared to other airfoil designs [22]. This study will investigate the less complex design of four-blade VAWT by using two opposite blades of one airfoil and two of the different airfoils. Performance in the form of torque coefficient, power coefficient, and self-starting capability will be stated by varying airfoil camber

2. METHODOLOGY

Geometric Modeling

The focus of this study is on VAWT wind turbine with four blades. As we will focus on multiple airfoil designs in one model, we have to keep the number of blades four, due to its stability characteristics. 2-D model of the wind turbine was generated by importing airfoil co-ordinates from Javafoil to CATIA. Figure 1 shows the airfoil samples to be used in study, whereas Figure2 provides information about the domain and design of the rotor. This study is divided into two parts non-hybrid and hybrid model comparison. In non-hybrid, performance comparison were made with experimental study. For hybrid airfoil VAWT, the same computational models were adopted as used for comparison with experimental study. In all the different models, solidity was kept same; only airfoil geometry was varied.

Table 1 expresses airfoil designs that were employed in combined form for generating four-bladed wind turbine models. It is shown that diagonal designs represent all models with same camber airfoil, whereas like C00, C11, C22, C33 and C44, where C represents camber, the first digit represents camber of two opposite blades airfoils and second represents camber of other two. A total of fifteen models were generated as models are symmetric along the diagonal. Mesh was refined into several stages of the selected model to reduce error from 20% to 4% thus satisfying grid independence.

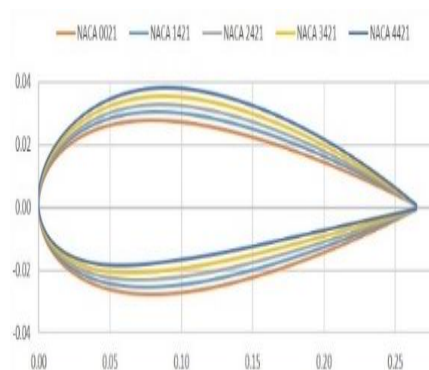


Figure 10: Airfoil models' sample

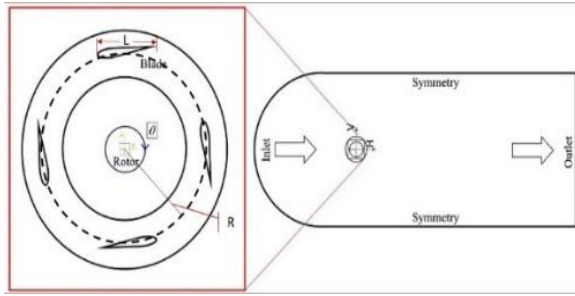


Figure 11: Domain geometry and turbine rotor

Table 11: VAWT models samples used for research.

C	0	1	2	3	4
0	NACA 0021	NACA 1421	NACA 2421	NACA 3421	NACA 4421
	NACA 0021				
1	NACA 0021	NACA 1421	NACA 2421	NACA 3421	NACA 3421
	NACA 1421				

Darrieus-type vertical axis turbines with straight-blades were studied with different airfoil designs [28-30]. However, in this research, we will use symmetric airfoil NACA 0021 for model generation. The wind turbine model consists of a 1m rotor radius and a 0.265m chord length. The simulation was performed by importing 2-D CAD model into the ANSYS Fluent module.

Mesh Generation

Authors Mesh element used for analysis was the triangular type with 0.68 mesh orthogonal quality and 3.1 aspect ratio. For 2-D models, a triangular mesh is considered appropriate if the geometry is complex [31]. On airfoil boundary, quadrilateral mesh with inflation at airfoil wall is used as it is preferred for boundary layer capturing. Furthermore, advanced front triangle surface meshes was used in patch conforming mode. Figure 3 shows a complete meshed domain of wind turbine model that validated results with experimental results.

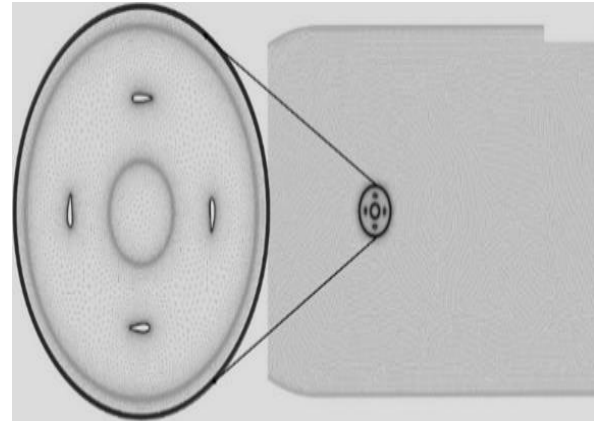


Figure 12: VAWT model and domain mesh

Grid independence was achieved from coarse (85734) to very fine mesh (193234) number of elements considering the mean coefficient of performance parameter as output for 1.5 TSR. Mesh was refined until the Cp value was stable. Figure 4 shows the grid independence graph as a function of the number of elements

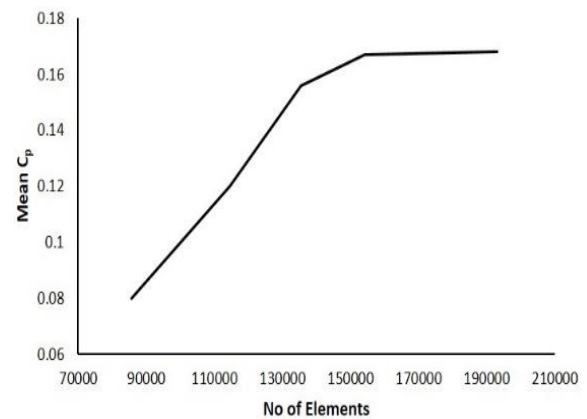


Figure 13: Grid independence of VAWT model

Governing Equations

In Computational Fluid Dynamics (CFD), we are primarily interested in velocity and pressure distribution, which is calculated by considering control volume and applying the conservation principle of mass and momentum. Using these principles, the governing equation of fluid is known as Navier Stokes (N-S) eq. is developed shown by eq. (2), (3) and (4).

$$\frac{\partial P}{\partial T} + \frac{\partial}{\partial X}(PU) + \frac{\partial}{\partial Y}(PV) + \frac{\partial}{\partial Z}(PW) = 0 \quad (1)$$

$$\frac{\partial(PU)}{\partial T} + \frac{\partial(Pu^2)}{\partial X} + \frac{\partial(PUV)}{\partial Y} + \frac{\partial(PUW)}{\partial Z} = -\frac{\partial P}{\partial X} + \frac{\partial}{\partial X}(\lambda \nabla \cdot \vec{V} + 2\mu \frac{\partial u}{\partial x}) + \frac{\partial}{\partial Y}[\mu(\frac{\partial v}{\partial x} + \frac{\partial u}{\partial y})] + \frac{\partial}{\partial Z}[\mu(\frac{\partial u}{\partial z} + \frac{\partial w}{\partial x})] + PF_x(2)$$

$$\begin{aligned}
 \frac{\partial(\rho v)}{\partial t} + \frac{\partial(\rho uv)}{\partial x} + \frac{\partial(\rho v^2)}{\partial y} + \frac{\partial(\rho vw)}{\partial z} \\
 = -\frac{\partial \rho}{\partial y} + \frac{\partial}{\partial y} \left(\lambda \nabla \cdot \vec{v} + 2\mu \frac{\partial v}{\partial y} \right) \\
 + \frac{\partial}{\partial x} \left[\mu \left(\frac{\partial v}{\partial x} + \frac{\partial u}{\partial y} \right) \right] \\
 + \frac{\partial}{\partial z} \left[\mu \left(\frac{\partial w}{\partial y} + \frac{\partial v}{\partial z} \right) \right] + \rho f_y
 \end{aligned}
 \tag{3}$$

$$\begin{aligned}
 \frac{\partial(\rho w)}{\partial t} + \frac{\partial(\rho uw)}{\partial x} + \frac{\partial(\rho vw)}{\partial y} + \frac{\partial(\rho w^2)}{\partial z} \\
 = -\frac{\partial \rho}{\partial z} + \frac{\partial}{\partial z} \left(\lambda \nabla \cdot \vec{v} + 2\mu \frac{\partial w}{\partial z} \right) \\
 + \frac{\partial}{\partial x} \left[\mu \left(\frac{\partial u}{\partial z} + \frac{\partial w}{\partial x} \right) \right] \\
 + \frac{\partial}{\partial y} \left[\mu \left(\frac{\partial w}{\partial y} + \frac{\partial v}{\partial z} \right) \right] + \rho f_z
 \end{aligned}
 \tag{4}$$

Finite Volume Method (FVM) is employed by fluent to calculate solutions at discrete points. We compute the average solution of an actual solution by using Reynolds-averaged Navier–Stokes (RANS) equation model, in which any turbulent flow variable can be found by the sum of the mean value and the fluctuating value. The RANS equation is shown in eq. (5).

$$\begin{aligned}
 \frac{\partial(\rho \bar{u}_i)}{\partial t} + \frac{\partial(\rho \bar{u}_i \bar{u}_j)}{\partial x_j} = -\frac{\partial(\bar{p})}{\partial x_i} + \frac{\partial}{\partial x_j} \left[\mu \left(\frac{\partial \bar{u}_i}{\partial x_j} + \frac{\partial \bar{u}_j}{\partial x_i} \right. \right. \\
 \left. \left. + \frac{2}{3} \delta_{ij} \frac{\partial \bar{u}_m}{\partial x_m} \right) \right] + \frac{\partial}{\partial x_j} (-\rho \bar{u}_i \bar{u}_j)
 \end{aligned}
 \tag{5}$$

Standard k-ε model computes turbulence energy using the transport equation as in eq. (6).

$$\begin{aligned}
 \frac{\partial(\rho k)}{\partial t} + \frac{\partial(\rho \bar{u}_i k)}{\partial x_i} = -\rho \bar{u}_i \bar{u}_j \frac{\partial \bar{u}_i}{\partial x_j} - \rho \epsilon \\
 + \frac{\partial}{\partial x_j} \left[\left(\mu + \frac{\mu_t}{\sigma_k} \right) \frac{\partial k}{\partial x_j} \right]
 \end{aligned}
 \tag{6}$$

Physics Modelling and boundary conditions

In this study, K-Omega model with SST turbulence model was used for Navier Stokes equations normalization because of its flow separation, wind velocity and swirl predicting capability [32, 33]. For solution, simple pressure-velocity coupling with least square Cell-Based gradient was employed. Moreover, the second order spatial discretization approach was used for pressure, momentum, dissipation rate and turbulent kinetic energy. Mesh motion feature in fluent was implemented for the blade region to mimic VAWT whereas the outer and inner domain were kept stationary. Mesh-motion was employed with 12 rad/s angular velocity representing 1.5 Tip Speed Ratio (TSR). Velocity was set to 8m/s for all models and

no-slip condition was selected on the wall. Solution was run until residuals were periodic and stable to get accurate data.

Data acquisition

Values of moment coefficients with respect to various azimuth angles can be calculated directly from fluent. Power coefficient was considered as a performance predicting parameter for wind turbines that depends upon certain parameters shown in eq. (8). Equation (8) can be used for calculating torque [34], whereas multiplication of torque with velocity gives

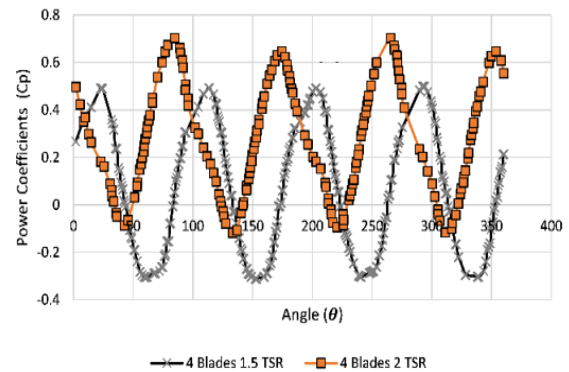


Figure 14: Power coefficient of blades

3. RESULTS AND DISCUSSION

Non-Hybrid

Figure 6 display non-hybrid model graph of vertical axis wind turbine with four blades which provides us information that as camber increases from 0 to 3 peak performance start increasing but after that it starts decreasing again, whereas, if we look towards mean Cp graph, we can see that as camber is increased, mean performance increases till camber 2, but then remain nearly the same till camber 4.

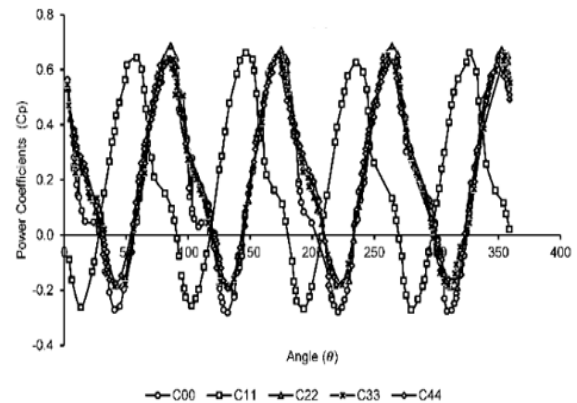


Figure 15: Nono hybrid models power coefficient

Hybrid models

For hybrid case data is divided into five major cambers which are 0,1,2,3,4 and 5. Figure 8 depicts 0 camber major series, Figure 8 shows 1 camber and so on. Data tell us that for 0 and 1 camber major series performance increases comparatively by fewer amounts as model varies from left to right. Whereas, in 2, 3 and 4 series model the variation in performance was very fluctuating. The camber 2 major cases, performance was increased as model varies from left to right and C24 model showed highest performance. The camber 3 major cases, model C34 showed the highest performance by sudden increase from the previous model. Cases of camber 4 series first increased and then start decreasing as shown in Figure 11. One benefit of cambered airfoil model is its improved self-starting capability power. Power coefficient and angular velocity can be calculated using eq. (7) and (9) [34].

$$C_p = \frac{P}{0.5\rho AV^3} \quad (7)$$

$$C_M = \frac{M}{0.5\rho AV^2 R} \quad (8)$$

$$TSR = \frac{\omega D}{2V} \quad (9)$$

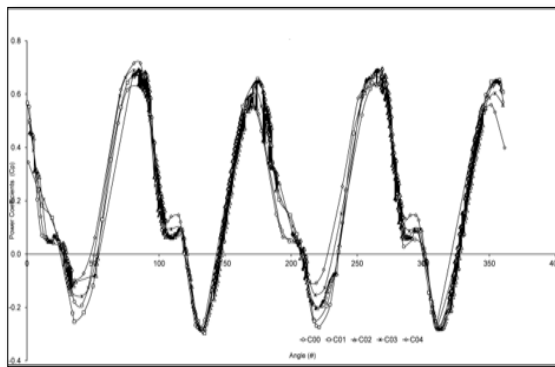


Figure 16: Main 0 camber hybrid model power coefficient

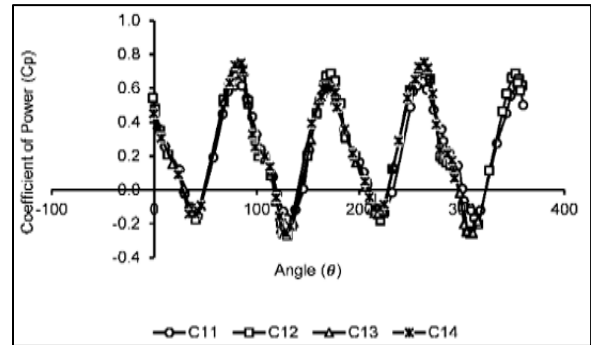


Figure 17: Main 1 camber hybrid model power coefficient

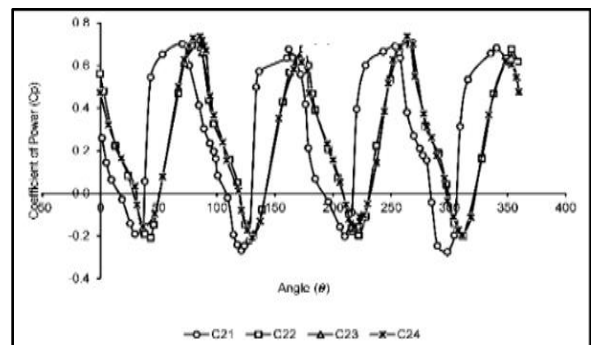


Figure 18: Main 2 camber hybrid model power coefficient

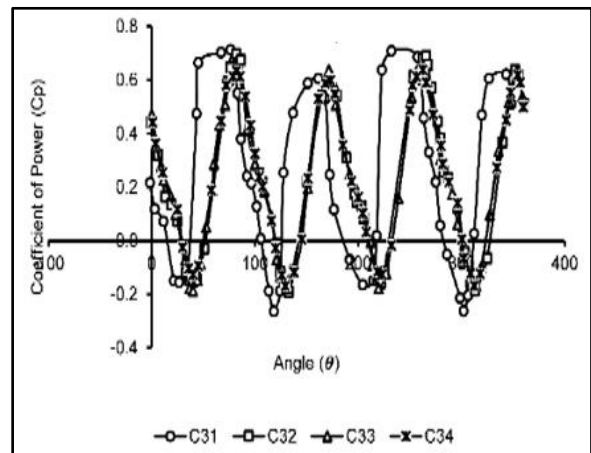


Figure 19: Main 3 camber hybrid model power coefficient

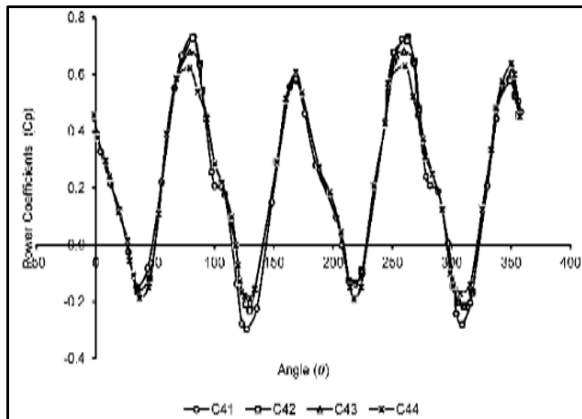


Figure 20: Main 1 camber hybrid model power coefficient

Figure 12 points out data from all models combined. It can be seen clearly that models C24 and C34 performed exceptionally when compared to other models with a mean coefficient of 0.288. This is probably due to low negative lift as shown in Figure 13. Thus, model C24 and C34 are generating more mean lift resulting in more rotation and less drag. Model C44 shows minimum lift, but it has more drag to tackle due to which its performance is on the third number.

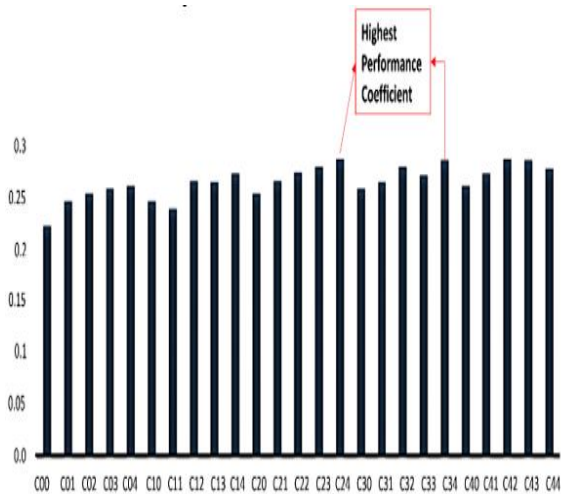


Figure 21: Complete models mean performance data.

Figure 13 points out data from all models combined. It can be seen clearly that models C24 and C34 performed exceptionally when compared to other models with a mean coefficient of 0.288

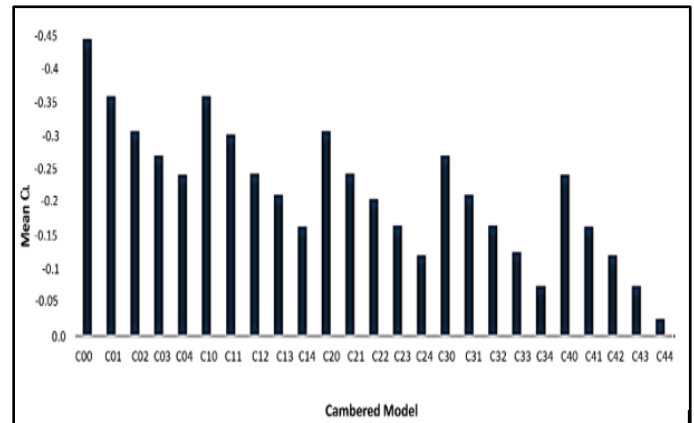


Figure 22: Complete models lift coefficient.

Figure 14 depicts that model C00 or model with all four airfoils of NACA 0021 shows the high value of negative lift, which starts decreasing.

Figure 15 contains contours of non-hybrid models (a, c); where (a) model consists of four blades of NACA 2421 and (c) model consists of NACA 4421 blades. On the other hand, two blades of model (b) are made up of NACA 1421 and two of NACA 2421. Likewise, model (d) is composed of two NACA 1421 blades and two NACA 4421 blades. Figure 14 showed that negative lift is higher in model (b) represented by C12 when compared with model (a) represented in Figure 15 by C22

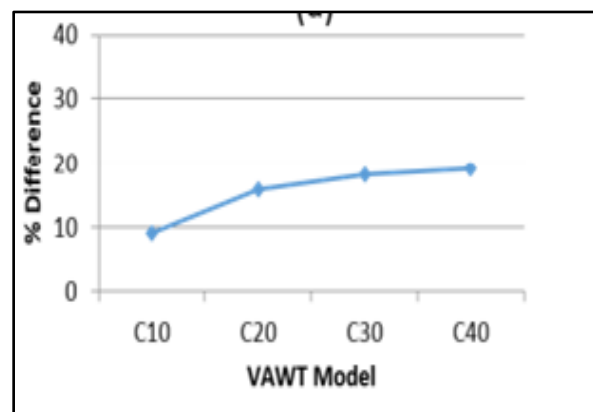


Figure 23: % Performance difference of cambered airfoils with a non-cambered airfoil

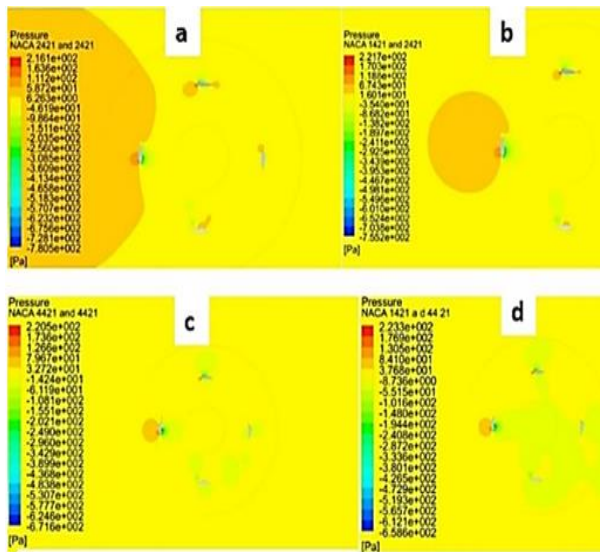


Figure 24: Pressure contours of non-hybrid vs hybrid model.

4. CONCLUSIONS

Various studies in this paper have proved that performance is increased by using cambered airfoil for VAWT. Design in this study involved multiple cambered airfoils in one model. It can be concluded from this study that a significant change in performance can be encountered by employing a hybrid model. The performance was increased to a high value with cambered model cases and then decreased as camber breached a limit. Whereas in case of a hybrid airfoil, the combination of different model samples proved efficient results, maximum of a 32% and a minimum of 9% increase in performance, was observed when the comparison was made with benchmark C00 model and other high camber symmetric vertical axis wind turbine models. Model with airfoil NACA 3421 and NACA 4421 showed 32% increase in performance whereas NACA 2431 and NACA 4421 combination VAWT model showed a 31% increase in performance.

REFERENCES

1. Chaichana, T.,S. Chaitep, Wind power potential and characteristic analysis of Chiang Mai, Thailand, *Journal of mechanical science and technology*, 24. (2010), 7, pp. 1475-1479
2. Bennett, R.,J. Elton, *History of Corn Milling*. Simpkin, Marshall and company, Ltd., 1899.
3. Valipour, M.,V.P. Singh, *Global experiences on wastewater irrigation: challenges and prospects*, in: *Balanced Urban Development: Options and Strategies for Liveable Cities*, (Ed., Editor^Editors), Springer. 2016, pp. 289-327.

4. Yannopoulos, S.I., *et al.*, Evolution of water lifting devices (pumps) over the centuries worldwide, *Water*, 7. (2015), 9, pp. 5031-5060
5. Fleming, P.,S. Probert, The evolution of wind-turbines: an historical review, *Applied energy*, 18. (1984), 3, pp. 163-177
6. Marie, D.G.J., *Turbine having its rotating shaft transverse to the flow of the current*. 1931, Google Patents.
7. Takao, M., *et al.*, A straight-bladed vertical axis wind turbine with a directed guide vane row— Effect of guide vane geometry on the performance—, *Journal of thermal Science*, 18. (2009), 1, pp. 54-57
8. Newman, B.,T. Ngabo, The design and testing of a vertical-axis wind turbine using sails, *Energy Conversion*, 18. (1978), 3, pp. 141-154
9. Morcos, V.,O. Abdel-Hafez, Testing of an arrow-head vertical-axis wind turbine model, *Renewable energy*, 7. (1996), 3, pp. 223-231
10. Marini, M., *et al.*, Performance of vertical axis wind turbines with different shapes, *Journal of Wind Engineering and Industrial Aerodynamics*, 39. (1992), 1-3, pp. 83-93
11. Baker, J., Features to aid or enable self starting of fixed pitch low solidity vertical axis wind turbines, *Journal of Wind Engineering and Industrial Aerodynamics*, 15. (1983), 1-3, pp. 369-380
12. Klimas, P.C.,M.H. Worstell, Effects of blade preset pitch/offset on curved-blade Darrieus vertical axis wind turbine performance. 1981, Sandia National Laboratories Albuquerque, NM, USA.
13. Paraschivoiu, I., *et al.*, H-Darrieus wind turbine with blade pitch control, *International Journal of Rotating Machinery*, 2009. (2009),
14. Ponta, F., *et al.*, On the aerodynamics of variable-geometry oval-trajectory Darrieus wind turbines, *Renewable energy*, 32. (2007), 1, pp. 35-56
15. WAKUI, T., *et al.* Optimum method of operating the wind turbine-generator systems matching the wind condition and wind turbine type, *World renewable energy congress*, 2000, pp. 2348-2351



16. Gorelov, D.,V. Krivospitsky, Prospects for development of wind turbines with orthogonal rotor, *Thermophysics and Aeromechanics*, 15. (2008), 1, pp. 153-157
17. Gupta, R..A. Biswas, Computational fluid dynamics analysis of a twisted three-bladed H-Darrieus rotor, *Journal of Renewable and Sustainable Energy*, 2. (2010), 4, p. 043111
18. Sharpe, T.,G. Proven, Crossflex: Concept and early development of a true building integrated wind turbine, *Energy and buildings*, 42. (2010), 12, pp. 2365-2375
19. Kim, D.,M. Gharib, Efficiency improvement of straight-bladed vertical-axis wind turbines with an upstream deflector, *Journal of Wind Engineering and Industrial Aerodynamics*, 115. (2013), pp. 48-52
20. Loya, A., et al., Dependency of Torque on Aerofoilcamber Variation in Vertical Axis Wind Turbine, *World Journal of Mechanics*, 6. (2016), 11, p. 472
21. Akansu, S.O., et al., Numerical Investigation of the Effect of Blade Airfoils on a Vertical Axis Wind Turbine, *Isı Bilimi ve Tekniği Dergisi*, 38. (2017), 1, pp. 115-125
22. Nguyen, C., et al., A numerical study of thickness effect of the symmetric NACA 4-digit airfoils on self starting capability of a 1 kW H-type vertical axis wind turbine, *Int. J. Mech. Eng. Appl*, 3. (2015), 3-1, pp. 7-16
23. Qamar, S.B.,I. Janajreh, Investigation of effect of cambered blades on Darrieus VAWTs, *Energy Procedia*, 105. (2017), pp. 537-543
24. Ahmad, A., et al., Roadside Vertical Axis Wind Turbine (VAWT): An Effective Evolutionary Design for Australian Highway Commuters with Minimum Dynamic Stall, *Engineering*, 12. (2020), 9, pp. 601-616
25. Antar, E., et al., A Dynamic Rotor Vertical-Axis Wind Turbine with a Blade Transitioning Capability, *Energies*, 12. (2019), 8, p. 1446
26. Sun, X., et al., Research on the aerodynamic characteristics of a lift drag hybrid vertical axis wind turbine, *Advances in Mechanical Engineering*, 8. (2016), 1, p. 1687814016629349
27. Wakui, T., et al. Optimum method of operating the wind turbine-generator systems matching the wind condition and wind turbine type, *World Renewable Energy Congress VI, 2000*, pp. 2348-2351
28. Bhutta, M.M.A., et al., Vertical axis wind turbine—A review of various configurations and design techniques, *Renewable and Sustainable Energy Reviews*, 16. (2012), 4, pp. 1926-1939
29. Claessens, M., The design and testing of airfoils for application in small vertical axis wind turbines, *Master of Science Thesis*. (2006),
30. Islam, M., et al., Aerodynamic models for Darrieus-type straight-bladed vertical axis wind turbines, *Renewable and Sustainable Energy Reviews*, 12. (2008), 4, pp. 1087-1109
31. Wu, J.-Y.,R. Lee, The advantages of triangular and tetrahedral edge elements for electromagnetic modeling with the finite-element method, *Antennas and Propagation, IEEE Transactions on*, 45. (1997), 9, pp. 1431-1437
32. Li, L., et al. The applicability of two-equation turbulence models in wind velocity prediction, *Applied Mechanics and Materials*, 2013, 291, pp. 518-521
33. Abraham, J., et al., Summary of Savonius wind turbine development and future applications for small-scale power generation, *Journal of Renewable and Sustainable Energy*, 4. (2012), 4, p. 042703
34. Cao, H., Aerodynamics Analysis of Small Horizontal Axis Wind Turbine Blades by Using 2D and 3D CFD Modelling, *Citeseer*, 2011.

Topology Optimization of Bell Crank Lever using FEA

Saghar Ali Rabbani, Shahid Mehmood

Mechanical Engineering Department, University of Engineering and Technology Taxila, Pakistan

sagharalirabbani@gmail.com

ABSTRACT

Topology optimization has emerged as a critical tool in the quickly developing field of engineering, helping to achieve high-performance, economical, and sustainable solutions. In lean manufacturing, when maximizing efficiency and lowering material usage are critical, this procedure is very important. Our research effort focuses on optimizing the mass of a 90-degree bell crank, a pivotal lever that is used to shift the direction of force in industrial, automotive, and aerospace applications. Bell cranks are traditionally over-engineered and can contain redundant material, which introduces additional weight and inefficiency. Using the technique of topology optimization with attention on mass reduction, we are able to significantly lower the weight of the bell crank without compromising its structural integrity or performance. In the present study, we mostly emphasize mass topology optimization, nonetheless there are other types as well, like compliance minimization and stress optimization.

KEYWORDS: Topology Optimization, Finite Element Analysis, Bell Crank Design, Mass Reduction, Structural Integrity, Factor of Safety.

5. INTRODUCTION

To determine the most effective load-bearing routes, topology optimization is a design technique that meticulously maximizes material distribution within a design space. It ensures efficient and effective material utilization by taking load conditions of use, targets for performance, and limits into account [1]. This method is now widely used in engineering, especially in the disciplines of aerospace [2][3], heat transfer systems [4], and architectural design [5], where efficient material distribution is critical to the structural integrity and effectiveness of the design. More economical, efficient, and ecological designs have resulted from these developments.

6. TOPOLOGY OPTIMIZATION DESIGN PROCESS

The process of design optimization via topology optimization can be seen in the flowchart [6] The process starts with the Source 3D-CAD Model, which identifies the sections that can be removed without sacrificing structural integrity. After that, the model is modified in 3D-CAD to produce the lighter, more effective version that is depicted in "Fig. 1." Design Verification then makes sure the optimized model satisfies all safety and

efficiency requirements. After validation, the design is completed for production, guaranteeing reliability and material efficiency.

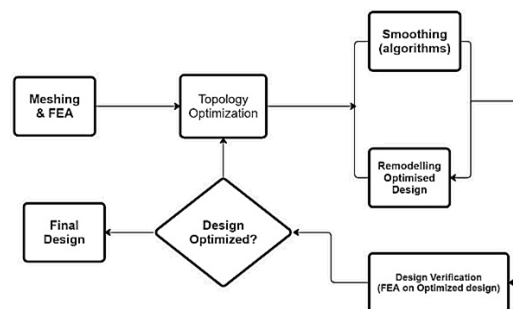


Figure 1: Topology optimized design process flow

Basic FEA on CAD Software

Establishing a baseline understanding of the bell crank's behavior under static conditions is crucial before beginning topology optimization. FEA has been used to analyze the stress, strain, deformation, and Factor of Safety (FOS) of the unoptimized design. The previously stated baseline metrics are essential for evaluating the impact of design modifications on material efficiency, structural integrity, and durability by contrasting them with the optimized design.

Design constraints & Boundary Conditions:

Bell In mechanical systems, particularly in automotive and industrial contexts, bell cranks; which are frequently constructed from annealed steel for strength and fatigue resistance—are crucial for adjusting the direction of forces [7]. With load capabilities ranging from 1000 to 3000 N, usually 2000 N in the automation and automotive industries, the typical dimensions are 120 mm in length, 115 mm in height, and 10 mm in thickness[8]. The middle hole of the bell crank lever is set in a pivotal position, and the end holes experience pulling pressures of 2000 N, which replicates the operational circumstances involved in stress and deformation analysis.

Mesh Convergence:

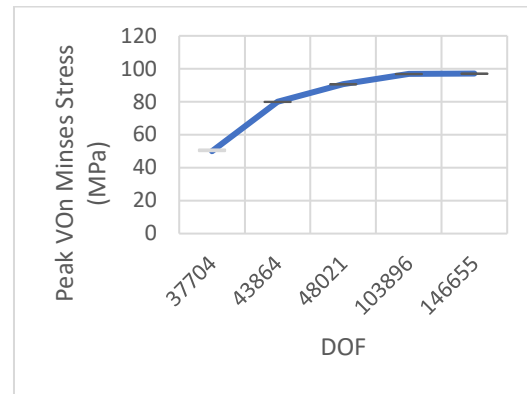
Moving on, we will do the mesh sensitivity analysis. For that, we will perform multiple stress analysis, by refining the mesh incrementally, until the stress is no longer affected by further refinement of mesh. So, the "Table 1" shows the analysis details for mesh convergence.

Table 1: Mesh Convergence Analysis Details.

Stress Analysis No.	1	2	3	4	5
No. of Elements	7728	8624	9887	22264	32006
No. of DOF	37704	43864	48021	103896	146655
Peak VM Stress (MPa)	50	80	90.63	96.93	97.12
Max Element Size(mm)	10	7	5	3	2.5

The given "Chart 1" displays the mesh curve, keeping the mesh type same, but refining the mesh size.

Chart 1 Mesh convergence



Meshing:

To assure accuracy, we employed the factory default mesh settings with high resolution and an element size of 1.83 mm for a thorough examination of the bell crank's stress distribution. The 1.4 aspect ratio of the mesh pieces ensures their good form and dependability for analysis.

Table 2: Mesh parameters for FEA

Parameters	Mesh type	Mesh Used:	Maximum element size	Minimum element size	Mesh Quality	Total Nodes	Maximum Aspect Ratio
Details	Solid Mesh	Curvature-based mesh	2.5 mm	0.182935 mm	High	138458	15.14

FEA Results:

Using the unoptimized design as a reference, the FEA results evaluate displacement, stress distribution, strain, and FOS to demonstrate the structural behavior of the bell crank under defined loads. The highest stress of 31.43 MPa was obtained by applying two 2000 N perpendicular forces at the ends, with the center hole operating as the pivot. This result is illustrated in "Fig. 2," which reveals the areas that are most subject to deformation.

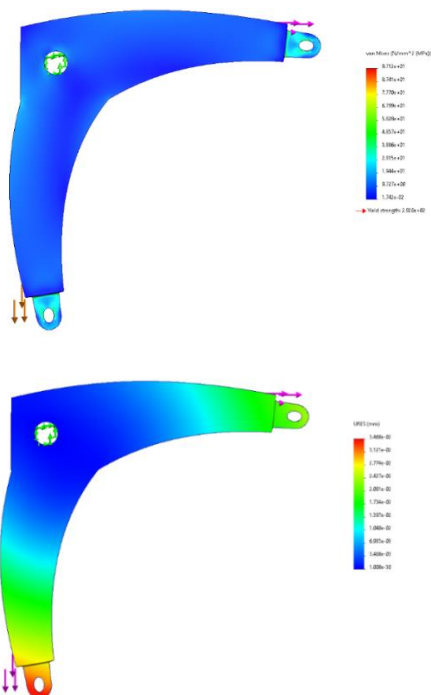


Figure 2 (a) Von-Mises Stress, (b) Resultant displacement.

According to "Fig. 2," the FEA findings indicate a maximum displacement of 0.023 mm and a Factor of Safety (FOS) of 3, which denotes little deformation and a substantial margin before yielding. The measures, which are listed in "Table 3," function as a foundation for contrasting the optimized design. The unoptimized bell crank has a mass of 384.56 g, a Von Mises Stress of 97.12 MPa, and a displacement of 0.0173 mm. These values will function as the basis for the topology optimization.

Table 3: FEA Results of Original Design

Properties	Unoptimized FEA Results
Von Mises Stress (MPa)	97.12
Displacement (mm)	0.034
Factor of Safety (FOS)	2.6
Mass (g)	384.56

Topology Optimization Study

With the objective to optimize the bell crank's topology and minimize its total weight by 60% while retaining structural integrity, we utilized SolidWorks 2022. To ensure functionality, important areas were kept intact, such as the two end holes and the central pivot hole. In sectors where weight reduction is critical, such as the aerospace and automobile industries, this optimization is critical to increasing efficiency.

Constraint settings in optimization:

We improved the bell crank's mass based on the FEA results, lowering it by over half without compromising structural integrity. Key "preserved regions", like the central pivot hole and the two end holes, must remain unchanged to maintain the bell crank's functionality and stability.

Optimized Topology Results:

By eliminating material from low-stress areas, the improved design successfully lowers mass yet retains crucial sections like the end holes and central pivot for safe functionality. Material was completely removed through the part's depth using demolding processes, preserving the stiffness-to-mass ratio along with improving performance.

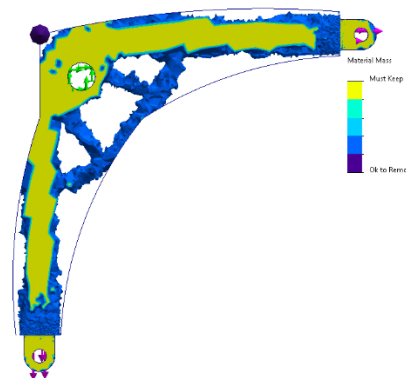


Figure 3 Topology Optimization material removal results

Optimized Design FEA

Redesigning the bell crank is the next step after achieving optimum geometry. To create a new CAD model, we will exclude the material that was discovered during topology optimization. Then, to make sure that the structural integrity is maintained despite the weight decrease, we'll run the same FEA as we did with the unoptimized design. Through this procedure, it will be proven that all performance requirements are met by the improved design without sacrificing usability.

Redesigning and Resolving:

For us to produce a new CAD model, we will first redesign the optimal geometry and remove any material that was found during the topology optimization. After that, in order to guarantee structural integrity while lowering weight, we will examine stress and deformation. To assess the optimized and original designs under the same conditions, we will run the FEA after remeshing with the same constraints and conditions.

7. RESULTS OBSERVATION

We examine the optimized design through analyzing the factors of safety (FOS), stress, strain, and deformation to make sure the structural integrity hasn't been damaged by the weight reduction. As demonstrated in "Fig. 4-a" for stress distribution, comparing these measurements with the original design reveals any enhancements or potential areas for improvement. We also pay consideration to displacement, and as "Fig. 4-b" illustrates, the improved design shows a tiny rise to 0.037 mm, which is still within the acceptable limits. The next section will include a thorough comparison.

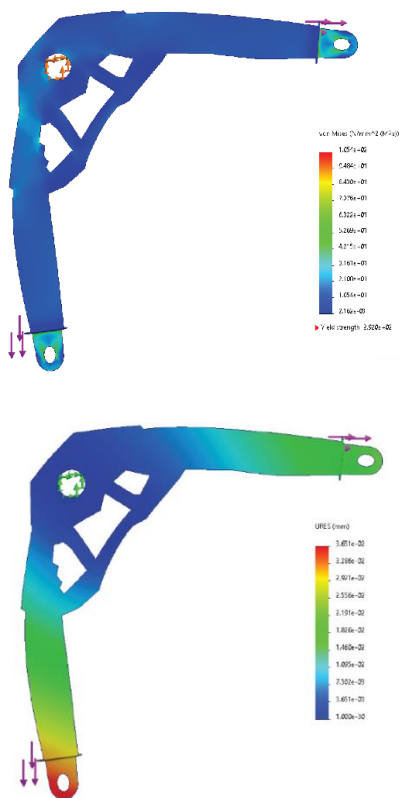


Figure 4 (a) von-Mises Stress, (b) Resultant Displacement

Design Validation and Comparison

Validating the improved design against the original across stress, strain, deformation, and Factor of Safety (FOS) is the last stage in the process. This comparison confirms that performance standards are met by the optimized design. To isolate the optimization's impacts, both designs will be evaluated with the same forces, materials, and sizes. Important metrics such as Von Mises Stress, resultant displacement, FOS, and mass will verify whether the optimized design reduces weight without sacrificing integrity. The outcomes, which are outlined in "Table 4,"

demonstrate the advantages and disadvantages of the optimization.

Table 4: FEA Results Comparison of original and optimized design

Properties	Unoptimized FEA Results	Optimized Part	Difference (%)
Von Mises Stress (MPa)	97.12	105.4	8.01
Displacement (mm)	0.034	0.037	8.45
Factor of Safety (FOS)	2.6	2.70	6.66
Equivalent Strain (x10-3 mm)	46.11	42.21	9.1
Mass (g)	384.56	170	56

8. CONCLUSION

In this work, we used topology optimization to optimize a 90-degree bell crank with an objective of reducing mass by 60% without compromising structural integrity. The baseline measurements for stress, strain, deformation, and Factor of Safety (FOS) were obtained from the initial finite element analysis (FEA). We omitted extraneous material while keeping important functional areas using SolidWorks 2022. The integrity of the design and considerable weight savings were confirmed by subsequent FEA, which revealed only slight increases in stress and deformation and FOS within the appropriate limits. This demonstrates how important topology optimization is for improving performance and efficiency, especially among the automobile and aerospace industries. According to a study on topology optimization, "topology optimization is a powerful tool in modern engineering because it may dramatically decrease material usage while maintaining structural strength." [10].

ACKNOWLEDGMENT

The authors would like to thank EUR ING Hafiz M Muddassir and Engr. Ali Saim for their support and feedback in improving the paper. This work was funded by MECESOL CO. (PVT) LTD. under grant No. PD2408001. Any opinions, findings, conclusions, or recommendations expressed in this material are those of the authors and do not necessarily reflect the views of MECESOL CO. (PVT) LTD



REFERENCES

Design, Vols. vol. 139, no. 6, pp. 065001-065011,
Jun. 2017.

1. M. Bendsøe and O. Sigmund, *Topology Optimization—Theory*, Berlin/Heidelberg: ISBN 978-3-642-07698-5., 2003.
2. G. Shi, C. Guan, D. Quan, D. Wu, L. Tang and T. Gao, An Aerospace Bracket Designed by Thermo-Elastic Topology Optimization and Manufactured by Additive Manufacturing, 33, 1252–1259.: *Chin. J. Aeronaut.*, 2020.
3. Z. Jihong, H. Fei and Z. Weihong, "Key Optimization Design Issues for Achieving Additively Manufactured Aircraft and Aerospace Structures," *Aeronaut. Manuf. Technol*, 2017, p. 16–21..
4. T. Dbouk, " A Review about the Engineering Design of Optimal Heat Transfer Systems Using Topology Optimization," in *Appl. Therm. Eng.*, 2017, pp. 112, 841–854..
5. L. Beghini, A. Beghini, N. Katz, W. Baker and G. Paulino, "Connecting Architecture and Engineering through Structural Topology Optimization," in *Eng. Struct*, 2014, p. 716–726.
6. A. W. Gebisa and H. G. Lemu, "A case study on topology optimized design for additive manufacturing," *IOP Conference Series:Materials Science and Engineering*, Vols. DOI:10.1088/1757-899X/ 276/1/012026, p. 276(1): 012026., 2017.
7. V. N. R. B. P. S. K. C. Sowjanya, "Optimum Design and Analysis of Bell Crank Lever for an Automobile," *Advanced Manufacturing Systems and Innovative Product Design*, no. Lecture Notes in Mechanical Engineering. Springer, pp. 16-17, 2021.
8. G. B. a. P. C. R. Saini, ""Optimization of Design Parameters of a Bell Crank Lever Using CAE Tools," *Optimization Methods in Engineering*, Vols. doi: 10.1007/978-981-15-4550-4_29, no. Lecture Notes on Multidisciplinary Industrial Engineering, pp. 455-462, 2021.
9. R. C. Hibbeler, *Mechanics of Materials* 10th ed. Boston, USA: Pearson: Boston MA, 2017.
10. L. Smith, "Advances in Topology Optimization for Engineering Design," *Journal of Mechanical*

Intelligent System for Real-time Health Monitoring of Power MOSFETs

Tabish Nawaz^{1,2}, Muhammad Asif¹

¹ Department of Mechatronics Engineering, University of Engineering and Technology, Taxila, Pakistan,

² Department of Computer Science, Middlesex University, London, United Kingdom

tn462@live.mdx.ac.uk

ABSTRACT

As Power MOSFETs play a significant role in the industrial manufacturing process, it is of immense value to study the failure modes of these MOSFETs. A typical MOSFET failure condition is caused by a short circuit between the source and drain. In addition, excessive current and excessive power dissipation are causes of MOSFET failure. The focus of this research was to create an intelligent data-driven system that uses Prognosis, Neural Networks, and Machine Learning Models to forecast the Remaining Useful Life (RUL) of power MOSFETs. After executing the train and test models on LSTM using a learning rate of 0.001, 50 epochs, and the Rul activation function, it was discovered that the MAE and model loss decreased substantially. A modest hardware setup was developed later for real-time testing of trained and tested LSTM models. After implementing data driven techniques, real-time testing was done under accelerated aging at 70°C. After 3 minutes of intensive accelerated aging, the MOSFET had 34.706 minutes of RUL. Future work will focus on developing a benchmarking circuit capable of operating under a wide range of temperature-controlled conditions. This will allow us to compare the activation energy derived from current models with that of the proposed model.

KEYWORDS: RUL, Prognosis, Predictive Health Maintenance, Remaining Useful Life, End-life Prediction

1. INTRODUCTION

Power MOSFETs are the key enabler of electrical gadgets. We all take for granted many modern electronics, from light-emitting diode lamps to high-definition televisions and digital cameras. They work by controlling electricity, much as a water valve controls water flow. Apart from these applications, power MOSFETs are widely used in the automotive industry. Electric bikes are a great example. This is borne out by the fact that no electronic device works without a MOSFET somewhere inside it. Power MOSFETs is the only MOSFET that makes high voltage very accessible for microcontrollers. A normal MOSFET cannot switch high voltages due to the dielectric breakdown of the gate insulator damaging the gate. The use of new manufacturing methods has led to a decrease in the thickness of gate oxide, which has led to an increase in dynamic characteristics and reduced power loss. The MOSFET may get overheated or get radiation, both of which will cause the oxide-trapped charge and interface traps to be considerably denser [1]. This causes instability in the system. Therefore, researchers have paid much attention to the failure problems of power MOSFETs in the past years. It's also important to note that bond wire-related failures like cracks and delamination in the die attach solder are considered one of the causes of increased on-state resistance. A typical failure condition in a Power MOSFET is a short circuit between source and drain.

Due to the increased demand for safety and maintenance requirements in industrial applications, prognosis has gained great importance in the last few decades. This makes the industry preplan its maintenance by adopting agility. In this project, an LSTM model was employed as a machine learning tool to be able to measure and predict the RUL of the power MOSFETs. The key results stated that the resistance of the junction of the MOSFETs is the main key element for its prognosis. The train, test, and real-time data sets each validated the response from the NASA datasets.

A. MONITORING METHODS AND ALGORITHMS

Various health monitoring methods have been employed to predict the degradation of power MOSFETs in previous studies. Health monitoring methods based on the threshold voltage [2], condition monitoring method for threshold voltage drift and packaging degradation [3] are some of the methods used for health monitoring of power MOSFETs. These approaches offer valuable insights into the operational reliability of power MOSFETs under stress. Several algorithms have been developed to enhance the accuracy of power MOSFET health monitoring, including:

- Particle-Based Filter Method [4]
- Platform Voltage Method (Miller Effect) [1]



Figure 1. Stepwise processes in the calculation of RUL

- Rain flow Counting Algorithm [5]
- Kalman Filter Method [5]
- Feed Forward Neural Network Mechanism [6]

These methods are particularly discussed in the 'State-of-the-art' section of this paper.

2. STATE OF THE ART

Power MOSFETs RUL can be predicted using prognostics, according to Celaya et al. [7] in 2011. Thermal cycling and Gaussian process regression were utilized for prediction. Temperature-dependent changes in ON -state resistance was employed as a warning sign that the device was about to fail. In order to make the proposed procedure work, several assumptions were made. During the accelerated aging process, the loads and conditions that would be applied to the device in the future were assumed to be constant. According to the findings, as more data becomes available, the predictions get more precise (as evidenced by the proximity of the predicted dashed lines to the crossing of the failure threshold by the ON resistance) and the prediction range becomes more precise.

Power MOSFETs that are subjected to electrical overstress at the gate area are subject to rapid aging, as proposed by Saha et al. [8] in 2011. The methods for accelerating the aging process, modeling the device degradation process, and a prognostics algorithm for predicting the future health of the device were all covered in the paper's presentation of the findings. In a particle filtering system, the degradation curve model was applied to predict RUL estimations. Although the prognostics routine was solid, it could not deal with aspects such as irregular rest intervals that occur with age as part of the natural process.

In 2014, Zheng et al. [9] studied to estimate the RUL of power MOSFETs, a technique merging RVM, and a deterioration model was suggested in this research. To begin, RVM used available power MOSFET deterioration data as training data to generate RVs. Secondly, using representative vectors and nonlinear least squares regression, the parameters of the deterioration model were determined. Then, by expanding the model of degradation to a failure threshold, the RUL of the power MOSFETs was calculated. Finally, throughout the prediction phase, the degradation model was updated according to the recommended approach. As a result, the model was able

to respond to the mutation promptly, and the prediction became more accurate.

Dusmez et al. [10], 2015, studied the Remaining Useful Life (RUL) of power MOSFETs which are degraded by the thermal cycling process. A data-driven approach is used in which data is collected through exhaustive tests. An exponential curve fitting algorithm was used to find empirical coefficients α, β online. The uncertainties such as noise errors were eliminated by using Kalman Filter (KF) method. Only on-state resistance parameters were observed as junction temperature measurements were not required in this model. It was concluded that the initial estimation errors, for exponential coefficients α, β , were reduced to 4.2% and 3.5% from 34.6% and 28.7%, by using more data points.

In 2017, Dusmez et al. [11] analyzed the degraded power MOSFETs failure due to thermal cycling. A data-driven approach RUL estimation algorithm was used, and the errors were removed by Random Sample Consensus (RANSAC) algorithm. In comparison to the case where the least-squares method is applied to all data points without removing errors, the proposed methodology yielded superior results to the actual RUL. The use of RANSAC ensures that the estimation is resistant to large levels of noise

In 2017, Chen et al. [1] devised an in-situ prognosis method for the study of power MOSFETs based on the miller effect. A new degradation precursor $\hat{\alpha}$ the miller platform voltage was identified. Algorithms like particle filters were used to predict the RUL of MOSFET using miller voltage data. It was concluded that degradation of power MOSFET is increased by increasing the gate bias voltage. Also, the degradation trend of miller platform voltage matched with a threshold voltage.

In 2018, Pugalenthil et al. [4] investigated the prognosis of power MOSFET microcontroller devices. They claimed that power MOSFETs degrade owing to thermal reasons, and they used ON-resistance variation as a failure indicator for prognosis. They adopted the particle filter algorithm for their purpose. They discovered an improvement in accuracy above the usual particle filter method towards the end of their analysis. The effect of varied roughening on RUL prediction accuracy is discussed and the results are obtained by using the parameters which were roughening to get knowledge such as comparative accuracy and computational period.

In 2021, Witzcak et al. [12] predicted the remaining useful life of power MOSFETs using analytical and datadriven methods. In the proposed approaches they obtained the degradation data from the historical data. As a datadriven technique, they employed the Takagi-Sugeno multiple models-based frameworks, while as an analytical approach, they used an exponential curve fitting online approach. Unlike the previous prognosis, they designed data on the basis of historical data to get the diagnostics decisions. It was concluded that the currently operating MOSFETs, went through the run-to-failure process. Finally, the suggested method is validated using real data obtained from NASA's prognostic data collection.

This paper presents a solution to this problem by proposing a machine learning approach for predicting the RUL of Power MOSFETs. The proposed model is based on LSTM and is an iterative process that uses a regression LSTM to estimate the error between the actual data and predicted values for each sample in the dataset. The final prediction is obtained by taking the average of all these estimates. The novelty of this work shows intelligent data-driven system will calculate the RUL of individual power MOSFETs, with minimum errors of MSE; RMSE; and MAE. Real-time model testing will be done on MOSFET to ensure its useability in industries.

3. METHODOLOGY

In this section, a comprehensive description of the proposed materials and methods is presented, along with a description of the complete experimentation that will be used for this work. Listed below are the different subdivisions of this section with detailed information about work and outcomes from this work.

A. DATA SETS

Model degradation datasets were acquired from the NASA Ames Prognostics Repository. The data consisted of 42 MOSFETs data which were run-to-failure under thermal stress. The dataset includes detailed measurements of the MOSFETs' electrical and thermal characteristics over time, providing insights into their degradation patterns. Various environmental factors, such as temperature swings, are applied to accelerate aging and observe the impact on performance. The wide temperature ranges from (-55 to +175°C). The format data was available in .mat format, in which transient response, steady-state response, and PWM data were formulated into multiple ensemble tables.

B. MODERN TOOLS USED

- MATLAB: Used for pre-processing and data analysis

- Jupyter-Labs: Environment for Python and Machine Learning
- Python: Keras, Pandas, Seaborn, NumPy, and TensorFlow libraries used
- Data Streamer: Used to extract real-time data

1. MATLAB

At primary the current and voltage values were available in the form of ensemble tables. Using the average values of the ensemble table data, such as MOSFET drain current and drain-to-source voltage, the data at one timestamp couldn't give noise in the values. Since we know that the RUL of MOSFETs is mostly dependent upon resistance, we used to drain current and drain-to-source voltage to determine the resistance. After the separation of all the variables in a CSV file, filters like median filter were applied to the resistance data to overcome the noise. Figure 2 shows the difference between the raw resistance and filtered resistance of the 26th MOSFET.

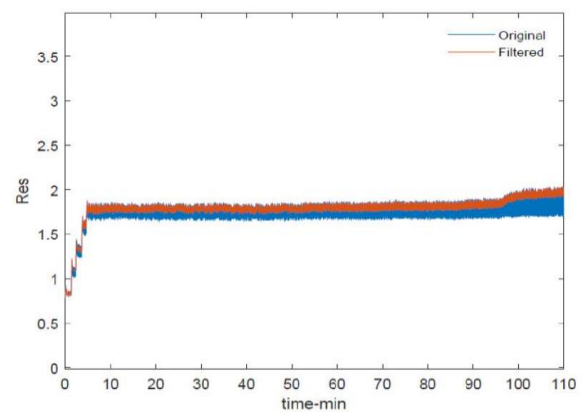


Figure 2. Filtered R using a median filter of the 26th MOSFET

2) Python

The results of the MATLAB algorithms were then used to carry out additional processing. We took the average values of 25 and 75 preceding data points to remove the spiky data. The reduction of background noise and data cleansing allowed the machine learning model to run more quickly and with fewer errors than previously. Data normalization was also performed on the data which rescaled the values to 0 and 1. Model training becomes less dependent on the scale of features when data normalization is utilized. Figure 3 shows the resistance values of the 17th MOSFET which was then filtered using the mean average filter in the python environment as shown in Figure 4.

C. CONDITION MONITORING

It was necessary to perform conditional monitoring to identify the factors that might affect the prognosis. The drain current reduces as the drain-to-source voltage rises over time, according to the results of the experiment. Because voltages and currents affect resistance, we can simply use the resistance values to get accurate results from the model. This means that the model can be implemented in a fraction of the computing time it would require if it had more

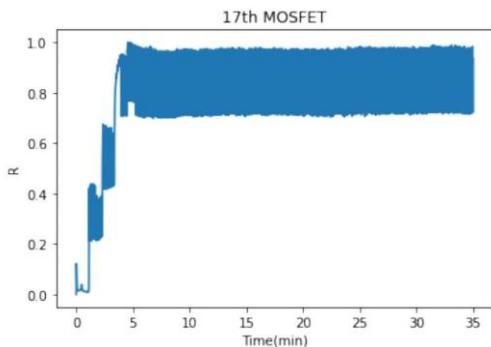


Figure 3: Resistance of the 17th MOSFET (normalized)

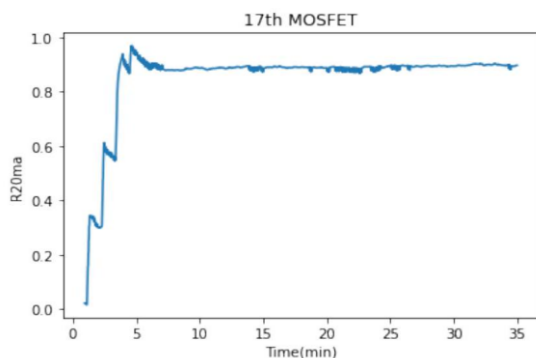


Figure 4: Filtered Resistance of the 17th MOSFET (normalized)

variables. Figure 5 depicts the relationship between the 26th MOSFET's R, VSD, and DC. This graph shows that all three variables are linked together. In this equation, R stands for resistance, VSD for drain-to-source voltage, and DC for MOSFET drain current. The graphs obtained from the conditional variable's identification are shown in Figure 6. From Figure 6, it can be seen that the resistance, drain current and the drain-to-source voltage along with the independent variable "time" will help calculate the RUL of the MOSFET.

Figure 7 shows the relationship between the filtered values of resistance of the three MOSFETs numbered 26, 17, and 21. It can be seen from the graph that the resistance of all the three MOSFETs is different from each other even if the operating conditions are the same for all of them.

D. MACHINE LEARNING MODELS

For the prediction of power MOSFETs, LSTM was used as a machine learning model. Due to its accuracy and ability to operate well with time series data, it was chosen. The long-term reliance problem is deliberately avoided with LSTMs.

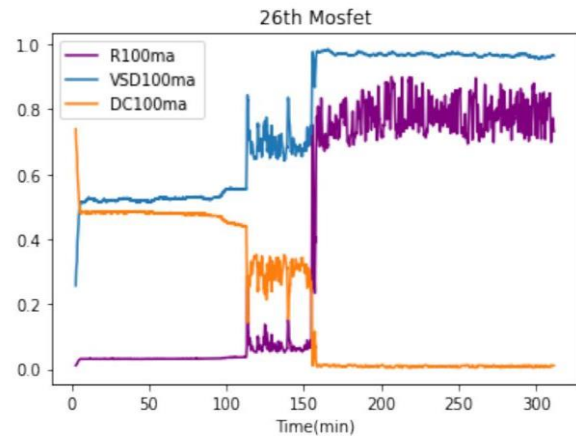


Figure 5: Resistance, VSD, and DC of the 26th MOSFET

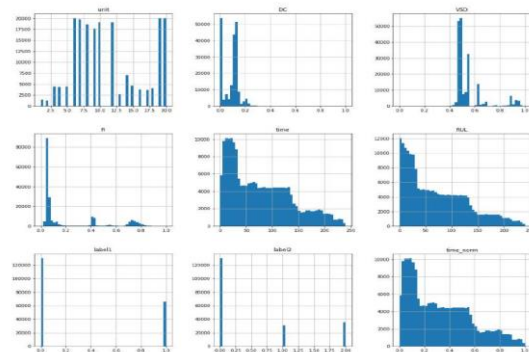


Figure 6: Dependent and independent variables for conditional indicators

For them, long-term memory is a natural situation, and they don't have to work at it. The RUL activation function was used with 30 epoch values in the LSTM's sequential model. The MSE (mean squared error) dropped with each occurrence of the following epoch value when the model was run under 30 epochs. 0.001 learning rate was adopted for training on LSTM.

E. RUL PREDICTION

RUL, to train the model, was calculated by using Eq 1 .

$$MTD - CTPI \tag{1}$$

Where;

MTD = Max time of degradation

CTPI = Current Time at the present instance

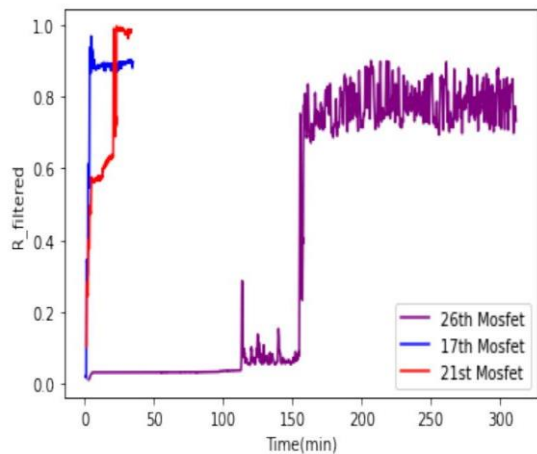


Figure 7: Filtered resistance values of 26, 17, and 21 MOSFET

Afterward, a health assessment of the power MOSFET was done by training the machine learning model, calculating the errors, and testing it with the remaining data.

F. REAL-TIME MONITORING SETUP

For the real-time testing of the trained and tested LSTM models, a small hardware setup was designed. The components include Voltage Measuring Sensor, Current Measuring Sensor, MOSFET 80nf70, Motor, Arduino Mega, Breadboard, Jumper wires, 5V Power Source, and Excel Data Streamer.

Excel's Data Streamer is a two-way data transmission that transfers data from Excel back to a microcontroller, as well as streaming live data into Excel from a microcontroller. Students are introduced to the fields of data science and the internet of things through the use of Excel, sensors, and microcontrollers that are included in the Data Streamer kit (IoT) [13]. Arduino was sending out data in the form of VSD and DC. Using Excel Data Streamer, these were saved in the format of tables as a comma-separated values (CSV) file. The raw data was pre-processed similarly as the training historical data and was normalized to ensure efficient model implementation. This data was then utilized to compute the resistance of the MOSFET, which, according to ohm's law, is the only condition indicator for the RUL. This value was found using Eq 2

$$R = \frac{V}{I} \quad (2)$$

4. RESULTS AND DISCUSSION

A. HEALTH ASSESSMENT

Table IV-A presents the LSTM model's MSE, RMSE, and MAE losses. Because of this, it can be concluded that the model has been properly trained and that its accuracy has increased over time. Using the MSE, researchers determine how closely a fitted line matches the data. The better the model fits the data, the lower the Mean Squared Error will be. Error rate divided by square root of MSE is RMSE. This statistic is the simplest to understand because it has the same units as the quantity depicted on the Y-axis or vertical axis.

Table 1. Error and Loss values of the trained LSTM Model

Error/Loss Type	Values
Mean Squared Error (MSE)	9.615992022829877
Root Mean Squared Error (RMSE)	3.1009663046911484
Mean Absolute Error (MAE)	2.340416395825946

$$MSE = \frac{1}{n} \sum_{i=1}^n (Y_i - \hat{Y}_i)^2 \quad (3)$$

$$RMSE = \sqrt{\frac{\sum_{i=1}^N (x_i - \hat{x}_i)^2}{N}} \quad (4)$$

The health assessment of the MOSFET, after its training, was accomplished by testing the model and pointing out the maximum errors in them. Data of the 20 MOSFETs were compared with each other. The testing model was run to fit the trained model of all the 20 MOSFETs.

After running the train and test models on LSTM, with configurations discussed in the methodology section, it was found that the MAE and model loss dropped significantly. This loss and MAE can be seen in Figure 8 and Figure 9. From the two figures, it is clear that running the learning algorithm within 50 epochs provides the best results for MAE and loss function. Changing the epoch values will result in overfitting or underfitting respectively. The model MAE in Figure 9 would stop at 4.6, and it would not decrease further. The train and test sets of the fitted data is almost same as shown in the figure. However, the test data MAE shows a further decrease in trend as compared to the training data. To put it simply, the test set was easier for the model to do well on than the training set, which resulted in a lower Test MAE!

Training and testing RUL data were plotted on a graph after losses had been calculated. It was obtained by fitting

the LSTM model with previously defined y -prediction values. It can be seen from the Figure 10 that the anticipated and real RUL for the training RUL data is nearly identical. An accurate test on historical and real-time data confirms that the model has been properly trained and can be moved along to test on the historical and real-time data. Similarly, in Figure 11, for the testing RUL predicted vs actual RUL data, the graphs also show the identical trend.

B. REAL-TIME PREDICTION

As discussed in the earlier sections, a real-time circuit was developed to validate the trained and the tested LSTM models in order to ensure the model inclusiveness. The same pre-processing techniques were applied as used for NASA Mosfet Degradation dataset.

The real-time tests were run for 3 minutes under highly accelerated aging process with the operating temperature of almost 70°C. The derived results from the machine

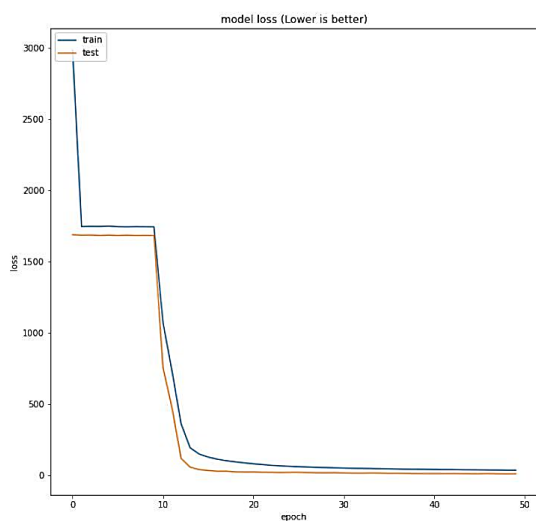


Figure 8. Model loss of the train and test data

RUL with minimal error, achieving MSE of 9.615, RMSE of 3.101, and MAE of 2.340. The LSTM-based model demonstrated significant improvements over traditional methods, particularly in handling time-series data and providing accurate long-term predictions.

Our approach offers practical implications for real-time health monitoring in industrial settings, enabling predictive maintenance and reducing the risk of unexpected power MOSFET failures. The real-time validation of the model under accelerated aging conditions confirmed its application for real-world scenarios.

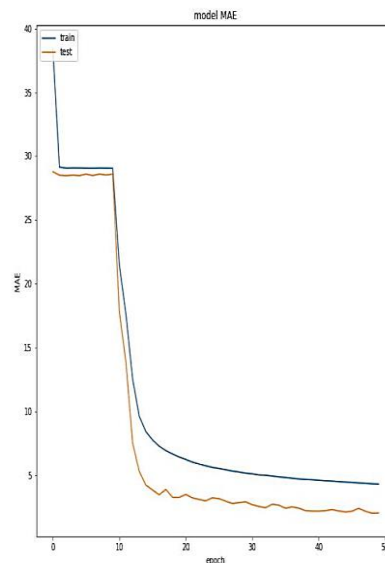


Figure 9. Model MAE of the train and test data learning model showed that after 3 minutes of intense accelerated aging, the MOSFET remaining useful life was 34.706 minutes. The derived results for the real-time RUL is shown in figure 10.

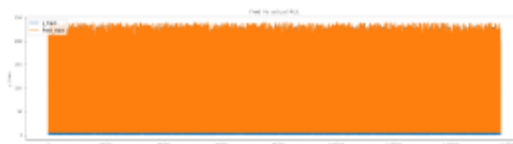


Figure 10. Original and Predicted values of the training dataset

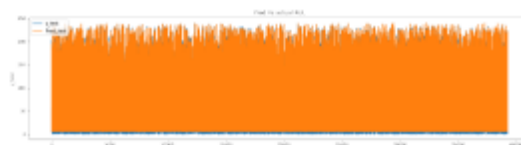


Figure 11. Original and Predicted values of the training dataset

While the results are promising, future work should focus on testing the model under a wider range of operating conditions to improve its robustness. Additionally, the development of a bench-marking circuit for comprehensive testing across varying temperatures will further enhance the accuracy and applicability of the proposed method.

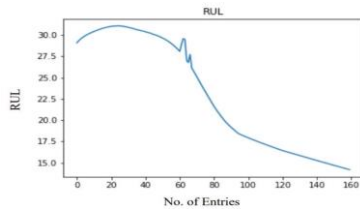


Figure 12. Real-time RUL of a power MOSFET

REFERENCES

1. C. Chen, X. Ye, H. Wang, G. Zhai, and R. Wan, "In-situ prognostic method of power mosfet based on miller effect," in 2017 Prognostics and System Health Management Conference (PHM-Harbin), 2017, pp. 1-5.
2. L. Ren, C. Gong, Q. Shen, and H. Wang, "A method for health monitoring of power mosfets based on threshold voltage," in 2015 IEEE 10th Conference on Industrial Electronics and Applications (ICIEA), 2015, pp. 1729-1734.
3. E. Ugur, C. Xu, F. Yang, S. Pu, and B. Akin, "A new complete condition monitoring method for sic power mosfets," IEEE Transactions on Industrial Electronics, vol. 68, no. 2, pp. 1654-1664, 2021.
4. K. Pugalenthil and N. Raghavan, "Roughening particle filter based prognosis on power mosfets using on-resistance variation," in 2018 Prognostics and System Health Management Conference (PHM-Chongqing), 2018, pp. 1170-1175.
5. S. Dusmez and B. Akin, "Remaining useful lifetime estimation for degraded power mosfets under cyclic thermal stress," in 2015 IEEE Energy Conversion Congress and Exposition (ECCE), 2015, pp. 3846-3851.
6. K. Pugalenthil, H. Park, and N. Raghavan, "Prognosis of power mosfet resistance degradation trend using artificial neural network approach," Microelectronics Reliability, vol. 100-101, p. 113467, 2019, 30th European Symposium on Reliability of Electron Devices, Failure Physics and Analysis. [Online]. Available: <https://www.sciencedirect.com/science/article/pii/S0026271419305323>
7. J. R. Celaya, A. Saxena, S. Saha, V. Vashchenko, and K. Goebel, "Prognostics of power mosfet," in 2011 IEEE 23rd International Symposium on Power Semiconductor Devices and ICs, 2011, pp. 160-163.
8. S. Saha, J. R. Celaya, V. Vashchenko, S. Mahiuddin, and K. F. Goebel, "Accelerated aging with electrical overstress and prognostics for power mosfets," in IEEE 2011 EnergyTech, 2011, pp. 1-6.
9. Y. Zheng, L. Wu, X. Li, and C. Yin, "A relevance vector machinebased approach for remaining useful life prediction of power mosfets," in 2014 Prognostics and System Health Management Conference (PHM2014 Hunan), 2014, pp. 642-646.
10. S. Dusmez, S. H. Ali, M. Heydarzadeh, A. S. Kamath, H. Duran, and B. Akin, "Aging precursor identification and lifetime estimation for thermally aged discrete package silicon power switches," IEEE Transactions on Industry Applications, vol. 53, no. 1, pp. 251-260, 2017.
11. S. Dusmez, M. Heydarzadeh, M. Nourani, and B. Akin, "Remaining useful lifetime estimation for power mosfets under thermal stress with ransac outlier removal," IEEE Transactions on Industrial Informatics, vol. 13, no. 3, pp. 1271-1279, 2017.
12. M. Witczak, M. Mrugalski, and B. Lipiec, "Remaining useful life prediction of mosfets via the takagiâsugeno framework," Energies, vol. 14, no. 8, 2021. [Online]. Available: <https://www.mdpi.com/1996-1073/14/8/2135>
13. Microsoft, "What is data streamer?" Online, 2023. [Online]. Available: <https://support.microsoft.com/en-us/office/what-is-data-streamer-1d52ffce-261c-4d7b-8017-89e8ee2b806f>

Superelasticity of Mesoscopically Porous Ni-Fe-Ga Shape Memory Alloy Foam with 69% Porosity

Muhammad Imran^{1,2}, Xuexi Zhang², Mingfang Qian² and Lin Geng²

¹Mechanical Engineering Department, University of Engineering & Technology Taxila, Taxila 47050, Pakistan

²School of Materials Science and Engineering, Harbin Institute of Technology, Harbin 150001, China

muhammad.imran@uettaxila.edu.pk

ABSTRACT

Superelasticity (SE) is mainly concerned with the stress-induced martensitic transitions (MT) under the application or removal of uniaxial mechanical stresses which is utilized in actuators, sensors and solid-state cooling devices based on elastocaloric effect. However, the intrinsic hysteresis of bulk shape memory alloys (SMAs) rigorously suppresses their applications in several crucial areas. Here, we report the superelastic properties in mesoscopically porous Ni-Fe-Ga SMA foams with 69% porosity, which exhibit less hysteretic superelastic response compared to their bulk counterparts. Ni-Fe-Ga SMA foam was initially prepared via replication casting with NaAlO₂ as pore carrier. Subsequently, the high porosity foam of 69% was obtained by chemical etching under several acid baths. Differential scanning calorimeter (DSC) tests revealed that the high temperature austenite finish temperature existed at room temperature in the annealed foam specimen. Compressive tests confirmed that a completely reversible superelastic response with 2.1% superelastic strain was achieved at 290 K. In addition, the specimen exhibited a perfect superelasticity in a broad temperature range of 288-303 K. The small hysteresis 7 MPa at room temperature was conducive to stable multiple martensitic transitions, which extended the fatigue life. Thus, the depreciation of grain boundary defects/constraints in high porosity Ni-Fe-Ga SMA foams breaks new ground for exploiting elastic strain engineering and the development of relevant porous materials by crafting the materials architecture.

KEYWORDS: Shape memory alloy (SMA) foams; Ni-Fe-Ga alloys; Superelasticity (SE); Martensitic phase transition (MT); Microarchitecture

1. INTRODUCTION

Ferromagnetic shape memory alloys (FMSMAs) have been garnering immense attention as smart materials that are sensitive to stress, temperature and magnetic field. In particular, Ni-Fe-Ga shape memory alloys (SMAs) demonstrate multifunctional mechanical and physical properties based on the reversible martensitic phase transitions (MT), confined superelasticity (SE) [1, 2], shape memory effect (SME) [3], magnetic-field-induced strain (MFIS) [4], magnetocaloric (MCE) [5] and elastocaloric effects (eCE) [6, 7], which make them potential candidates in energy conversion applications such as sensors, actuators, and solid-state heat pumps/refrigeration. However, polycrystalline (three-dimensional bulk alloy with characteristic length > 1 mm) Ni-Fe-Ga SMAs struggle to exhibit sufficient superelasticity and shape memory effects due to the inherent brittle behavior [8], where stress concentrations at grain boundaries may lead to catastrophic intergranular or cleavage fractures due to deformation incompatibility between adjacent grains [9].

In contrast, foams (three-dimensional porous alloy with characteristic lengths of nodes/struts < 1 mm) exhibit significantly reduced grain boundary constraints via

isolating the adjacent grains, where the diameter of their struts/nodes is comparable to the grain size [10]. Previous studies have shown that the inclusion of pores in bulk polycrystalline alloys may also be a possible route to improve the SE properties during recurrent MTs [11]. In addition, by adjusting the size of the structural characteristic length (i.e., nodes/struts or pores), high-porosity SMA foams can also be achieved at different scales, such as micro, meso, and macro, which is beneficial for achieving various structural and functional properties. For instance, Ni-Mn-Ga SMA foams with the porosity of 64-76% exhibited excellent MFIS over millions of thermomechanical cycles [12], Cu-Al-Mn SMA foams showed superb SE [13] and NiTi SMA foams demonstrated superior damping capacity [14] (69% porosity) and biocompatibility for long-term health effects (30-90% porosity) [15].

However, foams with a wider range of porosities can be prepared by tuning the materials architecture. Furthermore, foams with high porosities are expected to achieve lower stress hysteresis and excellent SE properties by restricting the nominal strength below the yield stress [16]. Therefore, mesoporous Ni-Fe-Ga SMA foams were prepared using liquid infiltration technique with NaAlO₂ as pore carrier. Subsequently, a porosity of 69% was achieved by sonochemical etching. The high-

porosity mesoporous foams demonstrated a fully reversible SE effects with a total recovery strain of 2.1% at 40 MPa while the stress hysteresis is very small i.e. 7 MPa. Thus, the reversible SE properties at room temperature can be ascribed to the depreciation of grain boundary defects in high porosity FMSMAs.

2. EXPERIMENT DETAILS

Ni₅₄Fe₁₉Ga₂₇ (at%, nominal component) SMA foams were prepared by liquid infiltration method by utilizing the NaAlO₂ as pore carrier. The in-depth production process can be found here [17]. Mesoporous foam with high porosity was obtained by sonochemical approach (chemical etching was performed at different acid concentrations and different ultrasonic ranges) [18]. Our earlier studies showed that alloy (Ni-Fe-Ga) was not significantly dissolved in etching solution-I (2% HF+10% H₂SO₄), while the alloy was highly dissolved in etching solution-II (2% HF+10% HNO₃), regardless of the dissolution of NaAlO₂ [8, 19]. Therefore, by completely removing NaAlO₂ and partially dissolving Ni-Fe-Ga alloy, high porosity foams can be obtained by saving the main weight-assisted parts of high porosity foams, i.e., high-integral nodes and struts, which can be plastically deformed during compression.

Figure shows that Ni-Fe-Ga SMA foam with the porosity of 50% (approximately) can be successfully obtained after long exposure in etching solution-I (Spell-I), where coarse The Ni-Fe-Ga SMA foams were encapsulated in quartz glass tube under high vacuum followed by heating to 1453 K for 5 h and then quenched in cold water to get single β-phase at room temperature. Parallelepiped (4 × 4 × 8 mm³) foam specimens were cut by using a diamond saw cutter instrument (SYJ-150). The actual chemical composition (at. %) of single β-phase foam was verified to be Ni_{53.5}Fe_{19.9}Ga_{26.6} by Oxford energy dispersive spectrometer (EDS), i.e., mounted on a scanning electron microscope (SEM, Zeiss Supra 55 SAPPHERE).

Olympus PMG3 optical microscope (OM) was utilized to determine the microarchitecture of foam, while the crystal structure was analyzed by PANalytical Empyrean X-ray diffraction (XRD) with Cu-Kα radiation in reflection mode. The MT temperature and latent heat were detected by a differential scanning calorimeter (DSC, Discovery-2500 from TA Instruments) with a cooling/heating rate of 10 K/min ranging from 250 K to 310 K. The SE experiments were performed in compression mode using a mechanical testing system, where Instron 5569 was used for ambient temperature experiments and Instron 5982 for super-room temperature experiments. Furthermore, the SE tests were conducted under isothermal conditions and to ensure such conditions, the strain rate had to be low, i.e., 1.7 × 10⁻⁴ s⁻¹. To obtain the stress-strain diagrams for the SE experiments, the foam samples were heated above the austenite finish temperature (Af) of 343 K for 10 min

NaAlO₂ particles are easily dissolved in it, while the tiny particles remain encapsulated in thin struts and nodes [19]. To remove tiny particles, etching solution-II was employed for short span of time (10 min) to reduce the thickness of struts/nodes by dissolving Ni-Fe-Ga alloy, followed by a long immersion (240 min) in etching solution-I (Spell-II). Consequentially, to achieve Ni-Fe-Ga SMA foam with the porosity of 69%, both etching solutions were iterated several times in sequence to thin struts/nodes (etching solution-I for 10 min) and to remove the remaining NaAlO₂ particles (etching solution-I for 240 min).

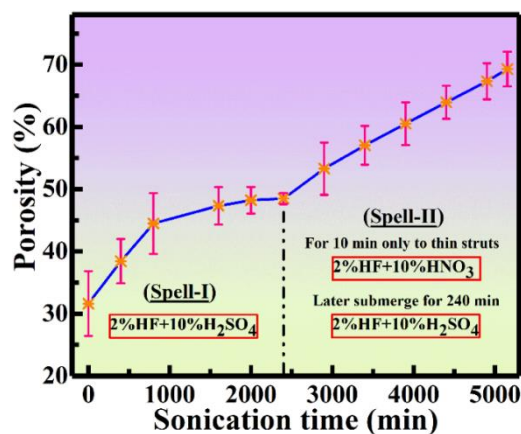


Figure 1: A time dependent porosity plot for Ni-Fe-Ga SMA foams under sonochemical etching

and then the temperature was reduced to the testing temperature.

3. RESULTS AND DISCUSSION

The nodes, pores, and struts are the essential parts of foam architecture, where pores are holes, nodes connect pores, and struts are the thin walls of nodes. The structural morphology of Ni-Fe-Ga SMA foam with 69% porosity is determined by OM micrographs, as depicted in Figure. The higher porosity (69%) results in thinner struts/nodes and larger pores. It is also observed that the pore size increases with the increase of porosity, implying that the alloy was dissolved in etching solution-II. As a consequence, the average pore size is 512 μm, which is larger than the designed value (355-500 μm) [17]. It should be noted that the mesoscopic level can be defined as an intermediate design between the microscopic and macroscopic levels, with an average pore size varying within a few micrometers, so it can be said to be a mesoporous foam. Since the sizes of nodes/struts depends upon the size of pores and porosity. Therefore, the average size of nodes is 328 μm, while the average strut length ranges from 418-448 μm and width ranges from 58-64 μm. The foam with high porosity (69%) exhibits a uniform and non-defective micro-architecture, which implies that the most critical struts/nodes are fully connected to pores.

However, OM micrograph confirms that the Ni-Fe-Ga SMA foam with high mesoscopic architectural integrity provides a structural basis for further investigation of SE performance.

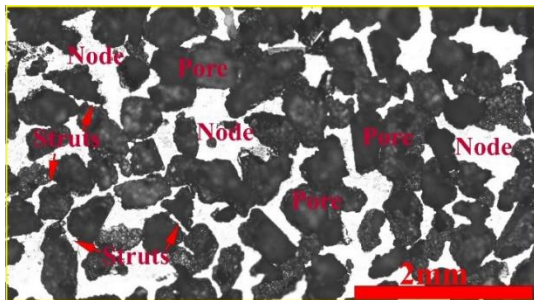


Figure 2: Optical micrograph of Ni-Fe-Ga SMA foam with mesoporous architectures at 69% porosity after sonochemical etching, where bright areas are nodes and struts and dark areas are pores

Figure(a) is the XRD spectrum of mesoporous Ni-Fe-Ga SMA foam (porosity 69%) at room temperature, which validates the austenite (β -structure) phase of the L21 structure with a lattice parameter of $a = b = c = 0.574$ nm. At the same time, the (220) diffraction peak has a high peak intensity, indicating that the (220) plane of the foam has a higher preferred orientation. Figure(b) depicts the DSC plots of Ni-Fe-Ga SMA foams during the endothermic and exothermic processes. The exothermic and endothermic processes are related to forward MT and reverse MT, respectively.

The MT starting (M_s), finishing (M_f) temperatures during exothermic process and austenitic starting (A_s), finishing (A_f) temperatures during endothermic process are determined to be 281 K, 277 K, 283 K and 288 K, respectively by tangent extrapolation technique. The thermal hysteresis ($\Delta T_{Hys} = (A_s - M_f + A_f - M_s)/2$) indicates the attribute of first order structural transition, which is caused by the presence of defects/internal stresses that hinder the reversibility of MT. Therefore, the thermal hysteresis is computed to be 6.5 K. This room-temperature MT behavior enables the realization of practical SE performance at room temperature.

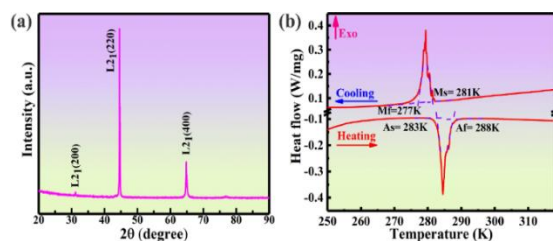


Figure 3: XRD and DSC plots of mesoporous Ni-Fe-Ga SMA foam with 69% porosity. (a) XRD pattern at room temperature displaying austenite structure. (b) DSC curves exhibiting MT temperatures

The mesoporous Ni-Fe-Ga SMA foam was subjected to compressive SE tests at different temperatures 283 K–303 K with a maximum nominal stress of 40 MPa (strain rate: $1.7 \times 10^{-4} \text{ s}^{-1}$) to prevent the occurrence of cracks. As a consequence of porosity (69%), the actual applied stress was considered to be $\frac{40 \text{ MPa}}{1-69\%} = 102 \text{ MPa}$. The typical stress-strain plots showing the stress-induced MT plateau at all temperatures (283-303 K) were presented in Figure(a). It can be seen that at 283 K, a residual strain of 0.25% appeared owing to the presence of both martensite and austenite phases (see Figure(b)). It is well known that a complete SE response occurs above austenite finish temperature. Therefore, the residual strain vanished at elevated temperatures, i.e., 290-303 K (above $A_f = 288$ K).

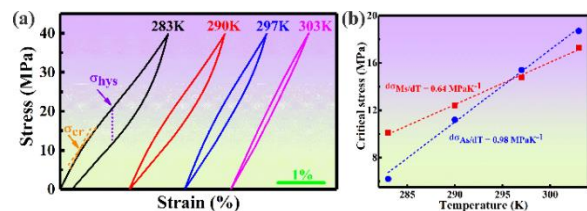


Figure 4: SE and temperature dependence critical stresses plots of mesoporous Ni-Fe-Ga SMA foam with 69% porosity. (a) Superelastic stress-strain curves at various temperatures. (b) Temperature dependence critical stresses plots for martensitic transitions

A completely reversible SE response was revealed in our mesoporous foam with 69% porosity at 290 K with the maximum recovery strain of 2.1% under the application of 40 MPa, which is identical to $\text{Ni}_{49.4}\text{Ti}_{50.6}$ foams with 53% porosity (2%) [20] and $\text{Cu}_{82.5}\text{Al}_{13.5}\text{Ni}_4$ foams with 58% porosity (2.6%) [21].

The temperature dependent critical stresses for activating MT during forward ($\sigma_{M_s/dT}$) and reverse ($\sigma_{A_s/dT}$) are determined to be 0.64 MPa/K and 0.98 MPa/K, respectively, as shown in Figure(b). Such low values can be ascribed to the less dependent of SE effects on the working temperature. However, the current values are comparable to Fe-Pd (100 MPa/K) [22] and Cu-Zn-Al (1.4 MPa/K) [23] alloys.

Furthermore, the low critical stress values (12.4 MPa at 290 K and 14.8 MPa at 296 K) and small stress hysteresis (7.7 MPa at 290 K and 6.4 MPa at 296 K), as mentioned in Figure(a), also favor the depreciation of grain boundary constraints/defects in high porosity foams for multiple stress-induced MT. Thus, high porosity mesoporous SMA foams with low stress hysteresis and completely reversible SE performance make them promising candidates for energy conversion machines, e.g., actuators, sensors and solid-state refrigerators/heat pumps (eCE-based).

4. CONCLUSIONS

Stress-induced MT and SE performances were demonstrated in mesoporous Ni-Fe-Ga SMA foams with 69% porosity fabricated by liquid infiltration followed by sonochemical etching. Single β -phase (austenite; L21 structure with lattice parameter of 0.574 nm) was formed at room temperature after annealing. The mesoporous annealed foam exhibited a perfectly reversible SE performance with a maximum recovery strain of 2.1% at a uniaxial stress of 40 MPa. At room temperature, a narrow hysteresis of ~ 6.5 K was achieved in foam with a porosity of 69%. Thus, the current research with narrow hysteresis and reversible SE properties in high porosity mesoporous foams provides motivation for further investigation of energy conversion applications in porous SMAs.

REFERENCES

1. Yang, H., K. An, and Y.D. Wang, *Anomalous high-temperature quasi-linear superelasticity of Ni-Fe-Ga-Co shape memory alloy*. Journal of Alloys and Compounds, 2022. **909**: p. 164808.
2. Tokhmetova, A.B., et al., *Effect of the Stress-Induced Martensite Aging Time on the Functional Properties of Heterophase Ni₄₉Fe₁₈Ga₂₇Co₆ Single Crystals*. Physical Mesomechanics, 2022. **25**(4): p. 287-295.
3. Belyaev, S., et al., *Shape memory effects in 001 Ni₅₅Fe₁₈Ga₂₇ single crystal*. Smart Materials and Structures, 2017. **26**(9).
4. Morito, H., et al., *Effects of partial substitution of Co on magnetocrystalline anisotropy and magnetic-field-induced strain in NiFeGa alloys*. Journal of Magnetism and Magnetic Materials, 2005. **290-291**: p. 850-853.
5. Hennel, M., L. Galdun, and R. Varga, *Analysis of magnetocaloric effect in Ni₂FeGa-based glass-coated microwires*. Journal of Magnetism and Magnetic Materials, 2022. **560**: p. 169646.
6. Kurlevskaya, I.D., et al., *Influence of Heat Treatments on Martensitic Transformations and Elastocaloric Effect in Two-Phase ($\beta + \gamma$) NiFeGa Alloys*. Physical Mesomechanics, 2024. **27**(4): p. 398-408.
7. Imran, M., et al., *Enhanced working stability of elastocaloric effects in polycrystalline Ni-Fe-Ga dual phase alloy*. Intermetallics, 2021. **136**: p. 107255.
8. Imran, M., et al., *Enhancing the Elastocaloric Cooling Stability of Ni-Fe-Ga Alloys via Introducing Pores*. Advanced Engineering Materials, 2020. **22**(4).
9. Huang, X.-M., et al., *Correlation between microstructure and martensitic transformation, mechanical properties and elastocaloric effect in Ni-Mn-based alloys*. Intermetallics, 2019. **113**.
10. Dunand, D.C. and P. Müllner, *Size Effects on Magnetic Actuation in Ni-Mn-Ga Shape-Memory Alloys*. Advanced Materials, 2011. **23**(2): p. 216-232.
11. Imran, M., et al., *Large Cyclability of Elastocaloric Effect in Highly Porous Ni-Fe-Ga Foams*. Materials, 2024. **17**(6): p. 1272.
12. Chmielus, M., et al., *Giant magnetic-field-induced strains in polycrystalline Ni-Mn-Ga foams*. Nature Materials, 2009. **8**(11): p. 863-866.
13. Li, H., et al., *Effect of oligocrystallinity on damping and pseudoelasticity of oligocrystalline Cu-Al-Mn shape memory foams*. Journal of Alloys and Compounds, 2019. **773**: p. 940-949.
14. Wei, L.S., X.X. Zhang, and L. Geng, *Microstructure and properties of NiTi foams with 69% porosity*. Vacuum, 2019. **162**: p. 15-19.
15. Yuan, B., M. Zhu, and C.Y. Chung, *Biomedical Porous Shape Memory Alloys for Hard-Tissue Replacement Materials*. Materials, 2018. **11**(9).
16. Yuan, B., et al., *Enhanced cyclic stability of elastocaloric effect in oligocrystalline Cu-Al-Mn microwires via cold-drawing*. International Journal of Refrigeration, 2020. **114**: p. 54-61.
17. Imran, M. and X. Zhang, *Ferromagnetic shape memory Ni-Fe-Ga alloy foams for elastocaloric cooling*. Journal of Physics D-Applied Physics, 2020. **53**(24).
18. Zhang, X.X., et al., *Effect of pore architecture on magnetic-field-induced strain in polycrystalline Ni-Mn-Ga*. Acta Materialia, 2011. **59**(5): p. 2229-2239.
19. Imran, M. and X. Zhang, *Elastocaloric effects in polycrystalline Ni-Fe-Ga foams with hierarchical pore architecture*. Physical Review Materials, 2020. **4**(6): p. 065403.
20. Aydoğmuş, T. and Ş. Bor, *Processing of porous TiNi alloys using magnesium as space holder*. Journal of Alloys and Compounds, 2009. **478**(1): p. 705-710.
21. Yuan, B., et al., *Effect of directional solidification and porosity upon the superelasticity of Cu-Al-Ni*



- shape-memory alloys*. *Materials & Design*, 2015. **80**: p. 28-35.
22. Xiao, F., et al., *Elastocaloric effect by a weak first-order transformation associated with lattice softening in an Fe-31.2Pd (at.%) alloy*. *Acta Materialia*, 2015. **87**: p. 8-14.
23. Mañosa, L., et al., *Large temperature span and giant refrigerant capacity in elastocaloric Cu-Zn-Al shape memory alloys*. *Applied Physics Letters*, 2013. **103**(21).

Optimization Analysis of Innovative Counter Flow Spiral Absorber Tubes for Thermal Management of Photovoltaic Modules

Muhammad Danyal¹, Abid Hussain¹, Mohsin Ali¹, Rehan Saghir¹, Aymen Nadeem¹

Mechanical Engineering Department, UET Taxila,

danyal.khan@students.uettaxila.edu.pk,

ABSTRACT

Effective thermal management is crucial for optimizing performance and extending the lifespan of photovoltaic (PV) modules. This study introduces a novel design incorporating a counter-flow spiral mechanism for fluid movement and Nano Phase Change Materials (PCM) to ensure consistent temperature distribution across PV cells. Investigation reveals that increasing the flow rate from 0.48 l/min to 2.4 l/min and the tube diameter from 10 mm to 15 mm enhances electrical efficiency up to 13.6% and reduces module temperature by 8.2 degrees Celsius. Additionally, utilizing a PCM with an optimal thickness of 25 mm proves essential for effective heat retention, thereby improving thermal management. This innovative design not only maintains uniform temperature across the modules but also substantially increases both electrical and thermal efficiencies by 3.2% and 22.5%, respectively. These advancements suggest that such a design can significantly enhance the efficiency and sustainability of solar energy systems.

KEYWORDS: PV Thermal Management, Nano PCM Integration, PV Efficiency, Thermal Uniformity, Heat Transfer Enhancement

1. INTRODUCTION

The rapid increase in the installation of photovoltaic (PV) systems worldwide reflects a growing global emphasis on mitigating climate change and enhancing energy security [1]. As these systems proliferate, research efforts have increasingly focused on improving their efficiency and performance [2]. Heat from infrared radiation reduces electrical efficiency in PV systems. Passively cooled systems can boost power output by up to 5% [1]. To address this issue, photovoltaic/thermal (PV/T) systems have emerged as a combined technology that integrates PV and solar thermal systems [3]. In PV/T systems, heat from PV cells is extracted by a fluid and used for low-temperature applications like domestic heating and cooling [4]. PV/T collectors have thermal efficiency around 9% lower than conventional flat-plate solar thermal collectors despite their advantages [5].

Extensive research on water-based PV/T collectors shows that their efficiency is greatly impacted by the fluid flow pattern within tube-sheet or tube-only absorbers [6]. Sheet-tube absorbers, while effective, can increase thermal resistance between the PV layer and the fluid stream, potentially reducing the thermal efficiency of the system [2]. Efficient heat removal is crucial for PV/T modules, especially in summer. 3D studies show optimal exergy efficiency at specific flow rates and cooling channel heights in water-based systems [7]. Models show cooling channels above the PV panel boost thermal efficiency but may lower electrical efficiency [8].

Despite these advancements, challenges remain in achieving uniform cooling and temperature regulation within PV/T systems [9]. PCMs in PV modules help manage cell temperature by absorbing heat during phase transition. Organic PCMs are preferred for their non-corrosive nature, stability, and high latent heat [10]. Integrating PCMs into PV modules reduces the average temperature by 10.35°C, leading to a 2% boost in electrical efficiency [11]. Panels with PCMs have shown up to a 30% increase in power output, with around 6% improvement in annual electrical yield in hot climates [12]. Experimental work with PCMs containing aluminum oxide particles and cylindrical fins has also shown substantial performance improvements [13]. However, challenges such as PCM leakage and reduced thermal conductivity continue to pose problems [14]. PCM containment methods, such as metallic pouches and leak-proof packets, address issues but increase costs and reduce heat exchange efficiency [15]. Multi-layered PV/T modules with various components have also been explored as potential solutions [16].

Current research on PV/T systems lacks focus on uniform thermal distribution and eliminating thermal spots. This study addresses these gaps by introducing a novel rectangular counter-spiral design to improve cooling uniformity and reduce thermal spotting on the PV plate. It also optimizes the wet area and material usage for better efficiency. Additionally, aluminium oxide particles are incorporated into the PCM to enhance thermal performance, overcoming limitations of conventional PCMs [16]. This study seeks to improve cooling

uniformity and thermal management, addressing unresolved issues in existing PV/T system research.

2. METHODOLOGY

System Components

Photovoltaic Panel

The PV panel (details in table 1) was used, measuring 1190 mm x 502 mm, features a multi-layer design with a glass cover, EVA layers, polycrystalline silicon cells, and a back sheet, delivering effective thermal and electrical performance.

Table 1: Solar module used in simulations

PV module Specifications
Watts: 100 W
Type: Monocrystalline
Length: 1190 mm
Width: 502 mm
Thickness: 3mm

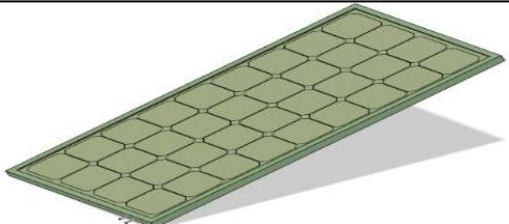


Figure 1: Photovoltaic Panel modelled for simulation

Circular Copper Pipes

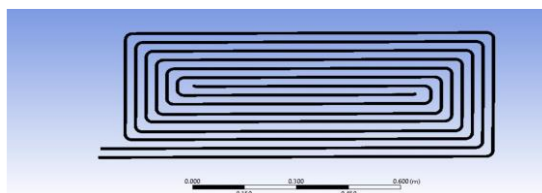


Figure 2: Copper tubes configuration

Circular copper pipes in a counter-flow spiral beneath the PV panel have two inlets and outlets, maximizing coolant contact and enhancing heat extraction and temperature uniformity.

Phase Change Material (PCM)

The PCM, an organic compound with 5% aluminum oxide by weight, enhances thermal conductivity and heat

absorption. It melts at about 43°C, absorbing excess heat during peak solar radiation, as detailed in Table 2.

Table 2: PCM Properties

PCM RT-42	-----
Specific Heat	2000 J/kgK
Thermal conductivity	0.2 W/mK
Melting Heat	174000 J/kg

Working Fluid

Water is used as the heat transfer fluid, circulating through the circular pipes at a flow rate of 0.48 to 2.4 l/min. This flow rate was selected to balance the cooling efficiency and pressure drop within the system.

Insulation

A polyethylene foam insulation layer, 13 mm thick, is installed behind the PCM layer to minimize heat loss and improve the overall thermal efficiency of the system.

Computational Model and Simulation Setup.

Geometry Creation

The computational domain includes the PV panel, spiral-patterned circular copper pipes, and the PCM layer, all modeled using ANSYS Design Modeler (see Fig 3) to closely mimic the actual PV/T system layout. The PV panel is structured in layers to reflect true operational conditions, consisting of the Glass layer, EVA upper and bottom layers, Solar cell, Tedlar, and a metallic heat spreader beneath the Tedlar, integrated with spiral metal tubes and a PCM layer, as detailed in Fig 4.

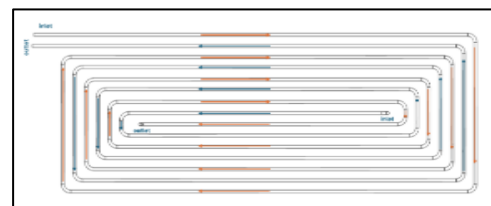


Figure 3: Geometry built in Design Modeler

The thermal management part of the geometry consists of two spiral tubing of copper placed on the heat absorber sheet which is aluminum in this case to cover the back side of the PV. Flow takes place in clockwise and counterclockwise directions to mitigate the effect of thermal spots built in the PV module which is damaging to the solar cells and hence needs to be addressed.

Figure 4 explains the detailed layers of geometry of the thermal collector i.e. from the top Glass EVA layer heat

absorber sheet and tubing embedded in PCM attached to the back side of PV module.

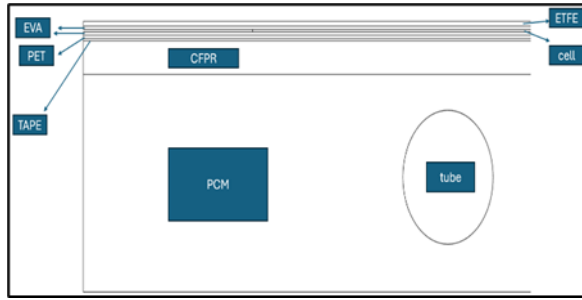


Figure 4: Layers of geometry modelled in simulation

Water circulates through tubing at variable flow rates to evaluate its effect on solar cell temperature reduction. A uniform PCM layer at the rear of the PV module absorbs waste heat, enhanced by spiral tubing for optimal heat transfer. The study also examines the impact of different tube diameters (see table 3) on the heat transfer coefficient and how PCM thickness affects temperature reduction, electrical, and thermal efficiency.

Table3: Process Input Variables

Factor	Level 1	Level 2	Level 3
Tube diameter	10 mm	12 mm	15 mm
PCM thickness	12 mm	18 mm	25 mm
Flow rate	0.48 l/min	1.44 l/min	2.40 l/min

Meshing

A structured mesh, with finer elements near the pipes and PCM regions, was used to accurately capture thermal gradients. A mesh independence study confirmed that a size of about 1 mm in critical areas (pipe-PCM interface) balances accuracy and computational efficiency.

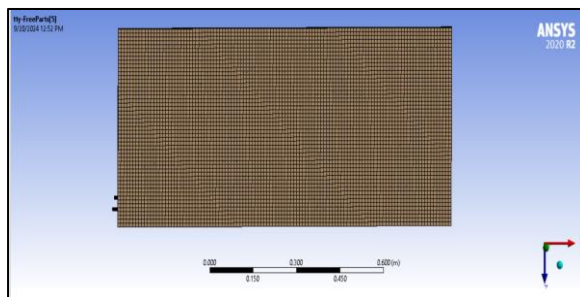


Figure 5: Mesh of the proposed setup

Boundary Conditions

- **Inlet and Outlet Conditions:** The inlet temperature of the working fluid is maintained at 25°C, and the flow rate ranges from 0.48 l/min to 2.48 l/min. The fluid exits the system at atmospheric pressure at the outlet.
- **Heat Flux:** A consistent heat flux between 300 and 1000 W/m² is applied to the PV surface, reflecting common outdoor solar irradiance levels.
- **PCM Boundary:** The PCM properties, including specific heat, thermal conductivity, and melting heat, are defined to accurately model the phase change behavior and its interaction with the cooling system.

Governing Equations and Numerical Methods

The simulations utilized the finite volume method in ANSYS Fluent to solve the governing equations of heat transfer and fluid flow.

Energy Conservation

The energy conservation equation is used to account for heat transfer within the PV panel, pipes, and PCM:

$$\frac{\partial(\rho c_p T)}{\partial t} + \nabla \cdot (\rho c_p \mathbf{u} T) = \nabla \cdot (k \nabla T) + Q$$

Where:

- ρ = density of the material (kg/m³)
- c_p = specific heat capacity (J/kg.K)
- T = Temperature
- \mathbf{u} = velocity vector (m/s)
- k = Thermal conductivity (W/m.K)
- Q = Internal Heat Generation (W/m³)

Phase Change Model

The PCM phase change is modeled using the enthalpy-porosity approach, capturing the melting and solidification processes:

$$H = H_{sensible} + H_{latent}$$

$$H = \int_{T_{ref}}^T c_p dT + Lf$$

Where:

- $H_{sensible}$ = Sensible Heat Component
- H_{latent} = Latent Heat Component
- L = Latent heat of fusion (J/kg)
- f = liquid Fraction

Fluid Flow Equations (Navier-Stokes Equations)

The fluid flow within the pipes is governed by the Navier-Stokes equations for incompressible flow:

$$\rho \left(\frac{\partial u}{\partial t} + \mathbf{u} \cdot \nabla \mathbf{u} \right) = -\nabla p + \mu \nabla^2 \mathbf{u}$$

Where:

- p = pressure (Pa)
- μ = dynamic viscosity (Pa.s)

3. RESULTS AND DISCUSSION

Numerical Analysis Validation

We decided to compare our findings with the design put forward by Dudul et al. [17] to ensure validity. Figure 4 presents a detailed comparison of the thermal and electrical efficiency validation results achieved using Fluent. The discrepancy between the validation results obtained from Fluent and the study carried out by [17] is only 1.8%. This comparison draws attention to how strikingly similar the results of the experimental research and the conclusions of our current investigation are. The presence of synchrony highlights the efficacy of the defined boundary conditions, hence reinforcing their significance in forecasting the PVT collector's performance.

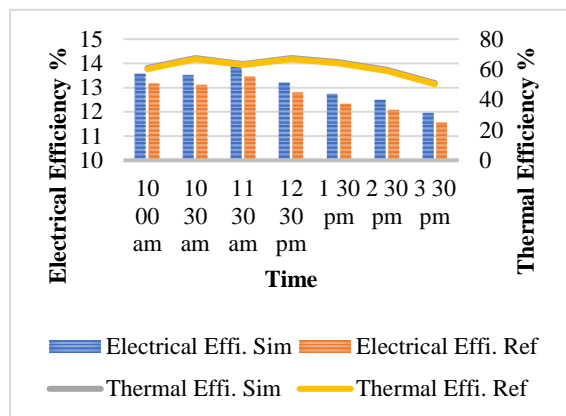


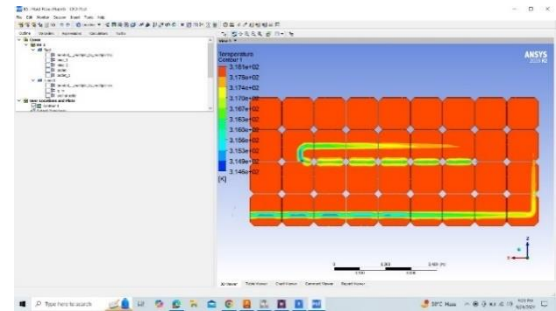
Figure 6: Comparison of current study with Dudul et al. [17] results

Optimization of System Design

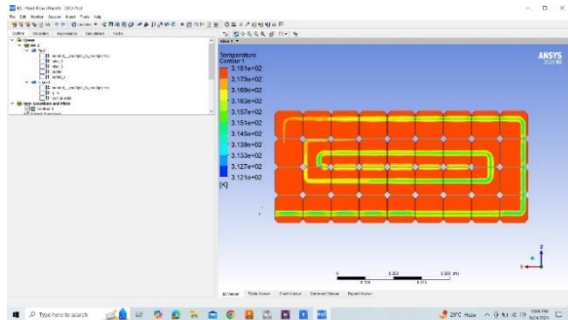
Temperature Distribution

The simulation results showed a significant improvement in temperature uniformity across the PV panel using the counter-flow spiral design. Figure 7 displays temperature profiles at different flow rates, highlighting better thermal management with this design.

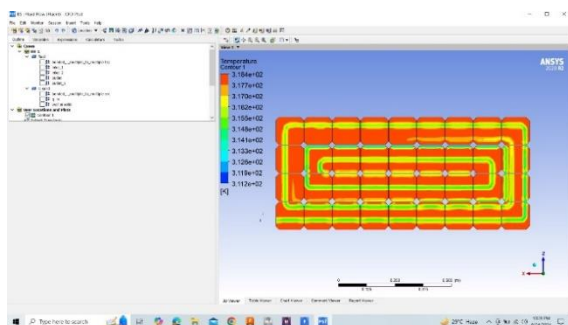
Increasing the diameter of tubes and PCM thickness causes reduction in PV module temperature.



(a)



(b)

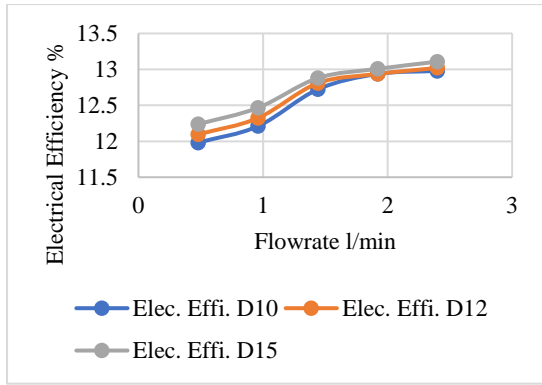


(c)

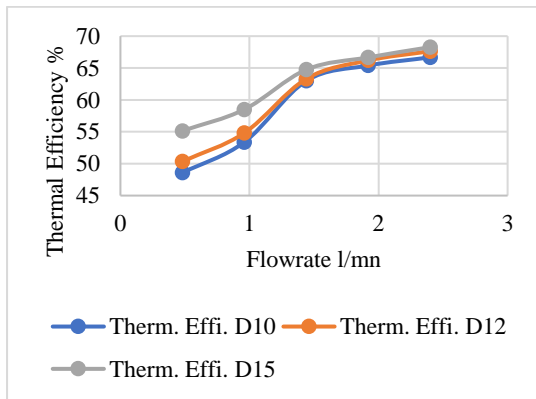
Figure 7: Effect of mass tube diameter and PCM thickness on temperature distribution (a) $d=10$ mm, $P=12$ mm, (b) $d=12$ mm, $P=18$ mm, (c) $d=15$ mm, $P=25$ mm

Optimal process parameters in simulation studies

To optimize the absorber dimensions for the PV/T module, extensive numerical analysis focused on copper tube diameters of 10, 12, and 15 mm and a PCM thickness of 25 mm, aiming to minimize the module's average temperature. Figure 7 illustrates the impact of these dimensions at mass flow rates between 0.48 l/min and 2.4 l/min under 1000 W/m² solar irradiation. The analysis revealed that a 15 mm tube diameter was optimal, balancing the module's thermal and electrical efficiencies by lowering temperatures and enhancing performance. Figure 8 and Figure 10 further detail how these dimensions influence thermal efficiency, establishing the most efficient configuration at a 15 mm tube diameter, 25 mm PCM thickness, and a 2.4 l/min flow rate.

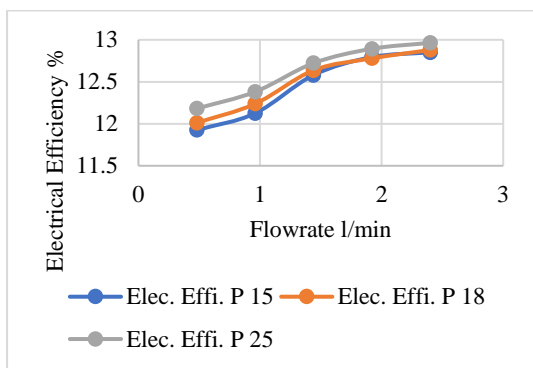


(a)

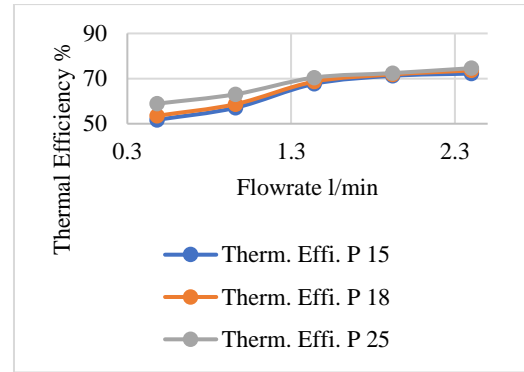


(b)

Figure 8: Effect of mass flow rate at different tube diameters ($d=10$ mm, $d=12$ mm, $d=15$ mm) on (a) Electrical Efficiency (b) Thermal Efficiency



(a)



(b)

Figure 9: Effect of mass flow rate at different PCM thickness ($P=12$ mm, $P=18$ mm, $P=25$ mm) on (a) Electrical Efficiency (b) Thermal Efficiency

Discussion

Cooling significantly enhances the photovoltaic and thermal performance of the panel, leading to variable improvements in total efficiency across scenarios. The PV panel achieves high thermal efficiency and a notable boost in electrical performance, making it suitable for simultaneous thermal and electrical energy generation. Tube diameter plays a key role, with larger diameters increasing the interaction area and improving heat transfer. A 15 mm tube diameter, combined with 25 mm PCM thickness and a fluid flow rate of 2.4 l/min, delivers optimal results by enhancing heat absorption and lowering the PV module temperature.

4. CONCLUSIONS

This study utilized predictive modelling and extensive testing to optimize the design of a PVT unit with counter-flow rectangular absorber tubes, considering temperature, electrical, and thermal performance with and without phase change materials (PCMs). Key results are:

- Numerical simulations determined that increasing the tube diameter from 10 mm to 15 mm and PCM thickness to 25 mm reduced the PV module surface temperature from 52.34°C to 44.14°C.
- Experiments showed PVT systems significantly outperformed conventional PV units in converting solar radiation into electrical and thermal energy. The highest PV module surface temperature in the PVT-PCM system reached 44.14°C, with the lowest at 24.48°C under varying flow rates.
- Thermal efficiencies of PVT and PVT-PCM systems were 40.73% and 63.31%, respectively, with electrical efficiency peaking at 13.61% for

a 15 mm tube and 25 mm PCM thickness, and a minimum of 13.09% with a 10 mm tube and 12 mm PCM thickness.

REFERENCES

1. D. Das, P. Kalita, and O. Roy, "Flat plate hybrid photovoltaic- thermal (PV/T) system: A review on design and development," *Renewable and Sustainable Energy Reviews*, vol. 84, pp. 111–130, Mar. 2018, doi: 10.1016/J.RSER.2018.01.002.
2. V. Weitbrecht, D. Lehmann, and A. Richter, "Flow distribution in solar collectors with laminar flow conditions," *Solar Energy*, vol. 73, no. 6, pp. 433–441, Dec. 2002, doi: 10.1016/S0038-092X(03)00006-9.
3. J. Bigorajski and D. Chwieduk, "Analysis of a micro photovoltaic/thermal – PV/T system operation in moderate climate," *Renew Energy*, vol. 137, pp. 127–136, Jul. 2019, doi: 10.1016/J.RENENE.2018.01.116.
4. S. Y. Wu, C. Chen, and L. Xiao, "Heat transfer characteristics and performance evaluation of water-cooled PV/T system with cooling channel above PV panel," *Renew Energy*, vol. 125, pp. 936–946, Sep. 2018, doi: 10.1016/J.RENENE.2018.03.023.
5. G. Vokas, N. Christandonis, and F. Skittides, "Hybrid photovoltaic–thermal systems for domestic heating and cooling—A theoretical approach," *Solar Energy*, vol. 80, no. 5, pp. 607–615, May 2006, doi: 10.1016/J.SOLENER.2005.03.011.
6. M. S. Hossain, A. K. Pandey, J. Selvaraj, N. A. Rahim, M. M. Islam, and V. V. Tyagi, "Two side serpentine flow based photovoltaic-thermal-phase change materials (PVT-PCM) system: Energy, exergy and economic analysis," *Renew Energy*, vol. 136, pp. 1320–1336, Jun. 2019, doi: 10.1016/J.RENENE.2018.10.097.
7. J. Bigorajski and D. Chwieduk, "Analysis of a micro photovoltaic/thermal – PV/T system operation in moderate climate," *Renew Energy*, vol. 137, pp. 127–136, Jul. 2019, doi: 10.1016/J.RENENE.2018.01.116.
8. M. S. Hossain, A. K. Pandey, J. Selvaraj, N. Abd Rahim, A. Rivai, and V. V. Tyagi, "Thermal performance analysis of parallel serpentine flow based photovoltaic/thermal (PV/T) system under composite climate of Malaysia," *Appl Therm Eng*, vol. 153, pp. 861–871, May 2019, doi: 10.1016/J.APPLTHERMALENG.2019.01.007.
9. R. Simón-Allué, I. Guedea, R. Villén, and G. Brun, "Experimental study of Phase Change Material influence on different models of Photovoltaic-Thermal collectors," *Solar Energy*, vol. 190, pp. 1–9, Sep. 2019, doi: 10.1016/J.SOLENER.2019.08.005.
10. S. Ramakrishnan, X. Wang, and J. Sanjayan, "Effects of various carbon additives on the thermal storage performance of form-stable PCM integrated cementitious composites," *Appl Therm Eng*, vol. 148, pp. 491–501, Feb. 2019, doi: 10.1016/J.APPLTHERMALENG.2018.11.025.
11. R. M., L. S., R. S., A. H., and D. A., "Experimental investigation on the abasement of operating temperature in solar photovoltaic panel using PCM and aluminium," *Solar Energy*, vol. 188, pp. 327–338, Aug. 2019, doi: 10.1016/J.SOLENER.2019.05.067.
12. A. Hasan, J. Sarwar, H. Alnoman, and S. Abdelbaqi, "Yearly energy performance of a photovoltaic-phase change material (PV-PCM) system in hot climate," *Solar Energy*, vol. 146, pp. 417–429, Apr. 2017, doi: 10.1016/J.SOLENER.2017.01.070.
13. H. E. Abdelrahman, M. H. Wahba, H. A. Refaey, M. Moawad, and N. S. Berbish, "Performance enhancement of photovoltaic cells by changing configuration and using PCM (RT35HC) with nanoparticles Al₂O₃," *Solar Energy*, vol. 177, pp. 665–671, Jan. 2019, doi: 10.1016/J.SOLENER.2018.11.022.
14. H. E. Abdelrahman, M. H. Wahba, H. A. Refaey, M. Moawad, and N. S. Berbish, "Performance enhancement of photovoltaic cells by changing configuration and using PCM (RT35HC) with nanoparticles Al₂O₃," *Solar Energy*, vol. 177, pp. 665–671, Jan. 2019, doi: 10.1016/J.SOLENER.2018.11.022.
15. D. Das, U. Bordoloi, H. H. Muigai, and P. Kalita, "A novel form stable PCM based bio composite material for solar thermal energy storage applications," *J Energy Storage*, vol. 30, p. 101403, Aug. 2020, doi: 10.1016/J.EST.2020.101403.
16. D. Das, U. Bordoloi, H. H. Muigai, and P. Kalita, "A novel form stable PCM based bio composite material for solar thermal energy storage applications," *J Energy Storage*, vol. 30, p. 101403, Aug. 2020, doi: 10.1016/J.EST.2020.101403.
17. D. Das, U. Bordoloi, A. D. Kamble, H. H. Muigai, R. K. Pai, and P. Kalita, "Performance investigation of a rectangular spiral flow PV/T collector with a novel form-stable composite material," *Appl Therm Eng*, vol. 182, p. 116035, Jan. 2021, doi: 10.1016/J.APPLTHERMALENG.2020.116035.

Corrosion Inhibition through Biofilms: A Comprehensive Review

Maheen Siddiqi¹, M. Musa Raja¹, Aqsa Saeed¹, Adnan Maqbool¹, Ehsan Ul Haq^{1*}

¹Department of Metallurgical and Materials Engineering, Faculty of Chemical Metallurgical and Polymer Engineering,
University of Engineering and Technology, Lahore, Punjab, Pakistan

[*amonehsan@uet.edu.pk](mailto:amonehsan@uet.edu.pk)

ABSTRACT

Corrosion causes a massive loss of money, energy and products. The prevalent corrosion control systems currently in use have the drawbacks of being sometimes ineffective, expensive, and sensitive to the environment. Research indicates that a variety of environmental factors contribute to the promotion of material corrosion. The latest developments in the use of biofilms to control corrosion in various materials are compiled in this review study. Among the various methods are artificial biofilms, layer-by-layer techniques, nano-coatings, vibrio species, polymer compounds, and so on. The primary viewpoint for each of these treatments is that they are eco-friendly. In addition to offering corrosion protection, these processes and the materials or microbial biofilms also lessen the requirement for hazardous products and chemicals. Utilizing organic materials, natural materials, or inhibitor biofilms provides a non-toxic and biodegradable solution to corrosion. In general, effective use of this viewpoint can aid in advancements in the fields of biofilm biology and corrosion engineering research.

1. INTRODUCTION

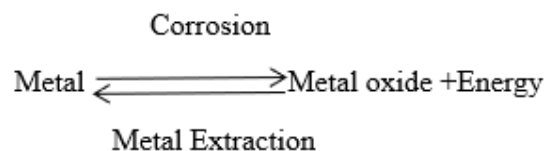
There are several definitions of corrosion in the literature [1]. Some of them are cited here. Corrosion is a process that causes metals to deteriorate due to a combination of chemical, physical, and microbiological interactions with their environments. These interactions can lead to the breakdown of materials such as steel and stones [2, 3].

The irreversible response of an interlayer (polymer, metal, concrete, wood, or ceramic) with the environment that results in the ingestion or dissolution of the ambient component material is known as corrosion, according to the International Union of Pure and Applied Chemistry [3]. Both biological and electrochemical agents (the impact of some microbes) can cause damage to electrolyte solutions when they come into contact with metals [1].

Metal dissolution is a common electrochemical reaction that occurs during a corrosion process. Metals corrode when they come into touch with water. This process continues when oxygen is present because electrons move between the metal's various components. This may cause corrosion products to build, including iron oxide, which could damage the metal. Numerous elements can affect the rate and kind of corrosion, such as the kind of metal, the water's composition, and the existence of microbes [4].

It is important to remember that both thermodynamic and kinetic processes condition corrosion processes while characterizing them. Metal corrosion is an inherent spontaneous phenomenon, it must be noted while examining the corrosion process from the standpoint of chemical thermodynamics. Only certain metals, often known as noble metals (gold, platinum), in their disconnected state, are thermodynamically stable in the natural world [1]. Since most metals are found in oxide

form, removing them into a free state requires a large amount of energy. This energy enables them to revert to their combined state when they come into touch with oxygen, moisture, or other components of the outside world. For instance, when iron is exposed to the elements, it corrodes and becomes hydrated ferrous oxide, which has a brown hue. This demonstrates how the process of corrosion runs counter to the extraction of metals [5].



Corrosion is considered to be a worldwide issue [5]. Diverse contexts have handled various types of material degradation [3]. Any kind of environment, such as a solid, liquid, or gas, can be corrosive. Generally speaking, these settings are referred to as electrolytes. These electrolytes facilitate the formation of two processes (anodic and cathodic) and the transfer of ions (cations and anions) [5]. Environmental hazards like corrosion have an impact on industry, chemicals, cars, mechatronics, metallurgy, and medical applications. They can also be detrimental to the economy, preservation, and public health. Mostly the corrosion process occurs due to electrochemical reactions driven by marine environments, oxidative environments, and microorganisms present as biofilms.

Because metal corrosion in oil and gas well production systems can lead to issues with resource safety and protection in addition to financial losses, it is a major concern and a risky mode of failure. Therefore, to construct a sensible corrosion prevention design and advance the exploration and development of oil and gas fields, it is imperative to understand the causes of

corrosion that occur in the oil and gas systems at all levels, from downhole to surface equipment and processing facilities [6].

There are many categories for corrosion damage: 1) Stress corrosion, 2) Pitting, 3) General intergranular corrosion, 4) General (unlocalized) corrosion, etc. The first of these weaken the least, and the last two weaken the most. Stress corrosion is distinct from corrosion fatigue in that it is dependent on pre-existing weak points, which are typically but not always intragranular. As a result, it only happens to particular materials following specific heat treatments. Almost any material subjected to alternate loads in a corrosive environment can develop corrosion fatigue, which causes the material to become disorganized as the fracture spreads [5].

2. TYPES OF CORROSION

The different kinds of corrosion are divided into the following groups:

General Corrosion

It is also referred to as dry corrosion or uniform corrosion; it is the kind of corrosion that essentially uniformly destroys the bare metal surface. It can also be described as a kind of corrosion that spreads throughout the entire arid region at the same rate. Oxygen is one of the primary causes of this degradation. In general, the materials that corrode the most are steel and cast iron. They take on a rust-like look when they are exposed to damp environments [5].

Studies on the behavior of dry metals reveal that when they are kept over sulfuric acid, they do not corrode at all, and when they are maintained over water, they only corrode superficially [5].

Localized Corrosion

General corrosion and localized corrosion are very distinct from one another. While localized corrosion occurs comparatively at a smaller region, general corrosion occurs over a greater area. This corrosion happens when a metal surface corrodes more readily in small sections than it does throughout in a corrosive environment. Because the corroding medium is present in these small locations more quickly, the metal surface is partially corroded in these areas. The region with a restricted oxygen supply becomes the anode, whereas the region with an unlimited supply becomes the cathode. It also comes in two varieties: (i) corrosion in pitting and (ii) corrosion in crevice [1, 5].

Pitting Corrosion

Pitting corrosion is a specific kind of corrosion that develops in a small area and eventually leaves holes in the

surface. Because there is less oxygen present, the area covered in pollutants or water acts as the anode and cathode. Electrochemical mechanisms cause metal dissolution, with two theories: Hoar's connection to increased acidity in active sections and Russian investigators' connection to anions' displacement. The pitting factor measures the intensity of pitting corrosion [5].



Figure 1: Pitting corrosion [1]

Waterline Corrosion

Within the metallic tanks, this kind of corrosion takes place. When the tanks are only halfway full, the area beneath the water's surface is the anode due to its low oxygen content, while the area above the water's surface is the cathode due to its high oxygen content. The water line corrosion setup is displayed below. The region just below the water's level corrodes as a result, whereas the area above the level is safe [5].

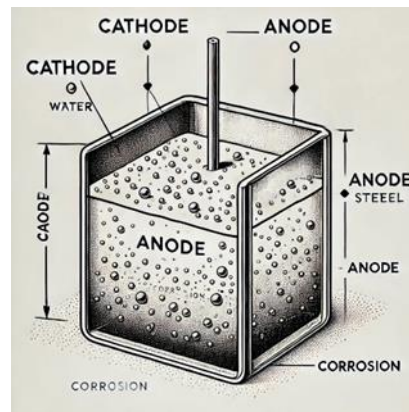


Figure 2: Waterline corrosion [5].

The majority of maritime engineers deal with this kind of corrosion. It can be somewhat decreased by applying anti-fouling coatings [5].

Types of corrosion in the oil and gas equipment

equipment:

Oil and gas production facilities may collapse due to internal and exterior corrosion also related to other articles [7]. Internal corrosion affects tubing, casing, wellhead assembly, field equipment, and pipelines. External corrosion occurs when cement sheaths and casings contact

corrosive water or oil, blocking flow routes and causing difficulties in downhole operations. Understanding the working environment, corrosive media, material choice, and other factors is crucial for analyzing corrosion severity and interactions [6].

Oxygen (O₂ related corrosion)

Oxygen is a major cause of corrosion in oil production equipment, including water injection tubing, surface processing, and rapid pitting. Oil treatment often exposes equipment to oxygen through leaky seals and vents, leading to corrosion in surface processing. Corrosion inhibitors and highly salinized water can help prevent corrosion, but dissolved O₂, Ca²⁺, and inorganic salts are the primary culprits. Oxygen also affects the cathodic and anodic reactions of carbon steel surfaces [6].

3. METHODS FOR CORROSION CONTROL USING BIOFILMS

Pitting Corrosion Control

Three distinct biofilm-forming bacteria were used in the study's aluminum 2024-T3 plate testing: *Bacillus subtilis*, *Bacillus licheniformis*, and *Escherichia coli*. The biofilms were developed in continuous reactors using PTFE, titanium counter electrode, and Ag/AgCl reference electrode. These biofilms decreased the rates at which active pits grew and enhanced the possibility for corrosion [8].

Artificial biofilm inhibits Carbon Steel Corrosion:

The bacteria in the water begin to stick to the surface of a metal when it comes into contact with it. At first, extracellular polymers may be used by these bacteria to cling non-specifically to surfaces; ongoing synthesis of these polymers increases the ability of other bacteria to stick to surfaces. If this procedure is carried out, a thick biofilm will form, which will support the growth of organisms by creating an anaerobic and aerobic habitat. The production of biofilms leads to corrosion that is influenced by microbes [9]. Carbon 30 mm in diameter and 0.35 mm in thickness are steel coupons. Fe, C, Mn, S, P, and Si are among the chemical elements [3]. It consists of 0.6% agarose treated with synthetic wastewater and diluted activated sludge from a municipal wastewater treatment plant [9]. The artificial biofilm covered only one side of the coupon, and the steel coupon's mass loss was 0.46 mg/ [cm] ²-day. When the artificial biofilm was completely covering both sides, the carbon steel corroded at a rate of 0.16 mg/ [cm] ². Using microelectrodes to measure pH and dissolved oxygen, structural analysis of this artificial biofilm showed that carbon steel corrosion was accelerated by the biofilm's asymmetric distribution of these two elements and that when the biofilm covered both sides of the steel coupons, the dissolved oxygen

concentration in the zone closest to the surface of the biofilm rapidly decreased. Steel oxidation was postponed until all of the oxygen in the biofilm had been consumed [9].

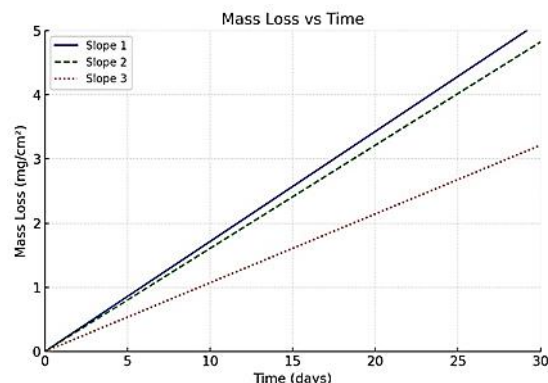


Figure 3: corrosion of carbon steel coupons in synthetic wastewater (sterile condition) Condition a “●” (two sides of sample covered with artificial biofilm. Condition b “○” (one side of sample covered with artificial biofilm). Condition c “Δ” (no artificial biofilm) [7].

Corrosion Control using Beneficial Biofilm

Significant economic loss results from corrosion. The downsides of the commonly utilized corrosion control technologies currently in use are that they can be costly, environmentally sensitive, and occasionally ineffective [4]. A biofilm is a bacterial population that is extremely well-organized, with its cells bound in an extracellular polymer matrix. Bacterial biofilms on metal surfaces have the potential to speed up or slow down corrosion. The formation of non-uniform patches by bacteria colonizing on metallic substratum is the factor that causes corrosion. In a differential aeration cell, the areas beneath thicker colonies that have higher oxygen concentrations and more respiration activity become cathodic, while the areas beneath thinner colonies that have higher oxygen concentrations and more respiration activity become cathodic, while the areas beneath thinner colonies that have lower oxygen concentrations and less respiration activity become anodic. This occurs when aerobic respiration takes place which can be studied in these articles [10, 11]. However, the biofilm matrix creates a transport barrier that may stop corrosive substances from penetrating and lowering their interaction with the metal surface, thus minimizing corrosion. Examples of these substances include oxygen, chloride, and others [4].

2.3.4. Hydrophobic nano-coatings:

Aluminum alloy 1050, 0.07 cm thick, 0.04 cm thick stainless steel, phosphoric acid, sulfuric acid, ethanol, acetone, and flax seed oil [12]. Because they are resistant to corrosive substances and exhibit minimal interaction between chemical species and substrate, nature-inspired hydrophobic coatings have attracted a lot of interest. As is

already known, aluminum exhibits outstanding anti-corrosion capabilities because of passive film production, which is accomplished through the anodization process. Anodization in the second stage can improve it even further. In previous research, the procedure of using chemical vapor deposition, or CVD, to introduce carbon into anodized alumina pores was an expensive and complex one. The chemical, petrochemical, and aerospace sectors, among others, will find more uses for aluminum alloys when anti-corrosion coating is fabricated using an easy and affordable technique. In this study, flaxseed oil is used as a carbon source for pyrolysis, which uses three different temperatures and a controlled atmosphere to penetrate porous alumina with pyrolytic carbon. In comparison to pyrolytic carbon infiltrated using CVD. The maximum amount of pyrolytic carbon that infiltrated the nanoporous alumina through polymer infiltration pyrolysis has been found [12].

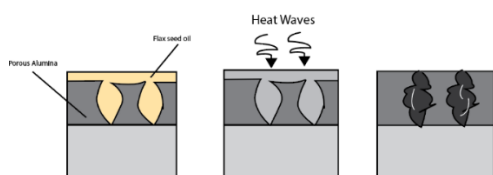


Figure 4: polymer infiltration pyrolysis process [12]

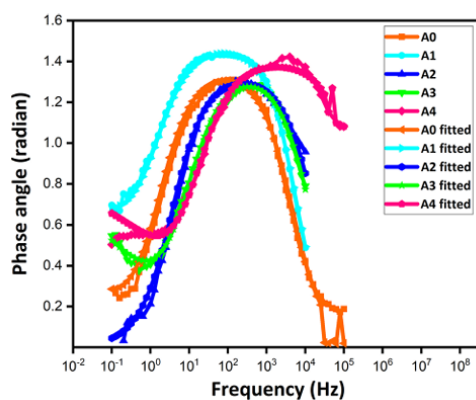


Figure 5: Bode plot used samples [12].

Advances in Corrosion Control using Biofilms:

Heterogeneous biofilms are created when bacteria that cause corrosion dwell closely together. The highest concentration of iron-oxidizing bacteria is found on carbon steel coupons, which results in the highest corrosion rates. Mild steel can be shielded from corrosion by the gramicidin S produced by Bacillus biofilm as described in this article [13]. Leptothrix discophora SP-6 joins the iron-oxidizing bacteria to create an oxygen-impermeable membrane that promotes the growth of SRB. However, when bacteria are destroyed by gramicidin S generated by the B. brevis biofilm, corrosion is not accelerated [4].

Engineered Living Biofilm for Corrosion protection:

Engineering metals can corrode in marine conditions, causing financial loss and safety issues related article [14]. Living microbial biofilms offer low-cost, environmentally friendly, and engineered corrosion protection through bio-passivation or microbiologically influenced inhibition. These biofilms have uses in electric conduction, biocatalysis, underwater hydrogels, bioremediation, virus elimination, and medicinal therapy. They can be altered with functional peptides, inorganic materials, or signaling pathways [15].

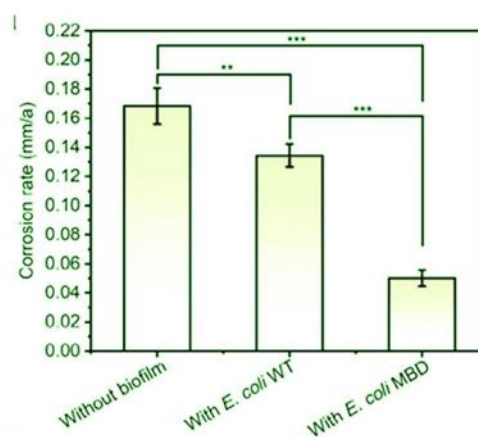


Figure 6: Aerobic E. coli MBD biofilm inhibited X70 corrosion (weight loss measurement) [15].

4. PERSPECTIVE

Corrosion, a persistent and costly issue that plagues metal structures, has long been addressed through traditional methods often involving harmful chemicals and materials. Bacterial biofilms have long been associated with microbiologically influenced corrosion (MIC), but their interactions with metals are more complex than previously thought. By changing the chemical and electrochemical conditions of metals, such as pH, ion concentration, and oxidation-reduction potential, biofilms can either encourage or prevent corrosion. Microbial inhibition of corrosion (MIC) has been studied in great detail as seen in the recent article [16]. MIC is less studied but becoming more and more interesting as additional microorganisms are discovered to protect metals. However, a promising and environmentally sustainable alternative is gaining traction: the use of biofilms and organic substances. Communities of bacteria known as biofilms, which stick to surfaces and create a protective matrix, provide a built-in defense against corrosive substances. When managed effectively, biofilms can create a shield that prevents corrosive substances from reaching the underlying metal. This approach not only provides protection but also reduces the need for toxic chemicals and materials. Organic materials, such as natural polymers and plant extracts, also offer a biodegradable and non-toxic solution

to corrosion. These materials can form a protective layer on metal surfaces through adsorption, a process where molecules adhere to a solid surface. Additionally, hydrophobic organic materials can repel water, preventing the formation of corrosive environments. The current review provided an overview of recent developments in bacteria biofilm-based corrosion prevention. Although these results open up new avenues for the development of eco-friendly corrosion management systems, additional investigation is required before these strategies can be successfully applied in everyday situations.

REFERENCE

1. Czaban, M.J.F.o.A.S., Aircraft corrosion—review of corrosion processes and its effects in selected cases. 2018. 2018(10): p. 5-20.
2. Karn, S.K., et al., The roles of biomolecules in corrosion induction and inhibition of corrosion: a possible insight. 2020. 38(5): p. 403-421.
3. Kadhim, A., et al., A mini review on corrosion, inhibitors and mechanism types of mild steel inhibition in an acidic environment. 2021. 10(3): p. 861-884.
4. Zuo, R.J.A.m. and biotechnology, Biofilms: strategies for metal corrosion inhibition employing microorganisms. 2007. 76(6): p. 1245-1253.
5. Harsimran, S., K. Santosh, and K.J.P.E.S. Rakesh, Overview of corrosion and its control: A critical review. 2021. 3(1): p. 13-24.
6. Kadhim, M.G., M.T.J.J.o.p.r. Ali, and studies, A critical review on corrosion and its prevention in the oilfield equipment. 2017. 7(2): p. 162-189.
7. Wang, J., et al., Corrosion inhibition study of marine Streptomyces against sulfate-reducing bacteria in oilfield produced water. 2023. 223: p. 111441.
8. Ornek, D., et al., Pitting corrosion control of aluminum 2024 using protective biofilms that secrete corrosion inhibitors. 2002. 58(9): p. 761-767.
9. Tanji, Y., Chemical Analysis of an Artificial Biofilm. 2001.
10. Jayaraman, A., et al., Corrosion inhibition by aerobic biofilms on SAE 1018 steel. 1997. 47: p. 62-68.
11. Chongdar, S., G. Gunasekaran, and P.J.E.A. Kumar, Corrosion inhibition of mild steel by aerobic biofilm. 2005. 50(24): p. 4655-4665.
12. Rashid, M., et al., Polymer-infiltration-pyrolysis (PIP) inspired hydrophobic nano-coatings for improved corrosion resistance. 2024. 59(3): p. 828-846.
13. Lamba, S., et al., Biogenic corrosion inhibition through Bacillus coagulans on mild steel in mild acidic medium. 2024. 59(8): p. 524-540.
14. Aydinsoy, E.A., et al., A SYSTEMATIC REVIEW OF CORROSION INHIBITORS IN MARINE ENVIRONMENTS: INSIGHTS FROM THE LAST 5 YEARS. 2024. 25(3).
15. Li, Z., et al., Engineered Living Biofilm with Enhanced Metal Binding Ability for Corrosion Protection in Seawater. 2024. 34(13): p. 2313120.
16. Wang, J., et al., Research progress on microbiological inhibition of corrosion: A review. 2022. 373: p. 133658.

Recent Advances in Energy Materials for Sustainable Energy Materials

Fatima Azhar¹, Ali Hassan¹, Arfa Ghaffar¹, Furqan Ahmed¹, Ehsan Ul Haq^{1*}

¹Department of Metallurgical and Materials Engineering, Faculty of Chemical Metallurgical and Polymer Engineering,
University of Engineering and Technology, Lahore, Punjab, Pakistan

[*amonehsan@uet.edu.pk](mailto:amonehsan@uet.edu.pk)

ABSTRACT

In pursuing global sustainability and the goals set by the Paris Agreement, which aims to limit global warming to below 2 degrees Celsius till the end of this century, advancements in energy materials have become critical for ensuring clean and sustainable energy solutions. This review discusses recent advancements within the domain of energy material research, focusing on different applications in energy storage, conversion, generation, and green synthesis of energy materials. Key aspects include lithium-ion batteries, supercapacitors, and hydrogen storage systems, whose functions have been focused on improving energy efficiency, storage capacity, power density, and environmental sustainability. Among these, lithium-ion batteries are particularly notable because of their good scalability and high energy density for extended applications like those in electric vehicles and grid storage by treating them with advanced cathode materials like Ni-rich layered oxides to improve fast-charging capabilities and energy density. Supercapacitors possess great cyclic stability, quick charging capability, and have shown enhanced performance through innovations in electrode materials and electrolytes. Hydrogen storage not only addresses the intermittent of renewable energy sources but also explores innovative methods such as chemical hydrogen storage to improve energy density, safety, and application efficiency. Furthermore, green synthesis techniques, utilizing microbes, fungi, and algae, have emerged as a sustainable alternative for producing nanomaterials. These methods reduce energy consumption by 30% and minimize environmental impact, offering significant advantages over conventional chemical processes. Research in optimizing these materials for greater scalability, faster charge times, and improved storage efficiency promises to reduce the reliance on fossil fuels and achieve global sustainability goals.

Keywords: Lithium-ion batteries, Supercapacitors, Hydrogen storage systems, Thermoelectric materials, Storage Capacity, Power Density, Cyclic stability.

1. INTRODUCTION

In the background of the world energy crisis and the disturbingly evident and present danger of global warming, the building of sustainable energy technologies has become the centerpiece of scientific inquiries. The Paris Agreement was the key mover in extending the commitment of nations to adhere to the objectives established for greenhouse gas emissions reductions via clean and renewable energy sources which would lead to a considerable transformation of the complete energy system. Energy materials are of the most significance these days. These materials are crucial in boosting the efficiency of energy storage and conversion systems. Materials that are such as lithium-ion batteries, supercapacitors, which are employed for rapid charging reasons or on the road, hydrogen storage systems and thermoelectric materials are being explored intensely of their potential influence in the sectors of energy efficiency, storage, and power. These materials are significantly taken into consideration towards the solution of renewable energy storage challenges, which enables the usage of renewable energy to be more consistent and flexible on a wider scale.

Recent breakthroughs in the area of energy materials have achieved great success in the improvement of energy

technology. For example, lithium-ion batteries are treated with chemicals to attain increased energy density and hence become acceptable for large-scale applications like electric cars and grid storage. [1]

2. ENERGY MATERIALS

Batteries and Supercapacitors

Lithium Based Batteries

Lithium-based battery systems are essential in the realm of energy storage technologies due to their scalability and favorable characteristics, such as high efficiency, extended lifespan, and superior energy density, making them well-suited for storing locally generated renewable energy. [1, 2] However, the impact of varying charge and discharge rates, as well as repeated cycling, on their energy and power performance remains ambiguous. [1, 3]. There are different Li-based batteries that are showing in the Table 1:

Table 1: Main kinds and frameworks of Li-based rechargeable batteries

Batteries	Anode	Cathode	Electrolyte
Li-ion	Graphitic carbon	Lithiated metal oxide	liquid organic carbonates, polymers, or solids
Li-metal	Li metal/Li alloy metal	Manganese dioxide, Vanadium oxide, Molybdenum disulfide	Nonaqueous solution
Li-air	Li metal	Air	Aqueous, aprotic, or solid
Li-S	Li metal	Elemental sulfur	Liquid organic electrolyte

Despite their potential, current battery energy storage solutions are still relatively costly, highlighting the need for innovative technologies to promote broader market adoption. Today, Li-ion batteries are extensively utilized in portable electronics, electric vehicles, grid storage

applications, and many other industries of space and technology. They remain the preferred choice because of their excellent energy density, long cycle life, high operating voltage, and low self-discharge rates. Consequently, there is a growing focus on enhancing energy density to further increase the driving range of electric vehicles [4, 5] [6].

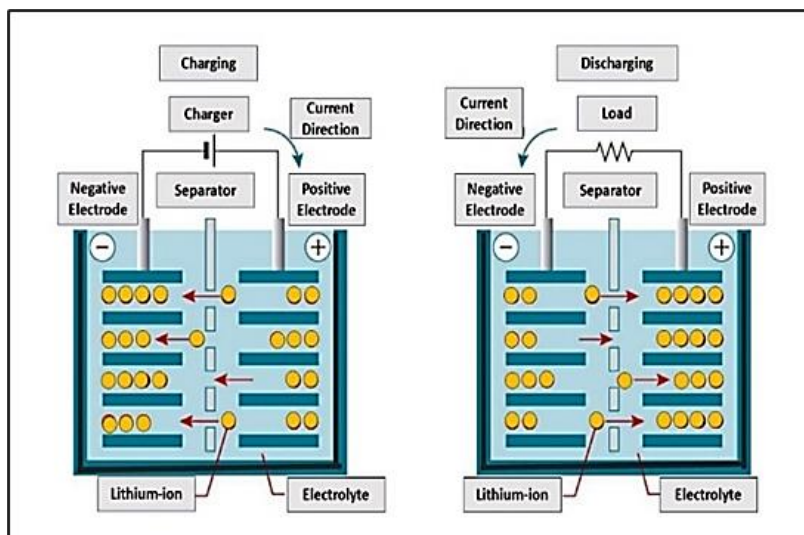


Figure 1: Representation in schematic form of Li-ion battery construction

Enhancing fast-charging capabilities in cathode materials for LIBs is essential to meet the growing power demands of modern applications. Prominent candidates include Ni-rich layered oxides ($\text{LiNi}_{1-x}\text{M}_x\text{O}_2$), spinel oxides (LiMn_2O_4), and polyanionic compounds like LiFePO_4 , which exhibit high energy densities but face challenges in improving their fast-charging characteristics. These limitations arise from factors such as low electronic and ionic conductivity, structural degradation due to lithium-metal (Li-M) cation mixing, oxygen release, and microcracks induced by mechanical stress during rapid cycling.

Following this will be the key requirement of significant performance improvements in LIBs and anode materials. The factors affecting cycle life, power density, and rate capability will be power, conductivity, and stability. (Potential candidates for optimization in

efficiency should hence be analyzed thoroughly in terms of their anode properties [7].

Super Capacitors

Electrochemical capacitors (ECs), commonly referred to as supercapacitors or ultracapacitors, have become highly sought-after energy storage devices. This popularity is attributed to their exceptional features, including fast charging and discharging capabilities along with long service life [9]. Supercapacitors offer energy storage capacity similar to that of batteries. However, they stand out due to their significantly higher power density and cycle stability, which are thousands of times greater than those of batteries, while their power density remains lower than that of traditional capacitors [10].

Supercapacitors are known for their remarkable energy storage capabilities, providing significant benefits such as

high energy density, power density, and extended cycle life. Recent advancements have focused on improving electrodes, developing better electrolytes, and introducing innovative manufacturing techniques to enhance efficiency and longevity. They are increasingly being integrated with renewable energy sources like solar and wind for energy storage and distribution, making them essential for stabilizing power grids and enabling smart energy systems. To ensure they become the preferred solution in the future, further research is needed in areas like flexible supercapacitors, novel materials, and advanced fabrication methods [11].

Table 2: Fast-charging properties of selected cathode materials for LIBs.

Cathode materials	High C-rate @ Capacity/ mAh g^{-1}	Cutoff voltage [V vs Li/Li ⁺]	Cycle life (Capacity retention)	Maximum capacity [mAh g^{-1}]	Reference
Nanocrystalline LiCoO ₂	100.0 C (75)	3.0–4.2	75 % after 20 cycles (10.0 C)	120 (1.0 C)	[9]
Mesoporous Li ₂ Mn ₂ O ₄	1,000.0 C (20)	3.4–4.5	90 % after 265 cycles (32.0 C)	44 (50.0 C)	[10]
Twin-boundaries LiMn ₂ O ₄	10.0 C (78)	3.4–4.5	94 % after 500 cycles (1.0 C)	132 (0.2 C)	[11]
Single-crystal LiMn ₂ O ₄	100.0 C (80)	3.4–4.5	63 % after 2,000 cycles (20.0 C)	121 (1.0 C)	[12]
Single-crystal LiNi _{0.5} Mn _{0.5} Co _{0.1} O ₂	10.0 C (165)	3.0–4.3	94 % after 100 cycles (6.0 C)	200 (0.1 C)	[13]
Semi-hollow microspheres Li _{1.2} Mn _{0.54} Ni _{0.12} Co _{0.12} O ₂	10.0 C (180)	2.5–4.8	94.5 % after 1,000 cycles (0.1 C)	275 (0.1 C)	[14]
Li _{1.15} Mn _{0.15} Cr _{0.15} O ₂ @rGO	60.0 C (145)	2.0–4.6	91.7 % after 100 cycles (3.0 C)	252 (0.5 C)	[15]
LiFePO ₄ /graphitic carbon	480.0 C (24)	2.0–4.2	96 % after 2,000 cycles (240.0 C)	89 (1.0 C)	[16]
Li ₂ V ₂ (PO ₄) ₃ /PIL	50.0 C (126)	3.0–4.8	70 % after 10,000 cycles (50.0 C)	158 (1.0 C)	[17]
Li ₂ V ₂ (PO ₄) ₃ /CA	10.0 C (100)	3.0–4.3	94.7 % after 100 cycles (1.0 C)	110 (0.5 C)	[18]
FeF ₂ -0.33H ₂ O@carbon nanosheets	5.0 C (143.4)	2.0–4.2	97.2 % after 200 cycles (1.0 C)	247.5 (0.1 C)	[19]

Table 3: An assessment of the merits and downsides related with key anode materials [8]

Material	Pros	Cons
Silicon	<ol style="list-style-type: none"> Enhanced capability range (3579 mA h g⁻¹) Isolated inexpensive 	<ol style="list-style-type: none"> Sudden alteration in volume surge (300 %)
Transition-metal oxides	<ol style="list-style-type: none"> Enormous specific capacity (600–1000 mA h g⁻¹) Adequate level of stability 	<ol style="list-style-type: none"> Low Columbic efficiency Maximum achievable hysteresis
Alloys	<ol style="list-style-type: none"> Excellent energy storage capability (400–2300 mA h g⁻¹) Adequate level of security Impressive durability over multiple cycles Columbic efficiency achieved to the satisfaction 	<ol style="list-style-type: none"> Reduced conductivity Significant volume fluctuation Decrease in capacity
Carbon	<ol style="list-style-type: none"> Enhanced safety Excellent structural integrity Superior conductivity characteristics Prolonged lifespan 	<ol style="list-style-type: none"> Limitation of capacity Irregularities in safety Extended lifespan Reduction in discharge rate

Types

- Electrochemical doubled-layer capacitors
- Pseudo-capacitor's
- Hybrid-capacitor's

Electrochemical double-layer capacitors (EDLCs), also known as supercapacitors, ultracapacitors, or liquid ionistors, are advanced energy storage devices using nanostructured carbon materials. Unlike traditional capacitors, EDLCs store energy through charge separation within the electrolyte, forming an electric double layer on each electrode.

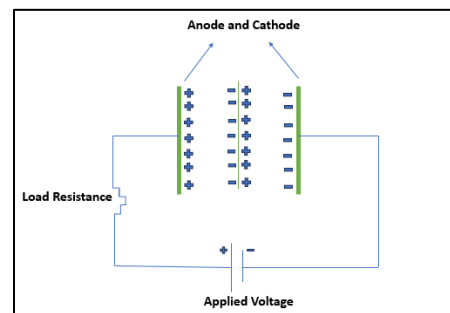


Figure 2: A schematic illustration of Electric double-layer capacitors

Pseudocapacitors (PCs) combine electric double-layer capacitance with faradaic charge-transfer processes, utilizing transition-metal oxides and conductive polymers to significantly increase capacitance and current density.

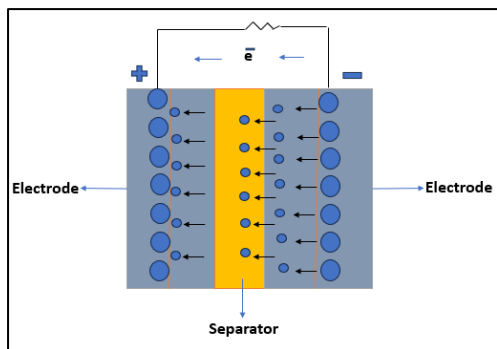


Figure 3: A schematic illustration of Pseudo capacitors

Hybrid supercapacitors, blending EDLC and PC mechanisms, use both faradaic and non-faradaic processes to achieve higher power and energy densities. They typically feature asymmetric designs with distinct materials for the positive and negative electrodes, such as nickel or lead oxides combined with activated carbon [12].

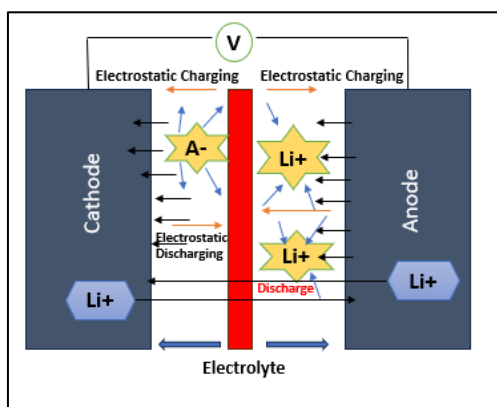


Figure 4: A schematic illustration of Hybrid supercapacitors

Photovoltaic Materials

The photovoltaic materials work in such a way that there is absorption of photons from incident sunlight, thereby forming electron-hole pairs and breaking the electric field. Common materials used include crystalline silicon, cadmium telluride, and perovskites; each has different solar cell efficiencies along with manufacturing processes.[13, 14]

Solar Cells

Solar cells work based on the photovoltaic effect. The PV effect involves three essential procedures.

1. Photon absorption in a p-n junction semiconductor excites electrons from the valence band to the conduction band, creating electron-hole pairs.[15]
2. When a p-n junction semiconductor is incidental by a light, it excites the electrons and produces

electron-hole pairs. If the incident light has more energy than required, then the excess energy accelerates the electrons and holes. However, this excess energy is lost as heat eventually.

3. Finally, isolated electrons can be utilized to power an electrical circuit. Once they move through the circuit, the electrons recombine with the holes.

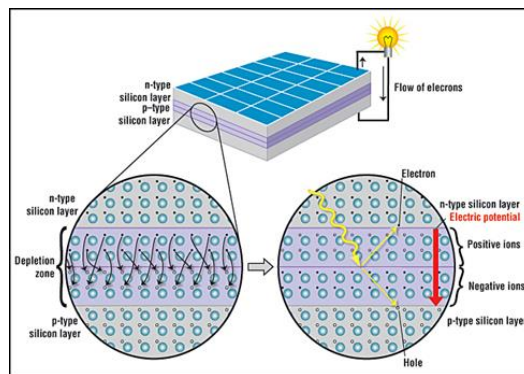


Figure 5: Solar cell working

Table 4: Generation-wise Materials for Solar [16]

Gen.	Solar cell materials	Characteristics	Efficiency	Manufacturing method	Band gap
I	m-Si	Stable & Expensive	24.4%	Czochralski	1.12 eV
I	p-Si	High Defect Content & Low Cost	19.9%	Siemens	1.7 eV
I	GaAs	Good Design Control & Expensive	18.4–28.8%	Epitaxial growth	1.43 eV
II	a-Si	Short Life Cycle & Non-Toxic	10.2–12.7%	Large-area deposition	1.73 eV
II	μc-Si	Good Degradability & Low Defect Content	11.9–14.0%	Roll-to-roll	1.6–1.8 eV
II	CIGS	Tunable Band Gap	22.3%	Deposition, co-evaporation	1.0–1.7 eV
II	CdTe	Low Foiling & High Temperature Tolerance	21.0%	Deposition	1.45 eV
III	DSSC	Robustness & Work in Low Light Conditions	5.0–20.0%	Roll-to-roll	3.0–3.2 eV
III	QDs	Efficient & Effective Conductivity	11.0–17.0%	Solution casting	Tunable
III	PVSC	Simple & Cheap	21.1–21.6%	Sputtering/printing	Tunable
IV	BiJ PSC with GO/PEDOT:PSS	Stable & Reproducible	4.28%	Solution casting	Tunable
IV	PVSC with rGO/PEDOT:PSS	Reduced e ⁻ -p ⁺ Recombination & Long Lifetime	5.7–11.95%	Solution casting	Tunable
IV	PSC with G/PEDOT:PSS	Good Functionality	2.82–11.8%	Solution casting	Tunable
IV	PSCs with B-doped CNTs	Improved e ⁻ Transport	4.1–8.6%	Solution casting	Tunable

Hydrogen Storage and Fuel Cells

Hydrogen has emerged as a possible renewable energy carrier, capable of mitigating the intermittent challenges linked to renewable energy. However, for hydrogen to serve as an optimal low or zero-carbon energy carrier, its storage and transportation challenges need to be resolved [17]. Hydrogen has the greatest degree of energy per unit mass, with 120 MJ/kg. However, it has low density under typical circumstances resulting in a very low volumetric energy density of just 0.01 MJ/L at ambient conditions, and even for liquefied hydrogen (LH2), it only reaches 8.5 MJ/L. In comparison, methane and gasoline have significantly higher volumetric energy densities at 0.04 MJ/L and 32 MJ/L respectively. This poses a major challenge for effective hydrogen storage, particularly in on-board applications where both gravimetric and volumetric densities are crucial. While stationary hydrogen storage is less constrained by weight, vehicles require storage methods that ensure high gravimetric and volumetric energy densities, along with manageable operating conditions, fast reaction kinetics, safety, and affordability. To address these needs, various physical and chemical hydrogen storage methods are being researched to advance the feasibility of a hydrogen-powered economy.

Hydrogen storage methods

The principal methods of hydrogen storage are given as [18]:

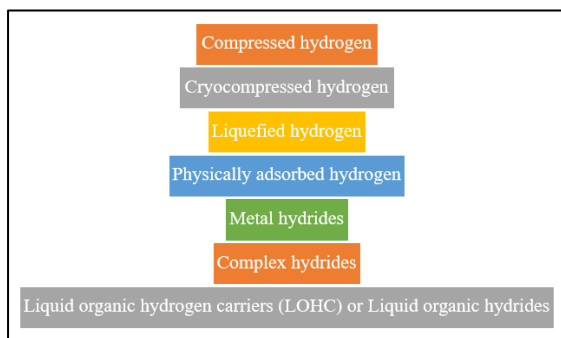


Figure 6: Different methods of hydrogen storage

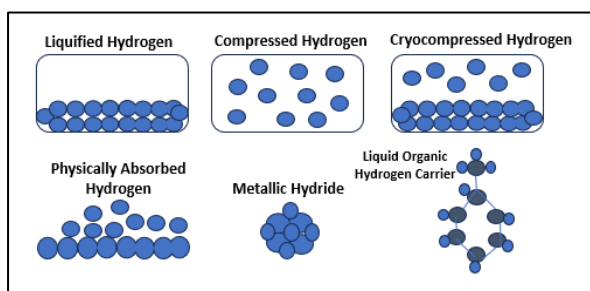


Figure 7: Pictorially depicts the notion of hydrogen storage ways

Table 5: Analysis of several hydrogen storage technologies

Storage method	Hydrogen content (wt% H ₂)	Volumetric density (g/L)	Volumetric energy density
Compression			
1 bar, RT	100	0.0814	0.01
350 bar, RT	100	24.5	2.94
700 bar, RT	100	41.4	4.97
700 bar, RT, (incl. Type IV tank)	5.7	40.8	4.9
Liquid hydrogen			
1 bar, -253 °C	100	70.8	8.5
1 bar, -253 °C (incl. tank)	14	51	6.12
Cryo-compression			
350 bars, -253 °C	100	80	9.6
Metal Hydrides			
MgH ₂	7.6	110	13.2
FeTiH ₂	1.89	114	13.7
Complex hydrides			
NaAlH ₄	7.5	80	9.6
Physical adsorbents			
Activated carbon @77 K and 30-60 bar	5.0	38.5	2.4
Zeolite (NaX) @77 K and 40 bar	2.55	20	2.4
MOF (MOF-210) @77 K and 80 bar	7.9	25.8	3.1
Liquid hydrogen organic carriers			
Methylcyclohexane/toluene	6.2	47.3	5.68
perhydro-benzyltoluene/benzyltoluene	6.2	56.0	6.72

3. SUSTAINABILITY AND ENERGY MATERIALS

Green Synthesis of Energy Materials

Nanomaterials have undergone significant advancements in recent decades, but conventional processes of production can be hazardous and unsustainable. [18, 19] Biomass used for synthesis includes microbes, fungus, plants, and agro-industrial bio-waste. Green synthesis reduces energy usage by 30%, saves up to 40% on costs, and increases industrial output by 50%.

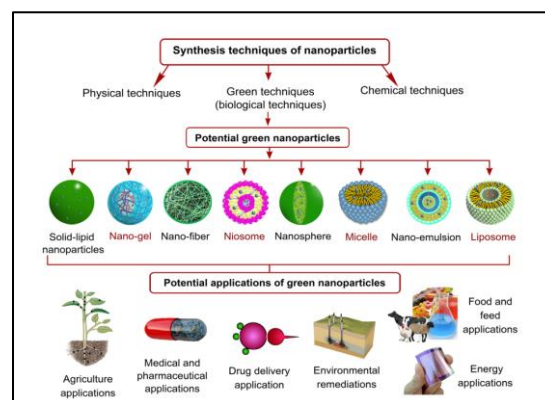


Figure 8: Nanoparticle synthesis and applications

The green synthesis techniques in energy materials, especially microbial, fungal, and algal-mediated methods, have tremendous environmental advantages because it

avoids the use of harmful chemicals. Instead, they use biological agents such as bacteria, algae, and fungi to produce nanoparticles in an environmentally friendly way. More promising is due to the synergistic interactions among the microorganisms that enhance many of these beneficial traits, from enhanced growth rates and upregulated production of secondary metabolites to even targeting and reducing environmental pollutants. Examples of such algae include *Chlorella* sp., which have been found to synthesize iron oxide nanoparticles with better control over the size of the particles and reduced toxicity of the end product [20]. Such biological processes also make the nanoparticles' production more sustainable for energy material applications, hence more beneficial compared to conventional chemical methods due to their reduced impact on the environment.

4. CONCLUSION

This review highlights key advancements in energy materials, including lithium-ion batteries with improved fast-charging, supercapacitors with enhanced electrode materials, and innovative hydrogen storage solutions. Green synthesis techniques offer sustainable alternatives for material production, reducing environmental impact. Continued research in these areas is essential for optimizing scalability, improving storage efficiency, and accelerating the shift toward renewable energy, thereby supporting global sustainability goals.

REFERENCES

1. L. Ahmadi, S. B. Young, M. Fowler, R. A. Fraser, and M. A. Achachlouei, "A cascaded life cycle: reuse of electric vehicle lithium-ion battery packs in energy storage systems," *The International Journal of Life Cycle Assessment*, vol. 22, no. 1, pp. 111-124, 2017/01/01 2017, doi: 10.1007/s11367-015-0959-7.
2. X. Li, B. Anvari, A. Palazzolo, Z. Wang, and H. Toliyat, "A utility-scale flywheel energy storage system with a shaftless, hubless, high-strength steel rotor," *IEEE Transactions on Industrial Electronics*, vol. 65, no. 8, pp. 6667-6675, 2017.
3. M. Gaberšček, "Understanding Li-based battery materials via electrochemical impedance spectroscopy," *Nature Communications*, vol. 12, no. 1, p. 6513, 2021.
4. B. Rowden and N. Garcia-Araez, "A review of gas evolution in lithium ion batteries," *Energy Reports*, vol. 6, pp. 10-18, 2020.
5. A. Manthiram, "An outlook on lithium ion battery technology," *ACS central science*, vol. 3, no. 10, pp. 1063-1069, 2017.
6. Y. Liang et al., "A review of rechargeable batteries for portable electronic devices," *InfoMat*, vol. 1, no. 1, pp. 6-32, 2019.
7. L. Zhang, L. Yu, O. L. Li, S.-Y. Choi, G. Saeed, and K. H. Kim, "FeF₃·0.33 H₂O@ carbon nanosheets with honeycomb architectures for high-capacity lithium-ion cathode storage by enhanced pseudocapacitance," *Journal of Materials Chemistry A*, vol. 9, no. 30, pp. 16370-16383, 2021.
8. M. H. Hossain, M. A. Chowdhury, N. Hossain, M. A. Islam, and M. H. Mobarak, "Advances of lithium-ion batteries anode materials—A review," *Chemical Engineering Journal Advances*, vol. 16, p. 100569, 2023.
9. F. Liu, X. Feng, and Z.-S. Wu, "The key challenges and future opportunities of electrochemical capacitors," *Journal of Energy Chemistry*, vol. 76, pp. 459-461, 2023.
10. M. E. Şahin, F. Blaabjerg, and A. Sangwongwanich, "A comprehensive review on supercapacitor applications and developments," *Energies*, vol. 15, no. 3, p. 674, 2022.
11. M. Girirajan, A. K. Bojarajan, I. N. Pulidindi, K. N. Hui, and S. Sangaraju, "An insight into the nanoarchitecture of electrode materials on the performance of supercapacitors," *Coordination Chemistry Reviews*, vol. 518, p. 216080, 2024.
12. Y. Maletin, N. Stryzhakova, S. Zelinskyi, and S. Chernukhin, "Energy storage technologies based on electrochemical double layer capacitors: a review," *Theoretical and Experimental Chemistry*, vol. 57, no. 5, pp. 311-324, 2021.
13. Y. Xing et al., "A review of concentrator silicon solar cells," *Renewable and Sustainable Energy Reviews*, vol. 51, pp. 1697-1708, 2015/11/01/ 2015, doi: <https://doi.org/10.1016/j.rser.2015.07.035>.
14. B. Askari Mohammad, V. Mirzaei Mahmoud Abadi, and M. Mirhabibi, "Types of Solar Cells and Application," *American Journal of Optics and Photonics*, vol. 3, no. 5, pp. 94-113, 2015, doi: 10.11648/j.ajop.20150305.17.
15. J. Tao and S. Yu, "Review on feasible recycling pathways and technologies of solar photovoltaic modules," *Solar Energy Materials and Solar Cells*, vol. 141, pp. 108-124, 2015/10/01/ 2015, doi: <https://doi.org/10.1016/j.solmat.2015.05.005>.
16. B. P. Singh, S. K. Goyal, and P. Kumar, "Solar PV



cell materials and technologies: Analyzing the recent developments," *Materials Today: Proceedings*, vol. 43, pp. 2843-2849, 2021.

17. P. Preuster, A. Alekseev, and P. Wasserscheid, "Hydrogen storage technologies for future energy systems," *Annual review of chemical and biomolecular engineering*, vol. 8, no. 1, pp. 445-471, 2017.
18. M. R. Usman, "Hydrogen storage methods: Review and current status," *Renewable and Sustainable Energy Reviews*, vol. 167, p. 112743, 2022.
19. C. M. Costa, J. C. Barbosa, R. Gonçalves, H. Castro, F. J. D. Campo, and S. Lanceros-Méndez, "Recycling and environmental issues of lithium-ion batteries: Advances, challenges and opportunities," *Energy Storage Materials*, vol. 37, pp. 433-465, 2021/05/01/ 2021, doi: <https://doi.org/10.1016/j.ensm.2021.02.032>.
20. E. O. Ogunniyi and H. Pienaar, "Overview of battery energy storage system advancement for renewable (photovoltaic) energy applications," in *2017 International Conference on the Domestic Use of Energy (DUE)*, 4-5 April 2017 2017, pp. 233-239, doi: 10.23919/DUE.2017.7931849.
21. K. Gudikandula and S. Charya Maringanti, "Synthesis of silver nanoparticles by chemical and biological methods and their antimicrobial properties," *Journal of Experimental Nanoscience*, vol. 11, no. 9, pp. 714-721, 2016/06/12 2016, doi: 10.1080/17458080.2016.1139196.

Eco-Transit Revolution: Design and fabrication of Three Wheeled reverse strike Vehicles

Mehmood ul Hassan Amjad¹, Waqas Javid^{1*}, Amar ul Hassan², Muhammad Sameer Jamil¹, Ahmed Shakeel¹, Ansar Mehmood¹ Muhammad Atif Niaz¹,

¹Mechanical Engineering Department, Wah Engineering College, University of Wah, Wah Cantt, 47040, Pakistan.

²Mechanical Engineering Department, University of Engineering and Technology, Taxila, Pakistan.

*waqas.javid@wecuw.edu.pk

ABSTRACT

This paper delves into the domain of three-wheeled reverse trike vehicles, emphasizing advancements in safety features, suspension systems, and lightweight body design. The primary objective is to enhance safety, optimize suspension performance, and incorporate cutting-edge lightweight materials. This research contributes to Sustainable Development Goals by promoting energy-efficient transportation solutions through innovative designs and eco-friendly materials. It also advances Energy Economics and Modelling, aiming for a sustainable future in transport. By integrating these elements, the study seeks to reduce carbon emissions, support the transition to a low-carbon economy, and provide a comprehensive framework for developing safer, more efficient, and environmentally friendly three-wheeled reverse trike vehicles.

KEYWORDS: Three-Wheeler, Reverse Strike, Suspension System, Aerodynamics, Economic, Light Weight Chassis, MS Body

1. INTRODUCTION

The purpose of working on a tri-wheeler project is driven by its recent evolution and potential to enhance safety and economic benefits for drivers, particularly at high speeds. Reverse trikes, with their innovative design, have a lower center of gravity, which significantly improves stability and reduces the risk of rollovers. This makes them a promising option for high-speed transportation. Personal Mobility Vehicles (PMVs), including tri-wheelers, are emerging as a new category of transportation devices. These vehicles offer solutions for mobility issues, supporting the development of low-carbon transportation and addressing the needs of the elderly and urban revitalization. A reverse trike's unique design, which includes two wheels at the front and one at the rear, enhances stability compared to traditional two-wheeled vehicles. The rear configuration resembles that of a car, contributing to better balance and control. Furthermore, the unique front-end design of reverse trikes improves the rider's visibility on the road, a crucial factor for safety in traffic. Research indicates that rollover speeds increase as the center of mass shifts rearward in three-wheeled vehicles, and notably, they tend to have lower rollover speeds compared to four-wheeled counterparts.

2. MODEL DESCRIPTION

The three-wheeled reverse trike model is meticulously designed to optimize stability, safety, and performance. Key features include a lightweight chassis constructed from advanced materials, which not only enhances the vehicle's structural integrity but also contributes to its overall efficiency and agility. The aerodynamic design reduces air resistance, improving fuel efficiency and high-speed performance. The trike's configuration, with two front wheels and one rear wheel as shown in fig.1, provides a lower center of gravity and balanced weight distribution. This setup significantly enhances stability and reduces the risk of rollovers, even during sharp turns or sudden manoeuvres.

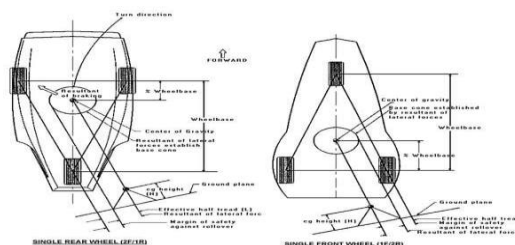


Figure 1. single Rear and Front Wheel

The specifications of different components have been given in Table.1.

Design and Selection of Material

As The safety factor for the chassis material, as per the book 'Design' by Khurmi, must lie between 0 and 4. In this project, two types of chassis were designed using mild steel with circular and rectangular pipes.

Table 1: Specifications of Components

Sr.	Components	Specifications
1	Overall Length	108 in =2.743m
2	Track width	48 in = 1.2192m
3	Wheel Base	54in = 1.38m
4	Ground Clearance	5.4 in =0.13m
5	Overall Height of Vehicle	41.6 in = 1.057m
6	Overall Weight of Chassis	71kg
7	Overall weight of vehicle	450kg
8	Front to COG	1.097m
9	Rear to COG	1.646m

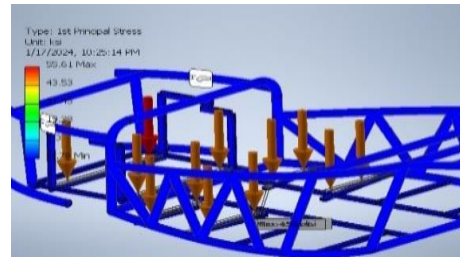
The safety factor for the circular pipe chassis was found to be 0.8, which falls below the required range, indicating a potential failure under stress. However, for the rectangular pipe chassis, the safety factor was calculated to be 2.43, meeting the safety criteria specified by automobile standards and regulations.



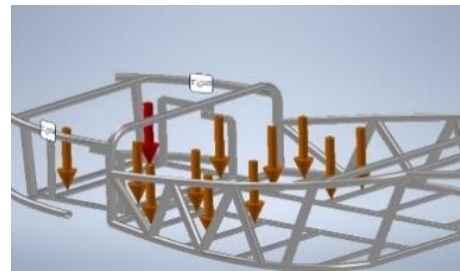
(a)



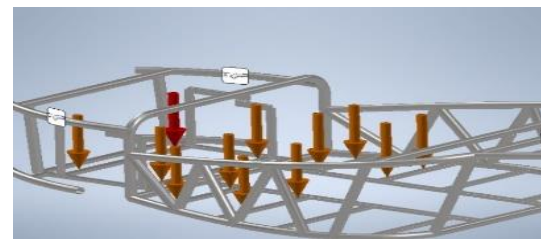
(b)



(c)



(d)



(e)

Figure.2 (a), (b) and (c) Design and Modal of Chassis (d) and (e) Safety factor of Modal.

Mathematical Calculation

Weight Distribution

For calculating weight distribution on the front and rear axles of a standard front-wheel-drive vehicle with a 660 CC Engine.

Front Weight Distribution (W_f)

The weight on the front axle (W_f) is directly proportional to the distance from the center of gravity to the rear axle (L_r) and inversely proportional to the total wheel base (L).

$$W_f = \frac{W \times L_r}{L}$$

$$W_f = \frac{700 \text{ kg} \times 1.60 \text{ m}}{2.667 \text{ m}}$$

$$W_f \approx 419.95 \text{ kg}$$

Rear Weight Distribution (W_r) :

The weight on the rear axle (W_r) is directly proportional to the distance from the center of gravity to the front axle (L_f) and inversely proportional to the total wheelbase (L).

$$W_r = \frac{W \times L_f}{L}$$

$$W_r = \frac{700 \text{ kg} \times 1.067 \text{ m}}{2.667 \text{ m}}$$

$$W_r \approx 280.05 \text{ kg}$$

So, for this simplified example, the weight distribution might be around 59.99% on the front axle and 40.01% on the rear axle.

Slip Angle (α)

$$\alpha = \tan^{-1} \left[\frac{0.5 \times \text{Front Trackwidth (a)}}{\text{Wheel Base (L)}} \right]$$

$$\alpha = \tan^{-1} \left[\frac{0.5 \times 1.75 \text{ m}}{2.667 \text{ m}} \right]$$

$$\alpha = \tan^{-1}(0.3280)$$

$$\alpha = 18.15^\circ$$

Minimum and Maximum Turning Radius

Fuel Consumption Rate

For the sake of calculation, let's assume the engine consumes 0.1 liters of gasoline per minute. Given the density of gasoline is approximately 0.74 kg/L, the mass flow rate of fuel F_f is;

$$F_f = \frac{0.1 \text{ L}}{\text{min}} \times \frac{0.74 \text{ kg}}{\text{L}} = \frac{0.074 \text{ kg}}{\text{min}}$$

Inflow Rate

To estimate the airflow rate, this can use the engine displacement, RPM, and volumetric efficiency (usually around 85% for naturally aspirated engines). Assuming the engine runs at 3000 RPM.

Engine displacement per revolution

Table.2: Comparison between Maximum and Minimum Radius

Maximum Turning Radius:	Minimum Turning Radius:
$\sin \alpha = \left[\frac{w}{R_{max}} \right]$ $= \left[\frac{L}{R_{max}} \right]$ $R_{max} = \left[\frac{L}{\sin \alpha} \right]$ $R_{max} = \left[\frac{L}{\sin(18.15^\circ)} \right]$ $R_{max} = 8.56 \text{ m}$	$\tan \varphi = \left[\frac{w}{R_{min}} \right] = \left[\frac{L}{R_{min}} \right]$ $R_{min} = \left[\frac{L}{\tan \varphi} \right]$ $R_{min} = \left[\frac{2.667 \text{ m}}{\tan(27.3^\circ)} \right]$ $R_{min} = 5.16 \text{ m}$

$$\text{Displacement per revolution} = \frac{659}{2} = 329.5 \text{ c}$$

Air mass flow rate:

Assuming air density is 1.225 kg/m³ (standard conditions), convert the volume flow rate to mass flow rate.

$$\text{Air mass flow rate} = 840 \times 65 \text{ L/min} \times \left(\frac{1.225 \text{ kg}}{1000 \text{ L/min}} \right) = 1.03 \text{ kg/min}$$

Calculating the Air-Fuel Ratio (AFR)

Using the mass flow rates of air and fuel;

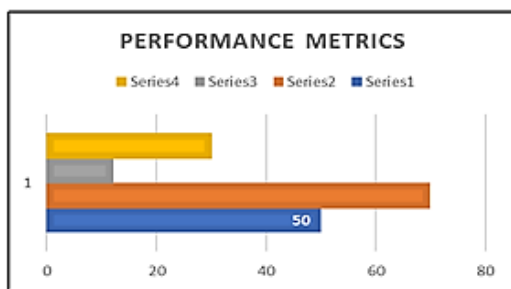
$$\text{AFR} = \frac{\text{Mass of air}}{\text{Mass of fuel}} = 1. \frac{0.03 \text{ kg}}{\text{min}} \cdot \frac{0.74 \text{ kg}}{\text{min}}$$

$$\approx 13.92$$

3. RESULT AND DISCUSSIONS

The findings underscore the heightened stability and safety attributes of three wheeled vehicles, positioning them as promising solutions for urban mobility. Notably, user assessments of Personal Mobility Vehicles (PMVs) vary with demo-graphic and environmental conditions, accentuating the necessity of incorporating these variables into design considerations. Furthermore, compromised road quality and higher speeds amplify ride discomfort and safety concerns, mandating suspension system enhancements and future powertrain modifications. The introduction of control systems contributes significantly to vehicle stability, while recognizing that three-wheelers exhibit a heightened susceptibility to rollovers, contingent upon the positioning of the mass center. In addition, suspension design emerges as a pivotal determinant of the handling and performance

characteristics of lightweight vehicles. Finally, the development of a robust tricycle frame, engineered to support a payload of 755 kg, underscores its pivotal role in ensuring dependable and efficient transportation solutions. The performance metrics of the reverse trike project are illustrated through two visual representations: a bar chart and a pie chart. The bar chart indicates that Series 2 has the highest performance metric, followed by Series 1, Series 4, and Series 3. Series 1 achieved a notable performance score of 50. The pie chart further breaks down these metrics into percentages, showing that Series 2 constitutes 43% of the overall performance, making it the dominant contributor. Series 1 follows with 31%, Series 4 with 19%, and Series 3 with 7%. These metrics highlight the significant contributions of Series 2 and Series 1 to the project's overall performance.



(a)



(b)

Figure 3: (a) and (b) perform on Metrics

Energy Efficiency

1 liter of gasoline typically contains around 8.9 kWh of energy. Using this conversion factor, you can calculate the energy usage in kWh,

$$\text{Energy Usage (kWh)} = \text{Fuel Consumption (liters)} * \text{Energy Content of Fuel (kWh/liter)}$$

$$\text{Energy Usage (kWh)} = 22 \text{ liters} * 8.9 \text{ kWh/liter} = 195.8 \text{ kWh}$$

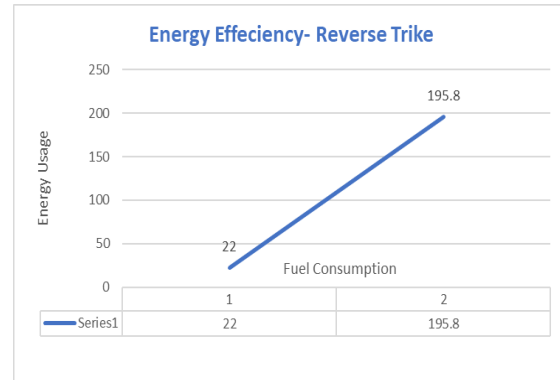


Figure.4: Relationship between Energy usage and Fuel consumption

4. CONCLUSIONS

This examination of three-wheeled vehicles concludes by stressing their inherent stability and safety features and pointing to them as possible enhancements to urban mobility. Improving the suspension system and possibly changing the engine in the future are important ways to address issues like worsening road conditions and higher speeds. A strong tricycle frame's ability to support large weights exemplifies the value of structural engineering. findings pave the way for future innovation and support a comprehensive approach to ensure that three-wheeled vehicles are both sustainable and tailored to meet a variety of needs while blending in seamlessly with urban environments. it is essential to continue research and development efforts aimed at enhancing three-wheeled reverse trike vehicles, with a specific focus on lightweight chassis design, aerodynamics, and safety features. These three critical facets can collectively contribute to making these vehicles not only more economical but also highly reliable in terms of their performance. In alignment with Sustainable Development Goals and the overarching objective of fostering a Low Carbon Economy, this pursuit should prioritize the championing of energy-efficient transportation solutions. By further advancing these key elements, this can pave the way for a sustainable, environmentally conscious future in the realm of three-wheeled reverse trikes.

REFERENCES

1. R. Ando and A. Li, "An Evaluation Analysis on Three-Wheeled Personal Mobility Vehicles," *Int. J. Intell. Transp. Syst. Res.*, vol. 14, no. 3, pp. 164–172, 2016, doi: 10.1007/s13177-015-0111-x.
2. J. A. K. Lodhi and N. P. Khan, "Performance Evaluation of Leaning Reverse Trike," *J. Res.*, vol. 02, no. 10, pp. 14–20, 2016, [Online].



- Available: <https://scihub.se/10.1109/MCS.2006.1700044>
3. A. Spanu, F. Stoenescu, M. Lorenzi, and M. Avram, "Analysis of three wheeled electric vehicle with increased stability on the road," IOP Conf. Ser. Mater. Sci. Eng., vol. 444, no. 4, 2018, doi: 10.1088/1757-899X/444/4/042010.
 4. J. Dizo and M. Blatnicky, "Evaluation of vibrational properties of a three-wheeled vehicle in terms of comfort," Manuf. Technol., vol. 19, no. 2, pp. 197–203, 2019.
 5. A. Doria, "Potentialities of A Light Three-Wheeled Vehicle for Sustainable Mobility Vittore," pp. 1–10, 2017, [Online]. Available: <http://journalmt.com/pdfs/mft/2019/02/04.pdf>
 6. Wibowo, L. Lambang, G. Pratama, and E. Surojo, "Simulation and analysis of three wheeled reverse trike vehicles with PID controller," AIP Conf. Proc., vol. 1983, 2018, doi: 10.1063/1.5046293.
 7. P. Deepak, S. V. Reddy, N. Ramya, M. B. Goud, and K. C. Shekar, "Design and Analysis of Three Wheeled Dual Steering Vehicle," Int. J. Eng. Res. Technol., vol. 3, no. 4, pp. 36–42, 2014.
 8. T. B. Raju and D. Hithaish, "International Journal of Research in Aeronautical and Mechanical Engineering," Int. J. Res. Aeronaut. Mech. Eng., vol. 2, no. 3, pp. 224–231, 2014.
 9. Saeedi and Kazemi, "Stability of Three-Wheeled Vehicles with and without Control System," Int. J. Automot. Eng., vol. 3, no. 1, pp. 343–355, 2013.
 10. J. C. Huston, B. J. Graves, and D. B. Johnson, "Three wheeled vehicle dynamics," SAE Tech. Pap., vol. 91, pp. 591–604, 1982, doi: 10.4271/820139.
 11. F. Will, J. N. Davdison, P. Couchman, and D. Bednall, "Tomorrow's car - For today's people: Can tilting three wheeled vehicles be a solution for the problems of today and the future" SAE Tech. Pap., 2011, doi: 10.4271/2011-28-0001.
 12. P. R. Pawar and M. R. Saraf, "Ride Comfort Evaluation of Different Three-Wheelers Based on the Probability Density Distribution," SAE Tech. Pap., vol. 2007-Janua, no. January, 2007, doi: 10.4271/2007-26-073.
 13. A. G. Nalecz, "Investigation into the effects of suspension design on stability of light vehicles," SAE Tech. Pap., vol. 96, pp. 512–545, 1987, doi: 10.4271/870497.
 14. R. Perera, "Analysis of structural crashworthiness of a conventional three-wheeler incorporating a passenger restrain system" no. September, 2023, [Online].
 15. P. A. Desai, "Manufacturing Trike-the Helper," vol. 8, no. 06, pp. 179–182, 2019, [Online]. Available: <https://www.ijert.org/research/manufacturing-trike-the-helper-IJERTV8IS060145.pdf>
 16. W. Aryadi, A. Setiyawan, Kriswanto, and A. Rizky, "Design and static testing of electric vehicle chassis trike front-wheel drive," IOP Conf. Ser. Earth Environ. Sci., vol. 969, no. 1, 2022, doi: 10.1088/1755-1315/969/1/012022.

NUMERICAL ANALYSIS AND PERFORMANCE OPTIMIZATION OF MULTI-STAGE REGENERATIVE HEAT AND MASS EXCHANGER

Hurmat Fatima^{1*}, Muhammad Usman¹, Muzaffar Ali^{2,3}, Guiqiang Li³

¹Mechanical Engineering Department, University of Engineering and Technology, Taxila.

²Energy Engineering Department, University of Engineering and Technology, Taxila

³ Department of Thermal Science and Energy Engineering, University of Science and Technology of China, China.

* hurmat.96@gmail.com

ABSTRACT

The maisotsenko cycle (m-cycle) revolutionizes the concept of indirect evaporative cooling by achieving sub-wet-bulb temperatures without moisture addition or harmful refrigerants, outperforming conventional vapor compression systems in efficiency and environmental impact. The integration of m-cycle with solid desiccant cooling system is numerically investigated in this research. It further optimizes the perforated, regenerative, multi-stage m-cycle through a novel analytical model integrating python with trnsys. The optimization reduced the unmet cooling from 63.17 kw to 33.4 kw in summer, enhanced thermal performance indicators (dew point and wet-bulb effectiveness), and enhanced seasonal cooling capacity from 7685 kw to 8294 kw. The thermal comfort indicator predicted percentage of dissatisfied (ppd) was 15.87% for the base case on average, which reduced to 9.03% after optimization. These results demonstrate that the optimized solid desiccant m-cycle cooling systems (sdmc) can achieve higher performance and improved thermal comfort, establishing it as a sustainable alternative for traditional cooling in hot and humid climates.

Keywords: Maisotsenko cycle, Indirect Evaporative Cooler, Desiccant system, TRNSYS. Genetic algorithm

1. INTRODUCTION

The global demand for energy-efficient cooling has emphasized the potential of indirect evaporative cooling systems. Cooling below wet-bulb temperatures without adding moisture or harmful refrigerants is achieved by Maisotsenko cycle making it a strong and promising alternative to traditional vapor compression cycles, garnering significant research interest since its inception [1].

Mcycle indirect evaporative coolers, based on the Maisotsenko cycle patented in 2003 [1], offer substantial energy savings and improved thermal comfort, particularly in hot, dry climates. Recent studies [2] demonstrated energy efficiency ratios up to 40% higher than conventional systems. Dizaji et al. [3] developed an analytical model for multi-stage regenerative M-cycle air coolers, while Wang et al. [4] and Li et al. [5] optimized heat and mass transfer processes.

Hybrid Mcycle solid desiccant cooling systems address limitations in humid environments. Chen and Liu [6] reported potential energy savings of up to 60% across diverse climatic zones. Patel et al. [7] explored innovative desiccant materials with enhanced moisture adsorption capacities. Computational fluid dynamics has played a crucial role in system optimization. Kim and Park [8] optimized Mcycle heat exchanger geometry, while Sharma et al. [9] developed novel control strategies. Rodriguez et al. [10] investigated the integration of renewable energy sources. Challenges remain, including thermal storage integration [11] and the development of compact, cost-

effective designs [12]. Previous research highlights opportunities for future research in this evolving field, focusing on enhancing efficiency, expanding applicability, and improving sustainability of Mcycle-based cooling systems.

This study builds on previous work by extending the analytical model to a three-stage regenerative M-cycle HMX integrated with a desiccant system using TRNSYS. The research focuses on optimizing performance by adjusting HMX parameters to improve the thermal comfort and population satisfaction, helping to establish a framework for real-world applications and contributing to the development of sustainable HVAC systems for hot and humid climates.

2. METHODOLOGY

Numerical Framework

The SDMC system is modelled to analyze thermal performance, airflow, and energy efficiency. The desiccant dehumidifies the incoming air, and the M-cycle enhances cooling through indirect evaporative processes. Simulations focus on heat and mass transfer, airflow distribution, and system efficiency under varying climatic conditions. In current, numerical framework, the analytical model implemented in Python and combined with the desiccant system simulation in TRNSYS for the humid subtropical temperature zone of Taxila city as shown in

figure 1. This integrated approach allows for a holistic understanding of the mechanism of entire system.

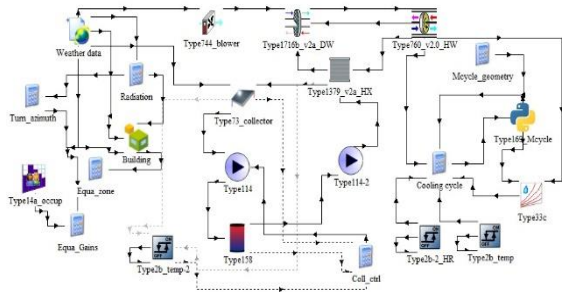


Figure 1: TRNSYS Simulation Model of a Solar Desiccant- Maisotsenko Cycle Cooler

M-cycle Modelling

The mathematical model for the M-cycle, based on Dizaji et al [3] work, adapts a single-stage M-cycle to a perforated cooler. In this setup, supply air is slowly released into wet channel. As shown in Figure 2, dry air portions (ϵ_a , ϵ_b , and ϵ_c) are released at points A, B, and C. These fractions are defined as $\epsilon_a = \dot{m}_{1A} / \dot{m}_1'$, $\epsilon_b = \dot{m}_{1B} / \dot{m}_1'$, and $\epsilon_c = \dot{m}_{1C} / \dot{m}_1'$, with the condition $\epsilon_a + \epsilon_b + \epsilon_c < 1$.

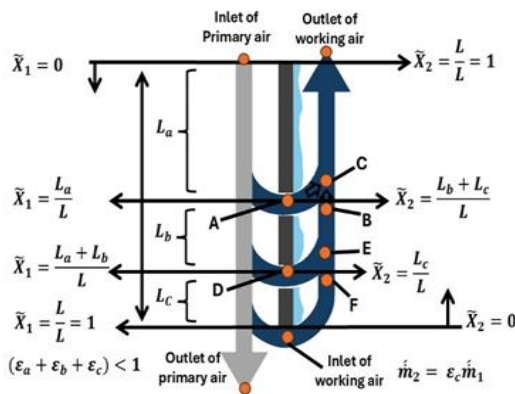


Figure 2: 1-D view of Three Stage dual perforated M-Cycle heat exchanger

In a multistage M-cycle exchanger thermodynamic properties (T, W , and \dot{m}) are specified for every stage. The inlet air (T_1') undergoes sensible cooling inside dry channel, exiting at a lower temperature (T_1'') but with unchanged humidity. A portion of this air becomes the product air, while the working air in wet channel cools further through sensible and latent cooling. This results in a notable temperature drop and increased humidity. The working air exits the system through dual outlets: one for the vented air and one for the conditioned product air.

Analytical Model

The analytical model extends Dizaji et al.'s work to a three-stage regenerative M-cycle heat and mass exchanger

(HMX), incorporating perforation, multiple stages, and regenerative design. Key equations derived from thermodynamics and fluid dynamics address energy balance, mass transfer, perforation effects, and regenerative staging to enhance cooling efficiency. Also, in developing this analytical model, key assumptions include one dimensional steady-state operation, negligible heat losses, and uniform water film thickness. A significantly higher flow rate of sprayed water is considered to keep plate surfaces fully wet.

The analytical model builds up on the fundamental laws of heat transfer. The counter-flow arrangement is considered in this model. The model accounts for both sensible and latent heat transfer processes occurring simultaneously in the cooler. The key governing equations of the system are as follows;

Heat Balance Equations:

Dry Channel: $\dot{Q}_{dry} = \dot{m}_{dry} \cdot (h_1 - h_2)$ (1)

Wet Channel: $\dot{Q}_{wet} = \dot{m}_{wet} \cdot (h_3 - h_4)$ (2)

Overall: $\dot{Q}_{total} = \dot{Q}_{dry} + \dot{Q}_{wet}$ (3)

Mass Balance Equations:

Mass Balance (Dry): $\dot{m}_{dry} = \dot{m}_{in} - \dot{m}_{out}$ (4)

Mass Balance (Wet): $\dot{m}_{wet} = \dot{m}_{in} + \dot{m}_{evap} - \dot{m}_{out}$ (5)

Energy Distribution:

Sensible Heat Transfer:

$\dot{Q}_{sensible} = \dot{m}_{air} \cdot c_p \cdot (T_{in} - T_{out})$ (6)

Latent Heat Transfer:

$\dot{Q}_{latent} = \dot{m}_{water} \cdot h_{fg}$ (7)

Total Energy:

$\dot{Q}_{total} = \dot{Q}_{sensible} + \dot{Q}_{latent}$ (8)

Optimization Approach

The optimization methodology aims to enhance wet-bulb and dew-point effectiveness by analyzing the effects of inlet air conditions, channel, perforation characteristics, and the number and configuration of stages. The geometrical parameters of a M-cycle channel for the base case are obtained from a previous study Dizaji et al. [3], which are optimized for the lower and upper bounds, as given in the Table 4. The flow rate of supply air was set to 0.14 kg/s with 35 channels in the base case. Key output parameters from the model include temperature and absolute humidity at channel outlets, wet-bulb effectiveness, cooling capacity and dew-point effectiveness. Figure 3 describes the optimization workflow approached for this case.

Table 1: Parameters for base case and optimization

Parameters	Base case	Optimization	
		Lower bound	Upper bound
L_a (m)	0.231	0.10	0.40
L_b (m)	0.231		
L_c (m)	0.231		
ϵ_a	0.06	0.05	0.20
ϵ_b	0.06		
ϵ_c	0.06		

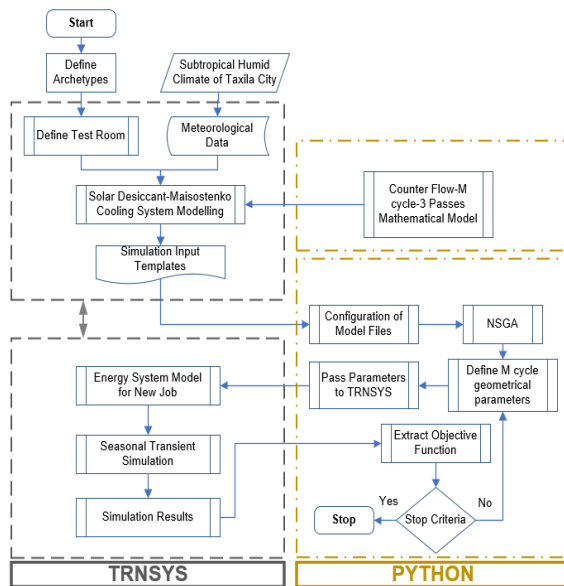


Figure 3: Workflow Diagram for Integrated TRNSYS-Python Co-Simulation of SDMC

3. RESULTS AND DISCUSSION

Initially, results of base case are analyzed to establish a reference point. Following this, an optimization process is carried out, and the outcomes are compared with the base case to demonstrate the improvements achieved.

A. Thermal Performance of SDMC base case:

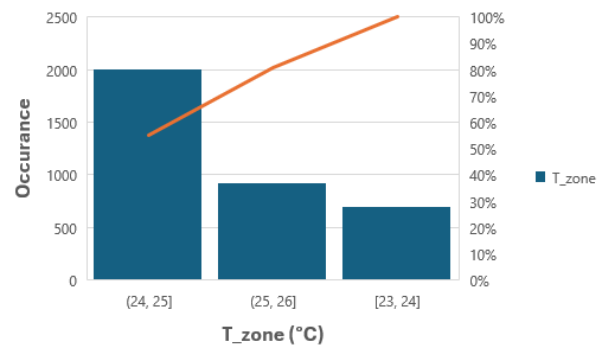


Figure 4: Zone Temperature of Base case

The simulation results show the process enters the dry channel with temperature varying between 38°C and 44°C during the months from May to September, which are categorized hot and humid weather months in humid subtropical zones such as Taxila city in Pakistan. In base case, the product air coming out of the dry channel and entering the zone is maintained at an average value of 23°C, that falls within the typical range for indoor thermal comfort. Also, the humidity ratio remains constant (0.01kg/kg) as the air passes through dry channel. Maximum wet-bulb effectiveness is noted to be 0.967, dew point effectiveness is 0.933 and cooling capacity for base case achieved to be 3.83kW.

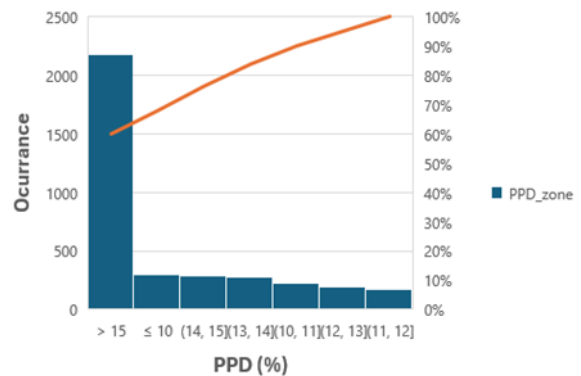


Figure 5: PPD for base case

B. Zone Temperature and predicted percentage of dissatisfied (PPD) index of base case:

The simulation illustrates the thermal performance of SDMC. Figure 4 illustrates the frequency of zone temperatures, with the cooler most often operating in the (24, 25) °C range. Although fewer occurrences are seen at lower temperatures like [23, 24] °C, the system's performance improves as temperature decreases, as indicated by the rising percentage trend.

The Predicted Percentage of Dissatisfied (PPD) can be seen in figure 5. It shows that most instances occur with a PPD greater than 15%, indicating significant dissatisfaction with thermal comfort. However, as the PPD decreases, the system performs better, improving thermal satisfaction.

C. Optimization for enhanced performance of SDMC

The performance optimization of SDMC was carried out by using a genetic algorithm (GA). Over 3000 iterations, the algorithm minimized the penalty function to 33.4 kW, demonstrating significant improvement in system efficiency.

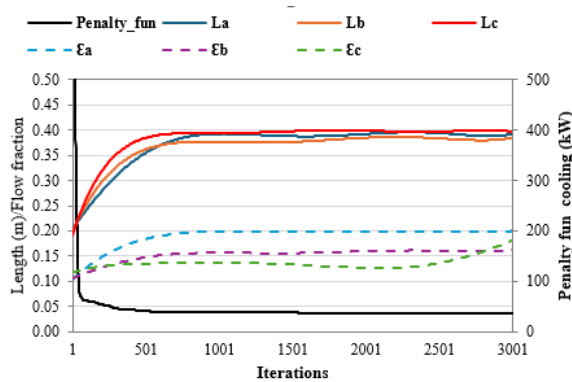


Figure 6: Convergence of penalty function, channel lengths (L), and errors (E) for a three-stage M-cycle heat exchanger

The optimization targeted key design variables—heat exchanger lengths (L_a , L_b , and L_c) emissivity values (ϵ_a , ϵ_b and ϵ_c) which converged to 0.38, 0.38, 0.40 for lengths and 0.17, 0.20, 0.16 for emissivity, respectively.

The graph in figure 6 illustrates a clear stabilization of these variables, highlighting the GA's ability to fine-tune the system's design for optimal performance. The final fitness score of 33.4 kW, achieved within a computing time of 51419 seconds, confirms the GA's effectiveness in handling this complex multi-variable optimization problem.

D. Integrated Assessment of optimized thermal performance and user comfort in the SDMC:

The optimized results show that the temperature of product air is maintained at an average of 20.55°C.

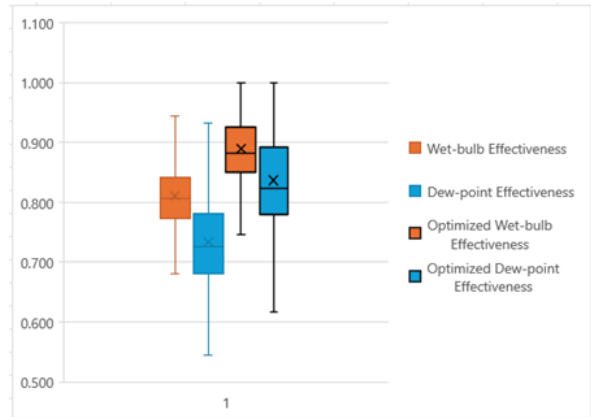


Figure 7: Effectiveness comparison of base case with optimized case.

Figure 7 compares effectiveness of base case with optimized case. Maximum values have increased from 0.967 and 0.933 to 1. The cooling capacity has also improved to 4.35 kW as shown in figure 8.

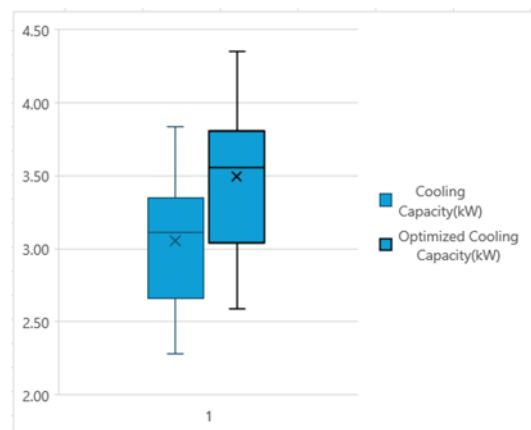


Figure 8: Cooling capacity of base case vs optimized

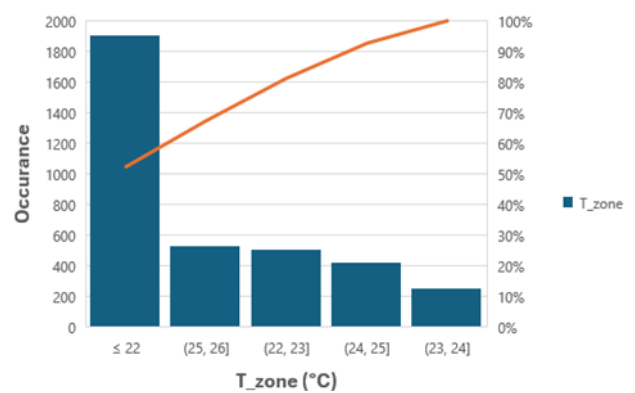


Figure 9: Optimized Zone temperature

Figure 9 depicts the temperature distribution of the desiccant M-Cycle indirect evaporative cooler across four zones: $\leq 22^{\circ}\text{C}$, $[24, 25]^{\circ}\text{C}$, $(25, 26]^{\circ}\text{C}$, and $[23, 24]^{\circ}\text{C}$. The cooler primarily operates at temperatures $\leq 22^{\circ}\text{C}$, with fewer occurrences in higher ranges. The orange cumulative percentage line shows enhanced efficiency at lower temperatures. User satisfaction has improved significantly, with over 1400 instances in the low PPD range ($\leq 6\%$), indicating minimal dissatisfaction as shown in figure 10. The cumulative percentage for PPD values $\leq 15\%$ nears 100%, ensuring almost all users are within acceptable comfort levels.

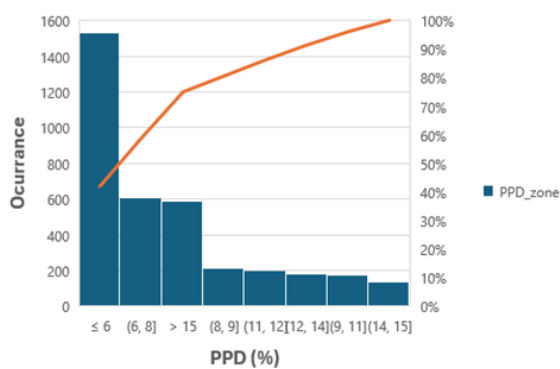


Figure 10: Optimized PPD

4. CONCLUSION

The base and optimized case results of SDMC reveal substantial improvements in both system efficiency and user comfort. The penalty function was minimized to 33.4 kW during optimization, reflecting a significant reduction of 47% in cooling penalties associated with system incapability. This improvement was achieved through the optimization of heat exchanger lengths and emissivity values using a genetic algorithm.

As a result, thermal performance indicators of M-cycle, such as wet-bulb effectiveness reached a maximum of 1 and dew-point effectiveness also improved to maximum value of 1.0. The maximum cooling capacity increased from 3.83 kW to 4.35 kW. Additionally, user satisfaction saw a marked improvement, with a shift in the PPD distribution toward lower values. Over 1400 occurrences now fall in the low PPD range ($\leq 6\%$), indicating that most users experience minimal discomfort. The cumulative percentage for PPD values $\leq 15\%$ quickly approaches 100%, suggesting that almost all users are within acceptable comfort levels post-optimization. These findings demonstrate that through effective optimization, the cooler can maintain higher efficiency while providing enhanced thermal comfort for users, particularly in challenging hot and humid climates.

REFERENCES

- Maisotsenko, V., Gillan, L. E., Heaton, T. L., & Gillan, A. D. (2003). Method and plate apparatus for dew point evaporative cooler. U.S. Patent No. 6,581,402. Washington, DC: U.S. Patent and Trademark Office.
- Zhang, L., Wang, Y., & Chen, J. (2023). Comparative analysis of energy efficiency in Mcycle indirect evaporative coolers and conventional vapor compression systems. *Energy Conversion and Management*, 277, 116512.
- Dizaji, H. S., Hu, E. J., Chen, L., & Pourhedayat, S. (2020). Development and validation of an analytical model for perforated (multi-stage) regenerative M-cycle air cooler. *Applied Energy*, 228, 114816.
- Wang, Y., Chen, J., & Liu, H. (2022). Optimization of heat and mass transfer in Mcycle indirect evaporative coolers. *International Journal of Heat and Mass Transfer*, 194, 123015.
- Li, J., Wang, X., & Zhang, L. (2023). Advanced heat and mass transfer processes in Mcycle indirect evaporative coolers. *Applied Thermal Engineering*, 218, 119352.
- Chen, X., & Liu, Y. (2024). Performance analysis of hybrid Mcycle solid desiccant cooling systems in diverse climates. *Energy and Buildings*, 280, 112567.
- Patel, R., Singh, S., & Kumar, A. (2023). Novel desiccant materials with enhanced moisture adsorption for hybrid Mcycle cooling systems. *Applied Energy*, 331, 120325.
- Kim, S., & Park, J. (2024). CFD-based optimization of Mcycle heat exchanger geometry for enhanced thermal performance. *International Journal of Heat and Mass Transfer*, 203, 123789.
- Sharma, V., Gupta, R., & Verma, S. (2023). Innovative control strategies for optimizing Mcycle cooling system performance. *Energy Conversion and Management*, 278, 116674.
- Rodriguez, C., Martinez, A., & Lopez, J. (2024). Integration of renewable energy sources with Mcycle cooling technologies. *Renewable Energy*, 210, 114680.
- Hassan, M., & Ahmed, K. (2023). Thermal storage integration in Mcycle cooling systems: Challenges and opportunities. *Journal of Energy Storage*, 55, 105787.
- Yamamoto, T., Suzuki, K., & Tanaka, N. (2024). Development of compact and cost-effective Mcycle cooling systems for residential applications. *Energy*, 270, 126870.

Unmanned Under Water Vehicle (UUV) Pressure Hull Design using Composite Materials

Muzammal Hussain^{1*}, Riffat Asim Pasha¹, Aneela Wakeel¹, Muhammad Ammar Akram²

¹University of Engineering and Technology Taxila

²Mechanical Engineering Department, HITEC University Taxila

*muzammalh280@gmail.com

ABSTRACT

Unmanned Underwater Vehicles (UUVs) play a critical role in underwater warfare and exploration, traditionally relying on steel or aluminum pressure hulls. This project compares two pressure hull designs, one constructed from steel HY100 and the other from carbon fiber-reinforced epoxy composites. While steel offers high stiffness for deep-water operations, it presents a problematic magnetic signature. In contrast, aluminum is less suited for significant depths, and composite materials emerge as a superior alternative, featuring non-magnetic properties, high stiffness-to-weight ratios, and low density. The pressure hulls, both with identical dimensions (300 mm diameter, 1000 mm length) and designed without dish ends, feature internal rectangular ring stiffeners. Under 3 MPa external pressure (simulating 300 meters depth), ANSYS simulations assessed their structural performance and buckling behavior. Results showed the composite hull, though significantly lighter than the steel version, had comparable or superior buckling resistance, allowing for greater operational depths and improved stress distribution under pressure. Despite the potential trade-offs in durability and maintenance particularly regarding impact damage and delamination. This Project highlights the advantages of using carbon fiber-reinforced epoxy composites for UUV applications. The findings underscore the viability of composites in enhancing the performance and capabilities of underwater vehicles.

KEYWORDS: Submarine Pressure hull, HY100 Steel, Carbon Fiber, Buckling Analysis.

1. INTRODUCTION

Underwater vehicles, such as AUVs and HOVs, use cylindrical pressure shells to withstand deep-sea pressures [1]. Composites provide an attractive alternative due to their high strength-to-weight ratio and corrosion resistance, crucial for underwater applications. Large composite structures further require precise fiber alignment, void minimization, and dimensional stability to prevent warping, each of which can be achieved through controlled curing techniques and vacuum infusion processes. [2]. Temme (2003) compared analytical solutions from two classification society design rules with experimental results to predict failure modes in ring-stiffened cylindrical shells [3]. Radha (2006) examined the ultimate strength of submarine pressure hulls under inelastic buckling, evaluating three approaches: Johnson-Ostenfeld inelastic correction, the imperfection method, and finite element analysis (FEA). They found that Johnson-Ostenfeld's predictions closely matched FEA results, though deviations occurred in ring-stiffener failure predictions [4]. Graham (2007) assessed non-linear elastic-plastic collapse of ring-stiffened cylinders, comparing experimental and FEA models that accounted for real-world imperfections, achieving a prediction accuracy within 6% [5]. Azarafza et

al. (2009) utilized a Multi-Objective Genetic Algorithm (MOGA) for multi-objective optimization to reduce the structural weight and dynamic response of composite cylindrical shells [6]. Sadeghi Far et al. (2010) and Bagheri et al. (2011) introduced stiffeners to composite cylindrical shells under axial loading, both employing MOGA to minimize weight, with Sadeghi Far exploring various stiffener types and configurations, while Bagheri focused on optimizing ring-stiffened designs [7]. Firl and Bletzinger (2012) investigated shape optimization of thin-walled structures using FEA and the Conjugated Gradient Method. They analyzed three unstiffened models: a flat square plate, a tunnel shell, and an elliptical bulkhead, successfully enhancing load-carrying capacity while simplifying the FE models [8]. Keulen (2013) developed a standardized modeling procedure for predicting collapse pressure in submarine hulls, introducing a partial safety factor and demonstrating that a less conservative safety factor could be achieved with high confidence [9]. Ghasemi and Haji Mohammad (2017) optimized composite cylindrical shells under external hydrostatic pressure using the NSGA-II algorithm to minimize weight and cost while maximizing collapse pressure [10]. Imran et al. (2020) focused on optimizing submerged cylindrical pressure hulls with MOGA to minimize buoyancy and maximize

collapse pressure capacity, setting fiber orientation and material properties while varying laminate ply layers [11]. Imran et al. (2021) optimized an egg-shaped composite pressure hull by minimizing the buoyancy factor through a genetic algorithm, validating

the model with non-linear buckling FEA [12]. Yang et al. (2022) developed a novel aluminum ring- stiffened arched cylindrical hull, also minimizing the buoyancy factor using an evolutionary algorithm and validating with FEA [13]. Gao et al. (2023) optimized a rib- reinforced ultra-thick composite pressure hull using NSGA-II, first maximizing bearing capacity through geometry optimization and then minimizing buoyancy by adjusting thickness in various regions [14]. Heuristic optimization of stiffened cylindrical shells has mainly focused on composites due to their adaptable properties, such as fiber orientation and layer count, offering greater optimization flexibility than metals [15]. Additionally, composite construction methods enhance their suitability for optimization. The composite material for a UUV pressure hull offers advantages over traditional materials like steel, aluminum including higher strength-to-weight ratio, corrosion resistance, and customizability in layer orientation to handle specific stresses. Although it may have higher cost, complex manufacturing [16].

2. METHODOLOGY

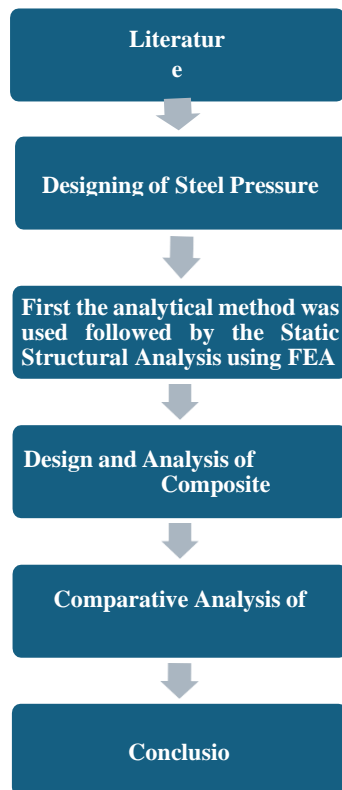


Figure 1: Methodology Flow Chart

This project evaluates and compares the performance of structural steel and composite materials in marine hull design. It starts with designing a structural steel hull using traditional analytical methods, followed by validation through static structural analysis in ANSYS Workbench 2023 to assess deformation and stress distribution. Next, a composite hull using carbon fiber-reinforced polymers is developed and analyzed under identical conditions. The comparison focuses on durability, buckling behavior, and weight efficiency, aiming to identify the optimal hull construction. The findings will guide vessel design decisions, enhancing safety and performance in marine environments.

Hull Geometry and Properties:

In this study, the pressure hull is designed as a cylindrical structure with both a steel and composite shell for comparison. Each shell has a diameter of 300 mm, a length of 1000 mm, and a thickness of 2.08 mm, reinforced by internal rectangular ring stiffeners with a width of 8.5 mm, a height of 17 mm, spaced at 250 mm intervals along the length. The composite shell consists of 7 layers [45/90]°, designed to provide enhanced strength and weight efficiency under external pressure, with the same stiffener arrangement for structural reinforcement.

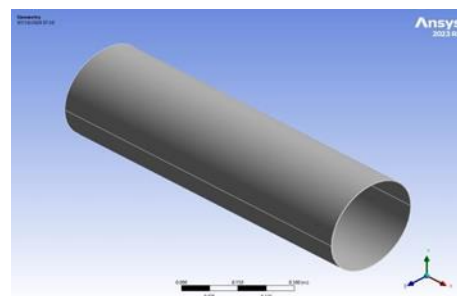


Figure 2: Steel Hull

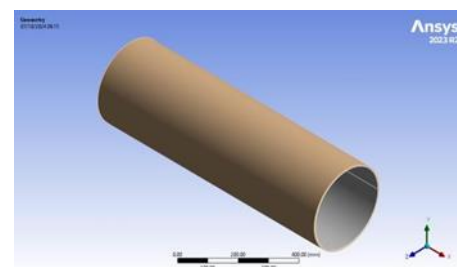


Figure 3: Composite Hull

Mesh and Boundary Conditions

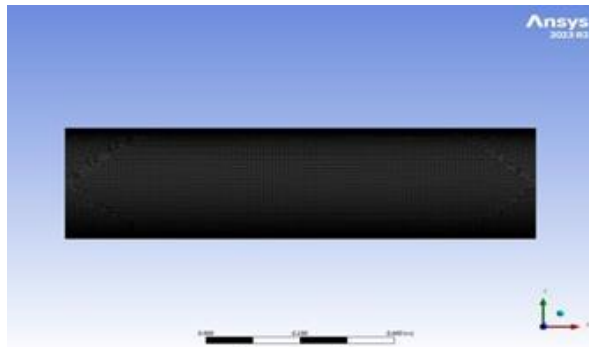


Figure 4: Mesh (Quad)

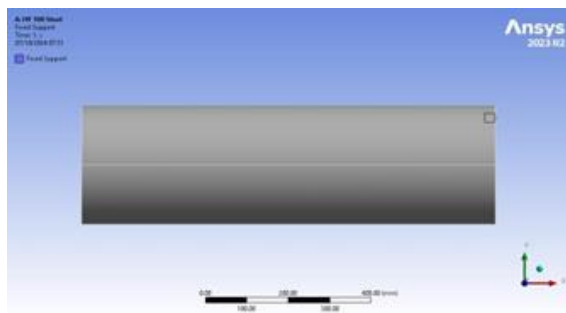


Figure 5: BC (Fixed at both ends)

A structured mesh with quadrilateral elements was applied to the cylindrical shell to accurately capture stress distribution and deformation. Boundary conditions were imposed by fixing both ends of the shell, restricting displacement and rotation to real-world constraints under external pressure.

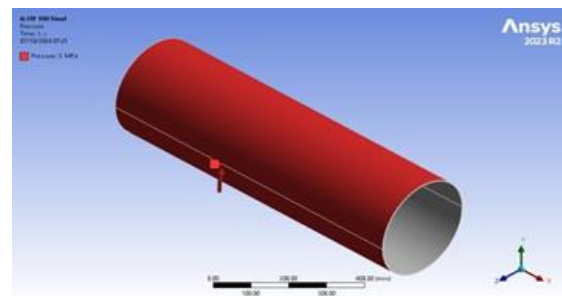


Figure 6: Applied Pressure

Table 1: Design Parameters

	HY100	Carbon fibers
Length of cylindrical shell	L=1000mm	L=1000mm
Thickness of shell	s=2.08mm s=7*0.5=3.5mm	
Diameter of shell	D= 300mm	D= 300mm
Height of Stiffener Ring	h=17mm	h=17mm
Mean radius of wall	R= 149mm	R= 147.21mm
External pressure	p=3 N/mm ²	p=3 N/mm ²
Length between Stiffeners	L1=250mm	L1=250mm
Weight	W= 16.5KG	W= 9.7KG

Mathematical Model

I. Number of stiffeners: $N_s = \frac{L}{a}$ (2.1)

II. Stiffener Spacing (a): $a = \sqrt{\frac{Rt}{p.k}}$ (2.2)

III. Shell thickness: $t = \frac{p.R}{f.\eta}$ (2.3)

IV. Mean radius: $R = \text{Outer radius} - \frac{t}{2}$ (2.4)

V. Deformation: $\delta = \frac{p.D^2}{64.E.t^3}$ (2.5)

VI. Directional Deformation Along X-axis (u_x):

$$u_x = \frac{px.L}{AE} + \frac{Mx.y}{EI} + \Delta_{\text{stiffener}} \quad (2.6)$$

- Axial Deformation: $\frac{px.L}{AE}$
- Bending Deformation: $\frac{Mx.y}{EI}$

**Deformation Contribution from Ring
Stiffeners (Δ stiffeners):**

$$\Delta_{stiffener} = \Sigma \left(\frac{Fs.hs}{As.E} \right)$$

VII. Mass = $M_{shell} + M_{Stiffener}$ (2.7)
 $M_{shell} = \rho \cdot \pi \cdot D \cdot t \cdot L$

$$M_{str} = n \cdot \rho \cdot A_{str} \cdot L_{str}$$

VIII. Equivalent Elastic Strain

$$\epsilon = \frac{p \cdot \left(\frac{D}{2}\right)}{t \cdot E} \quad (2.8)$$

IX. Critical Buckling Pressure

$$P_{cr} = \frac{2E}{3(1-\nu^2)} \cdot \left(\frac{t}{R}\right)^3 \quad (2.9)$$

Composite Material

The mechanical performance of the composite pressure hull is analyzed using Classical Laminate Theory (CLT), which provides a theoretical framework for understanding the behavior of multilayered composite materials.

I. Hoop stress (σ_h):

$$\sigma_h = \frac{p \cdot R}{t_{total}} \quad (2.10)$$

II. Longitudinal Stress (σ_L):

$$\sigma_L = \frac{p \cdot R}{2 \cdot t_{total}} \quad (2.11)$$

III. Von Mises stress (σ_{vm}):

$$\sigma_{vm} = \sqrt{\sigma_h^2 + \sigma_L^2 - \sigma_h \cdot \sigma_L} \quad (2.12)$$

IV. Mass of Composite Hull:

$$M_{total} = M_{shell} + M_{stiffeners}$$

$$M_{shell} = \rho_c \cdot \pi \cdot D \cdot (t_{shell} + t_{layers}) \cdot L$$

$$M_{str} = n \cdot \rho_{stiffener} \cdot b \cdot h \cdot (\pi \cdot D)$$

V. Equivalent Elastic Strain:

$$\epsilon = \frac{\sigma}{E_{composite}} \quad (2.13)$$

VI. Total Deformation:

$$\delta = \epsilon \cdot L \quad (2.14)$$

X. Stress Calculation for Each Ply:

The stress in the layers of a composite laminate is calculated using the relationship between the material properties and the applied load.

$$\sigma_i = [\sigma_x \cdot \sigma_y \cdot \tau_{xy}]_i = Q_i \cdot \epsilon_i \quad (2.15)$$

Hashin's Criterion

The failure criterion selected for the numerical analysis is the Hashin Criterion, which serves as the damage initiation criterion for fiber-reinforced composites in ANSYS. This criterion evaluates four distinct damage initiation mechanisms fiber tension, fiber compression, matrix tension, and matrix compression. Criticality of tensile loads in the fiber direction ($\sigma_{11} \geq 0$) is predicted with the expression. Under compressive loads in the fiber direction ($\sigma_{11} < 0$), failure is predicted with an independent stress condition (for both 2D and 3D):

$$f = (\sigma_{11}/X_C)^2 \quad (2.16)$$

In the case of tensile transverse stress ($\sigma_{22} + \sigma_{33} \geq 0$), the expression for predicting matrix failure is:

$$f_m = \left(\frac{1}{Y_T}\right)^2 * (\sigma_{22}^2 + \sigma_{33}^2) * \left(\frac{1}{S_{23}}\right)^2 * (\tau_{23} + \sigma_{22} * \sigma_{33}) + \left(\frac{1}{S_{12}}\right)^2 * (\tau_{12}^2 + \tau_{13}^2) \quad (2.17)$$

The following expression is used when the transverse stress is compressive ($\sigma_{22} + \sigma_{33} < 0$):

$$f_m = \left(\frac{1}{Y_C}\right) * \left[\left(\frac{Y_C}{2 * S_{23}}\right)^2 - 1\right] * (\sigma_{22} + \sigma_{33}) + \left(\frac{1}{2 * S_{23}}\right)^2 * (\sigma_{22} + \sigma_{33})^2 + \left(\frac{1}{S_{23}}\right)^2 * (\tau_{23}^2 + \sigma_{22} * \sigma_{33}) + \left(\frac{1}{S_{12}}\right)^2 * (\tau_{12}^2 + \tau_{13}^2) \quad (2.18)$$

In addition, and optionally, the following expression is an out-of-plane version of the Hashin's Criterion that predicts delamination (tension and compression)

$$f_d = \left(\frac{\sigma_{33}}{Z_i}\right)^2 + \left(\frac{\tau_{13}}{S_{13}}\right)^2 + \left(\frac{\tau_{23}}{S_{23}}\right)^2, i =$$

$$C \text{ if } \sigma_{33} < 0, i = T) \quad (2.19)$$

Safety Factor

The safety factors for the design of composite material shell are determined by the Bureau Veritas Regulations, each safety factor is influenced by various coefficients that account for factors such as material aging, the fabrication process, and other material-related considerations.

More specifically, for material failure, the safety factor is defined as follows:

$$SF = CCS * CF * CV * Ci \quad (2.20)$$

And for buckling, the safety factor is

$$SF_{buck} = C_{buck} * CF * CV * Ci \quad (2.21)$$

CCS: is the coefficient for combined stresses

C_{buck}: is the buckling coefficient

CF: is the coefficient related to the fabrication process and reproducibility.

CV: is the coefficient related to the ageing effect of the composite materials.

Materials Properties of Steel And Composite Hull

Table 2: Steel hull properties

Material	HY 100 Steel
Young Modulus (MPa)	207000
Poisson's Ratio	0.3
Density (Kg/m ³)	7890
Ultimate Strength (MPa)	739.5
Compressive Yield Strength (MPa)	690

Table 2 shows the properties of hull, made of HY 100 steel, is characterized by high stiffness, excellent strength, and density, making it highly suitable for withstanding deep-sea pressures. Its mechanical properties ensure durability and resistance to failure under extreme conditions.

Table 3: Properties of the Carbon Fiber

CFRP	Fiber	Carbon Fiber (230)
	Matrix	Epoxy Resins
Elastic Modulus	E1	230000
	E2	23000
	E3	23000
Poisson's ratio	V12	0.2
	V13	0.4
	V23	0.2
Shear Modulus	G12	9000MPa
	G13	8214.3 MPa
	G23	9000
Tensile Strengths	XT	750MPa
	YT	40MPa
	ZT	25MPa

Table 4: Properties of Epoxy Resins

Material	Epoxy Resins
Density γ [g/cm ³]	1.20
Poisson's Ratio	0.37
Young Modulus E[MPa]	3000
Tensile Strength σ_r [MPa]	85
Compressive Strength σ_c [MPa]	130

Table 3 and 4 outline the properties of carbon fiber and epoxy resin, offers high stiffness and strength, ideal for reinforcing stressed structures. Epoxy resin, with a lower tensile modulus of 3 GPa, provides durability, environmental resistance, and effective stress transfer

between fibers. Combined, these materials deliver high performance, making them suitable for lightweight, strong pressure hulls in underwater vehicles.

3. RESULTS AND DISCUSSION

This project focuses on comparing the structural performance of HY100 steel and carbon fiber composite pressure hulls using ANSYS simulations. Key parameters like total deformation, directional deformation, elastic strain, and weight were analyzed under external pressure. Additionally, the buckling behavior of both materials was studied to determine their resistance to failure at high depths. The findings aim to provide insights into the advantages and trade-offs of using composites in underwater vehicle applications.

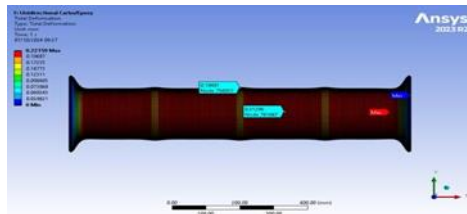


Figure 7: Total deformation in pressure hull constructed from HY100 Steel

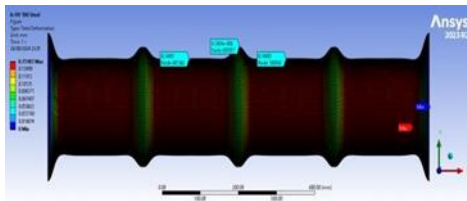


Figure 8: Total deformation in pressure hull

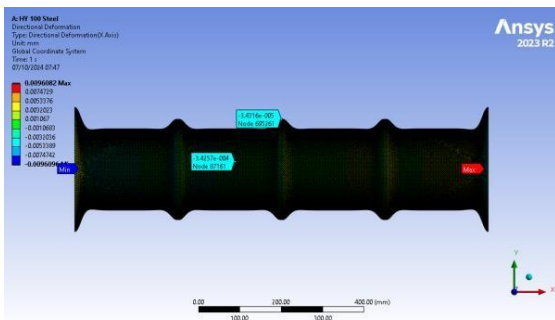


Figure 9: Directional Deformation along X-axis in pressure hull constructed from HY100 Steel

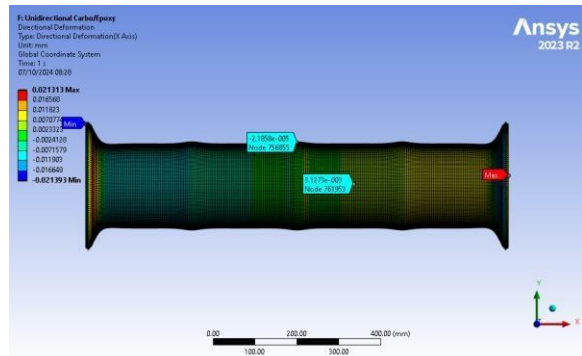


Figure 10: Directional Deformation along X-axis in pressure hull constructed from Carbon Fiber

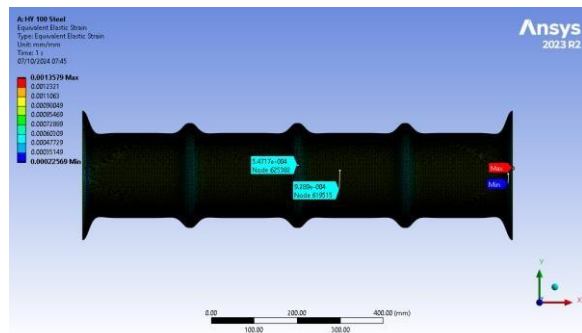


Figure 11: Equivalent Elastic Strain in pressure hull constructed from HY100 Steel

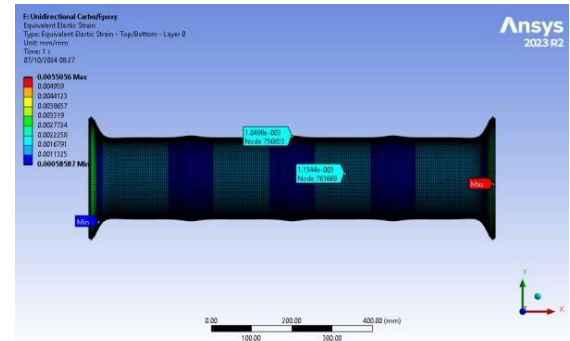


Figure 12: Equivalent Elastic Strain in pressure hull constructed from Carbon Fiber

Table 5: Properties of the Carbon Fiber

Material	Total Deformation (mm)	Directional Deformation X-axis (mm)	Mass (KG)	Elastic Strain
HY100 Steel	0.1518	0.0096	16.492	0.0014
Carbon Fiber	0.2215	0.0213	9.778	0.0055

Table 3 illustrates the differences in deformation characteristics between carbon fiber and HY100 steel. Carbon fiber exhibits greater total deformation, measuring

0.2215 mm, compared to HY100 steel's lower total deformation of 0.1518 mm. Similarly, the directional deformation along the X-axis for carbon fiber is 0.0213 mm, while HY100 steel shows only 0.0096 mm. This indicates that carbon fiber is more adaptable and can withstand larger deformations under similar loading conditions, making it a favorable choice for applications requiring flexibility. Moreover, the significantly lighter weight of carbon fiber, at 9.778 kg, contrasts with HY100 steel's 16.492 kg, enhancing payload capacity and efficiency in structural applications. The higher elastic strain of carbon fiber, measured at 0.0055, compared to 0.0014 for HY100 steel, reflects its ability to endure substantial deformation before returning to its original shape. While this property is advantageous in terms of flexibility, it also necessitates careful consideration when used in high-pressure environments. In such conditions, the material's strain tolerance could affect long-term durability and structural integrity. Thus, while carbon fiber presents numerous benefits, its performance in extreme conditions must be thoroughly evaluated to ensure reliability and safety.

Buckling of Hulls:

As the hydrostatic pressure increased, the cylindrical structure gradually lost stability. The failure mode resulting from the combination of material and geometric nonlinearities may differ from the predictions of linear buckling analysis.

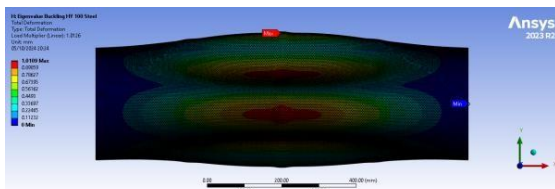


Figure 13: Buckling mode 1 for Steel Hull

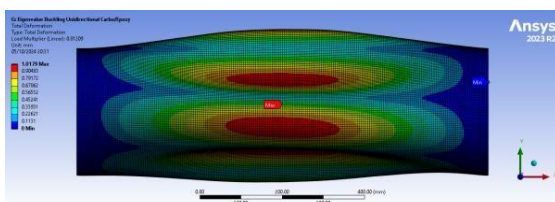


Figure 14: Buckling mode 1 for Composite Hull

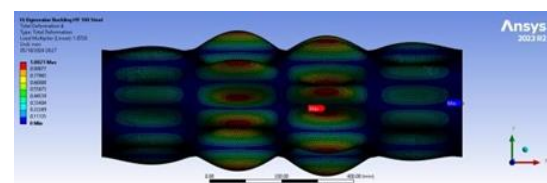


Figure 15: Buckling mode 6 for Steel Hull

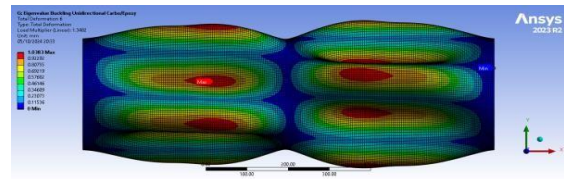


Figure 16: Buckling mode 6 for Composite Hull

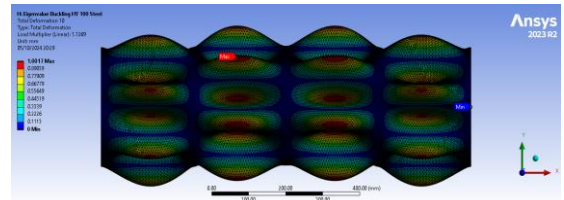


Figure 17: Buckling mode 10 for Steel Hull

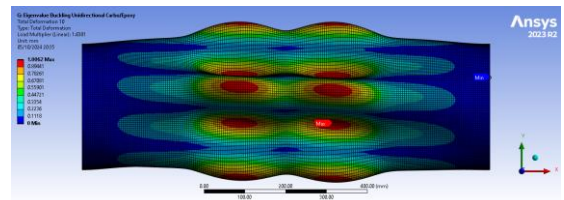


Figure 18: Buckling mode 10 for Composite Hull

Table 6: Buckling mode (Steel)

Steel Shell	
Eigenvalue number	Value
1	1.0109
2	1.0108
3	1.0302
4	1.0001
5	1.0019
6	1.0021
7	1.024
8	1.0011
9	1.0002
10	1.0017

The eigenvalues for steel show lower variation. In contrast, the composite values show more variation. The higher eigenvalues for composite materials suggest that while they can resist buckling, they are more prone to deformation. Steel, being stiffer, demonstrates more consistent performance, while the composite offers more flexibility but is more susceptible to mode shifts under pressure.

Table 7: Buckling mode (Composite)

Composite Shell	
Eigenvalue number	Value
1	1.0179
2	1.0181
3	1.0022
4	1.0493
5	1.0011
6	1.0383
7	1.0146
8	1.0146
9	1.0074
10	1.0062

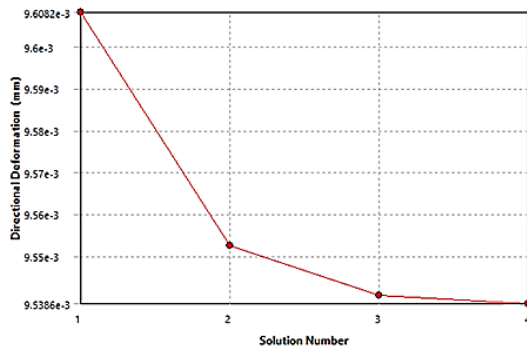


Figure 19: Directional Deformation

Table 8: Convergence of Dir. Deformation

	Directional Deformation (mm)	Change (%)	Nodes	Elements
1	9.6082e-003		725675	364095
2	9.5525e-003	-0.58182	1391053	779187
3	9.5406e-003	-0.12409	4665511	3024727
4	9.5386e-003	- 2.14 49e-002	1670597 8	11685488

The convergence graph and table show decreasing directional deformation as the mesh is refined. With an increasing number of nodes and elements, the changes in deformation become minimal, indicating improved accuracy. The percentage change reduces significantly with finer meshes, demonstrating stable convergence towards an accurate solution.

4. CONCLUSIONS

This research presents a comprehensive comparative analysis of pressure hulls made from HY100 steel and carbon fiber composite using ANSYS simulations. The findings reveal that carbon fiber composites exhibit distinct advantages over traditional steel in key performance areas

1. The composite hull showed higher total deformation (0.2215 mm) compared to the steel hull (0.1518 mm), indicating greater flexibility.
2. Directional deformation along the X-axis was also higher for the composite (0.0213 mm) than steel (0.0096 mm), allowing it to endure greater bending or deflection under pressure without structural failure.
3. Carbon fiber composite hulls are significantly lighter, with a mass of 9.778 kg, compared to 16.492 kg for the steel hull.
4. The composite hull displayed superior equivalent elastic strain (0.0055) compared to the steel hull (0.0014), highlighting its capacity to absorb and withstand higher deformation before experiencing permanent damage.

Carbon fiber composites offer a compelling alternative to HY100 steel for advanced marine technology applications. Their superior strength-to-weight ratio, enhanced flexibility, and sufficient buckling resistance make them highly effective for deep-sea operations. These characteristics position carbon fiber composites as a transformative material for the next generation of underwater vehicles, advancing performance, efficiency, and innovation in marine engineering.

REFERENCES

1. Lee, K. Y. "Advances in AUV Design: Material Selection and Structural Integrity." Proceedings of the International Conference on Underwater Technology, Tokyo, Japan, 2021, pp. 75-80. IEEE,
2. Yang, Y., and Zhang, X. "Geometric Imperfections and Buckling Analysis of Thin-Walled Cylinders." Proceedings of the ASME 2019 Pressure Vessels and Piping Conference, San Antonio, Texas, 2019, pp. 1-9. ASME.
3. Temme, W., 2003. Comparison of Analytical and Numerical Approaches for Determining Failure of Ring-Stiffened Cylindrical Shells. Massachusetts Institute of Technology
4. Radha, P., Rajagopalan, K., 2006. Ultimate Strength of Submarine Pressure Hulls with Failure Governed by Inelastic Buckling. Thin-Walled Structures 44, 309-313.
5. Graham, 2007. Predicting the Collapse of Externally



- Pressurized Ring- Stiffened Cylinders using Finite Element Analysis. *Marine Structures* 20, 202–217.
6. Azarafza, R., Khalili, S., Jafari, A.A., Davar, A., 2009. Analysis and Optimization of Laminated Composite Circular Cylindrical Shell Subjected to Compressive Axial and Transverse Transient Dynamic Loads. *Thin- Walled Structures* 47, 970–983.
 7. Sadeghifar, M., Bagheri, A.A., Jafari, 2010. Multi-objective Optimization of Orthogonally Stiffened Cylindrical Shells for Minimum Weight and Maximum Axial Buckling Load. *Thin- Walled Structures* 48, 979–988
 8. Firl, K., Bletzinger, 2012. Shape Optimization of Thin-Walled Structures Governed by Geometrically Nonlinear Mechanics. *Computational Methods in Applied Mechanics and Engineering*, 107–117.
 9. Mackay, J.R., Keulen, F., 2013. Partial Safety Factor Approach to the Design of Submarine Pressure Hulls using Nonlinear Finite Element Analysis. *Finite Elements in Analysis and Design* 65, 1–16.
 10. Ghasemi, A.R., Multi-Objective Hajmohammad, M.H., 2017. Optimization of Laminated Composite Shells for Minimum Mass/Cost and Maximum Buckling Pressure with Failure Criteria under External Hydrostatic Pressure. *Structure and Multidisciplinary Optimization* 55,
 11. Imran, D., Shi, L., Tong, A., Elahi, H., Waqas, M., Uddin, 2020. Multi- Objective Design Optimization of Composite Submerged Cylindrical Pressure Hull for Minimum Buoyancy Factor and Maximum Buckling Load Capacity. *Defence Technology*.
 12. Imran, D., Shi, L., Tong, H.M., Waqas, M., Uddin, 2021. Design Optimization of Composite Egg-Shaped Submersible Pressure Hull for Minimum Buoyancy Factor. *Defence Technology*, 1817–1832
 13. Yang, Y., Wang, Y., Chen, C., Wang, Y., Liang, S., Yang, 2022. Data- driven Optimization Design of a Novel Pressure Hull for AUV. *Ocean Engineering* 257, 111562.
 14. Gao, Y., Gao, J., Song, X., Ding, H., Wang, H., 2023. A Collaborative Grading Optimization Method of Rib Reinforced Ultra-Thick Composite Pressure Hull. *Ocean Engineering* 274, 114038.
 15. V. Birman and L. W. Byrd, “Modeling and Analysis of Functionally Graded Materials and Structures,” *Applied Mechanics Reviews*, vol. 60, no. 5, pp. 195-216, 2007.
 16. L. M. K. W. A. de Almeida, “Finite Element Analysis of Composite Structures,” *Journal of Composite Materials*, vol. 43, no. 16, pp. 1577- 1597, 2009, doi: 10.1177/0021998308102213.
 17. Shigley, J. E., & Mischke, C. R. (2011). *Mechanical Engineering Design* (9th ed.). New York: McGraw-Hill.
 18. Karam, S. A. (2012). *Analysis of Thin- Walled Structures: Beams, Plates, and Shells*. Springer.

Effect of Pressure on Rough Piston Skirt in Iso-Thermal Hydrodynamic Lubrication Case for High Torque Low Speed Diesel Engine

Arslan ul Hafeez¹, Syed Adnan Qasim²

¹University of Engineering & Technology, Taxila.

²NUTECH, Islamabad

Engr.arslanhafeez@gmail.com

ABSTRACT

Performance, consistency and life of a high-torque low-speed internal combustion (IC) diesel engine are affected by adhesive wear which occurs due to friction, insufficient lubrication and contact of rough piston and cylinder liner surfaces. The heat generation due to viscous shearing increases the engine lubricant temperature which reduces its viscosity, film thickness and load carrying capacity. Under steady conditions 2-D Reynolds Equation is modified by introducing pressure factor for Iso-thermal condition. Finite difference method (FDM) based numerical technique is employed to determine the pressure distributions in the lubricant film formed between the rough piston surfaces interacting with the cylinder liner. The study determines hydrodynamic pressures generated at different speeds due to lateral motion and wedge action of sliding piston skirts.

KEYWORDS: Piston Skirt, Iso-Thermal, Hydrodynamic Pressure, Rough Surfaces Interaction, Wedge Action.

1. INTRODUCTION

Internal combustion diesel engines are widely used in transportation, industrial sector for power generation and many other applications. Depending upon the bore size, diesel engines have various applications. As compared to the SI engines, diesel engines are low speed and due to the higher air fuel ratio, their output power is more, that's why it is known as high torque engine. Performance, reliability and enhanced life are major considerations in IC engines, which are affected by adhesive wear. Adhesive wear may occur due the friction, insufficient lubrication and contact of relative rough surfaces which ultimately reduces the efficiency of IC engine. It is widely accepted that piston assemblies are major contributor in mechanical friction and adhesive wear within the IC engine, having a worse effect on the engine fuel efficiency.

IC engine has a component moving in a relative motion with each other, both sliding and rotary motions. If we typically talk about the piston, it has a sliding motion with respect to the liner. Whenever two bodies are in relative movement with respect to one and other, friction and contact between the moving surfaces may occur. In order to avoid contact between the two, lubricants are used to fill the gap and carry the applied load.

Piston skirt is the area of piston below the ring pack. As it lies under the oil control ring, it has a thick film lubrication as compared to that of piston rings. The surface of the piston skirt is generally left rough to retain the lubricant. The diameter of skirt is slightly larger than the piston in

order to prevent damage to liner surface during the movement of piston. Piston Skirt may also serve as a guide, as the piston moves up and down in the cylinder.

Lubricant viscosity has a direct relation with the applied pressure, as pressure increases, viscosity of the oil increases. This effect is of particular importance of highly loaded concentrated contacts, pressure experienced in these aspects are so high that the lubricating oil may act as a solid.

Surface Roughness domain

MATLAB code was generated for the evaluation of surface directionality, and the input parameters used are given below:

Table 1: Input parameters for rough surface generation

Parameters	Values
RMS roughness of Piston Skirt, σ_1	1.2 μ m
RMS roughness of cylinder liner, σ_2	1.4 μ m
Clearance b/w the skirt and liner surface	1.04mm
Characteristic Length	63.8mm
Number of sample points	100

The surface and contours generated by using the MATLAB code are given below:

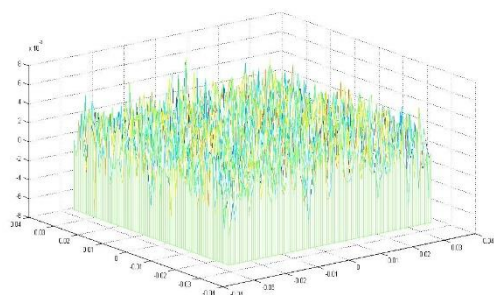


Figure 1: Rough Skirt surface

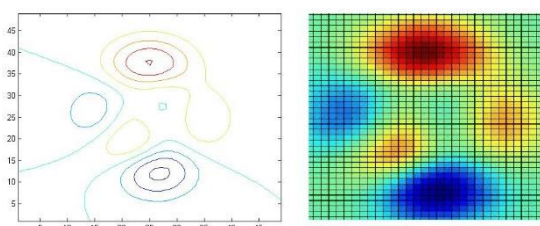


Figure 2: Rough Surface Orientation

In spite of having any specific direction, the roughness with analogous circles is assumed to be isotropic. From the above orientation diagrams it is clear that the given geometry is isotropic.

2. MATHEMATICAL MODEL

Reynolds equation is used as a mathematical model to get the hydrodynamic pressures. In this research, the Reynolds equation is derived or formulated by considering the fluid element in equilibrium condition and then applying the continuity of flow. Continuity principle said that “under steady conditions the flow coming inwards must balance the flow in outwards direction”. Considering the uni-directional velocity, steady film thickness, no slip condition between the fluid and solid plate at boundaries and assuming the constant viscosity; the basic model for hydrodynamic pressure of sliding surfaces will be:

$$\frac{\partial}{\partial x} \left(\frac{h^3}{\eta} \frac{\partial p}{\partial x} \right) + \frac{\partial}{\partial z} \left(\frac{h^3}{\eta} \frac{\partial p}{\partial z} \right) = 6 \left(\frac{W dh}{dz} \right)$$

(1)

When the surfaces are considered as rough surfaces, the correction factors must be added in the mathematical model. By incorporating the flow factors in equation (1) we have;

$$\frac{\partial}{\partial x} \left(\frac{h^3}{\eta} \phi_x \frac{\partial p}{\partial x} \right) + \frac{\partial}{\partial z} \left(\frac{h^3}{\eta} \phi_z \frac{\partial p}{\partial z} \right) = 6 W \left(\frac{dh}{dz} + \sigma \frac{\partial \phi_s}{\partial z} \right)$$

(2)

Where, ϕ_x and ϕ_z are pressure flow factors acting as a correction factor for pressure in ‘x’ and ‘z’ directions and ϕ_s is the shear flow factor which defines the extra flow due to combine effect of sliding and surface roughness.

3. RESULTS AND DISCUSSIONS

The change in piston top & bottom hydrodynamic pressure due to roughness are analysed for the isothermal case. Along with the axial motion, piston also has a lateral motion towards the liner. As the cylinder liner is fixed and rigid, for the change in position of piston towards the liner; there is a change in hydrodynamic pressure.

Engine running at 900 RPM

At low rpm or idling speed i.e. 900 rpm, the hydrodynamic pressure generation is less and increases as the rpm increases. Pressure generates from the mid of the piston skirt to top of the surface. Results shows that there is a shift in pressure from top of the skirt to the bottom of the skirt after expansion stroke for the rough piston skirt surface.

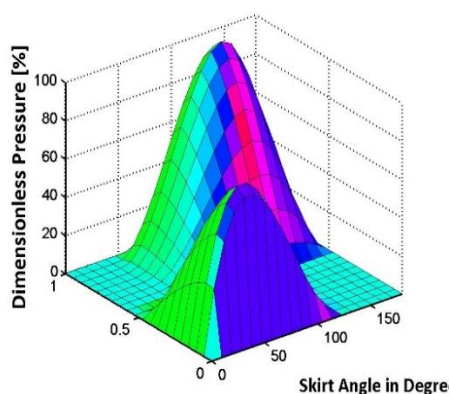


Figure 3: Pressure at 1degree

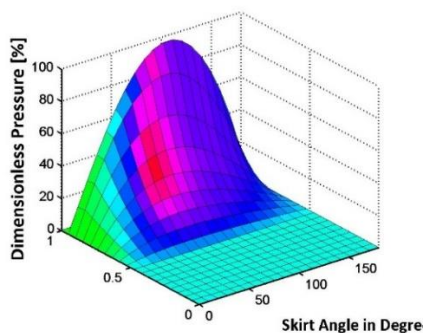


Figure 4: Pressure at 90 degree

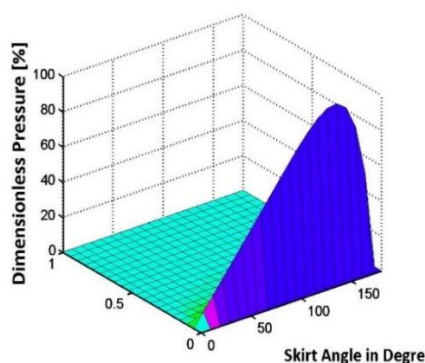


Figure 7: Pressure at 450 degree

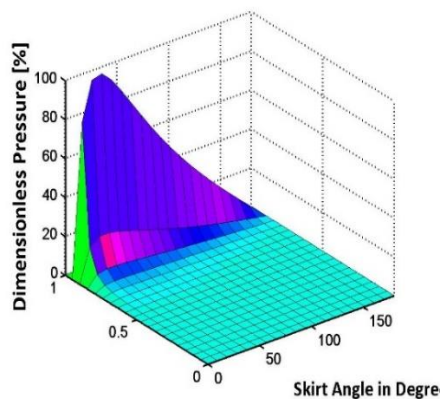


Figure 5: Pressure at 180 degree

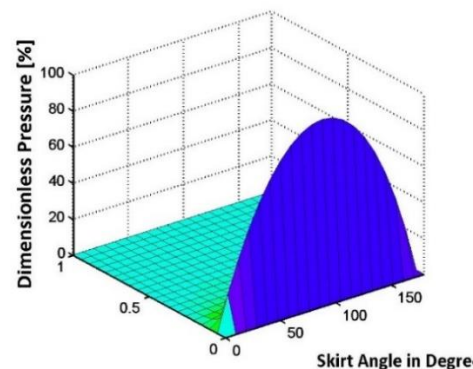


Figure 8: Pressure at 540 degree

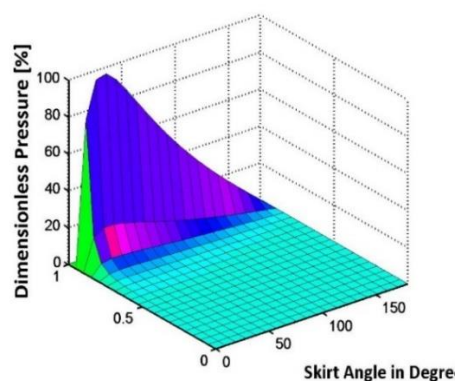


Figure 6: Pressure at 270 degree

Engine Running at 1600 RPM

As the speed and load increases, there is a reduction in lubricant film. The hydrodynamic pressure generation is higher for the thin lubricant film at high load and speed. Hydrodynamic pressure is generated from the middle of the skirt to the top surface of the skirt for the induction and compression stroke. But at the end of compression stroke it is shifted towards the left side and just after the compression when expansion takes place, hydrodynamic pressure is shifted towards the bottom of the skirt due to thrust load during expansion. Results show that pressure generation at high rpm incorporating the roughness is slightly higher. As at high rpm values the change in piston position or lateral motion is comparatively more, there is a non-conformal or uniform pressure distribution just after the compression stroke between the skirt and liner towards the bottom of skirt during to thrust produced due to expansion.

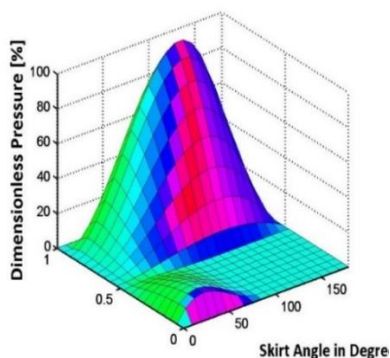


Figure 9: Pressure at 1 degree

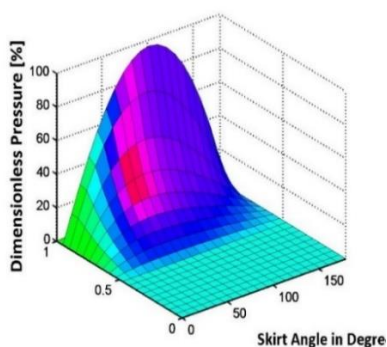


Figure 10: Pressure at 90 degree

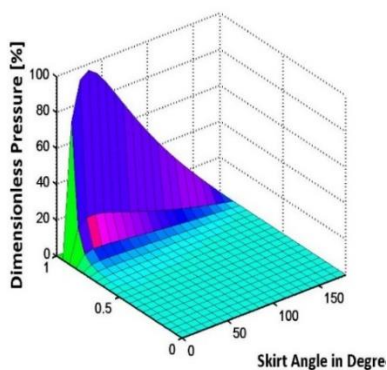


Figure 11: Pressure at 180 degree

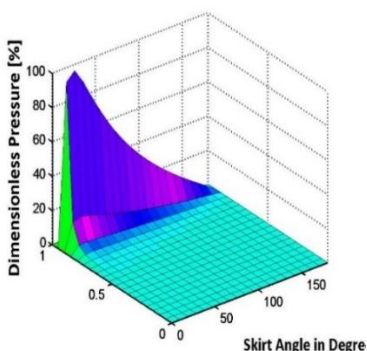


Figure 12: Pressure at 270 degree

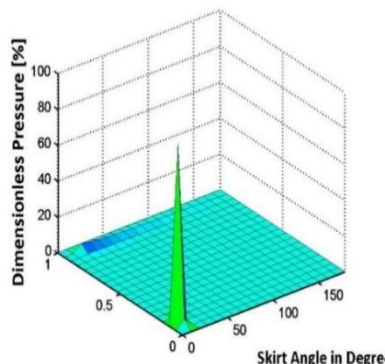


Figure 13: Pressure at 450 degree

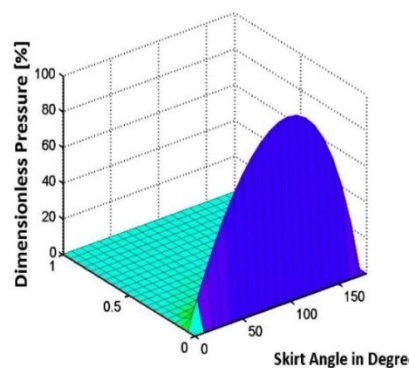


Figure 14: Pressure at 540 degree

4. CONCLUSION

User defined data/specifications for piston and lubricant were used, like radius of piston skirt, skirt-liner clearance, piston skirt height, roughness of piston and skirt and viscosity of lubricant etc. For the induction stroke, the pressure profile is generated from the middle of skirt to the top surface of the skirt. Hydrodynamic pressure generation shifted towards the left side for the compression stroke and shift of pressure toward the bottom of the skirt during expansion. At high rpm value there is a non-uniform pressure (after compression stroke/ during expansion stroke) which may be due to point contact due to thrust produced by expansion or presence of dirt particle which act like a solid between the skirt and liner surface.

ACKNOWLEDGMENT

First, I would like to thank Almighty Allah for blessing me with the ability and potential to do research and work.



First International Conference on Advances in Mechanical, Materials, Mechatronics, and Energy Engineering (ICAME-24)



I would like to thank my supervisor, Dr. Syed Adnan Qasim, Dr. Riffat Asim Pasha (Chairman Mechanical Dept. UET Taxila) and Dr. Mubashir Gulzar for their kind advice, suggestions, motivation and encouragement during my research work.

REFERENCES

1. Shukla, J.B., *A new theory of lubrication for rough surfaces*. *Wear*, 1978. **49**(1): p. 33-42.
2. Mishra, P.C., *Modeling the root causes of engine friction loss: Transient elastohydrodynamics of a piston subsystem and cylinder liner lubricated contact*. *Applied Mathematical Modelling*, 2015. **39**(8): p. 2234-2260.
3. Gulzar, M., S. Qasim, and R. Mufti, *Modeling Surface Roughness Effects On Piston Skirt Ehl In Initial Engine Start Up Using High And Low Viscosity Grade Oils*. 2013.
4. Patir, N. and H.S. Cheng, *Application of Average Flow Model to Lubrication Between Rough Sliding Surfaces*. *Journal of Lubrication Technology*, 1979. **101**(2): p. 2



Designed by :
Abdul Haseeb
Shoaib Zafar